Predicting the internal structure of fault zones in basalt sequences, and their effect on along- and across-fault fluid flow

Rachael Ellen
B.Sc. (Hons) University of Glasgow

Thesis submitted for Degree of Doctor of Philosophy

Department of Civil and Environmental Engineering
Faculty of Engineering
University of Strathclyde

December 2012

Declaration

This thesis is the result of the author's original research. It has been composed by the author, and has not been previously submitted for examination which has led to the award of a degree. The research was supervised by Prof. Zoe Shipton, Prof. Rebecca Lunn, Prof. Martin Lee and Dr. David Brown. Any published or unpublished work by other authors has been given full acknowledgment in the text.

Rachael Ellen

December 2012

Dedication

For Grandpa Emmerson and Grandpa Ellen.

You were both very special to me in so many ways. Grandpa Emmerson, you inspired me from an early age to love rocks and the outdoors, and it is undoubtedly down to you that I have delved this far into the vast depths of geology – for that I will always be grateful. As you said, I have come to truly realise the meaning of 'the more you learn, the less you know'! Grandpa Ellen, you were so very supportive of me always, and so keen to know how my 'rockateering' was progressing and where I was going next.

Even though you couldn't be here, your constant wisdom, support, care and love has played a huge role in seeing me through to the end of this PhD.

Abstract

Interest in the architecture and fluid flow potential of fault zones in basalt sequences has intensified over recent years, due to their applications in the hydrocarbon industry and CO_2 storage. In this study, field mapping is combined with micro-structural analyses and flow modelling to evaluate fault growth, evolution, fluid-rock interactions, and permeability changes over time in faults in basalt sequences.

Twelve brittle fault zones cutting basalt sequences in the North Atlantic Igneous Province were studied. This study finds that fault architecture is ultimately controlled by displacement and juxtaposition. Self-juxtaposed faults (i.e. basalt faulted against itself) are characterised by wide zones of brecciation, cataclasis, fracturing, mineralisation and alteration. Non self-juxtaposed faults (i.e. basalt faulted against an inter-lava unit) are characterised by relatively narrow principal slip zones, filled with clay smears or clay-rich gouge derived from inter-lava beds.

This study also finds that brittle deformation of basalts at the grain scale is mineralogy dependent. Fe-Ti oxides and pyroxenes deform by intragranular fracturing and grain size reduction, whereas olivines and feldspars are susceptible to replacement by clay and zeolites. Fault rock bulk chemistries are likely to differ from their host rocks, and this is controlled by secondary mineral formation, with zeolite and clay minerals playing an important role.

Flow modelling in this study shows that controls on along- and across-fault fluid flow can significantly change fault zone bulk permeability over time, as a result of mineralisation and alteration of the fault zone as it evolves.

The results from this study are used to propose a model for how fault strength, fault-related alteration, and permeability change over time in fault zones in basalt sequences. Results highlight the impact that fault-related alteration could have on CO_2 storage. A predictive model for fault structure at depth, developed from this study's findings, is presented for fault zones in basalt sequences, which has particular relevance to the hydrocarbon and CO_2 industry.

Table of Contents

List of Figures

List of Tables

Acknowledgements

This PhD studentship and a large part of the fieldwork were possible due to funding by the Carnegie Trust for the Universities of Scotland – thank you very much for your support over the last three years.

Firstly, I would like to say a huge thank you to my supervisors Zoe Shipton, Rebecca Lunn, Martin Lee and David Brown for their invaluable support, time, advice, guidance, friendship and help. Zoe, thank you for always believing in me and for all your words of encouragement! Becky, thank you for always being honest with me about my ideas, and explaining things to me in terms of Olympic canoeists! Martin, thank you so much for your patience and for always having time for me, even when zeolites were being 'the work of the devil'. Davie, thank you for being there for me with all my basalty questions and good banter!

I'd also like to thank Brian Bell for his excellent guidance with fault locations in Mull and Skye. Thank you also to Amy Clifton and Kirby Young for their help and advice in Iceland, and particularly to Kirby for showing us some good field sites. Thank you so much to Mikael Attal as well for finding my first fault in Iceland, thanks to an entirely random coincidence. Thank you also to Richard Walker for locations, advice and fieldwork assistance on the faults in the Faroe Islands.

A big thank you must also go to Yannick, Ali, Euan, Stella, Heather, Grainne, Susan, Stewart, George, Erica and Chris (fellow FAFFers), for supporting and helping me out with my PhD at some point or another. In particular a huge thank you to Yannick for showing me how to run the MATLAB models! Thank you to Peter Chung, for your invaluable SEM help and thank you also John Gilleece, for gallantly coping with my awful fragile samples and persevering to give me excellent thin sections. Thank you Craig Barrie for all your time, help and advice regarding stable isotopes. Thanks also to the girls (Laura, Clare, Susan, Joanne, Penne, Rebecca, Heidi, Marie) and Mahmood in the Gregory Building for the chats and laughs, as well as Ross and Steph at Strathclyde. Thanks also to Dawn Stewart and Lisa Lyons for much needed help with the paperwork side of things during this PhD. I must also thank 'Itsashame' for his wise words regarding MMORPGs and PhDs…they don't mix well!

Rachael Ellen

Susan, thank you so much for finding the Lawther Fault (named proudly after you!) and for coming with me to Kerrera for some fault/puppy spotting. Joanne, thank you for 'reluctantly' agreeing to be my field assistant for Iceland and helping me navigate the Miklabraut road!

Words cannot express how thankful I am to my family for braving the wilds and the geological unknown to be my field assistants, so a very special thank you goes to Dad, Mum and Auntie Shelagh for being so willing to field assist and to learn about geology – thank you so much for your enthusiasm, willingness to learn, and for not complaining!!! Dad, in particular thank you for always bringing the fieldwork essentials (picnic rug, tent, camp-fire, umbrella and chocolate) and for driving whilst I 'fault-spotted' and for taking more than your fair share of the rucksack weight! Thank you Mum for being my 'professional' photographer, for braving the Faroese roads (and Torshavn during St Olaf's Festival!), and for being my print and Word genius.

I'd also like to say a very special thank you to my family and friends for being such a huge source of support and love for me during this PhD – Dad, Mum, and Becca, thank you for your encouragement and for believing in me throughout this PhD, particularly when I couldn't believe in myself. Through all the ups and downs you have always been there for me with your full support. Thank you Subby for being around for silly time (and proof-reading!), a welcome relief from PhD-ing, and again to Auntie Shelagh for her support! A big thank you to Pie for forcing writing-breaks on me by sitting on my laptop and being cute, and for generally being the best cat in the world! Thank you also to Lisa, and a big thank you to Carly for distracting me by whisking me off to Orkney for a much needed break, and for your unwavering understanding and support! And of course, last but in no way least, a massive thanks to Phil. You have been so patient and supportive throughout my PhD, and despite me often being a complete stress-bucket, you haven't complained! So, to all my family and friends - all of your endless support and love has helped me through this PhD, and for that I will always be so grateful.

Rachael Ellen

1. Introduction

1.1. Fault classification

Characterising fault zone properties is important in predicting fault zone architecture, permeability and strength. Predicting the internal structure of faults, and their evolution through time, is important because faults accommodate brittle displacement in the Earth's crust (by earthquakes), and control fluid flow in the sub-surface. As a fault grows (by increasing displacement), its internal structure changes, subsequently varying the hydraulic structure and strength of the fault through time. It is therefore critical to gain an understanding of fault behaviour in order to predict these properties, which are essential to earthquake, industry and CO_2 applications. This chapter reviews the current knowledge on fault zone classification, architecture and fluid flow characteristics, focussing particularly on extensional faults cutting a range of lithologies. By reviewing these, it can then be determined if extensional faults cutting basalt sequences (the focus of this thesis) are unique with respect to faults cutting other lithologies.

1.1.1. Fault initiation

Brittle faults in the upper crust initiate on opening-mode structures, and develop into faults through linkage of pre-existing and precursory structures (Crider and Peacock, 2004). Pre-existing structures (such as joints) form as a result of a previous deformation and/or cooling events, unrelated to the developing fault (e.g. Forslund and Gudmundsson, 1992; Gudmundsson, 1992a; Gudmundsson, 1992b). Pre-cursory structures form earlier in the same deformation event related to faulting (Crider and Peacock, 2004). Faults grow by linkage of en-echelon joints and splay-fractures at the tips of the developing faults (Martel, 1990; Segall and Pollard, 1982). This mode of fault initiation has been found in a range of lithologies (e.g. carbonates, layered clastic sequences, crystalline rocks).

Fault initiation by incorporation of fractured wall rocks into the developing fault is also found. This behaviour has been recorded by Soden (2008) in faults cutting ignimbrites, who suggests dilation of joints has allowed joint surfaces to move past one another.

1.1.2. Fault architecture

Observations of fault structure at depth are difficult to obtain. Exhumed faults from depth, now exposed at the surface, have been studied to understand fault architecture and permeability history. Studies of fault structure are classically described following Caine et al's (1996) classification (Figure 1.1). They describe fault zones as being composed of a **protolith** (the type of rock being faulted), and a **damage zone** (fractured protolith, in which original protolith features are discernable) which surrounds a **fault core** (the zone which has accommodated most displacement and where original protolith features are destroyed). It is generally accepted that fault core material is formed as a result of wear and attrition of wall rocks and asperity removal (Scholz, 1987; Power et al., 1998; Childs et al., 2009).

The damage zone and fault core characteristics differ depending on a number of factors, such as the lithology the fault is cutting, displacement value, stress state, fluid chemistry and degree of strain localization (Caine et al., 1996). Generally in extensional high angle faults (60-85°), the higher the displacement, the more complex the fault zone is (e.g. Shipton et al., 2006; Childs et al., 2009).

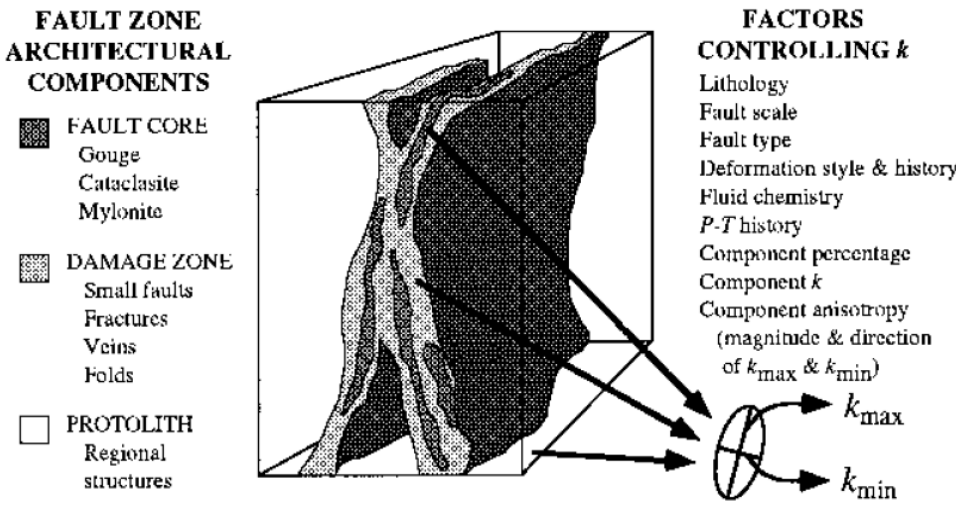

Figure 1.1: Conceptual cartoon for fault architecture and factors controlling K, with fault components labelled (from Caine et al., 1996).

Fault architecture in **crystalline** rocks (e.g. metamorphic rocks, granites) is typically dominated by fractures in the damage zone, and a fault core of phyllosilicate-rich fault rock (e.g. Chester and Logan, 1986) or multiple zones of phyllosilicate-rich fault gouge cores bounding fractured protolith (e.g. Faulkner et al., 2003; Mitchell and Faulkner, 2009).

Damage zones in **carbonate** hosted faults are dominated by sub-parallel joints or solution cleavage surfaces (e.g. Billi, 2010), and fault cores are dominated by cataclastic rocks. Where large displacement faults have cut multiple host rocks (e.g. layered carbonate sequences with shale units), continuous, composite fault cores are found composed of cataclasites and shale gouges (e.g. Bastesen and Braathen, 2010; Billi, 2010).

Faults in clean, porous **sandstone** initiate and grow by the formation and linkage of deformation band clusters (Aydin and Johnson, 1978). Deformation bands are high strain localization zones that develop in response to faulting of granular rocks. Deformation occurs at the grain scale by grain sliding and rotation (Fossen et al., 2007). In sandstones, one or more through-going slip surfaces are surrounded by deformation bands, and fault cores are composed of cataclastic fault rocks (Shipton and Cowie, 2001; Fisher and Knipe, 2001; Saillet and Wibberley, 2010).

Deformation bands are also found in other high porosity granular lithologies such as unconsolidated sediments (Rawling and Goodwin, 2003; Loveless et al., 2011) and, more importantly for this study of faults cutting basalt sequences, hyaloclastites (Tewksbury, 2010), porous volcanic tuff (Evans and Bradbury, 2004) and ash-rich friable ignimbrites (Soden, 2008).

1.1.3. Effect of mechanical stratigraphy on fault architecture

Layering of the host rock lithology also controls fault structure. Faulting in mechanically layered sequences results in variations in fault dip (Ferrill and Morris, 2003). This fault refraction causes fault dilation/dilational jogs in competent (strong) layers, where the rock fails by hybrid mode. Competent layers have steeper fault dips than incompetent (weak layers), where shear failure occurs (Figure 1.2).

Refraction of fault dip can occur as a result of linkage of originally vertically segmented faults. For example, Childs et al., (1996) and Peacock and Zhang (1994) interpret that refracted faults in layered sequences initiate as extensional fractures in competent layers, and propagate upward or downward in incompetent layers. Discrete element modelling by Schöpfer et al., (2006) in brittle/ductile multilayer sequences finds that faults localise initially as Mode I fractures (tensile opening with no shear) in brittle layers, and monoclinal folding prior to failure is accommodated by ductile flow in the ductile layers. Schöpfer et al., (2006) find that vertically segmented faults in competent layers link via shallow dipping faults in the incompetent layers.

Therefore, it is important to consider the behaviour of faults cutting both individual lithology types and the overall sequence of those lithologies (i.e. layered vs. massive), as mechanical stratigraphy has a strong control on fault architecture and permeability structure (discussed in the next section).

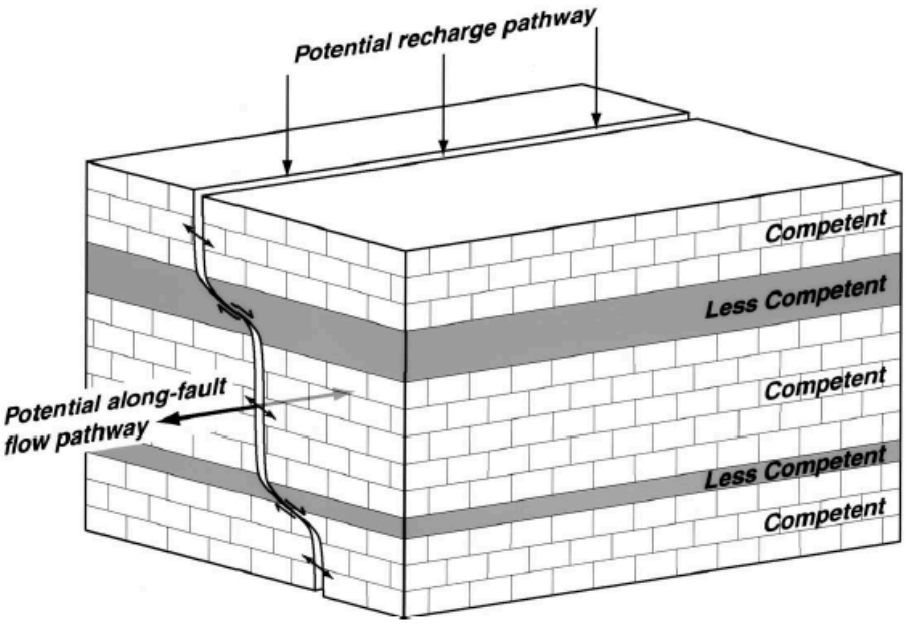

Figure 1.2 Block diagram from Ferrill and Morris (2003), illustrating dilational fault segments and their role in subsurface groundwater flow.

1.1.4. Faults and fluid flow

Although it is well established that faults can act as barriers and/or conduits to fluid flow, fault permeability changes over time as a result of fault evolution (e.g. open pathways sealed by cataclasis or formation of clay gouge). In layered sequences, faults in competent layers will enhance fluid flow, and faults in incompetent layers will inhibit fluid flow (Figure 1.2). However, with increasing displacement, smearing of incompetent layers across competent layers could impede fluid flow and act as a barrier. For example, phyllosilicate-rich layers in sedimentary sequences (such as mudstones) will likely result in an impermeable barrier to fluid flow as a result of clay smearing along the fault at high displacements (Fisher and Knipe, 1998; Knipe, 1997). Deformation bands (in sandstone hosted faults) often result in a reduction in porosity and permeability (Fossen et al., 2007) but, over time, deformation bands can evolve into slip surfaces at higher strains. These slip surfaces can act as high permeability conduits (Shipton and Cowie, 2001; Shipton et al., 2002).

Fluids flowing along permeable pathways can alter the surrounding rock via fluid-rock interactions and therefore change the character of the fault zone. Depending on the original composition of the host rock, dissolution and reprecipitation of certain minerals will occur. Cataclasis results in reduced grain sizes, increasing the surface area for fluids to act upon, and promoting reactions (Fitz Gerald and Stunitz, 1993).

Depending on reactions between the fluid and the rock following faulting, pore space can be created (e.g. by dissolution of $CaCO_3$ in carbonate rocks) or filled (e.g. by precipitation of phyllosilicate minerals in crystalline rocks). In carbonate hosted faults, pressure solution seams and calcite veins are commonly found as a result of dissolution and reprecipitation of $CaCO_3$ (Billi et al., 2003). In crystalline rocks, hydrothermal alteration forms new minerals of mica, chlorite, and epidote along the fault (Bruhn et al., 1994).

Fluid-rock interactions can also result in weakening or strengthening of the fault zone, depending on which minerals are precipitated. Cementation of fault rocks by K-feldspar and quartz strengthen the fault zone, whilst clays and micas weaken it, resulting in fault-strengthening and fault-weakening respectively (Wintsch et al., 1995; Wibberley, 1999). However, this behaviour is stress and depth dependant. Frictional laboratory experiments find that clay gouges undergo strain hardening at high normal stresses (Morrow et al., 1992), but at lower normal stresses strain weakening can be achieved (Saffer et al., 2001). At 2-3km in the crust, clays in the San Andreas Fault are dominated by smectite clays and exhibit weakening behaviour (Holdsworth et al., 2011).

It is therefore important not only to understand the permeability structure (i.e. pathways, connectivity, etc) of a fault, but also the effect fluids have had on the fault zone over time (i.e. alteration, weakening etc).

1.1.5. Predicting fault structure

Predictions of fault structure are important for understanding fault growth and evolution in 4D, and for understanding its effect on fluid flow. Attempts at predicting fault structure have looked at thickness-displacement relationships (Scholz, 1987, Hull, 1988), where a correlation between the thickness of the fault zone and its displacement is found, i.e. the higher the displacement, the thicker the fault zone. However, for a single fault, fault zone thickness can vary by three orders of magnitude (e.g. Shipton et al., 2006), and thus predictions on fault thickness based on displacement are not reliable. Fault displacement is proportional to fault length (Cowie and Scholz, 1992), and so there is a constant displacement to length ratio as faults grow. Faults usually have little or zero displacement at their tips, and maximum displacement at their centres (Walsh and Watterson, 1988; Kim and Sanderson, 2005). The displacement length profile of faults has been used to predict how faults have grown, e.g. as a result of coalescence of kinematically related faults (Walsh et al., 2003).

In industry, predictions of fault structure at depth are calculated using fault-seal analysis methods. Allan diagrams are a map of the fault plane with hanging wall and footwall intersections superimposed on the fault surface, and show possible fluid pathways and locations of flow seals and conduits (Allan, 1989), e.g. sandstones juxtaposed against impermeable rocks such as shales would be expected to seal, whereas sandstones juxtaposed against themselves or other sandstones may leak (Fisher and Knipe, 1998). This is important within reservoirs containing faults, and for assessing where hydrocarbon migration may have occurred across a fault. Allan diagrams commonly require detailed seismic data to interpret horizons offset across the fault. A simpler approach to this can be applied using juxtaposition triangle diagrams (described further in Chapter 7), where the juxtapositions of hanging wall and footwall rocks can be determined across a range of fault throws (Knipe, 1997). Fault rocks expected from juxtapositions of certain units can also be superimposed on

juxtaposition diagrams. For example, Fisher and Knipe (1998) classified siliciclastic fault rock and resulting permeability according to juxtaposition type.

Allan and juxtaposition triangle diagrams are used to estimate reservoir juxtapositions due to faulting, thus predictions on fault seal properties are based on which lithology is juxtaposed against another across a fault, rather than on what the fault properties are. Therefore, actual fault properties (such as thickness and composition) cannot be predicted from Allan diagrams and juxtaposition triangle diagrams.

One of the main methods developed to estimate fault rock composition is the shale-gouge ratio (SGR) algorithm (Yielding et al., 1997). The SGR estimates clay content from the faulted lithology, and how that is mixed within the fault zone. It calculates the total amount of clay within the host rock that is displaced past a certain point on the fault, using the following equation from Yielding et al., (1997):

$$SGR = \frac{\sum[(rock\ thickness)\,x\,(zone\ clay\ fraction)]}{Fault\ throw}\ x\ 100\%$$

Faulting of shale layers can result in continuous clay smears along the fault, which would promote fault sealing. Therefore, if the above calculation is applied in a shale-rich sequence, the resulting SGR % will be high, and the fault will be modelled as a seal. If, however, the calculation is applied in a mixed sand-shale sequence, the fault will be modelled as a combined conduit-seal, due to different juxtaposition types across the fault.

However, Allan and juxtaposition diagrams, and the SGR algorithm do not take into account how much material from the host rock is actually incorporated into the fault zone; the heterogeneous nature of faults; mechanism of faulting; thickness variations along the fault; or alteration

style. Whilst a clay smear can be continuous, it can also be very thin, and therefore may not act as a seal. Also, depending on permeability history and fluid-rock interactions, permeability may have been increased in the gouge due to breakdown of clays or cementation of the gouge by stronger minerals, followed by fracturing.

1.2. Rationale for studying faults in basalt sequences

Existing studies of faults formed at depth have mostly focused on siliciclastic lithologies (e.g. Shipton and Cowie, 2001; Fisher and Knipe, 1998; Foxford et al., 1998; Aydin and Johnson., 1978; Walsh and Watterson 1988). However, interest in the architecture and fluid flow potential of fault zones in igneous rocks, and particularly basalt sequences, has intensified over recent years, due to their applications in the hydrocarbon industry, CCS, and nuclear waste storage (Petford and McCaffrey, 2003). Over 20% of hydrocarbon reservoirs in igneous rock are found in basalt lava sequences (basalt and volcaniclastic rocks), and hydrocarbon exploration in these lithologies is ongoing in Greenland and the North Atlantic Margin (Schutter, 2003; Rogers et al., 2006; Skaarup and Chalmers, 1998). Hydrocarbons are either found in basalt reservoirs (accommodated by fractures within basalt) as a result of hydrocarbon migration from a source rock beneath the basalt, or basalts can also act as a cap rock to reservoir units (Petford and McCaffrey, 2003). Basalt sequences are also becoming increasingly important for CO_2 storage: basalt is naturally rich in Ca and Mg, which can react with supercritical CO_2, and lock in CO_2 as carbonate (Alfredsson et al., 2008; McGrail et al., 2006).

1.2.1. Previous studies of faults in basalt sequences

Studies of fault structure formed at depth in sub-aerially erupted basalts are in their infancy. Studies of faults in basalt have largely concentrated on near-surface faults cutting recent lava flows at spreading centres such as Iceland (Forslund and Gudmundsson, 1992; Gudmundsson, 1992a;

Gudmundsson, 1992b), the Ethiopian Rift (Acocella et al., 2003) and Hawaii (Holland et al., 2006; Martel and Langley, 2006). Other studies of faults in basalt have been carried out for kinematic analysis for palaeostress reconstructions, particularly from Iceland (Fjader et al., 1993; Bergerat et al., 1990; Bergerat and Angelier, 1998; Villemin et al., 1994; Khodayar and Einarsson, 2002; Khodayar, 2004; Tentler, 2005; Young et al., 1985), and the British-Irish Palaeogene Igneous Province (e.g. Mathieu and Vries, 2009).

Studies of faults in oceanic crust basalt have found damage zones of fractured and mineralised basalt surrounding fault cores of breccias and cataclasites, with a matrix of chlorite and quartz (Hayman and Karson, 2007; Hayman and Karson, 2009). Significant hydrothermal alteration of the fault rocks has occurred, with chlorite and saponite prominent, and replacement of pyroxenes by amphibole and replacement of plagioclase feldspars by albite (Hayman and Karson, 2007). Hydrothermal alteration of basalts to epidosites and serpentinites have also been recorded at the Troodos Ophiolite, Cyprus (e.g. Jowitt et al., 2007; Cann and Gillis., 2004; Nuriel et al., 2009).

Only relatively recently have the controls of fault structures in basalt sequences been considered. Tentler and Temperley (2006) compare fault structure in three mineralogically identical lithologies with different pre-existing structures: hyaloclastite, pillow basalt, and columnar jointed basalt. They find that faults in hyaloclastite are characterised by deformation bands and undulating slip surfaces, with gouge along slip surfaces. In faulted pillow basalts, no continuous slip surfaces develop, as strain is accommodated within pervasive pre-existing structures within the pillows. In columnar jointed lava, strain is also accommodated in pre-existing fractures, particularly within blocky lavas with cooling joints reactivated as slip surfaces. Tentler and Temperley (2006) therefore concluded that whilst the lithologies are chemically similar, their

significantly different pre-existing structure has an impact on the resulting fault structure.

Walker et al., (2012a) studied fault growth and evolution in layered basalt sequences in the Faroe Islands, with a particular emphasis on the fault-related deformation and fault rocks associated with faulting in basalt lava flows. They found deformation is typically dominated by extensional fractures, and with increasing distance from the principal slip surface, a decrease in extensional-shear veins/fractures and fault rocks. With increasing displacement, Walker et al., (2012a) noted a greater intensity of fractures and more complex fault rocks (e.g. chaotic breccias and cataclasites). They also found that all faults contained clays, calcite and zeolites. Walker et al., (2012a) describe fault zone evolution as protofaults linking to form through-going, irregular fault surfaces with phases of asperity removal.

A summary of previous studies of fault structure and fault rocks found in basalt sequences is presented in Table 1.1.

Table 1.1: Summary of data from faults in basalt sequences identified in previous studies.

Previous Study and Host Rock	Displacement	Fault Width	Fault Characteristics
Walker et al., 2012a **Layered Basalt Sequences**	<30m	Damage Zone: <6m Fault Core: ~1m	**Damage zone** – high fracture and vein density tensile. **Fault Core** – fine grained gouge, altered products. Chlorite and saponite in breccia, actinolite and amphibole replacement. Albitisation.
Mathieu and Vries, 2009, **Basalts**	-	-	Fault breccia
Hayman and Karson, 2007, 2009 **Oceanic Crust Basalt**	<100m	Damage Zone: 1-10m Fault Core: ~1m	**Damage zone** - high fracture and vein density tensile. Breccias, cataclasites, foliated. **Fault core** - fine grained gouge, altered products. Chlorite and saponite in breccia, actinolite and amphibole replacement. Albitisation.
Gudmundsson, 2007, **Basalts**	200m-1400m	Deformation Zone: 300m Fault Core: 10m	Fault rocks crushed and altered. Cataclastic rocks, microbreccias and minor hematite planes. Zeolite and calcite mineralisation. Multiple faults in damage zones.
Tentler and Temperley, 2006 **Hyaloclastites, pillow lavas, columnar jointed lava**	<25m	-	**Hyaloclastites** - undulating slip surfaces, minor deformation bands, fine grained cemented gouge; **Pillow lavas** - strongly influenced by primary fractures, commonly reactivated as shear planes; **Columnar lavas** - system of linked fractures. Strongly controlled by pre-existing cooling joints.
Tentler, 2005 **Basalt, hyaloclastite**	-	Positive correlation in fault breccia thickness to throw.	Fault breccias, alteration in fractures. Shallowing of fault dip in hyaloclastites.
Khodayar and Einarsson., 2004 **Basalt, ignimbrites**	50m, 12m	25m, 1.3m	Fault breccia
Khodayar and Einarsson., 2002 **Basalt, scoria, tuff**	22m, 23m	6m, 8.7m	Mineralised fault breccia, matrix of basalt or scoria. Quartz calcite and zeolite mineralisation. Gouge/altered cataclasite (smectite).
Fjader et al., 1993 **Basalts**	-	-	Striated fault surface with mineralised steps. Extension fractures. Brecciated. Calcite quartz zeolite.
Forslund and Gudmundsson, 1992 **Basalts**	3.5m, 45m	0.7m,1.8m	Incohesive and cohesive crush breccias, basalt clasts in a matrix of hematite and zeolite. Occasional incohesive gouge.
Bergerat et al., 1990, **Basalts**	4m	-	Striated surfaces, crushed.
Young et al., 1985 **Basalts, ash-rich ignimbrites**	200m-1400m	-	Cataclastic rocks, sheared, brecciated, heavily mineralised. Quartz, calcite and zeolite mineralisation.

1.3. Aims of this study

As faults can act as barriers and/or conduits to fluid flow, understanding the behaviour of faults in basalt sequences is extremely important for CO_2 and hydrocarbon applications. Whilst previous studies of faults in basalt provide important details and insights as to how basalt itself deforms due to faulting, the studies do not exclusively address the following in detail:

a) how extensional faults (formed at depth, i.e. not surface faults) grow and evolve through time in basalt sequences (i.e. basalt flows with interbedded siliciclastic/clay-rich units);

b) what effect basalt sequences as a whole (i.e. basalt lavas with intersedimentary units) and as individual units (i.e. without intersedimentary units) have on fault architecture;

c) what chemical and mineralogical changes sub-aerially erupted basalt undergoes as it deforms as a result of faulting at depth (important for CO_2 storage);

d) how the bulk permeability of faults in basalt sequences evolves over time;

e) equivalent predictive classification schemes for fault rocks in basalt sequences (important for hydrocarbon industry and CO_2 storage).

By addressing these research gaps, this thesis aims to improve predictions of fault structure and fault fluid flow at depth within basalt sequences. As has already been discussed, considering how a fault evolves over time (as a result of, for example, lithology, displacement, fluid-rock interactions and stress), is very important for fault prediction and reducing uncertainty. These controls are explored throughout this thesis.

The main focus of this thesis is to address the above research gaps, using the following aims:

- develop a model for fault growth and evolution in basalt sequences, based on detailed mapping of normal faults cutting basalt sequences exhumed from <2km depth;

- identify controls on fault architecture through time by carrying out field work on faults in basalt sequences;

- carry out detailed microscopic analyses of samples obtained from field work to evaluate mineralogical changes as a result of faulting, and to further understand how faults evolve over time;

- decipher permeability history as faults evolve over time, by using field and microscopic observations with simulations of fluid flow using groundwater simulation models;

- develop a fault rock prediction scheme based on the above points.

By addressing these aims using a mixture of field-, lab- and modelling work, initial predictions on fault structure and permeability at depth can be made for basalt sequence hosted faults.

1.4. Definitions

Throughout this thesis, fault rocks are described using the Woodcock and Mort (2008) terminology, described in Figure 1.3. The zone that has accommodated the most slip, and therefore contains the most fault rocks, is termed the principal slip zone (PSZ), and the slip surface that has accommodated the most slip is termed the principal slip surface (PSS). The fractured rock surrounding the PSZ is described as fault-related deformation surrounding the PSZ in the hanging or footwall.

			non-foliated	foliated
>30% large clasts >2 mm	75-100% large clasts (>2 mm)		fault breccia: crackle breccia	
	60-75% large clasts (>2 mm)		mosaic breccia	
	30-60% large clasts (>2 mm)		chaotic breccia	
<30% large clasts >2 mm	incohesive[1]		**fault gouge**	
	cohesive	glass or devitrified glass	**pseudotachylyte**	
		0-50% matrix (<0.1 mm)	**protocataclasite**	**protomylonite**
		50-90% matrix (<0.1 mm)	**(meso)cataclasite**	**(meso)mylonite**
		90-100% matrix (<0.1 mm)	**ultracataclasite**	**ultramylonite**
		pronounced grain growth		**blastomylonite**[2]

[1]incohesive at present outcrop

[2]some blastomylonites have >30% large porphyroclasts

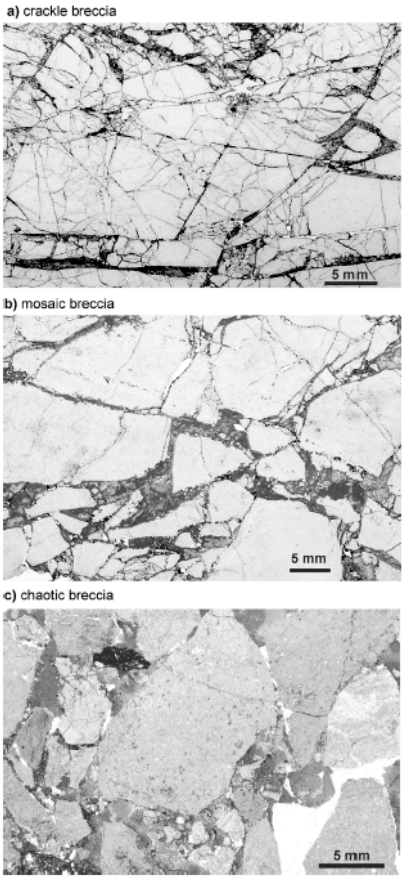

Figure 1.3: Fault rock classification scheme used in this study, from Woodcock and Mort (2008).

Fractures formed as a result of shearing of rocks develop a reproducible pattern, and are classified as 'riedel shears' (Riedel, 1929; Logan et al., 1979; Swanson, 1988). The relationship of these riedel shears to fault zones is shown in Figure 1.4, and where possible, this classification is used to describe fault-related fractures throughout this thesis.

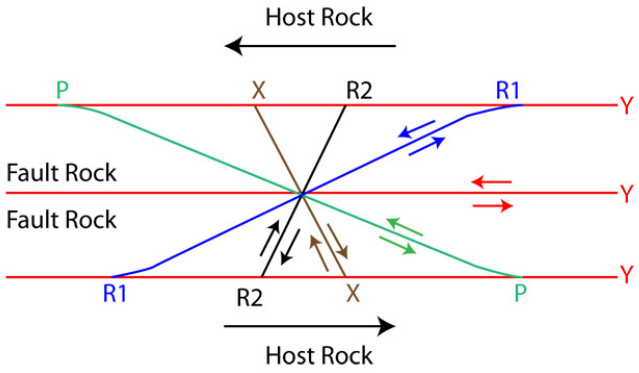

Figure 1.4: Orientations of fractures associated with fault shear zones. R1 and R2 fractures are commonly known as riedel shears (Riedel, 1929). Modified from Logan (2007).

1.5. Thesis outline

Chapter 2 discusses the geological setting for each of the 12 fault localities in Scotland, Iceland and the Faroe Islands. Chapter 2 also discusses the host rocks within each geological setting and at what likely depth each fault formed.

Chapter 3 describes the field observations of faults studied, by presenting detailed fault maps for each fault. The faults have a displacement range from protofaults to 25m faults, and a range of juxtaposition type.

Chapter 4 compares the microstructures found within each host rock and fault rock equivalent, and looks at how mineralogical changes as a result of faulting have occurred.

Chapter 5 looks at the fault structures associated with a 125m displacement fault cutting an ancient (Devonian) basalt layered sequence, exposed on Kerrera. Stable isotope analysis of calcite found within the fault is used to understand the fluid history of the fault.

Chapter 6 utilises the fault maps created in Chapter 3 and microstructural observations from Chapter 4 to model fluid flow through the mapped faults as they evolved over time.

Chapter 7 discusses the observations from the previous chapters and compares them with previous studies of faults, before presenting a new model for predicting fault rocks in basalt and what implications these have in the CO_2 and hydrocarbon industry.

Chapter 8 summarises the conclusions from this study and suggests further work that could be carried out to enhance our knowledge of faults in layered basalt sequences.

2. Geological Setting

2.1. Introduction

In this chapter, the geological setting of each fault site studied is described with the aim of constraining the conditions of fault initiation, growth, type and overall architecture. These conditions depend on many factors governed by the geological setting, and include geological age, level of background alteration, burial depth, host rock type and thickness.

The North Atlantic Igneous Province (NAIP), and the Lorne Plateau Lava Formation (LPLF) were chosen as the study area for this thesis, due to their excellent exposures of extensive basalt sequences. Field sites were chosen based on good exposures of faults cutting these basalt sequences. The geographical location of each field site is given in Figure 2.1, along with the generalised geology of the area. In the following sections of this chapter, each fault site is described by its wider geological setting, followed by a detailed account of the local geology and the host rocks on either side of the studied fault. The local geology description comes partially from the literature but, for all sites, the local geology surrounding the fault was also logged for this thesis. Geological maps for Scotland, digitised from published BGS maps, are also provided for the local geology. For the local geology in Iceland, the surrounding geology was mapped for this thesis. Detailed host rock descriptions of each fault are provided in Chapter 4 for easy reference between host rock and fault rock microstructural comparisons.

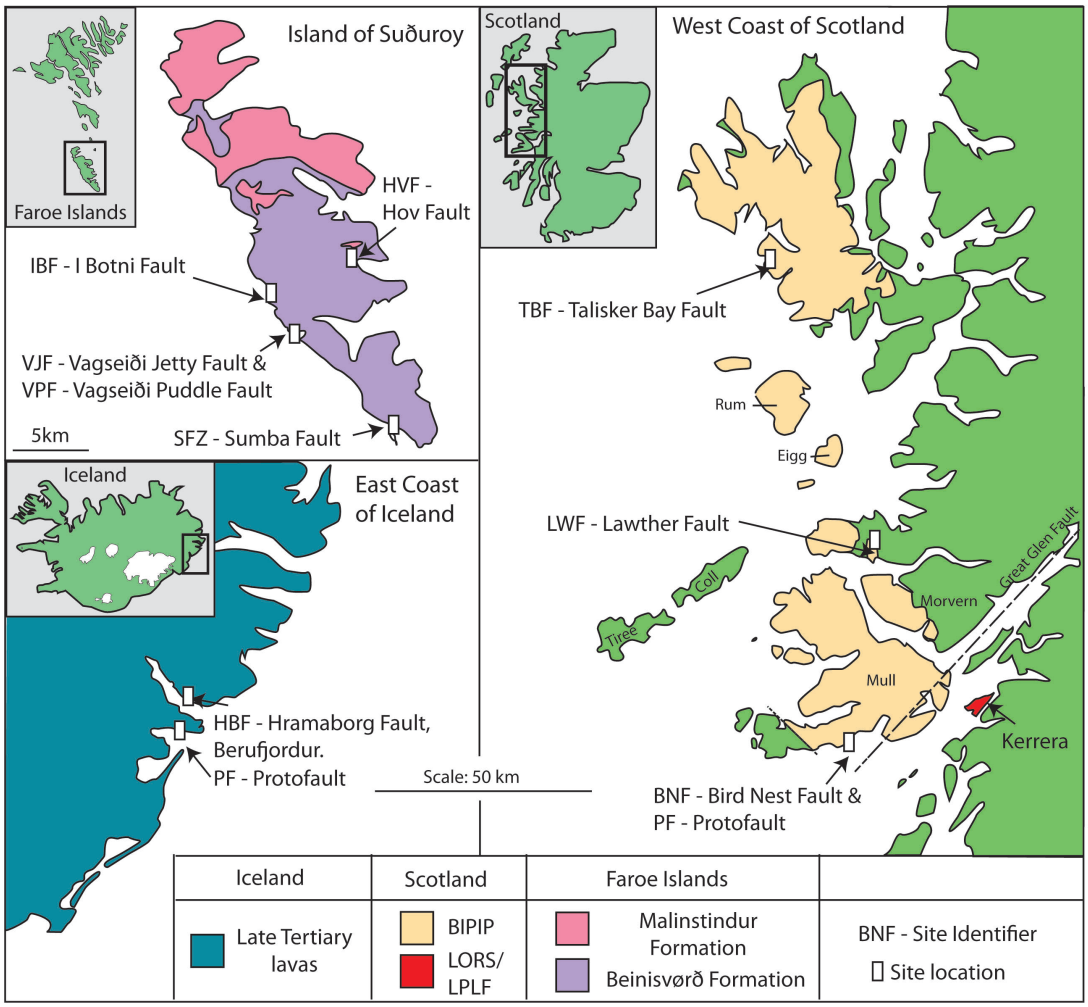

Figure 2.1: Location map showing field sites in Scotland, Iceland, and the Faroe Islands. The distribution of the BIPIP is shown schematically, and the geology of east Iceland has been simplified. At this scale, the geology of Kerrera has been simplified.

2.2. North Atlantic Igneous Province

The North Atlantic Igneous Province (NAIP) is one of the first recognised Large Igneous Provinces (Saunders et al., 1997). It formed in response to the rifting episode that created the North Atlantic Ocean during the early Palaeogene, generating widespread volcanism across the pre-rifted Laurasia and Eurasia continents (Lundin and Doré, 1997). The formation of a major hotspot in the Faroe-Greenland region led to thermal uplift and thinning of the crust, which split between the Palaeocene and Eocene, initiating sea-floor spreading and generating major, fissure-fed, volcanism (Woodcock and Strachan, 2000). The earliest volcanism of the NAIP

occurred ~61 Ma, (Chambers et al., 2005), and volcanism continued across present day Scotland until 58 Ma (Chambers and Pringle, 2001). Following continental breakup, the hotspot derived volcanism migrated northward, forming the flood basalt sequences of east Greenland and the Faroe Islands, emplaced at 59-56 Ma (Larsen et al., 1999; Waagstein et al., 2002). The hotspot is currently active in Iceland and is responsible for the formation of the 13Ma to present day basalt sequences (Ross and Musset, 1976). Thinning of the crust (related to the hotspot migration) was accommodated by dyke intrusion and extensional faulting, a feature typical of plate-spreading centres (e.g. Buck et al., 2005).

Today, the NAIP is exposed as thick flood basalt sequences outcropping in east Greenland, the Faroe Islands (Faroe Islands Basalt Group, FIBG), Iceland, and in north-eastern Ireland and Scotland as part of the British-Irish Palaeogene Igneous Province (BIPIP). The geographical locations of these sequences define the present North-East Atlantic volcanic passive margin. This margin, like many other volcanic passive margins, is becoming an increasingly important target for hydrocarbon exploration and thus the need for understanding the structure, and fault structures, of flood basalt sequences is of great importance.

Fieldwork was undertaken on the BIPIP where it outcrops on the Scottish west coast, on the island of Suðuroy within the FIBG, and in flood basalts on the east coast of Iceland (see Figure 2.1 for maps and location of each study site).

2.3. East Iceland (Hramaborg Fault location)

Iceland forms the most recent portion of the North Atlantic Igneous Province (NAIP), and consists of magmatic formations of three age groups: the Late Tertiary, Early Pleistocene and Late Pleistocene to Holocene (Jóhannesson and Saemundsson, 1998). Each formation is related to crustal spreading on active rift centres (with a shift in the location of rifting

between each) and, therefore, the youngest (Holocene) rocks are found at the present day active rift zone in the centre of Iceland, with the oldest (Late Tertiary) at the outer edges of the island. The eastern coast of Iceland is dominated by Late Tertiary (Upper Miocene to Lower Pliocene) basalt sequences, with a total thickness of over 10km, and dated at ~13Ma by 40Ar/39Ar analysis (Ross and Musset, 1976). Approximately 80% of the total volume of volcanic rocks comprising the eastern coast are flood basalts, with the remainder consisting of silicic lavas and pyroclastic lithologies (Walker, 1963a). Zeolite assemblages found within amygdales in the basalt lavas of Berufjörður, one of the eastern fjords, indicate burial to around 1300-1500m in the study area (Walker, 1960). Subsequent glacial erosion has revealed the stratigraphy and structure of these lavas above sea level in the present day. The lavas are deformed into a monoclinal structure, dipping gently westward in response to down-sagging toward the Late Tertiary rift axis (Walker, 1975). The lavas are dominated by undifferentiated, sub-aerial tholeiitic basalts with subordinate feldspar porphyritic and olivine basalt flows, pyroclastic units (Walker, 1963b) and thin intersedimentary units, including coal. The regionally extensive Skessa Tuff (a green/blue welded ignimbrite unit) crops out within the study area, and is overlain by the Graenavatn Porphyritic Group (Walker, 1958). The surrounding lavas are separated by red volcaniclastic and sedimentary units.

The lavas in the study area are cut by a series of NNE-SSW trending dykes and occasional faults, which are related to the nearby Tertiary volcanic centres (extinct) of Breiðdalur and Álftafjörður. The dyke swarms are purely extensional (Gudmundsson, 1983) and are of similar composition to the lavas they cut, suggesting that these dykes acted as feeders to the volcanoes that produced the lava flows (Walker, 1963b). In active systems, such as the Hengill volcanic system in Iceland (see Figure 2.2), volcanic systems are characterised by magmatic fissures feeding fissure eruptions, with normal faults (induced either by magma movement in the crust or

tectonic extension) accommodating extension on the flanks of the fissure swarms (Tentler and Temperley, 2007). The trend of the dyke swarm at Berufjörður is sub-parallel to the Central Rift Zone of Iceland (i.e. the active Thingvellir Rift), suggesting the regional stress field has not changed much since the Tertiary. At the same orientation and dip as the dyke swarm in Berufjörður, faults are exposed in the study area, often intruded by dykes. Given the proximity of two extinct volcanic centres to these faults, and the fact the faults are parallel with the dyke swarms (i.e. perpendicular to the minimum compressive stress, parallel to the rift axis), the faults here could be related to a magmatically driven system when the volcanic centres were active. This possibly means the faults would have reached the surface of an active rift 13Ma, and the faults and dykes exposed today in the fjords represent a cross section of an ancient rift.

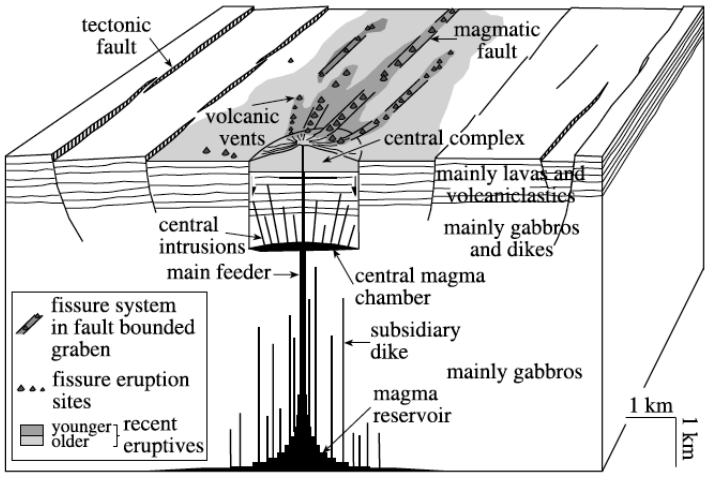

Figure 2.2: Cartoon of a typical volcanic system in Iceland from Tentler (2005). Note normal faults found on the flanks of the fissure swarm, accommodating extension.

An example of one of these rift-related normal faults is well exposed NW of the village of Berunes, Berufjörður. Locally, the fault displaces the Skessa Tuff, red mudstones with interlayered green mudstone, and porphyritic basalt lavas (Figure 2.3). The fault has also been intruded by dykes. The exposure is within a jog in a river gully, allowing 2D exposure of the fault to be mapped. The previously un-named fault is in this study termed the Hramaborg Fault (HBF), due to its proximity to the picturesque house of Hramaborg just to the south.

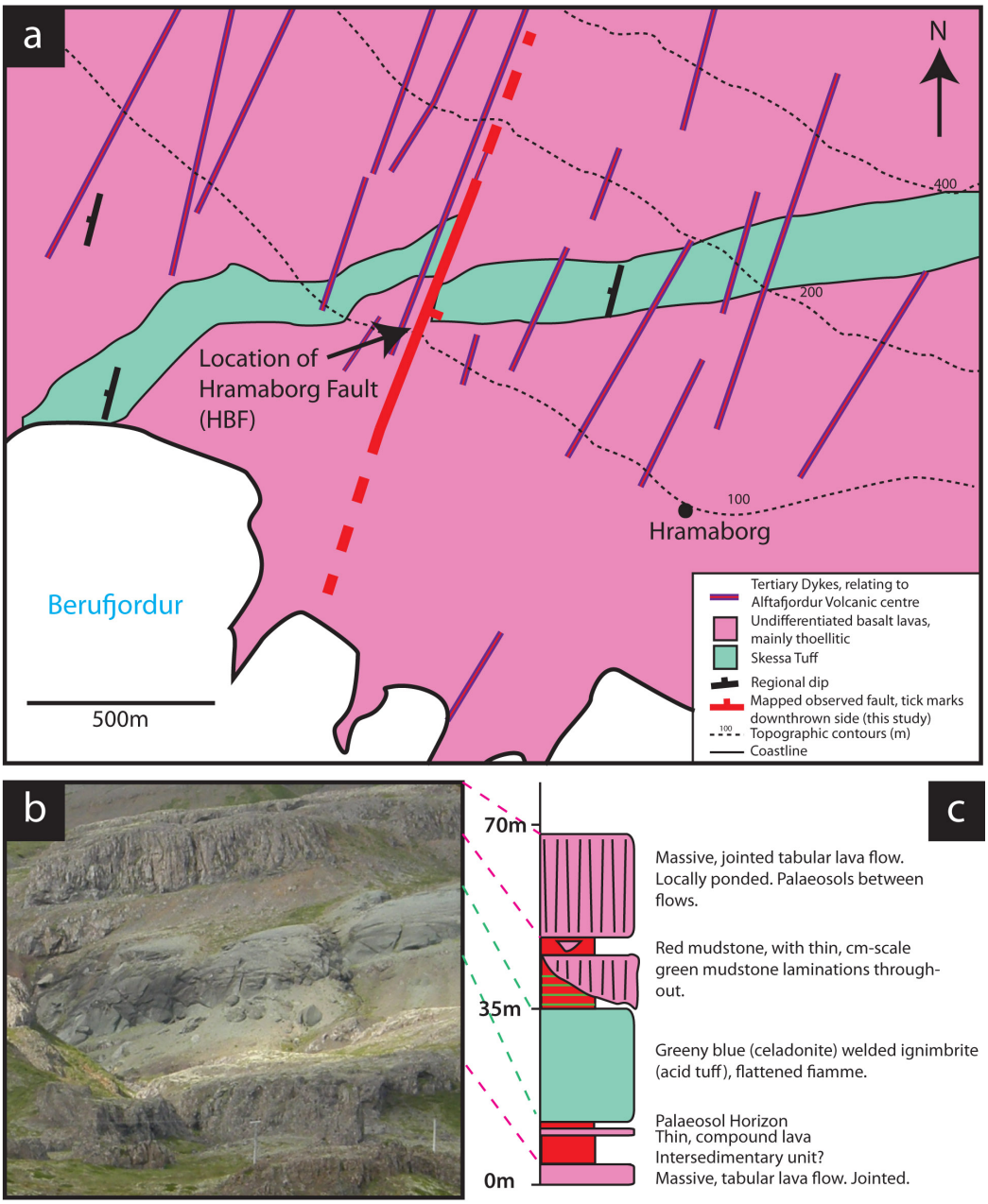

Figure 2.3: Local geology of the area surrounding the Hramaborg Fault. a) Simplified geological map of the study area at Berufjörður, east Iceland. The location of the studied fault is provided. b) Photo of geology surrounding the studied fault. c) Stratigraphic column based on the immediate geology surrounding the fault.

2.4. British-Irish Palaeogene Igneous Province

The BIPIP, part of the NAIP, crops out in the Inner Hebrides in the west of the Scottish Isles, and comprises the remnants of multiple rift-related continental flood basalt lava fields and related volcanic central complexes, which represent the eroded intrusive roots of larger volcanoes. These igneous rocks were emplaced onto Mesozoic sedimentary rocks (mostly Jurassic marine and estuarine deposits, as well as Triassic and Cretaceous deposits), and also pre-Mesozoic rocks (Emeleus and Bell, 2005). The earliest BIPIP-related volcanism (originating from fissure type feeders as sub-aerial flows) of the Inner Hebrides occurred ~61 Ma, forming the islands of Eigg, Rum and Canna (Chambers et al., 2005). At around 60 Ma, the lavas surrounding Ben Hiant on Ardnamurchan were emplaced, along with the Mull Lava Group (Chambers and Pringle, 2001). The Skye Lava Group is dated at around 58Ma by Ar/Ar and palynology dating (Bell and Williamson, 2002; Jolley, 1997). Locally, eruptions of lava into water formed hyaloclasites and peperites and hiatuses in eruptions caused weathering of existing lava tops as well as deposition of lacustrine and fluvial sediments (Emeleus and Bell, 2005).

Central complexes are distributed throughout the BIPIP, including centres in Skye, Ardnamurchan, Mull, Arran and Rum. The central complexes comprise a range of shallow intrusions including plutons, lopoliths, laccoliths, ring dykes, cone sheets and sills, together with rare subsided caldera fills and screens of country rock. Related to the emplacement of these complexes, and ultimately the lavas, are the regional dyke swarms, which have a general NW-SE trend (Figure 2.4). These dyke swarms allow the minimum compressive stress to be determined during the Tertiary, with the dominant extension direction being NE-SW. The lava flows of the BIPIP contain faults in the same trend as these dykes. Within the central complexes, faulting is common with orientations typically parallel to the dyke swarms. England (1988) states the faults are contemporaneous with dyke emplacement, and that the stress field remained constant after dyke

emplacement, therefore it can be suggested that faults with a NW-SE trend were formed in relation to emplacement of the dyke swarm. As the NW-SE faults are interpreted as syn-volcanic to immediately post-volcanic (i.e. active at the time of hotspot migration), normal faulting and dyking must be directly related to the dominant NE-SW extension that formed in response to sea-floor spreading (England, 1988). Therefore, faults and dykes are likely contemporaneous in formation.

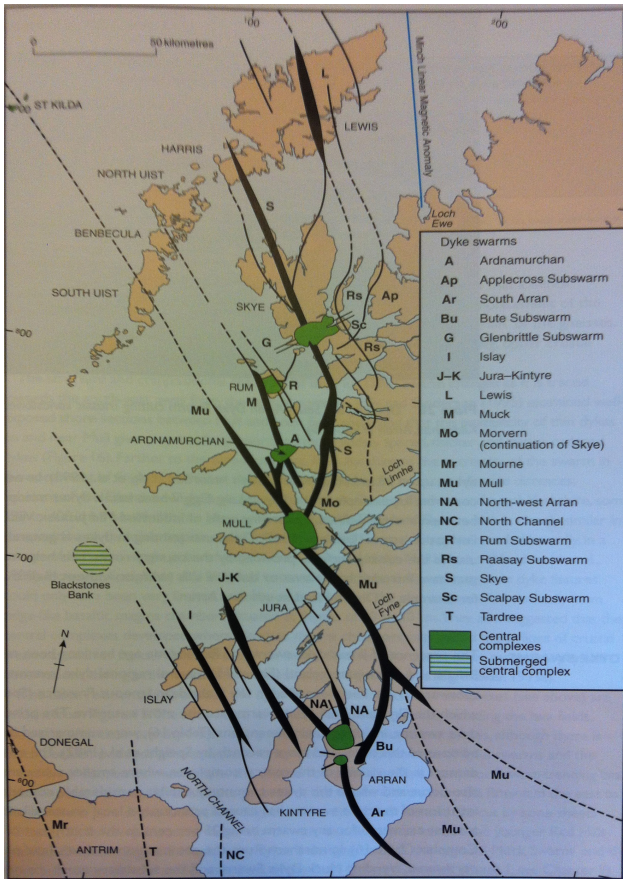

Figure 2.4: Simplified dyke distribution within the BIPIP, with a dominant NW-SE orientation, indicating NE-SW extension during emplacement. Broader lines indicate main axes of regional swarms relating to central complexes. Figure from Emeleus and Bell (2005).

The faults studied in the BIPIP of Scotland are located in Mull, Ardnamurchan and Skye (Figure 2.1), and the detailed geology of each study area is given below.

2.4.1. Mull (Bird Nest Fault location) – local geological setting

The south-central coast of Mull is dominated by flood basalt sequences belonging to the Mull Lava Group. The Mull Lava Group is sub-divided into three formations: the Staffa Lava Formation (SLF), Mull Plateau Lava Formation (MPLF) and the Mull Central Lava Formation (MCVF), in order of oldest to youngest (Bailey et al., 1924; Emeleus and Bell, 2005). The study area is within the MPLF, dated at 58.66 +- 0.18Ma by Ar/Ar dating (Chambers and Pringle, 2001). The MPLF is largely characterised by thin bedded, massive basaltic flows, whereas the older SLF flows are dominated by columnar-jointed sheet flows, as well as massive, amygdaloidal compound flows (Williamson and Bell, 2012). Petrologically, the MPLF is composed predominantly of mugearite, benmoreite, trachyte, some tholeiitic flows and rare plagioclase-macrophyric basalt flows (Emeleus and Bell, 2005). Sedimentary units within the MPLF are rare, but where present consist of volcaniclastic sandstones and siltstones (Brown et al., 2009). The total original thickness of the Mull Lava Group has been estimated at ~ 2500m, based on the mapping of zeolite assemblages (Walker, 1971). Only 1000m of the lavas are now preserved (Walker, 1971) meaning up to 1500m have been eroded from the Mull Lava Group.

The lavas are cut by the Mull Central Complex, which represents the remains of the ancient volcanoes that dominated the landscape in the Palaeogene. The Great Glen Fault (one of the major terrane bounding faults in Scotland) runs just to the south of the Mull Central Complex. It is believed to have been influential in controlling the location of the Mull Central Complex, by acting as a zone of weakness in the upper crust and allowing magma intrusion along it (Bailey et al., 1924). The Mull Central Complex comprises three distinct centres, all of which contain intrusive plutons (granites, gabbros etc), with multiple cone sheets intruding the surrounding rocks in a concentric fashion around the complexes. Two out of the three central complexes are related to the development of calderas (Bailey et al., 1924): Centre 1 (early caldera) and Centre 3 (late caldera).

The central complexes have subjected the surrounding rocks to hydrothermal alteration (Figure 2.5, Figure 2.6) as a result of hot fluids convecting through the previously emplaced lavas, thus overprinting the regional zeolite distribution pattern in the area. This alteration (pneumatolysis) occurred at around 400ºC, causing alteration of the main rock-forming minerals within the surrounding lavas (Emeleus and Bell, 2005). The epidote alteration zone of the complexes and Centre 1 cone sheets have been mapped within the study area (Walker 1971). This suggests that any faults within the study area could be related to central complex stresses (i.e. minimum compressive stress NE-SW), and any alteration could be due to the hydrothermal processes active during caldera emplacement. The main caldera is 10km away from the study area however, and it is therefore unlikely that structures studied here are ring faults related to the caldera (Branney, 1995; Holohan et al., 2005). It is more likely that they are related to other rifts formed at the time of active extension (e.g. the Assapol Fault/Carraig Mhor graben in Williamson and Bell, 2012). It is likely that faults found in a NW-SE orientation were formed and active either during volcanism, or immediately post-emplacement. In addition it has been noted that NW trending, parallel to regional dyke swarms, mineral-filled fractures form within the complexes or in the surrounding country rock (Emeleus and Bell, 2005).

The fault studied in the Carsaig Bay area on the south coast of Mull is located just to the east of the sea stack An Dunan (Figure 2.7). It trends NW/SE in orientation, similar to the dyke swarms, and is mineralised. This fault orientation suggests that the fault is more likely to be related to extensional processes associated with dyke emplacement at depth rather than directly to caldera processes. The fault is exposed on a raised platform in section view, and displaces massive, aphyric amygdaloidal basalt of the Mull Plateau Lava Formation (Figure 2.7). The fault has not been previously mapped, and is therefore named in this study the Bird Nest

Fault (BNF) due to a cosy little bird's nest found in the nooks and crannies the fault has made in the gully.

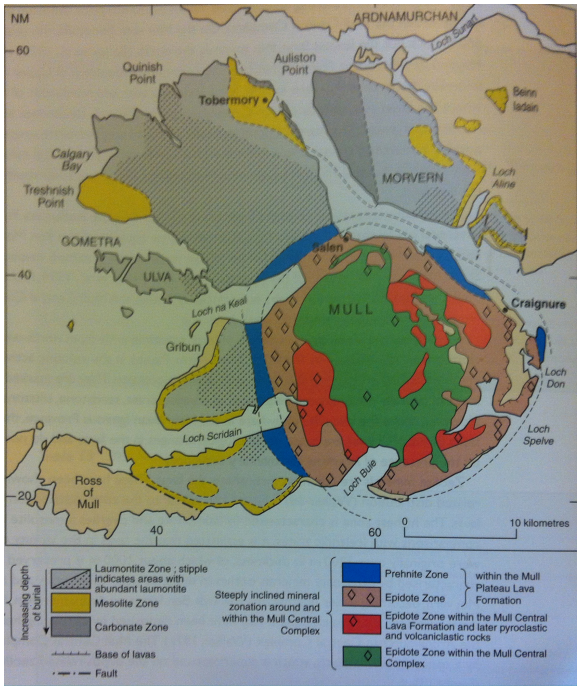

Figure 2.5: Map of hydrothermal alteration zones associated with the Mull Central Complex. The study area (at the 'L' of Loch Buie) is located within the epidote zone. Regional zones of zeolites are also shown. From Emeleus and Bell (2005).

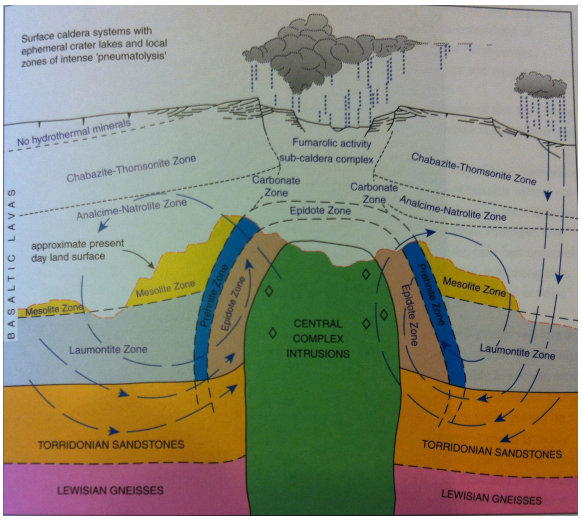

Figure 2.6: Schematic profile view of hydrothermal alteration associated with the Mull Central Complex, showing overprinting of the regional zeolite zones. From Emeleus and Bell (2005).

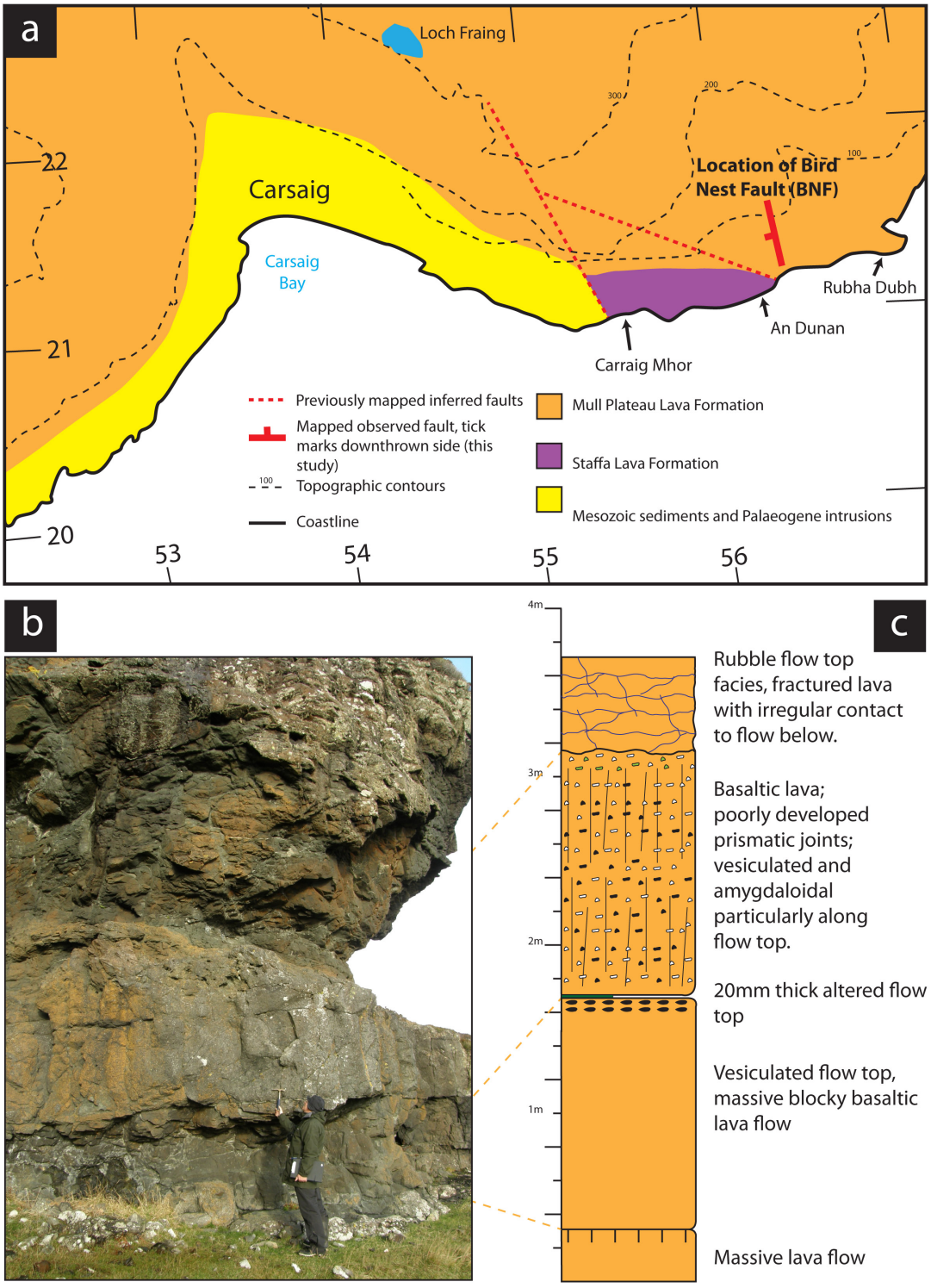

Figure 2.7: Local geology of the area surrounding the Bird Nest Fault. a) Simplified geological map (digitised from BGS, 1953) of the study area east of Carsaig, south Mull. Location of studied fault is marked on the map. b) Photo of geology adjacent to fault. c) Stratigraphic column of the geology immediately surrounding the fault.

2.4.2. Ardnamurchan (Lawther Fault location) – local geological setting

The study area on the Ardnamurchan peninsula is situated on the eastern side of the Ben Hiant Intrusion (Figure 2.8). Ben Hiant is made up of quartz dolerite intrusions, volcaniclastic breccias and conglomerates, and cone sheets relating to a nearby central complex, in the centre of the peninsula. East of Ben Hiant, the geology consists of basement Moine meta-sedimentary rocks, unconformably overlain in places by Jurassic sandstones, shales and limestones, and basalts of the Mull Plateau Lava Formation (described in the previous section). The MPLF here has had the same burial depth as the MPLF in the Mull field site i.e. 1.5km (Walker, 1971). Palaeogene volcaniclastic rocks have also been mapped in this area (Brown and Bell, 2007).

The Ardnamurchan Central Complex is composed of three distinct centres (Centres 1, 2 and 3), comprising a range of shallow intrusions including lopoliths, ring dykes, cone sheets and sills (Gribble et al., 1976). The intrusions post-date the Mull Plateau Lava Formation. The dominant faults in the area trend NW-SE, in a similar orientation to the regional dyke swarm. The largest fault mapped in the area is the Loch Mudle Fault, a 75m-displacement fault that throws down the basalts to the east and also cuts intrusions related to Centre 1 of the Ardnamurchan Central Complex. Displacement was measured based on the offset of geological units in map view. The fault itself is parallel to the axis of the dyke swarm related to the emplacement of the central complex, as well as to other faults occurring in Centre 3 of the Ardnamurchan complex. England (1988) suggests this relationship means that the Loch Mudle Fault has a late or post-volcanic origin, as the central complex emplaced the lavas in the study area.

The fault studied in this area is exposed within a recent road cut just south of Loch Mudle (Figure 2.8). This fault has the same orientation as the Loch

Mudle Fault (Figure 2.8), but it does not displace Moine rocks against Palaeogene lavas, and therefore cannot be the actual Loch Mudle Fault, and must have a displacement less than 75m. It does however offset a basalt lava against a fluidal peperite (both Palaeogene in age), and has a similar orientation to the Loch Mudle fault, which could suggest this fault is kinematically related to the Loch Mudle Fault, and may therefore have a late or post-volcanic origin relating to the emplacement of the dyke swarms. At the site, the stratigraphy of the surrounding geology is unclear due to poor exposure; however, a fluidal peperite[1] composed of black mudstone with clasts of basalt is overlain by a pervasively jointed and porphyritic basalt (Figure 2.8). Brown and Bell (2007) have described the Palaeogene landscape of Ardnamurchan as having numerous bodies of water (rivers, swamps, lakes) and it is therefore likely that the peperite formed within one of these, due to interaction of lava with water-saturated sediment (White et al., 2000). The peperite crops out 10m to the east of the field site, (D. Brown pers comm.) but due to poor exposure a reliable stratigraphy has not been determined. Pneumatolysis (alteration of surrounding rocks due to gases or fluids derived from magma) due to the emplacement of the Ardnamurchan Central Complex has not been recorded in the MPLF at this location. Because the studied fault has not been previously mapped and is not the Loch Mudle Fault, in this study it is named the Lawther Fault (LWF), after Susan Lawther who identified it in the field during an undergraduate fieldtrip.

[1] Definition of peperite from Skilling et al (2002): “clastic rocks comprising both igneous and sedimentary components, which were generated by intrusive processes, or along the contacts of lava flows or hot volcaniclastic deposits with unconsolidated, typically wet, sediments”.

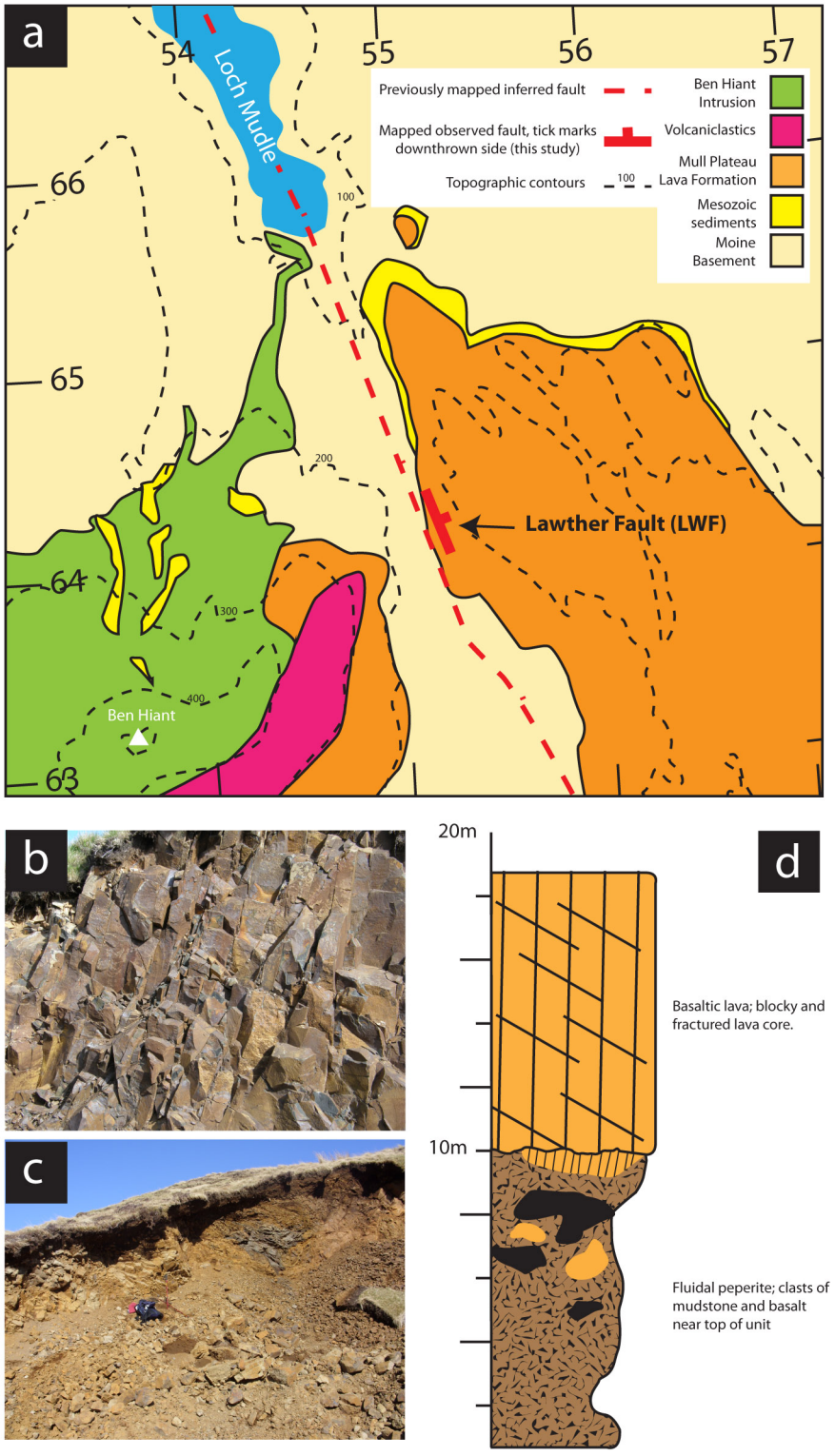

Figure 2.8: Local geology of the area surrounding the Lawther Fault. a) Simplified geological map (digitised from BGS, 1977) of the study area to the east of Ben Hiant, Ardnamurchan. Location of studied fault is marked on the map. The previously mapped fault is the Loch Mudle Fault. b) Photo of pervasively fractured basalt. c) Photo of fluidal peperite within the study site. d) Stratigraphic column of the geology immediately surrounding the fault.

2.4.3. Skye (Talisker Bay Fault location) – local geological setting

The study area of Talisker Bay, west Skye, is within part of the west-central Skye Lava Field, dated at 58Ma (Bell and Williamson, 2002). The west-central Skye Lava Field has been sub-divided into three architectural sequences, with the lowermost units termed as 'lower compound-braided lavas', the middle units as 'transitional lavas' and the uppermost as 'upper tabular-type lavas' (Single and Jerram, 2004). On the basis of lava architecture and the presence of interbedded sedimentary and volcaniclastic units, Williamson and Bell (1994) sub-divide these lavas into three formations of the Skye Lava Group: the Glen Caladale Formation, the Fiskavaig Formation and the Gleann Oraid Formation. The ~185m thick Fiskavaig Formation (Emeleus and Bell, 2005) is exposed on the cliffs to the north of Talisker Bay, and is predominantly composed of evolved, plagioclase porphyritic flows (such as mugearites and hawaiites) with thin olivine basalts (Williamson and Bell, 1994) and interbeds of mudstones and siltstones. Zeolite occurrences are well known from the Talisker area, and King (1977) has shown through zeolite mapping that the level of erosion of the lavas in Skye is similar to the level described by Walker (1971) in Mull (up to 1500m removal).

As these lavas are not adjacent to the Skye Central Complex, there has been no pneumatolysis of the lavas, and the structures encountered within them are therefore not directly related to the emplacement of the central complex. The structure of the west-central Skye Lava Field has been interpreted by England (1994) as an early, shallow NW-SE trending syncline (same trend as the regional dyke swarm), formed by lava accumulation and subsidence followed by faulting, which was either syn- or just post-eruption of the lavas. Binns et al., (1975) describe the faulting of the Skye Lava Field as being related to subsidence of the crust beneath the dense basalt flows, which resulted in the formation of NW-SE shallow syncline. As the

syncline and majority of faults in this area have the same orientation as the regional dyke swarm, this suggests they formed in the same regional stress field as the dykes (i.e. a result of NE-SW extension).

The study area is located in the Fiskavaig Formation (Figure 2.9) on the northern cliff edge in Talisker Bay. The cliff exposes a series of basalt lava flows, some thick with weakly developed joints and others thin with grey-blue mudstones, and reddened flow tops separating individual flows (see stratigraphic log, Figure 2.9). The only accessible exposure of the fault is at the top of the cliff. This fault has been previously mapped by the British Geological Survey (BGS, 2001) with the same orientation and dip, but is un-named. In this study, the fault is hereinafter referred to as the Talisker Bay Fault (TBF) due to it being the only well-exposed fault in the immediate area.

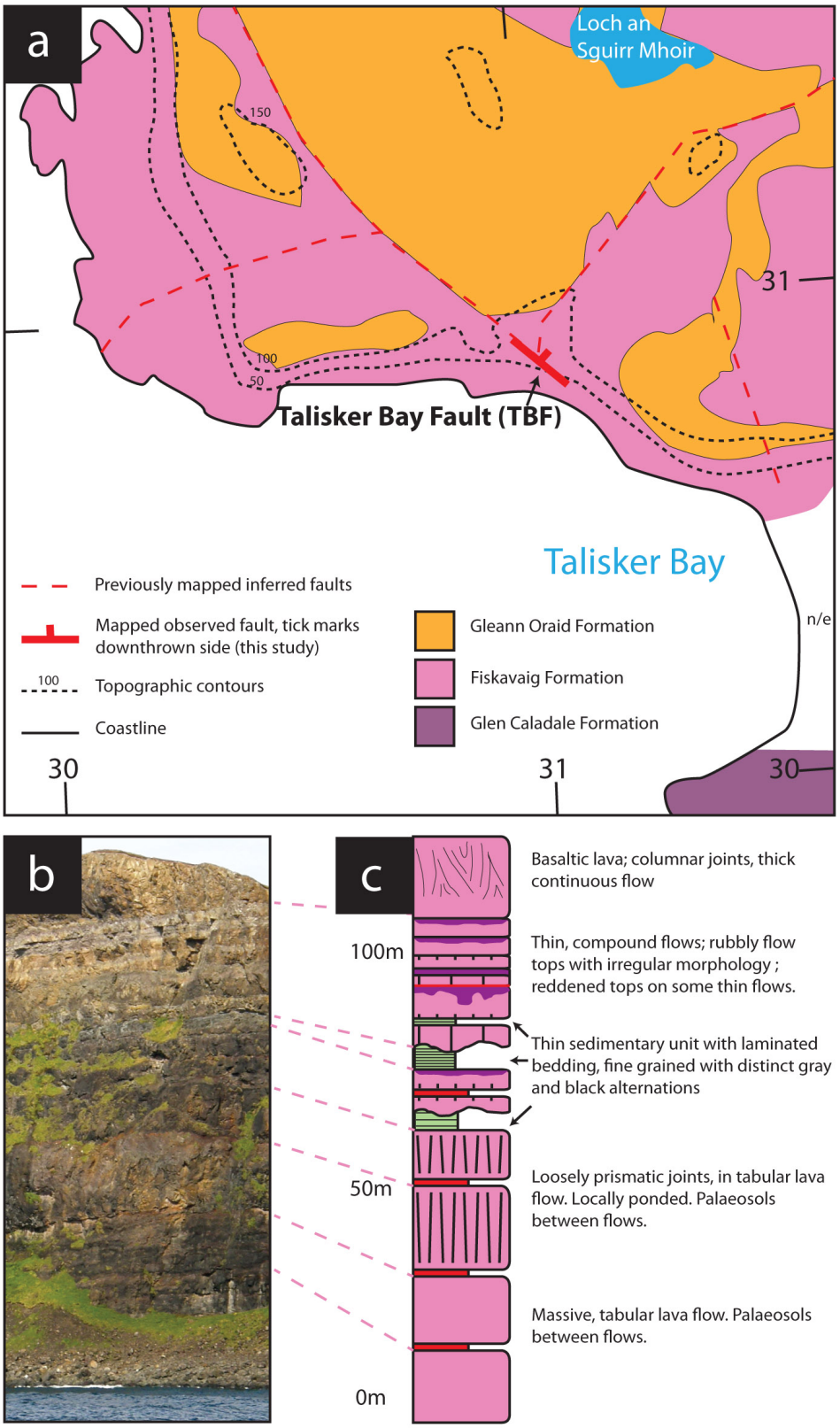

Figure 2.9: Local geology of the area surrounding the Talisker Bay Fault. a) Simplified geological map (digitised from BGS, 2001) of the study area at Talisker Bay, Skye. b) Photo of local stratigraphy in field site. c) Stratigraphic column of the geology immediately surrounding the fault.

2.5. Faroe Islands

The Faroe Islands Basalt Group (FIBG) crops out on the 18 islands that make up the Faroe Island archipelago. The FIBG is at least 6.6km thick (Passey and Bell, 2007), and is dominated by tholeiitic flood basalts which are subdivided into seven formations (Passey and Jolley, 2009; Rasmussen and Noe-Nygaard, 1969; Rasmussen and Noe-Nygaard, 1970). The faults in this study cut the lowest sub-aerially exposed formation, the Beinisvørð Formation, which is ~3.3km thick, with 900m exposed onshore (Passey and Bell, 2007). Waagstein et al (2002) have dated the lavas of the Beinisvørð formation at 58.8Ma, and characterised them as aphyric Fe-Ti-rich tholeiites. The FIBG has been subjected to low grade zeolite metamorphism; however, this metamorphism is not directly related to burial depth, but rather to NW-SE trending fissure swarms. Zeolite zones relating to burial depth would be expected to be regionally extensive, whereas zeolite zones related to fissure swarms would be localised and not correlate regionally. The NW-SE fissure swarms have locally disrupted palaeo-groundwater temperatures at depth, meaning zeolite zones are unlikely to be regionally extensive. Therefore, zeolite zones in the FIBG may be linked to the volcanic-tectonic systems which developed the Faroe Islands (Jørgensen, 2006), rather than linked to burial depth as is the case with zeolite zones in the BIPIP and east Iceland. Based on previous zeolite mapping by Jørgensen (1984), Waagstein et al (2002) suggest >1 km of erosion has occurred in the southern Faroe Islands. The sequence is unlikely to have been buried to more than 3km (Walker et al, 2012a), perhaps more likely to 2km, meaning that the lavas exposed at the surface today have been exhumed from approximately the same depths as those from the Iceland and Scotland field sites.

Recent work by Walker et al. (2011a, 2011b, 2012a) has identified six stages of faulting and dyke intrusion in the Faroe Islands: stages 1 and 2 are characterised by ENE-WSW to NE-SW extension and dyke intrusion, stage 3 by N-S extension and dyke intrusion, stage 4 by continued N-S extension

with minor E-W shortening, stage 5 by NW-SE extension, and stage 6 by post-magmatic reactivation of some faults. Walker et al. (2012a) state that stages 1-2 form the majority of structures regionally across the FIBG, with stages 3-4 interpreted as beginning toward the end of magmatism, with the remaining events forming post-magmatically. Faults categorised as stage 1 formed during emplacement of the FIBG (based on the stratigraphic height to which they occur), and have been mapped as generally dip-slip, sub-vertical, and as reactivating pre-existing cooling joints (Walker et al, 2011a). The stage 1 and 2 extension orientation is parallel to the extension direction recorded during earlier Palaeocene activity (i.e. emplacement of the BIPIP), and Walker et al (2011a) interpret the stage 1 & 2 extension as being caused by:

'*crustal buoyancy forces (excess gravitational potential energy in the Faroes region relative to its surrounding) arising from juxtaposition of hotter, stretched lithosphere against cooler, thicker unstretched lithosphere following the end of the failed Palaeocene rift event*'

Therefore, the extension mechanism is different in the Faroe Islands than in the BIPIP and east Iceland, where the extension mechanism was accommodated by stretching and subsidence relating to sea floor spreading. In this study, four field sites were studied on the southern-most island of the Faroe Islands, Suðuroy, in the Beinisvørð Formation. The formation is typified by thick, laterally extensive aphyric sheet lobes (Passey and Bell, 2007). Between the sheet lobes, volcaniclastic conglomerates, tuffs and saprolitic boles are observed within the field sites. Three out of the five faults described in this study are interpreted within Walker et al (2011a, 2012a) as belonging to stage 1. The remaining two faults in this study have characteristics consistent with stage 1 structures defined by Walker et al., (2011a) (i.e. dip-slip, with NW-SE, N-S trends).

Because the four field sites all occur within a relatively simple geological setting, individual local geology maps are not presented in this thesis for

the faults, and the following sections describe briefly the geology immediately surrounding the four sites. This information is also provided in log form in Figure 2.10. Locations of the faults on Suðuroy can be found in Figure 2.1. The faults studied previously by Walker et al., (2011a, 2011b, 2012a), were un-named. Therefore, for the purposes of this thesis, the faults are named after the location they are situated in, with the exception of the two Vagseiði faults where the fault closest to the jetty is termed the Vagseiði Jetty Fault (VJF), and the other (further away and above a puddle) is termed the Vagseiði Puddle Fault (VPF). The remaining faults are the I Botni Fault (IBF), Sumba Fault (SFZ) and Hov Fault (HVF).

2.5.1. Vagseiði (Vagseiði Jetty & Puddle Fault locations)

At Vagseiði, a raised platform exposes two faults with 3D exposure (cliff exposure and platform exposure). The VJF and VPF cut massive, thick (>5m) aphyric basalt sheet flows with thin (<50cm) reddened saprolitic bole horizons. The VJF and VPF are NW-SE trending.

2.5.2. Sumba (Sumba Fault Zone location)

At Sumba, the NW-SE trending SFZ cuts weakly jointed massive thick (>6m) aphyric lavas with rubbly, amygdale rich tops, interbeds of localised poorly sorted volcanic conglomerates, and reddened boles. The site is exposed on a raised rocky shoreline.

2.5.3. Hov (Hov Fault location)

The field site at Hov is exposed by the roadside in a natural cliff where a small waterfall has exposed the HVF. The HVF cuts a massive aphyric lava, overlain by a 3m thick bed of volcaniclastic conglomerate. Above this is a 1.5m thick red tuff, overlain by a weakly columnar jointed sheet flow, which marks the top of the exposure. The HVF trends N-S.

2.5.4. I Botni (I Botni Fault location)

At I Botni, the IBF is exposed in a rocky shoreline, cut back into a short cliff. The IBF cuts weakly jointed aphyric sheet lavas with rubbly tops, and an interbed of red tuff. The IBF trends NW-SE.

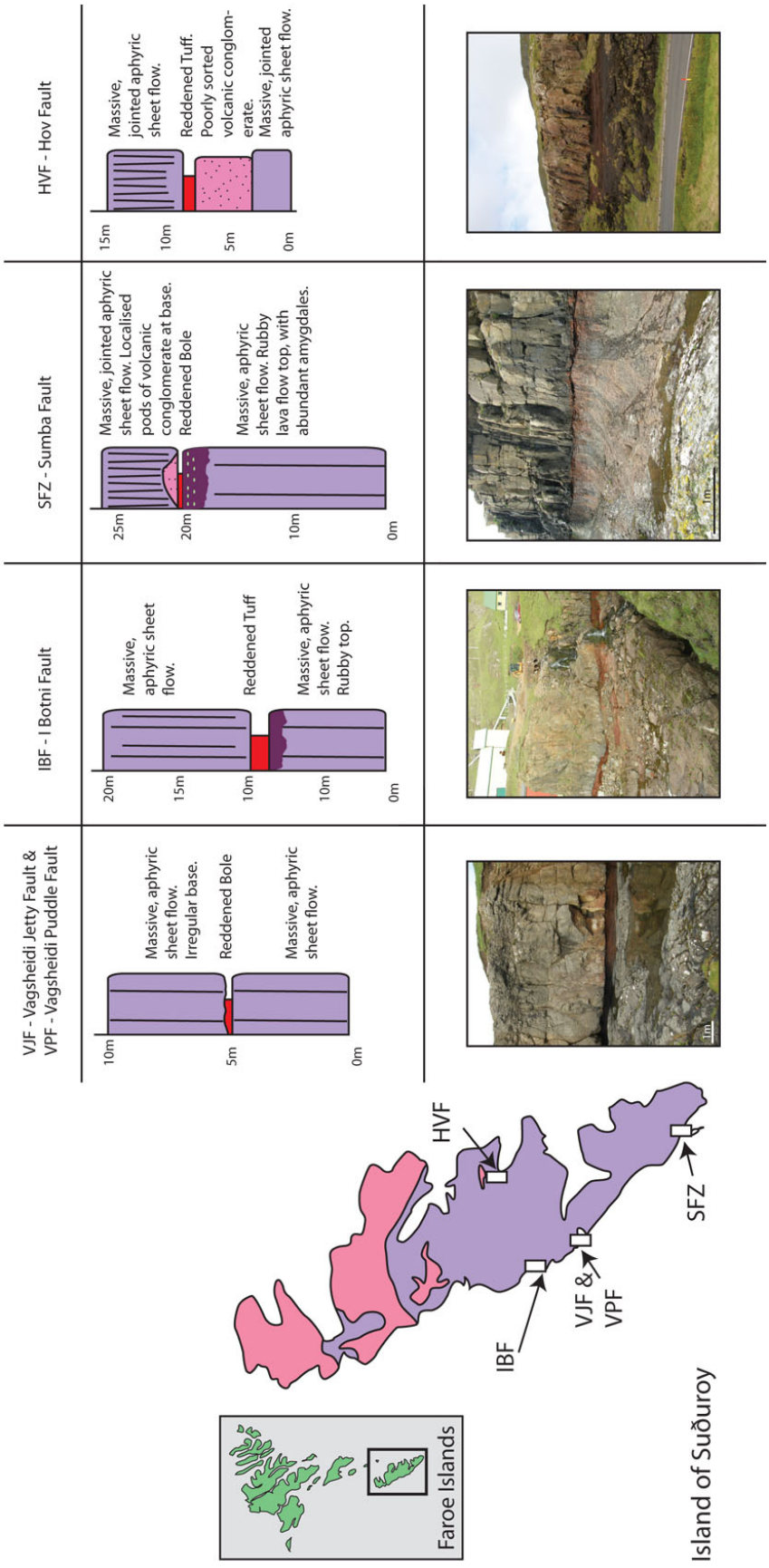
HVF - Hov Fault
SFZ - Sumba Fault
IBF - I Botni Fault
VJF - Vagsheidi Jetty Fault &
VPF - Vagsheidi Puddle Fault
Massive, jointed aphyric sheet flow.
Reddened Tuff. Poorly sorted volcanic conglomerate.
Massive, jointed aphyric sheet flow.
15m
10m
5m
0m
Massive, jointed aphyric sheet flow. Localised pods of volcanic conglomerate at base. Reddened Bole
Massive, aphyric sheet flow. Rubby lava flow top, with abundant amygdales.
25m
20m
10m
0m
Massive, aphyric sheet flow.
Reddened Tuff
Massive, aphyric sheet flow. Rubby top.
20m
15m
10m
10m
0m
Massive, aphyric sheet flow. Irregular base.
Reddened Bole
Massive, aphyric sheet flow.
10m
5m
0m
1m
1m
Faroe Islands
HVF
IBF
VJF &
VPF
SFZ
Island of Suðuroy

Figure 2.10: (Previous page) Localised stratigraphic log and photo showing host rock stratigraphy for each field site in the Faroe Islands.

2.6. Lorne Plateau Lava Formation (Kerrera)

The island of Kerrera, Lorne, (Figure 2.11) lies off the west coast of Scotland, just SE of the trace of the Great Glen Fault (Figure 2.1). The basement geology of Kerrera comprises Dalradian meta-sedimentary rocks, dominated by heavily folded black graphitic pyritous slates, and bands and lenses of dark subordinate limestones (Lee and Bailey, 1925). This sequence, the Easdale Slate Formation, is overlain unconformably by Lower Old Red Sandstone (LORS) deposits, which formed during the late Silurian to early Devonian period (Barclay et al., 2005).

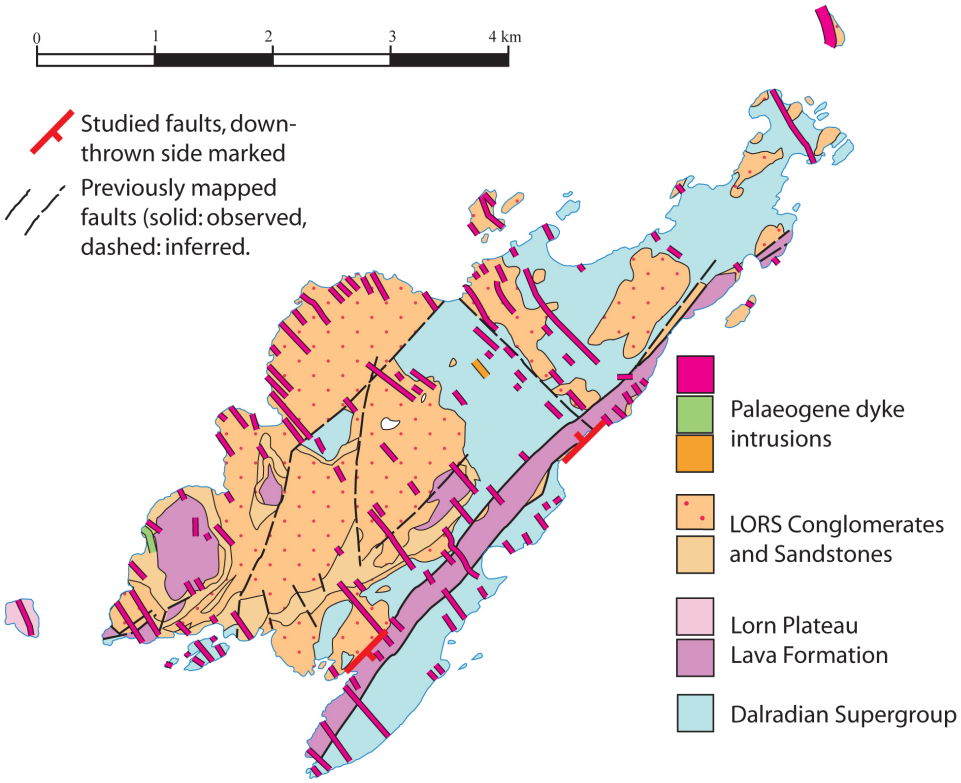

Figure 2.11: Geological map of Kerrera (digitised from BGS, 1992).

In the Lorne area, Kerrera has the thickest deposits of the LORS, up to 128m thick (Browne et al., 2002). The LORS comprises three members. The lowermost Lower Conglomerate Formation comprises a basal breccia

overlain by conglomerate (Morton, 1976). The localised basal breccias lie unconformably over the underlying Easdale Slate Formation (Judd, 1874).

The next member comprises the conglomerates of the LORS, which were fluvially deposited above the basal breccia and Easdale Slates. LORS conglomerates contain clasts of andesitic and basaltic lavas of LORS types and rhyolites plus rare granites (Morton, 1976), with the majority of clasts being crystalline quartzites. The differing proportions of clast populations suggest multiple provenances throughout the region at the time of LORS deposition (Lee and Bailey, 1925) and also very variable topography.

Coinciding with the deposition of the LORS on Kerrera was the eruption of the Lorne Plateau Lava Formation (LPLF), the lavas of which inter-finger locally with the LORS and overstep them elsewhere on the island, where they unconformably overlie the Dalradian meta-sedimentary rocks (Browne et al., 2002). Calc-alkaline magmatism was induced in the Grampian Terrane at c. 430 Ma (Palaeozoic), following the subduction of Avalonia beneath Laurentia. The intrusive and extrusive events that are linked to this subduction lasted ~22 Ma, and were responsible for the >800m thick Lorne Lava formations on Oban and Kerrera (Groome and Hall, 1974; Browne et al., 2002; Thirlwall, 1988; Watson, 1984), as well as for, amongst others, the volcanics at Glen Coe and Rannoch Moor (Neilson et al., 2009). It has been hypothesised that these and associated lavas may be the source for igneous clasts found in the LORS conglomerates, as they are of similar age and composition (Durant, 1999). The andesitic volcanism that provided the igneous clasts in the LORS on Kerrera originated either from volcanism in the palaeo-Great Glen drainage system or from the developing LPLF being reworked into palaeo-canyons within the Dalradian basement (Neilson et al., 2009). The LPLF, dated at 424 – 415 Ma (Thirlwall, 1988; Neilson et al., 2009) comprises flows of basalt, biotite andesite and biotite-augite andesite with brecciated tops and bases, and is related to the subduction of Avalonia beneath Laurentia, potentially in a back-arc-basin

setting (Durant, 1999). Volcanic breccias are consistently found at the base of the lava pile in multiple sites around Kerrera, sitting above and in places interdigitating with LORS sedimentary rocks. These brecciated units of the lava flows contain clasts of andesite in an andesite matrix (Kynaston and Hill, 1908) but these breccias are often referred to as having formed from the interaction of lava and wet sediment and could be classed as peperites (Durant, 1999; Geikie, 1897; Lee and Bailey, 1925), due to the presence of a sandy matrix between the volcanic clasts, and also jasper lenses. Higher up in the lava sequence, palaeosols are found as well as discrete beds of volcanic conglomerates, pillowed lobes, volcaniclastic sandstones and lava sheets. A final phase of magmatic activity occurred during the Palaeogene, with basalt and felsic dykes (NW-SE trend) extending from the Mull Central Complex intruding the Kerrera strata (Bailey et al., 1924; Durant, 1999).

Structurally, there are two dominant fault orientations on Kerrera: one that is NE-SW trending, and the other that is NW-SE trending (Figure 2.11). It can be inferred that the NW-SE structures are related to the emplacement of the dyke swarm associated with the Mull Central Complex as they are parallel to the dykes, and they cross-cut pre-Palaeogene rocks on the island. The NE-SW trending faults run parallel to the trace of the Great Glen Fault, a major, terrane-bounding strike slip fault, which initiated during the late Caledonian stage (Jolivet, 2007). The Great Glen Fault has been reactivated at least once, having been mostly sinistral in the later stages of the Caledonian Orogeny (Stewart et al., 2001), followed by a dextral movement during the Devonian (Rogers et al., 1989), and possibly a further 30km of dextral displacement following the emplacement of the Mull Central Complex (Holgate, 1969). The Great Glen Fault Zone has at the present day been exhumed from 9-16km depth, and is characterised by a 3km wide belt of ductile-brittle fault rocks (Stewart et al., 1999). Holgate (1969) suggested that the Lynn of Lorn Fault, situated between Lismore and the mainland to the southeast, accommodated some of the latest dextral movement on the Great Glen Fault. This fault trace passes

the island of Kerrera to the north, but lies parallel to the NE-SW trending faults on the island of Kerrera. One of the dominant structures on Kerrera is a graben running NE-SW along the eastern coast of Kerrera, down-throwing the LPLF against Dalradian basement. Due to the similarity in strike, this fault could be related to the Great Glen Fault, and this relationship will be discussed further within Chapter 5.

Within the two study areas on Kerrera, all three of the major geological units crop out (Dalradian, LORS and LPLF). Zeolites minerals have not been previously recorded in the LPLF, and therefore the depth of exhumation of these lavas is unknown. However, microstructural evidence from this study (see Chapter 5) suggests the lavas have seen low grade metamorphism, because chlorite replaces olivines and pyroxenes within the lavas. The lavas are highly altered, and therefore can be rather friable in the field. The detail of the structure of the graben will be described in Chapter 5.

2.7. Geological setting – summary

The basalt sequences studied in the BIPIP, FIBG and Iceland have all been subject to a similar amount of erosion (<2km), suggesting that all field sites are currently exposed from approximately the same crustal level. The morphology of the lavas in each site is different (ranging from thick sheet lobes to thin compound flows), as well as the nature of interunits within the basalt flows (i.e. the presence of volcaniclastic units or boles). The Mull and Ardnamurchan faults are related to central complexes and/or the emplacement of dykes, and Skye is related to emplacement of dykes/discrete synclinal folding. The structures exposed in east Iceland are directly related to volcanic centres and emplacement of dykes, very similar to the structures in the BIPIP. The faults of the Faroe Islands formed in a similar regional stress field direction to the BIPIP, related to crustal buoyancy differences.

On the other hand, the lavas of Kerrera were emplaced under different conditions to the Palaeogene lavas, are much older, and were faulted under different stresses, (unrelated to Palaeogene dyke emplacement), but possibly related to movements on the Great Glen Fault.

To conclude, in the NAIP exposures, conditions of formation and depth of burial are all similar, providing consistent geological contexts between all sites. However, local geology and lava morphologies differ. The Kerrera lavas were emplaced and faulted under entirely different conditions to the NAIP. Therefore, comparisons of these faults and their differing regional contexts/stress interpretations/local geology will aid understanding of the controls on structures of faults in basalt sequences.

Table 2.1 presents a summary of the host rocks from each site, burial depth, age, structural and regional context, and level of alteration. The morphologies of the lava used throughout this chapter and within the summary table are from the works of Walker (1972) and Jerram (2002), where the terminologies of tabular-facies lavas (thick, simple flows with sheet geometry) and compound-facies lavas (anastomosing lobes, generally thinner than tabular-facies) are described in detail.

Table 2.1: Summary table of field site geology.

Location	Host Rock (lava)*	Host Rock (other)	Burial Depth	Age	Structural Context	Regional Context	Level of Alteration
Iceland (HBF)	Alkali olivine basalt, and tholeiitic basalt. Massive jointed tabular-flow type.	Red mudstone with green laminations; welded acid tuff; bole	1.3-1.5km	13Ma	Volcanic centre emplacement	Iceland; spreading centre; NAIP	Fresh
Mull (BNF)	Aphyric, amygdaloidal tholeiitic basalt. Prismatically to jointed tabular flows, with amygdaloidal compound flows.	n/a	<1.5km	58.66Ma (*Mull Plateau Lava Formation*)	Dyke emplacement; central complex emplacement	BPIP; spreading centre; NAIP	Epidote zone of hydrothermal alteration related to central complex
Ardnamurchan (LWF)	Plagioclase microporphyritic basalt. Jointed tabular flow.	Fluidal peperite.	<1.5km	58.66Ma (*Mull Plateau Lava Formation*)	Dyke emplacement; central complex emplacement	BPIP; spreading centre; NAIP	Groundmass altered to clay.
Skye (TBF)	Plagioclase porphyritic mugearite and thin olivine basalts. Transitional flows (compound-braided to tabular type)	Boles and laminated silt/mudstones.	<1.5km	58Ma (*Fiskavaig Formation*)	Dyke emplacement; subsidence due to lava emplacement	BPIP; spreading centre; NAIP	Fresh
Vagseiði (VJF, VPF)	Olivine-phyric tholeiitic basalt, sparse phenocrysts of olivine. Massive tabular-flow type.	Saprolitic bole.	<1km	58.8Ma (*Beinisvørð Formation*)	Crustal buoyancy forces; parallel to Palaegene extensional stress.	FIBG; spreading centre; NAIP	Fresh - groundmass altered to clay
Sumba (SBF)	Olivine-phyric tholeiitic basalt, sparse phenocrysts of olivine. Massive/jointed tabular-flow type.	Bole, volcanic conglomerate.	<1km	58.8Ma (*Beinisvørð Formation*)	Crustal buoyancy forces; parallel to Palaegene extensional stress.	FIBG; spreading centre; NAIP	Fresh - groundmass altered to clay
Hov (HVF)	Olivine-phyric tholeiitic basalt, sparse phenocrysts of olivine. Massive/prismatically jointed tabular-flow type.	Tuff, volcanic conglomerate.	<1km	58.8Ma (*Beinisvørð Formation*)	Crustal buoyancy forces; parallel to Palaegene extensional stress.	FIBG; spreading centre; NAIP	Fresh - groundmass altered to clay
I Botni (IBF)	Olivine-phyric tholeiitic basalt, sparse phenocrysts of olivine. Massive jointed tabular-flow type.	Tuff	<1km	58.8Ma (*Beinisvørð Formation*)	Crustal buoyancy forces; parallel to Palaegene extensional stress.	FIBG; spreading centre; NAIP	Fresh - groundmass altered to clay
Kerrera (multiple fault localities)	Aphyric, locally amygdaloidal basalt. Massive tabular-flow type.	Conglomerate, volcaniclastic sediments, mudstones, sandstones.	unknown	424-415 Ma	Potentially kinematically related to the Great Glen Fault.	Subduction of Avalonia beneath Laurentia	Highly altered - high degree of alteration of minerals to chlorites and other clays.

3. Faults in Flood Basalt Sequences: Lithological Controls on Fault Rock Generation and Fault Zone Evolution

3.1. Introduction

To date, few studies have been published on the characterisation of brittle fault zones developed in basalt sequences at depth (e.g. Walker et al., 2012a; Gudmundsson, 1992b; Hayman and Karson, 2007), with most studies having previously focused on the structure of surface faults within basalts (e.g. Martel and Langley, 2006; Holland et al., 2006; Acocella et al., 2000; Acocella et al., 2003; Gudmundsson, 1992a). For example, Holland et al., (2006) recognised that talus blocks, formed from fault scarp collapse at the surface, become trapped within open cavities (a defining feature of surface faults in basalts) and are crushed at depth within the fault, forming breccias. However, Holland et al., (2006) focus more on the morphology and fracture evolution of the surface faults (i.e. at several hundred meters depth) with a passing mention of fault structure at higher depths (i.e. over 1km). Therefore, the aim of this chapter is to describe in detail the internal structure of twelve brittle fault zones, developed in basalt sequences at depths >1-<2 km. The faults were studied over a period of 55 days during fieldwork carried out within the basalt sequences of the North Atlantic Igneous Province (NAIP) in Scotland, the Faroe Islands and Iceland. The geological settings of these areas are described in Chapter 2. During this fieldwork, three protofaults from Kerrera, Mull and Iceland were studied to characterise early fault growth in basalt. Nine faults with displacements over mm-scale (i.e. not protofaults) were also studied and mapped, for the purposes of characterising the internal structure of fault zones in basalt, and how they evolve over time. The faults have a range of

displacement values from <18cm to >25m, and a range of lithological juxtapositions (e.g. basalt against basalt, basalt against sediment etc).

By examining fault zones with a range of displacements, deformation processes (e.g. brecciation, abrasion, asperity removal, etc) associated with faulting of basalt sequences can be identified. This is working on the assumption that small displacement faults represent early fault growth, and large displacement faults represent more evolved faults (i.e. faults which have seen multiple slip events, accruing high displacements over time). This approach has been used in many other fault growth studies, in other lithologies (e.g. Shipton and Cowie, 2001; Micarelli et al., 2006).

The faults in this study were mapped in detail in order to characterise the controls on deformation processes and fault architecture of fault zones in basalt sequences. Detailed fault maps generated from each fault are presented within this chapter, along with a detailed description of the fault rocks and structures from each site. Based on the field data obtained during the field campaign for this study, a conceptual model predicting the evolution of fault zones in basalt sequences is presented at the end of this chapter.

Whilst each fault is individually described, faults are grouped by displacement value and juxtaposition type, as these appear to have the dominant control on fault structure. Therefore, self-juxtaposed faults (i.e where a basalt unit is faulted against itself) are described first, starting with the lowest displacement fault to the highest displacement, followed by a description of non self-juxtaposed faults (i.e. where basalt is faulted against a basalt/sediment unit elsewhere in the basalt sequence) in the same format.

3.2. Methods and data collection

Given that documented examples of faults in basalt are few, potential fault locations were identified by desktop study prior to fieldwork, using geological maps and records for locating previously mapped faults cutting basalt sequences. A field reconnaissance was then undertaken to pinpoint the exact location of previously mapped faults from the desktop study. In most cases, these faults were not well exposed, being obscured by erosion or water. However, by trying to identify those faults, better exposed faults were found by looking for displaced marker horizons, and zones within the basalt sequences of increased fracturing. In other cases, locations of previously documented faults were provided by the author (e.g. Walker 2012a) or passed on by word of mouth from experts in the local area.

Characterisation of the internal structure of each fault zone was undertaken by constructing a square grid network (composed of string) over the exposed outcrop (Figure 3.1). Each square (<50cm^2) was photographed perpendicular to the square overlying the outcrop to minimise distortion and to allow ortho-rectifying of the photograph when digitising. This process made 'stitching' the fault together in the later stages of annotation easier, whilst incurring little error in the quality of the data recorded. Each photo taken was printed, and then annotated in the field (Figure 3.2). Annotations highlighted the key features within the fault zone, including deformation elements, fault rock distributions, slip surface locations, sites of mineralisation and alteration, fracture networks and offset markers. This method allowed a consistent recording of the internal structure of each fault. Orientation data were also recorded, and orientated hand specimens were collected for microscopic analysis of fault rocks and mineralogy.

Figure 3.1: Example of gridded outcrop. 50cm square grids were constructed in order to break down the complexity of the fault zone into manageable portions.

Figure 3.2: Apparatus used for obtaining printed photographs. Photographs were printed in the field, using a portable printer and laptop.

Upon completion of fieldwork, each photographed square was ortho-rectified using Adobe Photoshop to minimise distortion. The ortho-rectified images were then stitched together, and digitised using the annotated photographs collected from the field. This allowed a complete fault map to be produced for each fault.

Of the total of twelve faults studied (including the three protofaults), five were from Scotland, two from Iceland and five from the Faroe Islands. The faults are mainly exposed in 2D cliff sections, gullies, or raised sea platforms, with the occasional fault being exposed in 3D along a raised sea platform or similar. As the faults are described in the following section in order of displacement and juxtaposition, the following terminology is used within this chapter:

- **Self-juxtaposed**: where a basalt lava flow is faulted against itself;
- **Non self-juxtaposed**: where a basalt lava flow is faulted against a lithological unit elsewhere in the stratigraphy, i.e. against another lava flow or against a sedimentary unit;
- **Protofault**: linear trace (such as a fracture) with minimal (millimetres) shear displacement (e.g. An and Sammis, 1996);

- **Fracture Mesh**: interlinked extensional-shear and/or extensional veins/fractures (e.g. Sibson, 1996);
- **Low displacement**: Less than 1m displacement;
- **Medium displacement**: Equal to 1m displacement, and up to and including 10m of displacement;
- **High displacement**: Greater than 10m displacement.

Displacement is often difficult to measure within basalt sequences, due to the lack of stratigraphic markers within individual lava flows and the irregular geometries of flow margins. However in most cases, marker horizons were identifiable and displacement was measured using distinct stratigraphic markers such as reddened boles between lava units, or amygdale/vesicle zones within lava units. In faults where there were no marker horizons, an estimate is provided.

3.3. Self-juxtaposed faults

The best examples of self-juxtaposed low displacement faults were found in the Beinisvørð Formation in Suðuroy (Faroe Islands) and in the Mull Plateau Lava Formation in Mull (Scotland). Within this section, each self-juxtaposed fault (e.g. exposure along the fault where a basalt is faulted against itself) is described individually, in order of displacement from protofaults (fractures with a shear component) up to 32cm displacement. Locations of mapped faults can be found in Chapter 2.

3.3.1. Protofaults – examples from Kerrera, Mull and Iceland

Protofaults in basalt lava flows (Figure 3.3) are found in this study to be characterised by fracture meshes, through-going fractures, and alteration surrounding fractures.

Fracture meshes (Figure 3.3b) have formed as closely spaced (spacing 1cm) parallel fracture sets surrounding an incipient principal slip surface (IPSS). The IPSS is typically marked by a single through-going fracture (Figure 3.3a,c).

Where protofaults are further established, coarse crackle breccias bound by fractures form along the margins of the IPSS as a result of basalt between the fracture meshes becoming increasingly deformed (Figure 3.3c). Zeolite mineralisation is present within protofaults, forming particularly in the shear fractures/IPSS as thin films. The basalt immediately surrounding the protofaults is altered, represented by a colour change - generally from a host rock black/gray, to a more altered browny/gray.

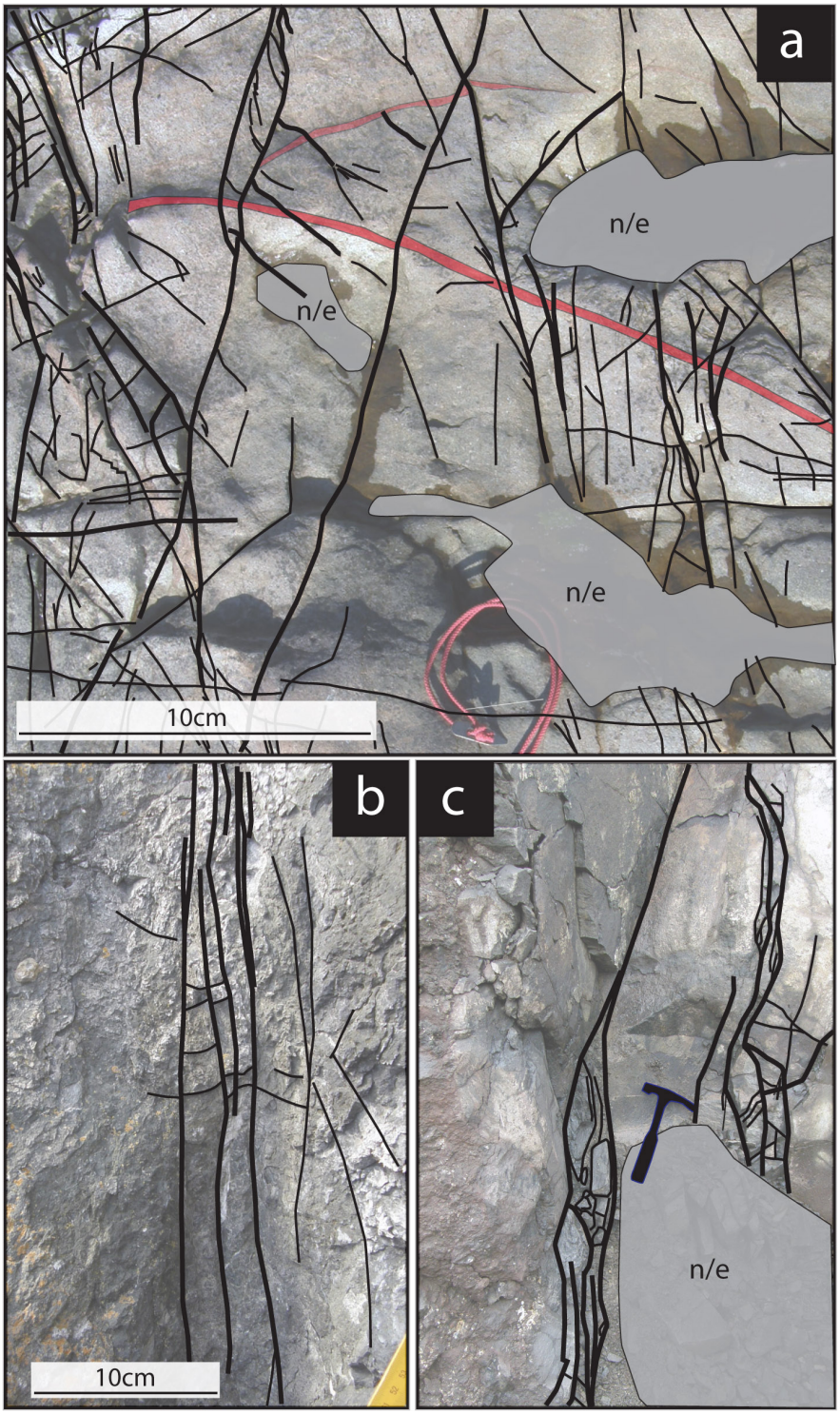

Figure 3.3: Protofault examples. a) Protofaults, Kerrera, with fractures highlighted in black. Marker horizons in red. Note fracture meshes and dominant through-going fractures acting as incipient principal slip surface. Plan view. b) Protofault, Mull, with fractures highlighted in black. Most fracture orientations are parallel to the developing fault. White zeolite coatings are present along fractures. Photo taken toward NW. c) Protofault, Iceland, with fractures highlighted in black. Note development of crackle breccia (left of hammer), and mineralisation along fault plane. Direction of photo is SW.

3.3.2. Self-juxtaposed: low displacement faults

From protofaults to low displacement faults, displacement values increase from mm-scale to the cm-scale. The Vagseiði Jetty Fault (VJF) and Vagseiði Puddle Fault (VPF) displace the same stratigraphy (a basalt lava flow with saprolitic bole beds), belong to the same deformation event identified in Walker et al (2011a), and have similar fault zone morphologies. They are therefore described together due to their similarities.

3.3.2.1. VJF, Faroe Islands

The 18cm displacement VJF (Figure 3.4) is exposed on a cliff section, and is characterised by a wide (>1m) zone of fault-related deformation, dominated by extensional (opening) and extensional-shear (opening with evidence of shear, i.e. slickenlines) fractures (Figure 3.4a). These fractures surround the principal slip zone (PSZ), characterised by a crackle breccia and zeolite mineralisation.

The fractures surrounding the fault zone occur in both the hanging and footwall, and become increasingly closely spaced approaching the immature principal slip surface (ImPSS). Extensional fractures, often filled with zeolite minerals as vuggy veins, dominate the fracture type furthest from the ImPSS, but approaching the fault, the fractures increasingly display extensional shear characteristics. Here, zeolite veins are present as a thin polished mineral films rather than as vuggy veins.

At around 50cm on either side of the ImPSS, the basalt is altered to a browny gray colour, and is slightly more friable than the surrounding host rock. Fault-related fractures outside this alteration zone also have a narrow (<1cm) halo of alteration surrounding them, the size of which is proportionate to the concentration of fractures (i.e. a cluster of fractures has a wider zone of alteration associated with it than a single fracture).

The ImPSS is discontinuous along strike, being interrupted by zeolite mineral veins, and is dispersed by parallel fractures on either side of the principal slip zone (PSZ). However, it is likely that the ImPSS is mineralised by the zeolite veins, thus obscuring the actual slip surface.

Within the PSZ, a discontinuous crackle breccia zone (~5cm thick), composed of parallel fractured basalt clasts, is found. This crackle breccia is clast supported, and is derived from the parallel fracture zone (Figure 3.4c). In the absence of crackle breccia along the ImPSS, zones (up to 20cm thick) of very closely spaced (<1cm apart), parallel fractures are found (Figure 3.4c). Where crackle breccia is formed, the thickness of these parallel fracture zones decreases. Zeolite mineralisation occurs throughout the crackle breccia zone, particularly along the ImPSS (where identified) and following the edges of the breccia clasts.

In addition to the cliff exposure (section view), the fault zone was also partially exposed in plan view, both on the shoreline platform at the base, and at the cliff top of the mapped exposure. Field sketches of the geometry of these were taken, and are shown in Figure 3.5. In plan view, crackle breccia have formed as discontinuous lenses along the fault, similar to section view observations. However, in section view, fracture zones appeared parallel to one another but in plan view, fracture zones are hard-linked and connect at an angle to one another (Figure 3.5a). Internally fractured host rock lenses, trapped between slip surfaces and fracture zones, were also found. In plan view, the ImPSS is also discontinuous, similar to its characteristics in section view.

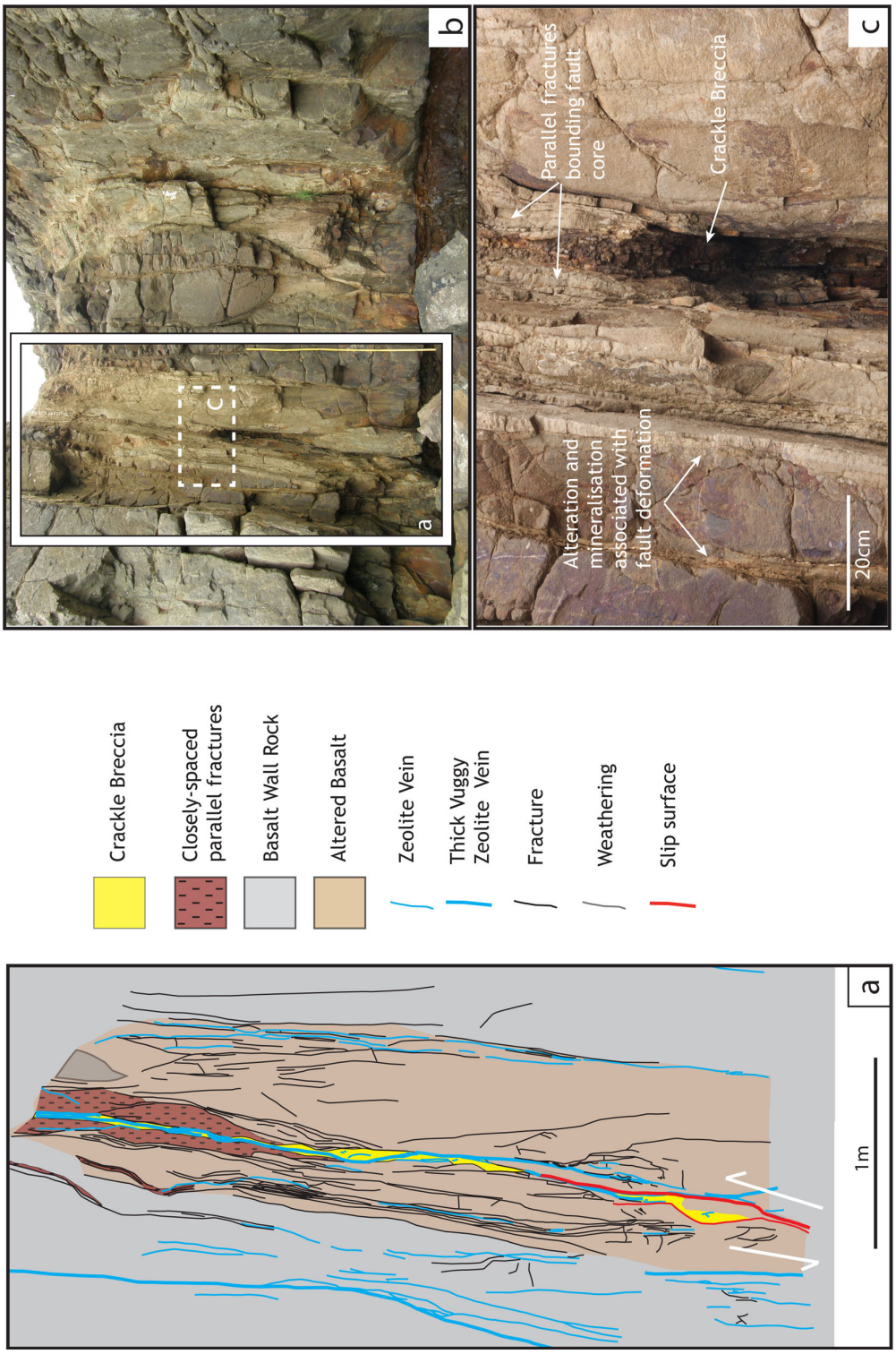

Figure 3.4: Detail of VJF, 18cm displacement (section view, all figures are viewed toward the north). a) Fault map produced from fieldwork, highlighting discontinuous nature of the lmPSS, narrow, discontinuous zones of crackle breccia surrounded by parallel, vertical fractures and mineralised fractures, surrounded by fault-related alteration. b) Location of a) without fault map overlay. c) Detail of internal structure of fault. Note the thin zone of breccia in the centre of the fault, where slabs of rock have been incorporated from the parallel fractured walls, and alteration and mineralisation along/within fractures.

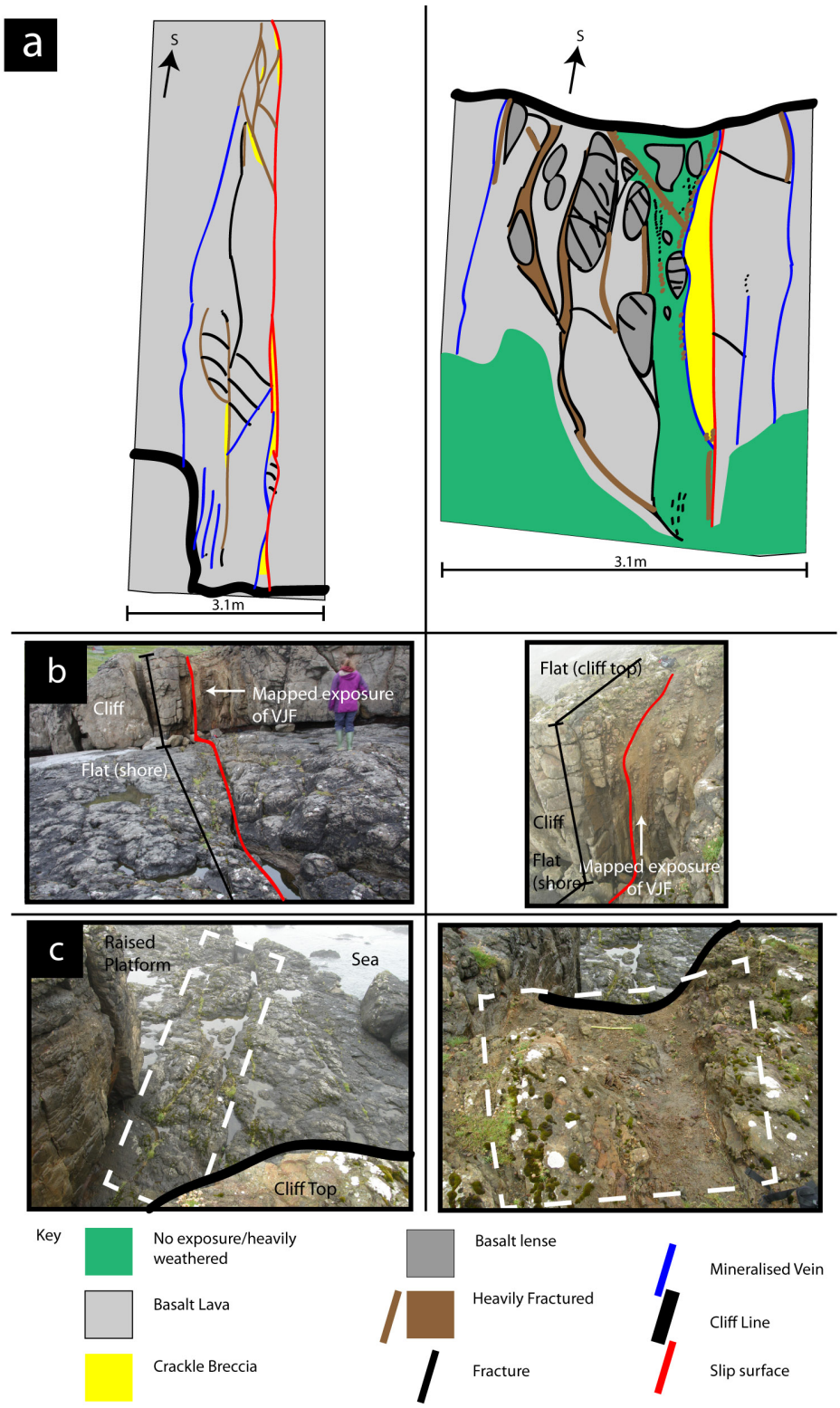

Figure 3.5: Field sketches of additional exposures of the VJF (plan view). a) Digitised field sketch of shore line plan exposure (left) and cliff top plan exposure (right). b) Field area photographs, showing relationship to mapped VJF exposure. c) Plan view of shoreline exposure (left) and cliff top exposure (right). White dashed lines represent sketch limits from a).

3.3.2.2. VPF, Faroe Islands

A similar style of deformation found in the VJF (18cm displacement) was identified in the 28cm displacement VPF. However, the major differences are that in the VPF, the fault-related deformation zone is ~5m wide, with zones of fracturing in the hanging wall of the PSZ. The PSZ is also characterised by crackle breccia, which is <20cm thick and continuous along strike, though variable in thickness (minimum 3cm). It can therefore be assumed when the VPF had a displacement of 18cm, it would have had a similar fault structure to the present day VJF, and if the VJF had incurred higher displacement, it would resemble the present day VPF. The VPF is described in Walker et al., (2012a), and therefore a brief description of the fault zone is provided below.

Like the VJF, extensional fractures (e.g. no evidence of shear and vuggy zeolite fill where zeolites are present) dominate the fracture type furthest from the principal slip surface of the VPF (PSS). The hanging wall of the PSS is composed of at least four condensed fracture zones (Figure 3.7a), one of which has components of shear (e.g. evidence of slickenlines), and two of which contain minor amounts of discontinuous crackle breccia. The fracture zones are composed of both extensional and extensional-shear fractures, with vuggy zeolite and zeolite films respectively forming along them. The fractures are also surrounded by alteration, zones of which are particularly wide in the widest fracture clusters (Figure 3.7c). Alteration within the hanging wall is restricted to halos surrounding these fracture zones (Figure 3.7a,c). Fault-related deformation is minimal in the footwall, though footwall exposure is poor due to erosion.

The principal slip surface (PSS) itself is continuous, identifiable along strike, and is therefore described as a mature slip surface, i.e. fully developed. Adjacent to the PSS is a 3-20cm thick crackle breccia zone (Figure 3.7d,e) that is continuous along strike. As in the VJF, the crackle

breccia is clast supported, and is composed of rotated clasts of basalt from the parallel fracture zone.

In places, the parallel fracture zone surrounding the crackle breccia zone can be seen in the deformation stage prior to brecciation (Figure 3.7e), i.e. prior to incorporation into the PSZ. Like in the VJF, the parallel fracture zone is widest where the crackle breccia thins out in the basalt. Zeolite mineralisation occurs throughout the crackle breccia zone, with veins up to 1cm thick.

When the PSS cuts the saprolitic bole horizon, the crackle breccia derived from the basalt thins out. The PSS continues through the bole, but fault-related damage is limited to a narrow zone (1-2mm), where bole is entrained along the PSS as a gouge smear (Figure 3.6). Zeolite veining (<3mm thick) is present within this narrow zone of faulting.

Figure 3.6: PSZ detail of VPF in the saprolitic bole layer. Note brecciation of basalt on either side of the slip surface, and then the narrowing of fault-related deformation within the bole itself. Photo toward north.

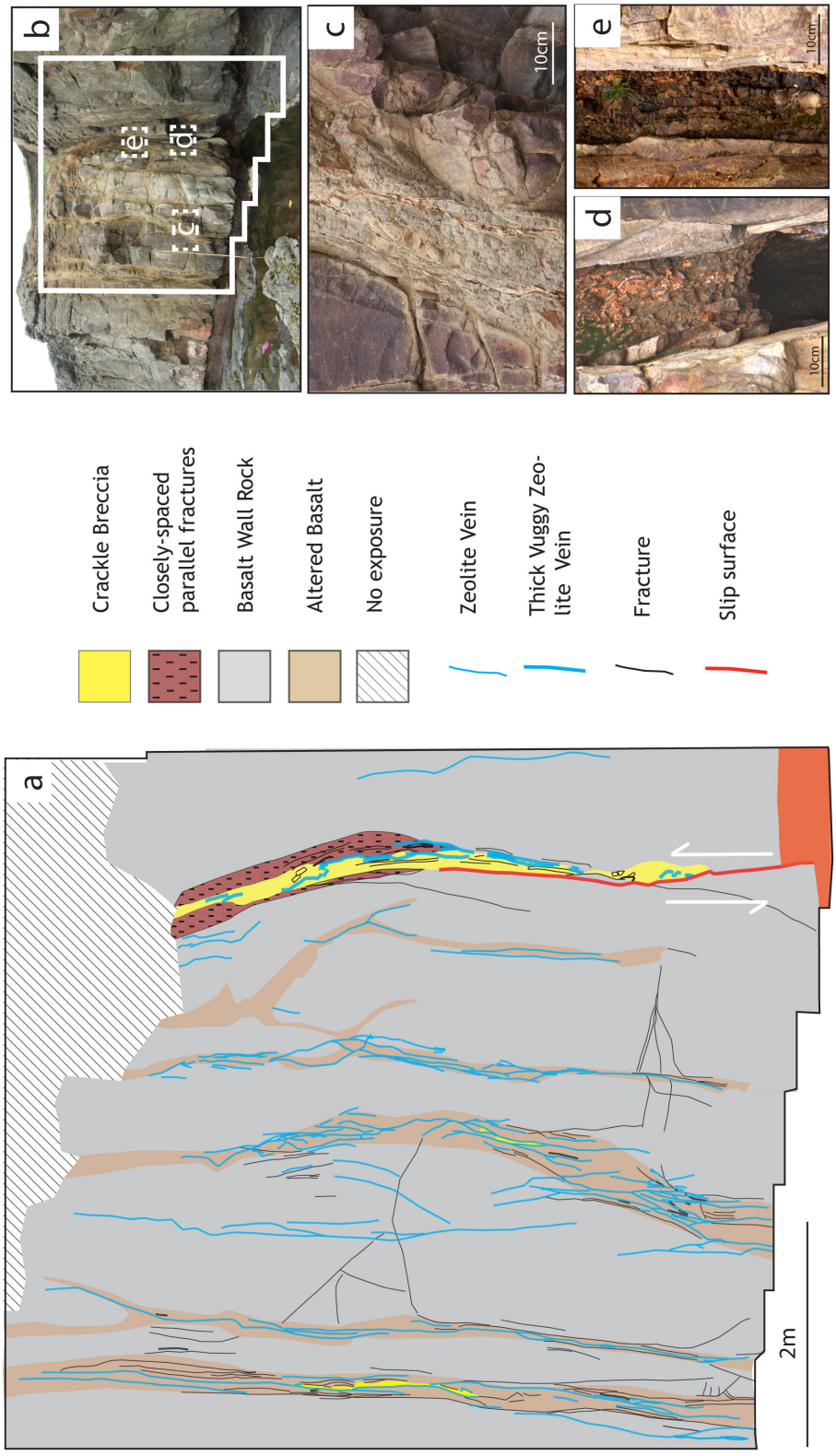

Figure 3.7: Detail of VPF, 28cm displacement. View toward north in all images. a) Fault map, highlighting main zone of deformation (slip surface) and hanging wall damage. b) Location of a) without fault map overlay. c) Detail of alteration and mineralised shear fractures. Note distinct colour change surrounding fractures. d) Detail of chaotic breccia. e) Detail of slabs of wall rock within chaotic breccia zone.

3.3.3. Self-juxtaposed: medium displacement faults

3.3.3.1. Bird Nest Fault (BNF), Scotland

The 1m displacement BNF (Figure 3.8) is exposed on a cliff section, and displaces an amygdaloidal- and massive-basalt flow. The BNF is characterised by a >40cm wide zone of fault-related deformation, dominated by a PSZ of alteration and zeolite mineralisation, along with fracturing and brecciation.

Unlike VJF and VPF, fractures surrounding the fault zone are difficult to distinguish from background fracture content (e.g. cooling joints), and so the true width of the fault zone may be obscured. Fractures surrounding the PSS are open, and present day fluid flow of water is noted within them. Therefore, fractures surrounding this fault zone are important to note when considering permeability, as they are still a permeable feature, regardless of whether they are fault or host rock related. In the hanging wall, mineral veins kinematically related to the fault zone are found, suggesting fault-related fracturing outwith the PSZ has occurred.

The PSZ is bound by slip surfaces. The PSZ is composed of altered basalt, cut by zeolite veins and secondary slip surfaces (Figure 3.8a). The alteration is distinct from the surrounding host rock, in that it is a brown-gray colour compared to the gray of the host rock, and is also more friable. The PSZ thickness varies along strike, and at its narrowest point is only as thick as the PSS (<1cm). Where the PSZ widens, mosaic breccias (Figure 3.8c) or basalt lenses bound by mineralised slip surfaces are encountered. The mosaic breccias are composed of rotated clasts of altered and fractured basalt wall rock, supported by zeolite minerals. The host rock lenses are altered internally, and contain zeolite veins.

The PSS is continuous along strike, and is located along the footwall margin of the fault zone. The PSS is polished, and mineralised by zeolite veins.

Secondary slip surfaces form the other boundary of the altered PSZ in the hanging wall, but these are not continuous, and are not always mineralised. Secondary slip surfaces within the altered zone are parallel to the PSS, and can therefore be considered as Y shears.

Zeolite veins have also formed within the altered zone (Figure 3.8d), in an orientation similar to that of the secondary slip surfaces (i.e. Y shear orientation) and also at other riedel shear orientations (at an angle to the PSS). These zeolite veins form a crack-seal type morphology in places within the alteration zone, and also cross-cut the secondary slip surfaces.

Whilst inaccessible, exposure of the fault higher up in the stratigraphy (~30m) could be seen with binoculars. Here, the displacement was minimal (i.e. cm value), suggesting displacement along the fault is dying out. From the limited view available, the fault morphology at small displacements was similar to that of the VJF, with parallel fractures dominating the fault zone, along with mineralisation.

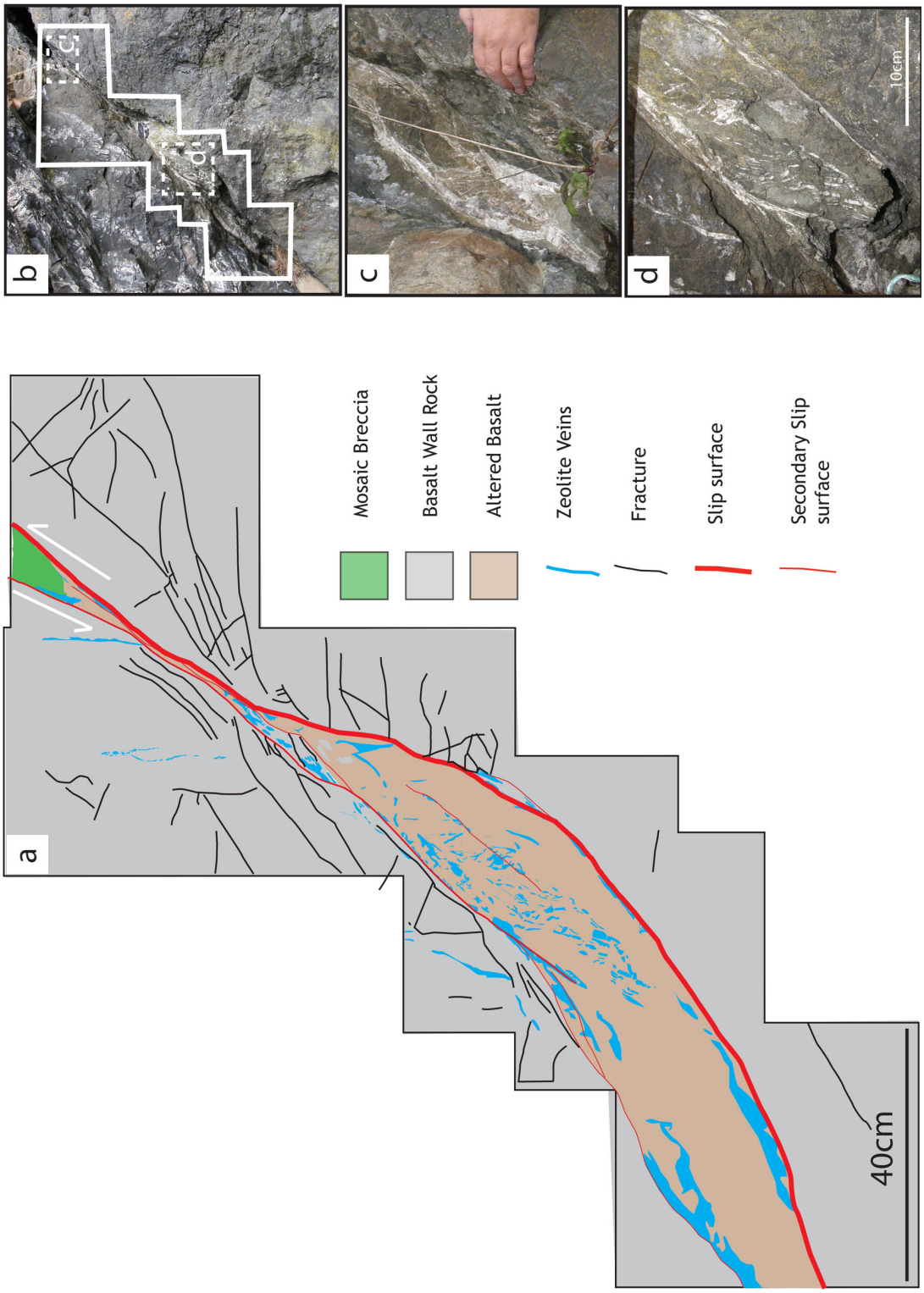

Figure 3.8: Detail of BNF, 1m displacement. View toward the north in all figures. a) Fault map, highlighting principal slip surface and zone of alteration. b) Location of a) without fault map overlay. c) Mosaic breccia with mineral matrix. d) Zone of alteration with mineralised fractures.

3.3.3.2. Sumba Fault Zone (SFZ), Faroe Islands

The Sumba Fault Zone (SFZ) has a total displacement of 5m, across a 6m wide zone. The SFZ contains two faults (Figure 3.9a,b) – a master, 4m fault which displaces basalt against volcanic conglomerate, and a subsidiary, 1m fault, which displaces basalt lava against itself. In this section the subsidiary fault morphology is described. The master fault's morphology description can be found in the non self-juxtaposed medium displacement section. The overall architecture and summary of fault structures of the SFZ have been described previously in Walker et al., (2012a) and therefore this description provides a detailed account of the deformation elements found within the fault, rather than the fault zone as a whole.

The subsidiary fault has a 50cm wide PSZ, dominated by extensional-shear fractures, and extensive alteration. A mature PSS is continuous along the whole of the outcrop and, along with secondary, discontinuous slip surfaces, bounds the PSZ.

The PSZ is composed of mostly fractured and altered basalt, with clasts of basalt (Figure 3.9c) set in an altered matrix. The PSZ is also composed of lenses of host rock, bound by slip surfaces, which are altered and mineralised along and adjacent to the slip surfaces (Figure 3.9d). Mosaic breccias are also found along the fault as discontinuous lenses, and are mineralised and altered. Other parts of the PSZ display parallel fracture zones that are heavily altered along the fracture lines (Figure 3.9e).

Alteration is present throughout the whole of the PSZ, particularly adjacent to slip surfaces. The slip surfaces themselves are heavily mineralised by zeolites (Figure 3.9f). The PSZ is variable in width along the fault, becoming thinner (13cm) where large blocks of basalt in the hanging walls are not fractured, and thicker (50cm) where footwall basalt is more fractured.

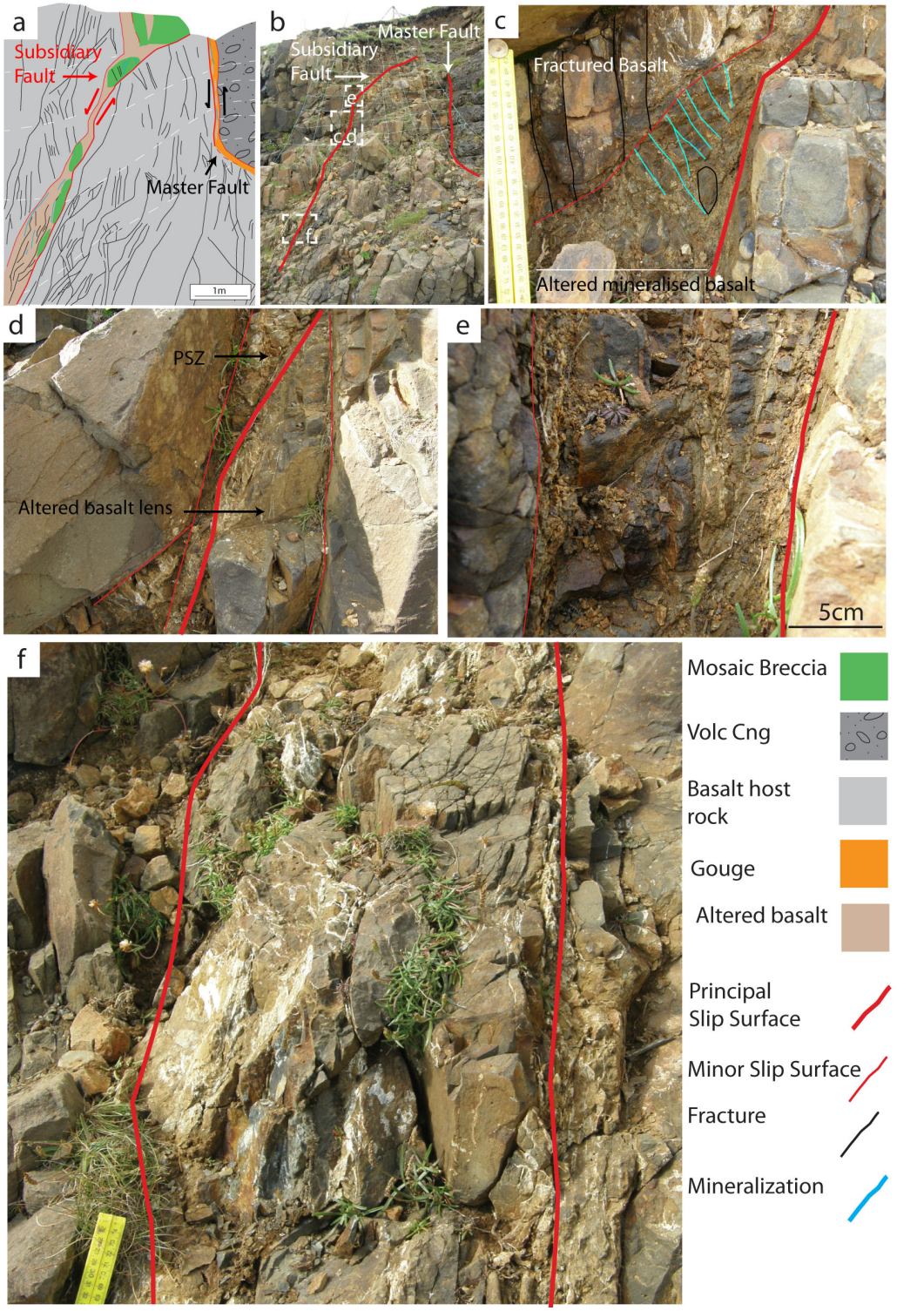

Figure 3.9: Detail of subsidiary fault from the SFZ. View toward NW in all images. a) Summary fault map of SFZ. b) Photograph of SFZ with photographs labelled. c) Detail of PSZ altered and mineralised basalt. Slip surfaces and mineralisation digitised. d) Example of slip surface bound altered basalt lens, adjacent to altered PSZ. e) Parallel fracture zone heavily altered along the fractures, leaving less altered host rock clasts between fractures. f) Detail of slip surface, with a lot of mineralisation and alteration. Ruler for scale (10cm).

3.3.4. Self-juxtaposed: high displacement fault – Hramaborg Fault (HBF), Scotland

The 25m displacement Hramaborg Fault (HBF) displaces lava flows in east Iceland across a >40m wide deformation zone (Figure 3.10a). This deformation zone is characterised by multiple faults and fractures, which locally displace the geological stratigraphy of the local area. Whilst individual faults within this zone have a displacement of less than 25m, overall they accommodate 25m of displacement, as evidenced by the displacement of the ignimbrite unit in the stratigraphy of the footwall. Here, the structure of the fault zone as a whole is described, with particular focus on a self-juxtaposed fault within the displaced basalt flow, which has a displacement value of less than 25m.

The 40m wide deformation zone is composed of a number of subsidiary faults that juxtapose mudstones with basalt lavas, and basalt lavas against themselves. The displacement value of these was undeterminable in the field due to the complex nature of faulting interrupting stratigraphic horizons, but estimated as between 1m-10m. The fault displacing basalt against mudstone is shown in Figure 3.10b, where the mudstone is sheared against the basalt as a thin (1-2cm) gouge smear, and the basalt is polished with normal slickenlines. The mudstone also has a minor, cm-displacement fault running through it (parallel to the previously described fault), as well as a <1m displacement normal splay fault, which also displaces the basalt.

Three metres to the right of this exposure, two minor (<1m displacement) subsidiary faults (one of which is the splay fault from Figure 3.10b) are exposed, again displacing mudstone against basalt. In the leftmost fault shown in Figure 3.10c, the mudstone is fractured adjacent to the fault, and the basalt retains its original morphology. However, the basalt to the right of this fault (i.e. between the two subsidiary faults) is partially rotated (deviates from the regional dip and strike), and is heavily fractured in situ.

The last exposure of basalt in the fault zone is also heavily fractured. This fractured zone is a good 10m wide, and increases in deformation to the right of the image shown in Figure 3.10c. Figure 3.10d shows the heavily fractured basalt, where blocks of altered basalt and brecciated basalt are bound by fractures. The fractured mass also contains cataclasite strands e.g. zones of localised cataclasite formation dispersed throughout the fractured zone (Figure 3.10e). These strands form in the same orientation as the dominant fracture orientation (Figure 3.11c), and these cataclasite strands can be traced upward in the exposure, where they vary in thickness. Adjacent to these cataclasite strands are zones of mosaic and chaotic breccia. The detail of one of these cataclasite strands is presented in Figure 3.11a. The cataclasite strand is composed of a mature PSS that is continuous along strike, as well as secondary slip surfaces that locally displace small, partially rounded clasts of host rock basalt. These rounded clasts are set in a fine-grained matrix of protocataclasite (Figure 3.11d). The mosaic and chaotic breccias surrounding this cataclasite strand contain rotated (evidenced by partial rounding of clasts), sub-angular to sub-rounded host rock clasts, and are clast supported (Figure 3.11e). The clasts are fractured and altered (Figure 3.11e). Mineralisation is largely absent in this high displacement fault, though thin mineral films of zeolites do occur along slip surfaces and subsidiary faults. Geochemical alteration is apparent throughout the site.

Considering these observations, the overall structure of the fault zone is presented in Figure 3.12 as a schematic, not to scale, cross section. The cross section takes into account present day topography, which explains the lack of ignimbrite found within the fault zone. The whole fault zone is a series of small-scale extensional horsts and grabens, with low-medium displacement faults accommodating displacement throughout the fault zone. It is likely the highly fractured lava at the right of the outcrop is taking up a large amount of displacement, as shown illustratively in Figure 3.12c, and may explain the presence of cataclasites strands (representing high strain zones).

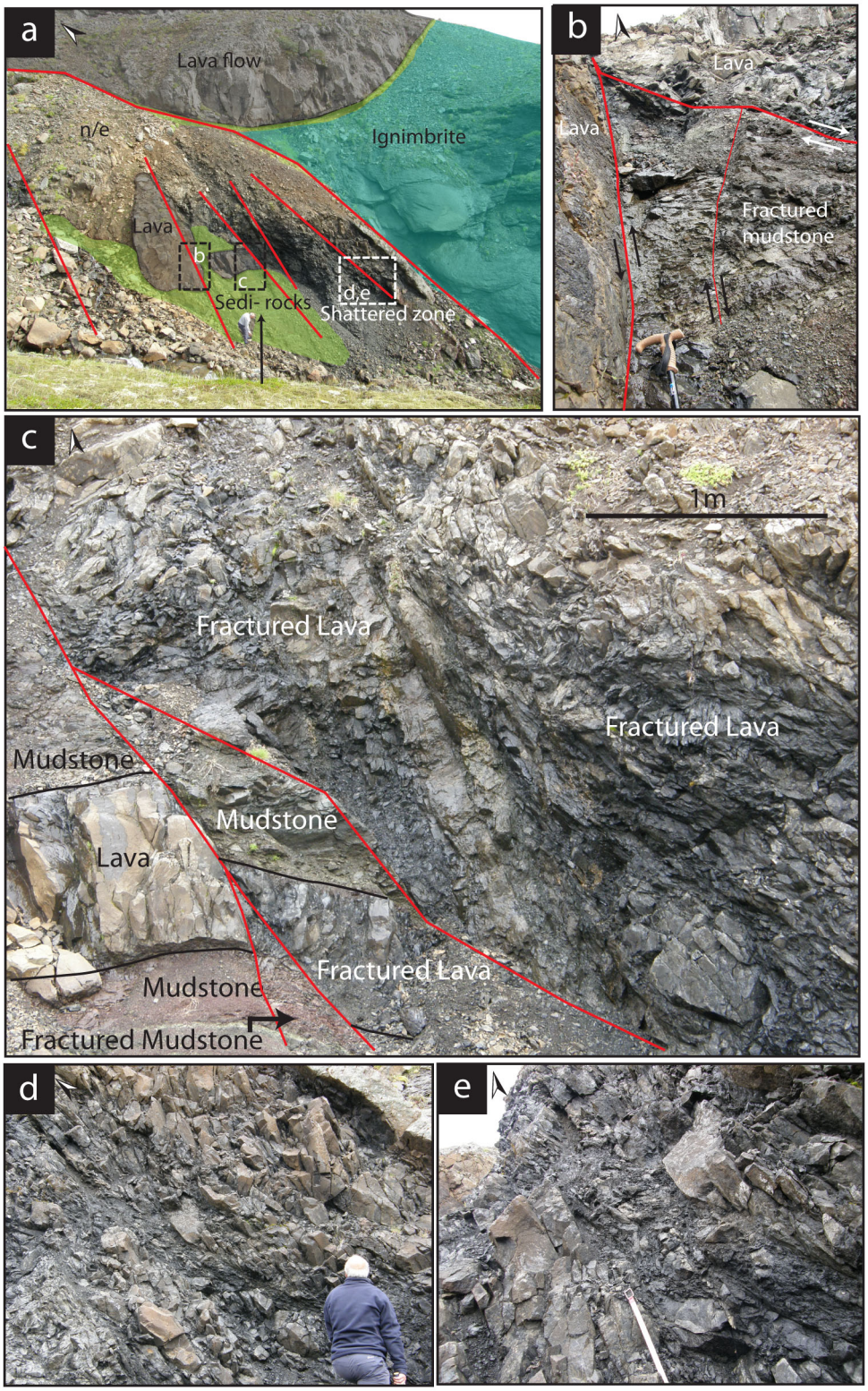

Figure 3.10: Photographs from the HBF zone. Arrows indicate north. a) Detail of fault zone. Red lines mark faults, and dashed boxes mark locations of photos within the rest of the figure. Dad for scale. b) Detail of fault displacing basalt against mudstone. Basalt very polished, with thin gouge line along slip surface. Note fractured nature of mudstone. c) Detail of faults displacing mudstones and lavas to the right of b). Note fractured lava between two faults. d) Detail of shattered zone of basalt. e) Detail of cataclasite strand running within shattered zone.

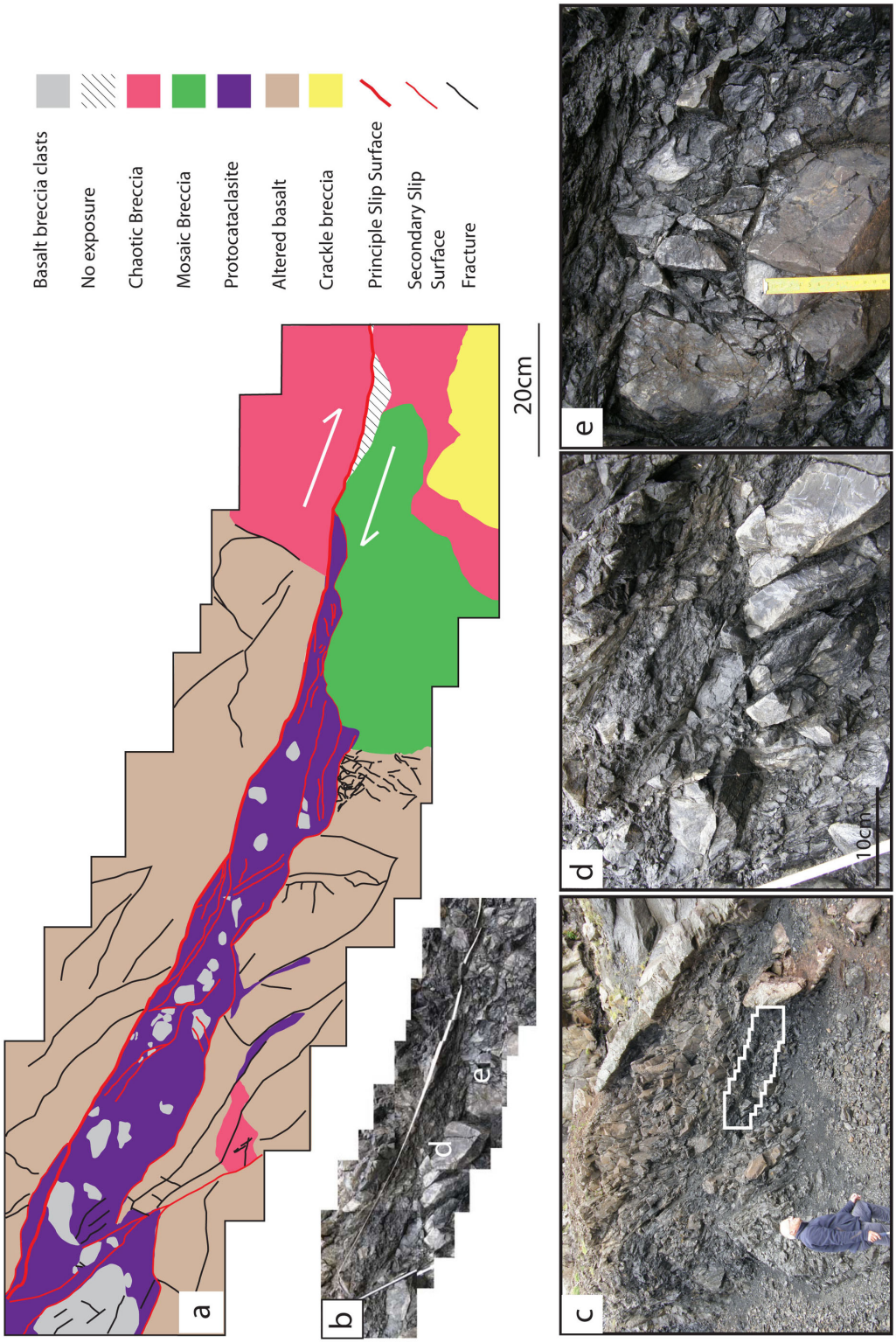

Figure 3.11: Detail of HBF, 25m total displacement. View toward NE in all images. a) Fault map, highlighting zones of complex fault rocks. b) Fault without map overlay, showing locations of e) and d). c) Location of fault strand within overall area of fault deformation. d) Complex fracturing and fault rocks surround a cataclasite zone with altered basalt clasts. e) Progressive fracturing adjacent to cataclasite zone.

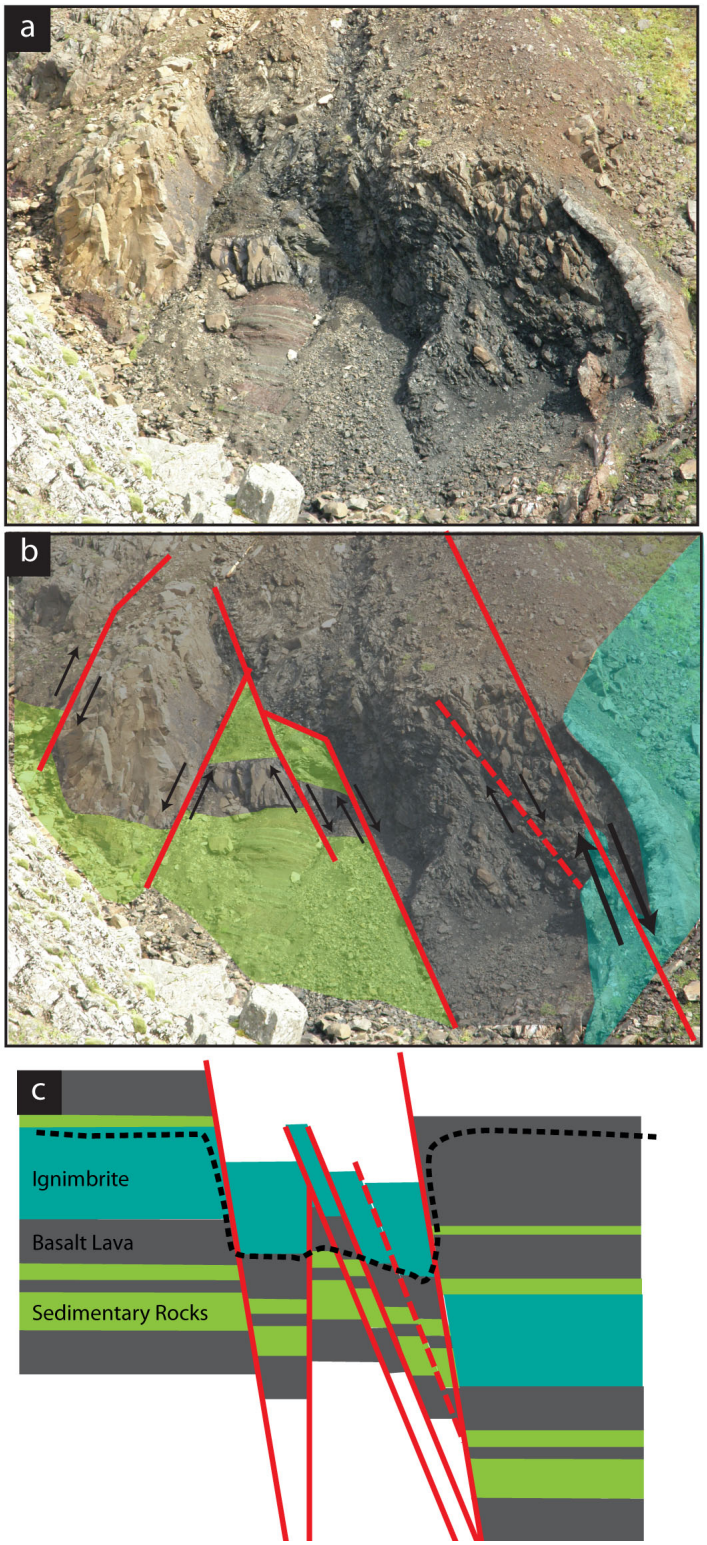

Figure 3.12: Interpretation of HBF zone, based on fieldwork. View toward north in all images. a) Photo overview of the site. b) Annotated photo from a), showing positions of faults located from fieldwork with slip sense. Colour of units are described in c). c) Interpretative cross section (not to scale) of HBF, with present day topography represented by dashed black line. River erosion has caused this dip in topography. Faults marked in red. Dashed red line represents fractured zone where cataclasite strand was mapped.

3.3.5. Self-juxtaposed fault summary from this study

Protofaults (minimal displacement) are defined by extensional fracture meshes and through-going incipient principal slip surfaces, with minor zeolite mineralisation.

Low displacement faults (<1m) are characterised by a relatively wide zone of deformation (accommodated by extensional/extensional-shear fractures), surrounding an immature-mature principal slip surface. The PSS is immediately adjacent to zones of parallel, closely spaced fractures, and crackle breccias. Zeolite veining and alteration is current throughout the whole fault zone particularly focused within fractures and breccias.

Medium displacement faults (≥1m -10m) are also characterised by a relatively wide zone of deformation (again accommodated by extensional/extensional shear fractures), a mature PSS, brittle fault structures (Y and riedel shears), crackle to mosaic breccias development, and zeolite mineralisation and alteration.

High displacement faults (>10m) are characterised by an intensely fractured wide zone of deformation with subsidiary faults accommodating small levels of displacement. Subsidiary faults include gouges where basalt is juxtaposed against sediments. With increasing displacement, where basalt is self-juxtaposed, protocataclasites have formed as strands and demonstrate foliated cataclasite development. Chaotic and mosaic breccia-type zones surround the cataclasite strands. Zeolite mineralisation and alteration also affect the fault.

The deformation elements present in the above fault displacement values are summarised in Table 3.1.

Table 3.1: Summary table of deformation elements in self-juxtaposed faults. (PF=Protofault, LDF=Low displacement fault, MDF=medium displacement fault, HDF=high displacement fault. ISS=incipient slip surface, IMS=immature slip surface, MSS=mature slip surface, F=fractures, PSZ=parallel fracture zone, CB=crackle breccia, MB=mosaic breccia, ChB=chaotic breccia, PC=protocataclasites, BFS=brittle fault structures, SF=subsidiary faults, Z=zeolite, A=alteration.)

	ISS	IMS	MSS	F	PSZ	CB	MB	ChB	PC	BFS	SF	Z	A
PF	X			X								X	X
LDF		X	X	X	X	X						X	X
MDF			X	X		X	X			X		X	X
HDF			X	X			X	X	X	X	X	X	X

Thickness/displacement relationships of all self-juxtaposed faults from this study were generated to determine if there is a relationship between fault displacement and PSZ thickness. Fault-related fractures surrounding the PSZ were not included in the PSZ thickness. This is because the PSZ is defined in this study as consisting of fault rocks, and is the zone that accommodates most displacement. Due to the HBF having multiple slip zones, the total thickness of the deformation zone associated with it was plotted, whereas for the rest of the faults, the PSZ variations in thickness were directly measurable, and only contained one PSZ. The results are presented in Figure 3.13. The results indicate a general increase in thickness with displacement, but each fault has a large variety of thicknesses within its PSZ, which vary by one order of magnitude.

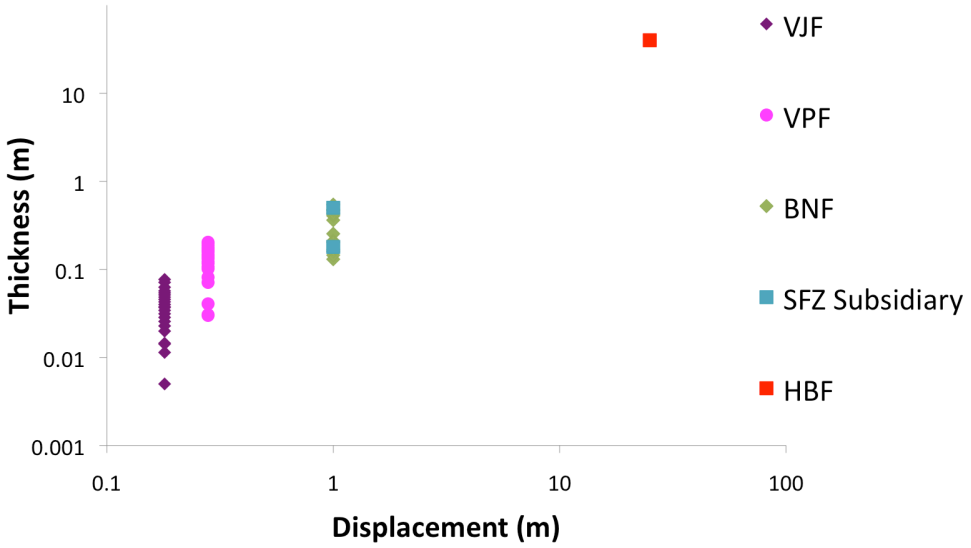

Figure 3.13: Thickness/displacement plot of self-juxtaposed faults. Variations of thicknesses are plotted as there is no uniform thickness of the PSZ in all faults. Displacements are well constrained within field sites, based on marker horizons.

3.4. Non self-juxtaposed faults

3.4.1. Non self-juxtaposed: low displacement faults

Non self-juxtaposed faults (e.g. exposure along a fault where a basalt sequence unit is faulted against another unit) require a fault to have a throw greater than the bed thickness of the faulted lithology, in order for a rock unit to be faulted against another rock unit from elsewhere in the stratigraphy. Given that basalt lava flows can be up to 20m thick, and are rarely thinner than 5m (depending on lava type), low displacement faults with a non self-juxtaposed relationship in basalt sequences are few, and were not found in this study.

3.4.2. Non self-juxtaposed: medium displacement faults

3.4.2.1. Hov Fault (HVF), Faroe Islands

The 1m displacement HVF displaces columnar basalt lava flow, tuff, volcanic conglomerates and massive basalt lava flow in a roadside cliff exposure (Figure 3.14a,b). The exposure was mapped from the bottom of the exposure up to 2m height, though 100% exposure of that part was not available due to the waterfall and vegetation. Therefore, the fault map presented in Figure 3.14a is more detailed in the bottom part of the map, and provides a generalised schematic of the fault rather than a fully detailed one.

The deformation zone surrounding the fault zone was difficult to discern due to the background fractured nature of the units, with the exception of the columnar jointed lava unit at the top of the exposure. This unit contains evenly spaced columnar joints, but, with decreasing distance to the fault, fracture density increases and columnar jointing is obscure (Figure 3.14c). These fractures are formed parallel to the PSS, similar to those parallel fracture zones observed in VJF and VPF.

The PSS is continuous along strike (i.e. mature), and is heavily polished and mineralised, particularly within juxtapositions of basalt and volcanic conglomerate. The PSS changes in dip, depending on which unit it intersects: it is near vertical within the upper basalt lava flow, and gradually develops a gentler dip to 70° within the volcanic conglomerate and lower level basalt. This observation can be attributed to the contrasting mechanical strength of the units faulted. Refracted fault trajectories are common in mechanically layered sequences, where variations in fault angle are due to differences in friction angle or failure mode in each unit (see Chapter 1; Ferrill and Morris, 2003).

Where exposed, fault rocks adjacent to the PSS are composed of crackle breccias, which are heavily mineralised particularly within juxtapositions of basalt and volcanic conglomerate. The thickness of the crackle breccia varies along strike, from 10cm to 60cm wide. The breccia zone thickens where the basalt is self-juxtaposed at the base of the exposure. Mineralisation is particularly concentrated within this thick breccia zone, and thick (<5cm) zeolite veins in a crack-seal morphology are exposed (Figure 3.14d,e), where rafts of host rock are trapped between parallel mineral veins. Within the narrower parts of the crackle breccia zone, zeolite vein thickness and distribution significantly decreases but does continue to form the matrix of crackle breccias in the upper levels of the fault. Geochemical alteration is apparent surrounding the basalt lava units.

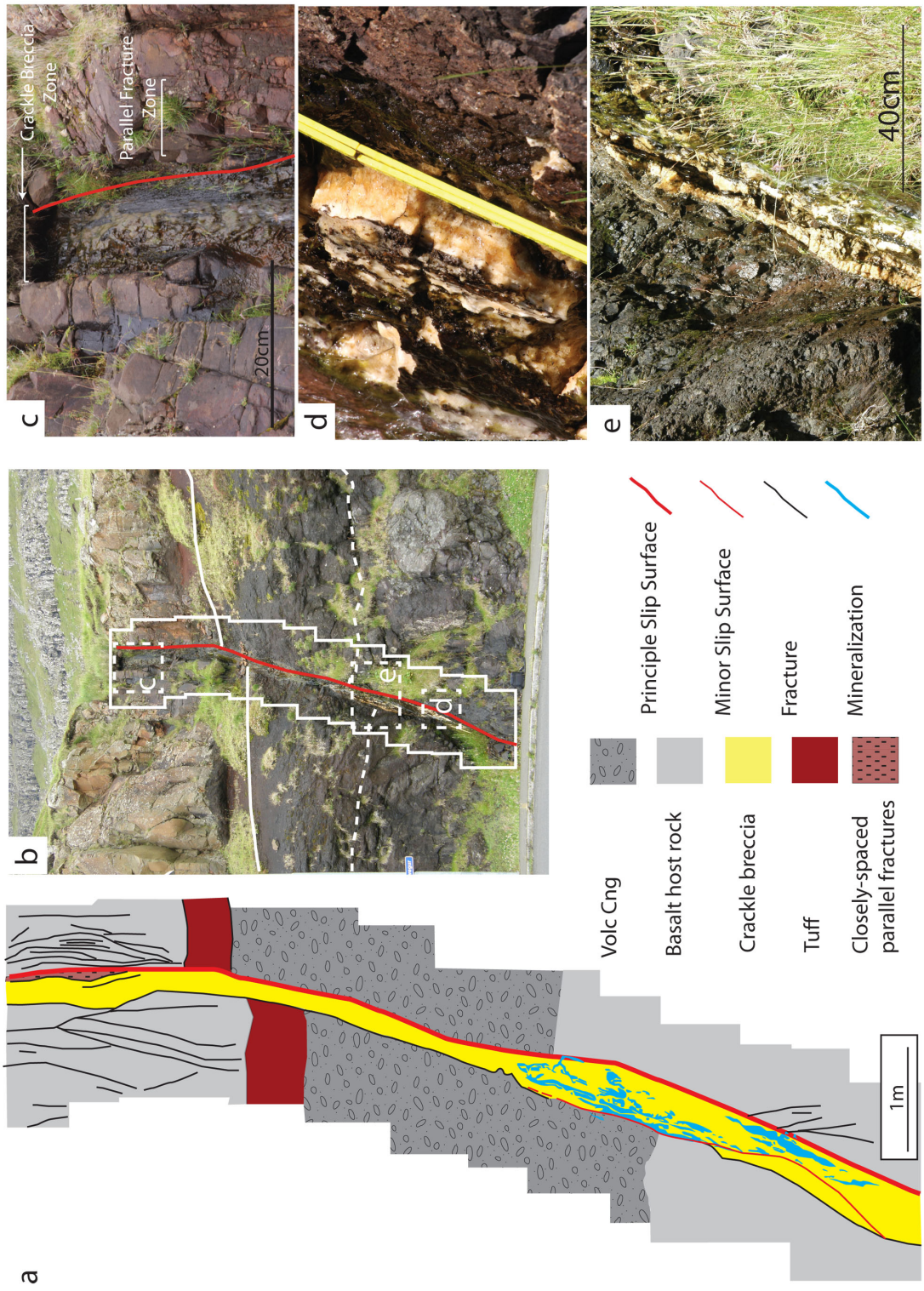

Figure 3.14: Detail of Hov Fault, 1m displacement. View toward north in all images. a) Fault map, highlighting change in fault trend from lava hosted fault to volcaniclastic hosted fault. b) Fault without map overlay, white lines represent tuff base (solid) and volcanic conglomerate base (dashed). c) Detail of self-juxtaposed fault relationship, with parallel fractures. d) Detail of non self-juxtaposed fault, showing narrow zone of fault zone with minimal distortion of bedding. e) Detail of fault in self-juxtaposed basalt, highlighting extensive mineralisation forming along the slip surface and encapsulating host rocks.

3.4.2.2. Sumba Fault Zone (SFZ), Faroe Islands

The SFZ has a total displacement of 5m, across a 6m wide zone. The SFZ contains two faults (Figure 3.15a,b) – a master, 4m fault which displaces basalt lava against volcanic conglomerate, and a subsidiary, 1m fault, which displaces basalt lava against itself (this fault is described in the self-juxtaposed medium displacement, section 3.3.3.2). In this section the master fault's morphology is described.

The master fault has a displacement of 4m, and displaces a basalt lava against a volcanic conglomerate (Figure 3.15a,b). The basalt fault wall is fractured and altered immediately adjacent to the PSS. The PSS is located at the interface between the basalt and the volcanic conglomerate, and is continuous along the exposure.

The adjacent PSZ is composed of two principal fault rock types. Fractured lenses of volcanic conglomerate and basalt are entrained along the fault, and are altered and mineralised by zeolite (Figure 3.15c). Mixed throughout the fractured lenses, and entrained along the slip surface is fault gouge, derived from the volcanic conglomerate matrix (Figure 3.15d). Mineralisation is largely absent from the gouge, though does exist as fine shear veins in places. Geochemical alteration is largely absent within the PSZ, though alteration of the PSS adjacent to the basalt has occurred. The PSZ is 20cm at its widest point, and varies along strike to a minimum of 5cm.

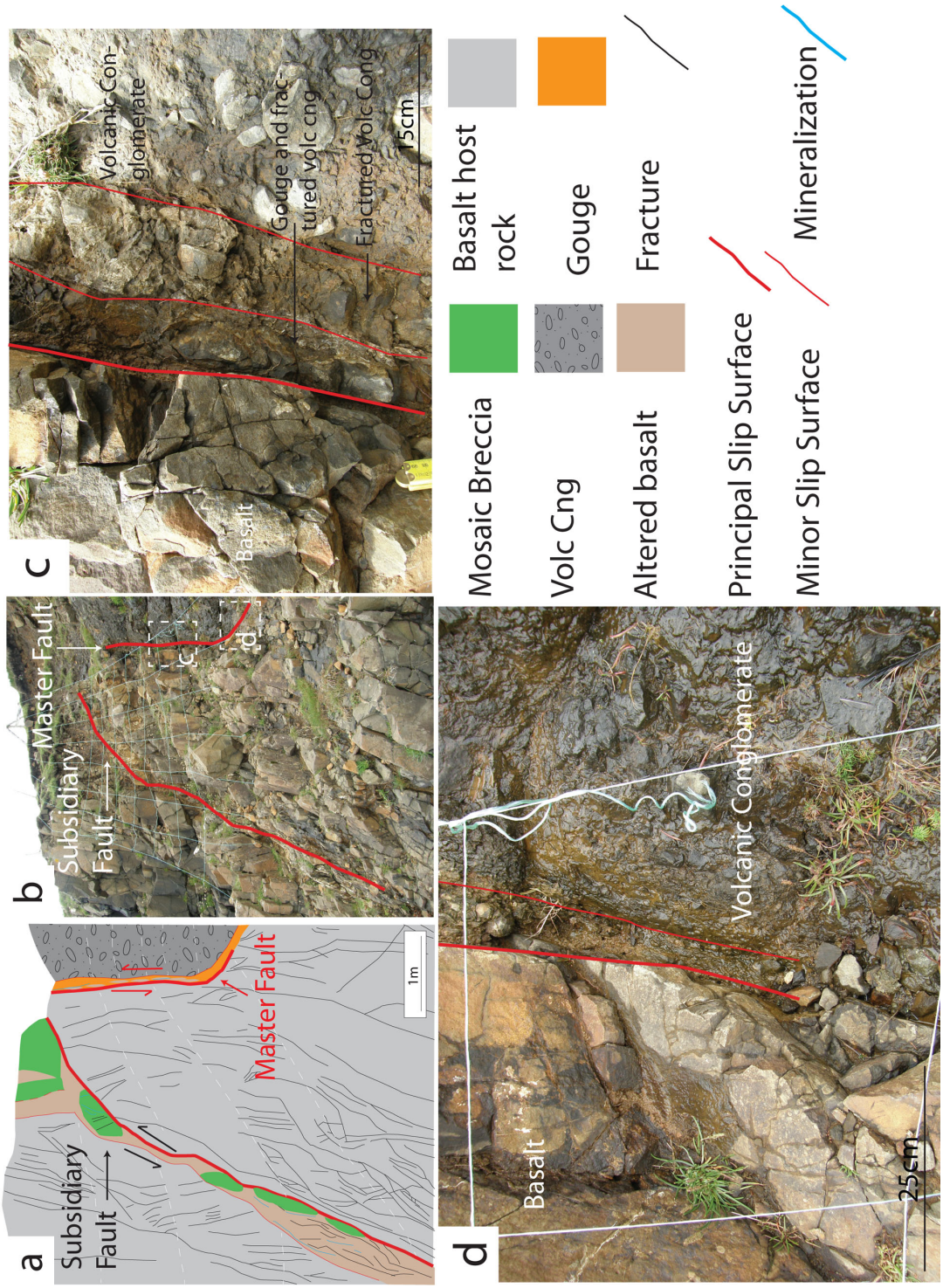

Figure 3.15: Detail of Sumba Fault Zone, 5m total displacement. View toward NW in all images. a) Fault map of Sumba fault, with the leftmost fault having 1m displacement and self-juxtaposed, and the rightmost fault having 4m displacement and non self-juxtaposed (basalt against volcanic conglomerate). b) Detail of a) without fault overlay, with positions of additional figures marked. c) Lenses of altered basalt caught within gouge layer formed between basalt and volcanic conglomerate interface. d) Gouge formation at interface of basalt and volcanic conglomerate.

3.4.2.3. I Botni Fault (IBF), Faroe Islands

The IBF has 5m displacement, and displaces basalt against another basalt, separated by a tuff layer (Figure 3.16a,b). The IBF has previously been described in Walker et al. (2011b), and therefore a summarised description of the fault (based on data from this study) is presented below.

Fault-related deformation surrounding the PSZ in the hanging wall is accommodated by low displacement subsidiary faults, extensional fractures and mosaic breccias. Where fractures within the hanging wall propagate into the tuff layer, the dip changes from near vertical in the basalt to around 70º in the tuff (Figure 3.16d). In the footwall, a chaotic breccia adjacent to the PSS is composed of rotated rounded clasts (<3cm) of altered basalt and tuff (Figure 3.16e). The chaotic breccia is matrix supported.

The PSS is mature, and continuous along the length of the exposure, and is polished and mineralised by zeolite. The tuff horizon (Figure 3.16a,b), has been entrained along the PSZ, forming a 'tuff smear' (Figure 3.16c), similar to shale smears observed in sand/shale sequences. The tuff smear is composed of a tuff-derived gouge, which is softer and more friable than the host tuff. The gouge also contains altered basalt clasts (Figure 3.16c), possibly derived from the fractured hanging wall basalt by asperity removal. Alteration of the basalt surrounding the PSZ is minimal, with alteration only affecting the basalt surrounding the fractures.

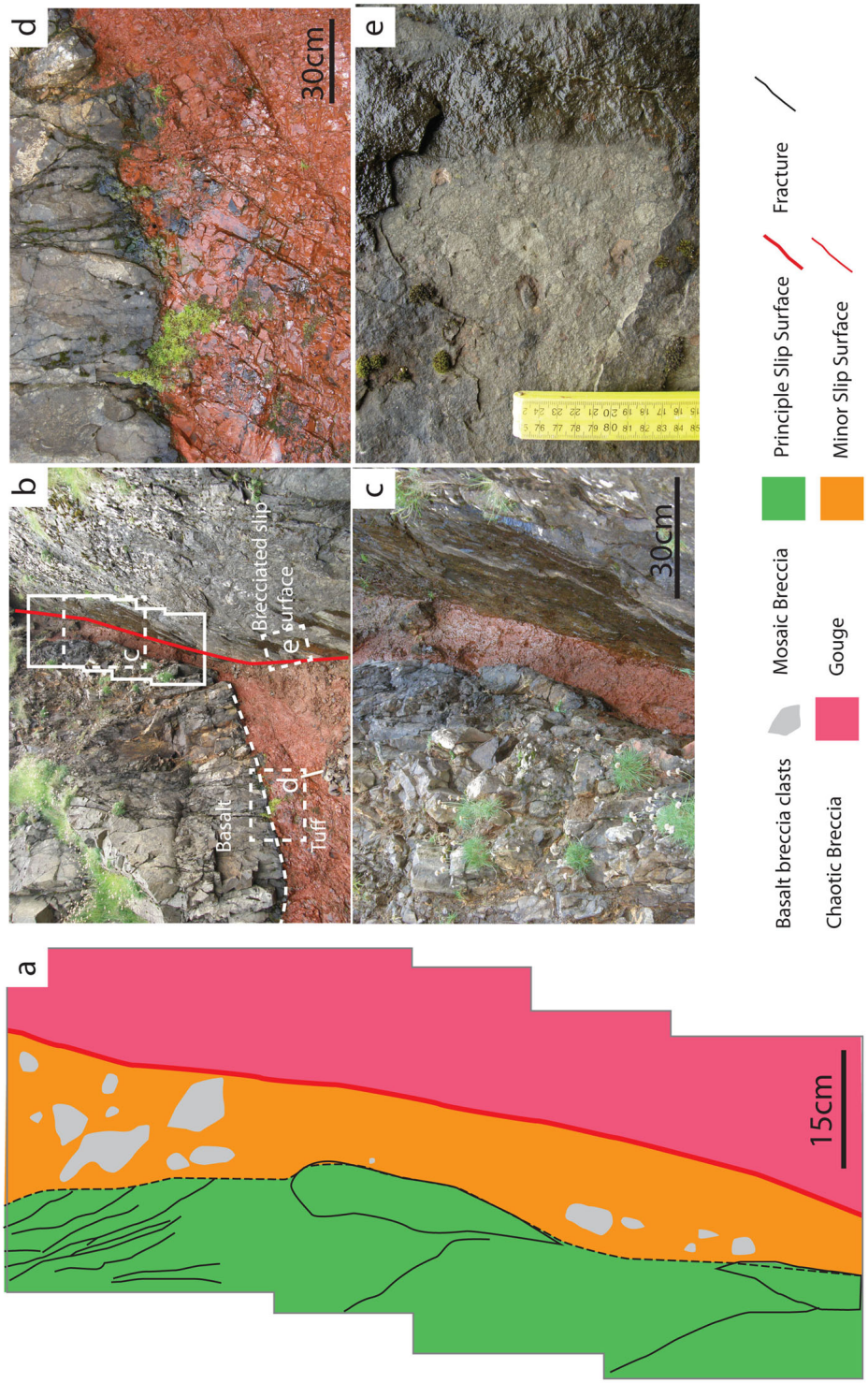

Figure 3.16: Detail of I Botni Fault, 5m displacement. View toward SE in all images. a) Fault map highlighting extensive gouge formation within the fault zone, and chaotic breccia formation on the footwall. b) Fault without fault map overlay, highlighting locations of additional figures. c) Detail of tuff-derived gouge (red) with clasts of altered basalt. d) Fractures within the overlying basalt continue within the tuff at a different angle. e) Chaotic breccia from the slip surface is composed of altered clasts of basalt and red tuff clasts.

3.4.3. Non self-juxtaposed: high displacement faults

3.4.3.1. Lawther Fault (LWF), Scotland

The LWF displaces basalt against fluidal peperite, with an offset of at least 10m (Figure 3.18a,b). The total displacement cannot be constrained due to poor exposure, but it must be over 10m, as the peperite in the footwall is exposed up to a height of 10m, and the overlying basalt is not exposed. The fault movement was determined as normal by dip-slip linear steps within slickenlines along the principal slip surfaces, and by mapping basalt stratigraphically higher than the peperite in a nearby exposure.

The peperite in the footwall is riddled with background fractures, and has multiple shear fractures across the exposure. Due to the peperite's very altered nature, fault-related fractures are difficult to distinguish from background fractures. However in the basalt hanging-wall, fracture frequency increases ~1m toward the fault (Figure 3.17a), and fracture dip changes 2.5m away from the fault (Figure 3.17b). These fractures are therefore considered fault-related at a maximum of 2.5m from the fault in the hanging wall.

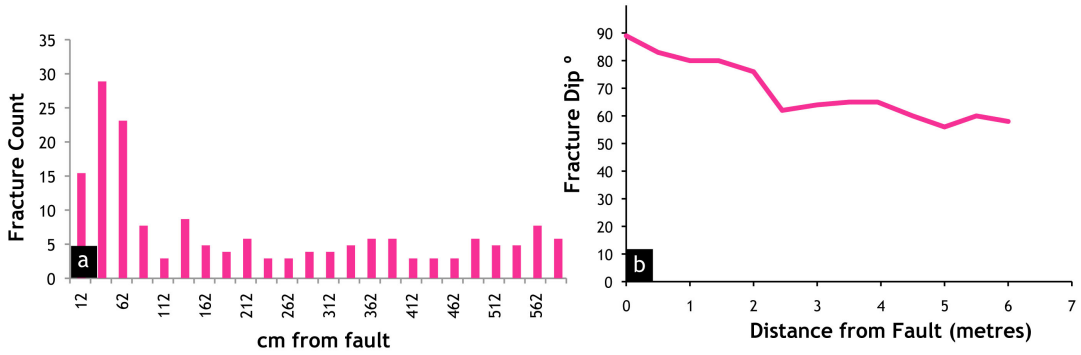

Figure 3.17: Fracture data from hanging wall of LWF. a) Fracture frequency from hanging wall. Results are binned from total amount of fractures counted in ~50cm intervals from the PSS to undeformed host rock. b) Average fracture dip data from 1m intervals within hanging wall.

Adjacent to the fault, fractures in the hanging wall basalt are curved (Figure 3.18c), between the mature PSS and a secondary slip surface formed within the basalt. Also in this hanging wall region, at the intersection of the PSS and secondary slip surface is a chaotic breccia zone.

Adjacent to the secondary slip surface running parallel between it and another fracture is a tabular zone of mosaic breccia (Figure 3.18d).

The PSS is mature, continuous along the length of the outcrop, and is well polished. In addition to the continuous PSS, secondary slip surfaces run parallel to the PSS within the PSZ (Y shears).

The PSZ is composed of three fault rock types, gouge, cataclasite, and altered basalt lenses, the distributions of which run parallel to the PSS. At its widest point, the PSZ (adjacent to the PSS) is 12cm, and 4cm at its narrowest point.

The gouges are brown and black in colour, and very fine grained with <1mm size clasts of altered wall rocks entrained within them. These gouges have formed adjacent to the slip surfaces (Figure 3.18e), and are derived from comminution of the peperite. The distribution of the gouge thins out toward the top of the exposure.

Cataclasites are brown in colour, and are unevenly distributed along the fault but are particularly common adjacent to the slip surface. The cataclasites are mostly derived from the peperite host rock, (and some from the hanging wall basalts), mostly where secondary slip surfaces have formed within the basalt wall.

Distributed within the gouge/cataclasite zone are very altered basalt lenses, and the extent and thickness of these increases toward the top of the outcrop. Mineralisation is sparse throughout the LWF, although mineral veins occur along minor slip surfaces within the basalt, and along fault-related fractures within the basalt wall.

Geochemical alteration (evidenced by the friable nature of the outcrop) is abundant as background alteration within the peperite, due to its high clay content, but within the basalt an obvious change from gray/black basalt into very friable brown basalt is observed within 1m of the fault. Also, all fault rocks contain a high proportion of clay and altered basalt.

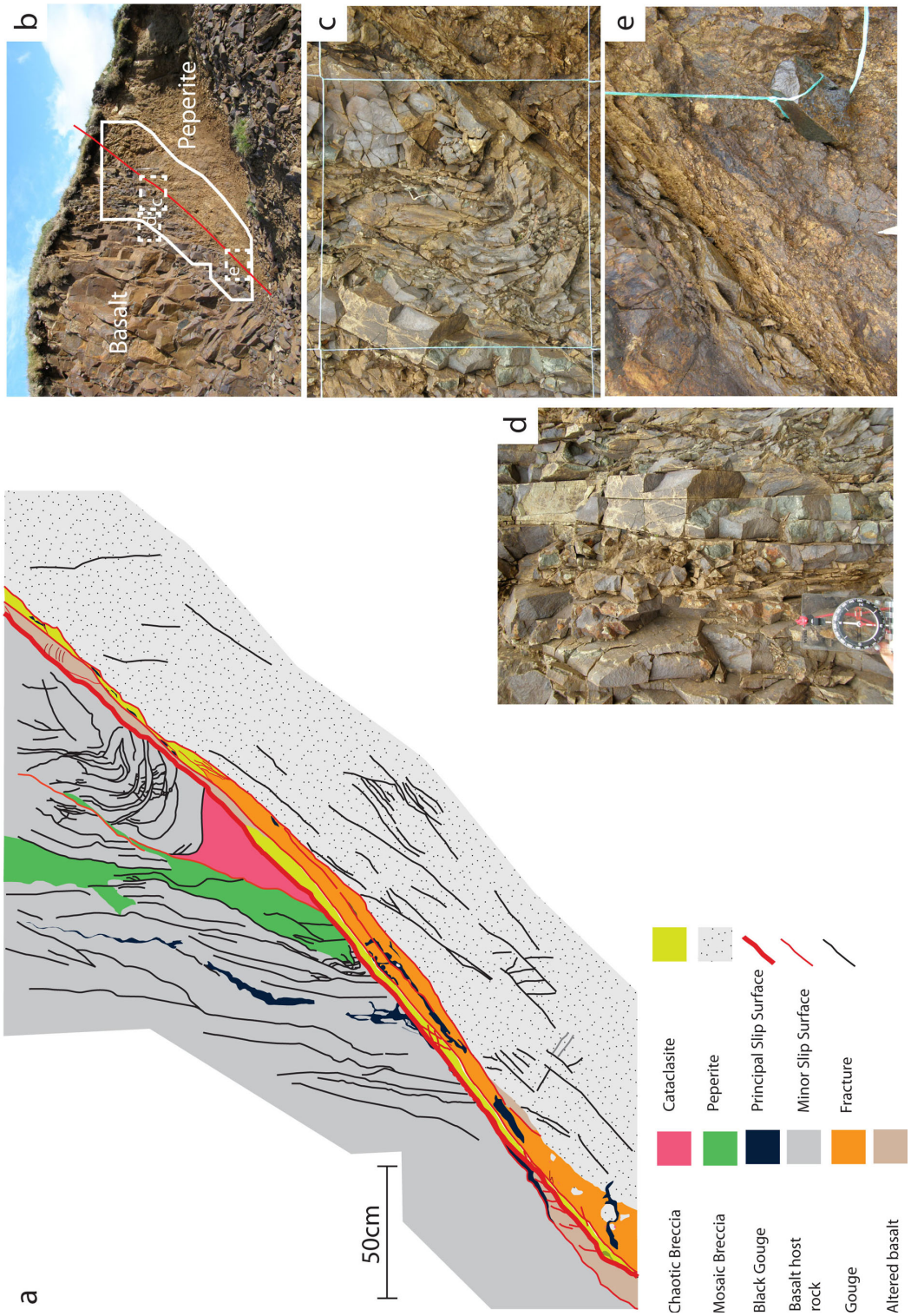

Figure 3.18: Detail of LWF, Ardnamurchan, >10m displacement. View toward south in all images. a) Fault map of LWF, highlighting localisation of gouge and cataclasite along slip surface, as well as brecciation of the basalt hanging wall and formation of curved fractures. b) LWF without fault map overlay, marking positions of additional figures. c) Curved fractures formed between the PSS and secondary slip surface. Grid is 40cm square for scale. d) Mosaic breccias form along secondary slip surfaces and between parallel fracture formations. e) Cataclasite and gouge formation on the peperite wall of the fault.

3.4.3.2. Talisker Bay Fault (TBF), Scotland

The TBF (Figure 3.19) has a cumulative displacement of ~28m, and displaces a series of lavas and intersedimentary units across a deformed zone at least 10m wide. The fault is exposed on a cliff ~75m in height, where the broad structure of the overall fault geometries and displacements can be seen. The broad structure of the TBF is shown in Figure 3.19a where, at the base of the cliff, the fault displaces an intersedimentary layer by 28m. As the displacement of the layers is followed upwards from this, the fault splits into two slip surfaces, where the leftmost one has a displacement of 18m, and the rightmost one a displacement of 10m (Figure 3.19b). Subsidiary slip surfaces connect the two faults in a riedel shear orientation, with small displacements along each. The PSS of the 18m displacement fault is not well exposed, and due to the vertical and exposed cliff face, a complete survey of the entire fault zone could not be carried out.

The deformation associated with the 18m displacement fault is well exposed at the top of the cliff (Figure 3.19c). The deformation zone is composed of a PSS, and three distinct zones of deformation surrounding that (Figure 3.20a), termed here: **Deformation zone 1 (DZ1)** in the footwall of the PSS; **Deformation zone 2 (DZ2)**, in the principal slip zone of the exposure; **Deformation zone 3 (DZ3)** in the hanging wall of the exposure.

In **DZ1** (footwall), the original morphology of the host basalt is retained. However, fault-related zeolite mineralised extensional/extensional-shear fractures cut the basalt, and increase in density with increasing proximity to the slip surface (Figure 3.20b). Mosaic breccias are also found adjacent to the slip surface (Figure 3.20c). The basalt is altered throughout the exposure, which is not found within the host rock. Alteration is particularly strong between mineralised fractures, and at the margins of zeolite veins and fractures (Figure 3.20b).

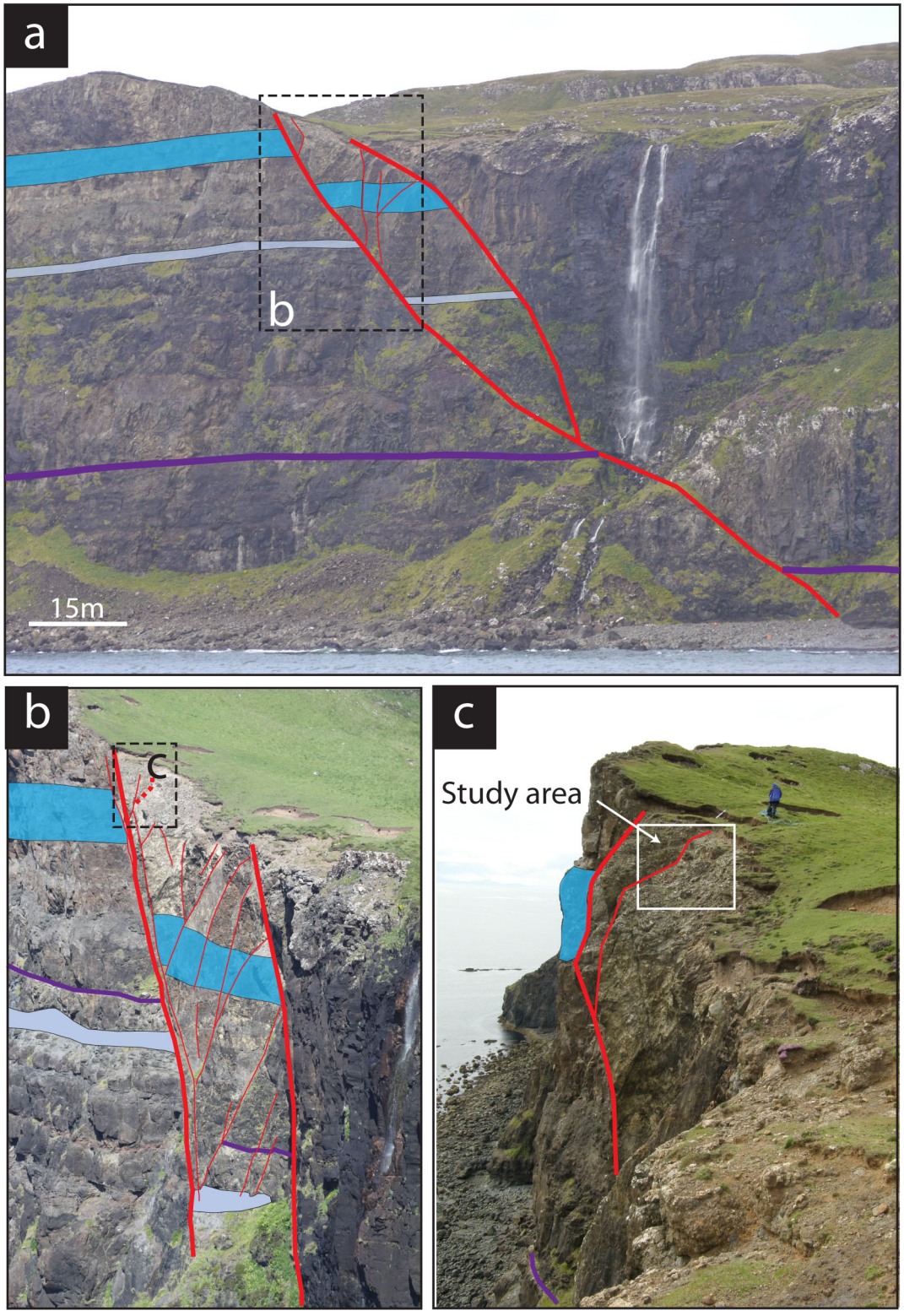

Figure 3.19: Overall structure of the TBF. a) Cliff exposure of TBF, with slip surfaces highlighted in red. Note splitting of fault into two. Marker horizons are blue: multilayered - lava flow; gray: laminated mudstone; purple: bole. Photo toward north. b) Detail of the upper part of the TBF, with slip surfaces outlined in red. The studied fault strand is highlighted as a dashed red line. Photo toward north. c) Study area of leftmost fault strand, Dad for scale. Photo toward west.

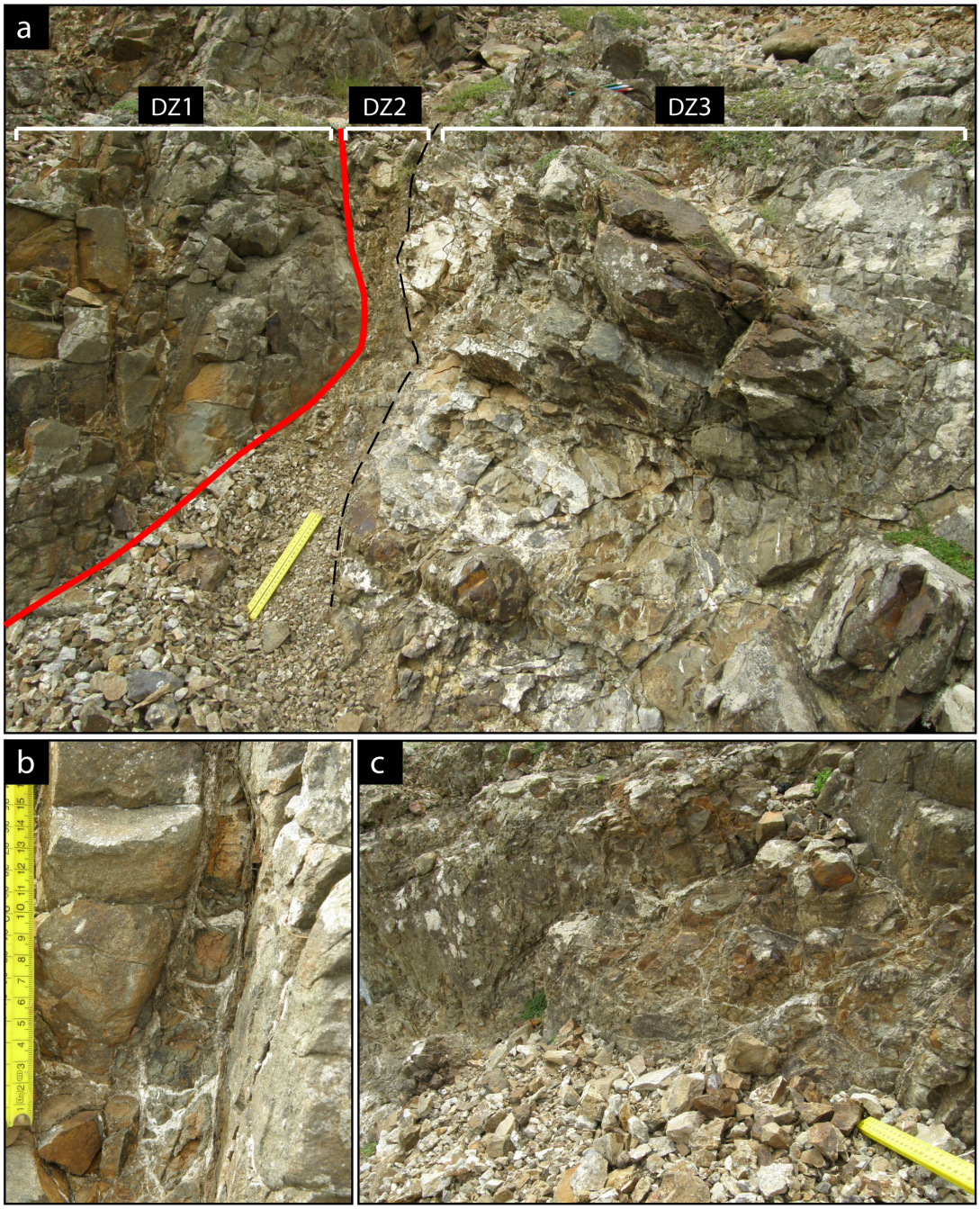

Figure 3.20: TBF deformation zones, and detail of DZ1. All photos viewed toward north. a) Photo overview of exposed fault in TBF, with deformation zones labelled. Red line marks principal slip surface of exposed fault strand, and black dashed line marks margin between DZ2 and DZ3. b) Mineralised fractures within the footwall basalt in DZ1. Note alteration increase between mineral veins and fractures. c) Increased fracture and mineralisation content approaching slip surface in DZ1 (under scree). Yellow ruler for scale (20cm long).

DZ2 contains the PSZ and the slip surface itself (a slip surface off the principal slip surface of the leftmost fault, Figure 3.19c). The zone is composed of a polished slip surface, foliated cataclasites, gouge, survivor clasts, chaotic breccias, and heavy alteration and mineralisation (Figure 3.21a).

The slip surface is mineralised with zeolite veins, and is continuous along the exposure. Secondary slip surfaces also cut across the PSZ, and control locations of survivor clasts and separate zones of cataclasites and gouge.

The PSZ varies along strike from 9cm to 20cm in thickness, with the thinner zones where gouges and foliated cataclasites are situated. Foliated cataclasites contain rounded basalt clasts (<5mm in size) in a matrix of crushed basalt, and are present in the fault zone as tabular zones (Figure 3.21b). Lenses of cataclasite are also found surrounded by gouge strands.

Gouges are very fine grained, and purply-gray in colour, forming anastomosing patterns throughout the PSZ (Figure 3.21c,d), surrounding cataclasite and survivor clasts. Gouge is always found along slip surfaces. Gouge is found both as incohesive (Figure 3.21c) and indurated (Figure 3.21d).

Survivor clasts in DZ2 are basalt (Figure 3.21c,e), and are rotated, heavily mineralised, fractured and altered, and are usually located between gouge strands. Chaotic breccias are formed adjacent to the cataclasites and gouges on the footwall side of the PSZ (Figure 3.21f), and are matrix supported (crushed, altered basalt) with rounded clasts of basalt. Chaotic breccias are also heavily mineralised.

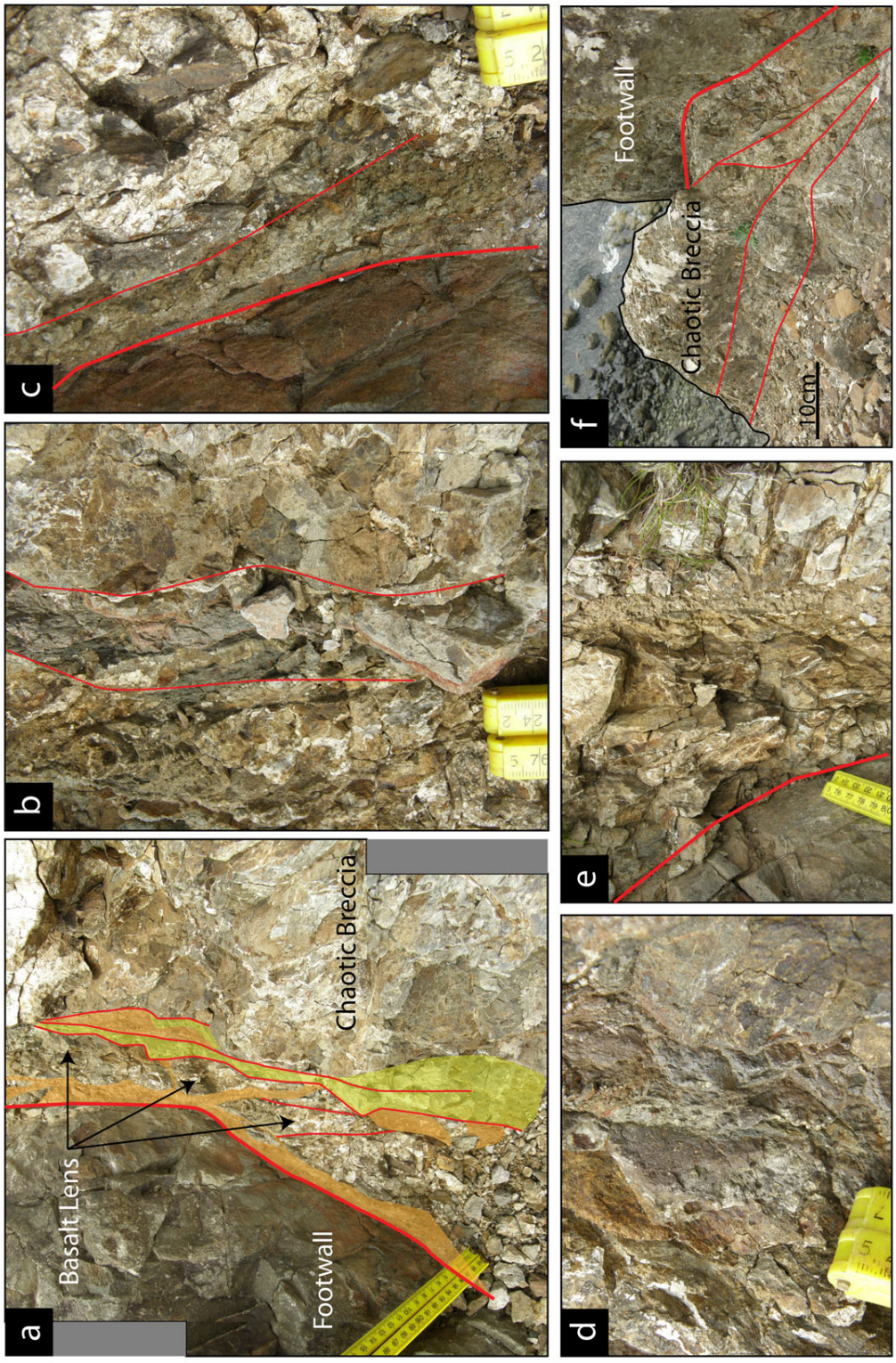

Figure 3.21: Detail of DZ2 in TBF. All photos viewed toward north. a) Overview of DZ2, with PSS marked by thick red line, secondary slip surfaces by thin red lines. Cataclasites marked in yellow, gouge in orange. b) Detail of cataclasite strands in PSZ. Ruler for scale (2cm). c) Detail of incohesive gouge adjacent to PSS. Basalt survivor clast to left of gouge. d) Example of indurated gouge (purply/gray), very fine grained. e) Example of heavily altered and mineralised basalt lens adjacent to PSS. f) Chaotic breccia lens adjacent to cataclasite and gouge bearing PSZ, heavily mineralised and fractured. Black line marks cliff edge.

DZ3 is in the hanging wall, to the right of the PSZ. This zone contains no gouge or cataclasite, but is dominated by mineralised and altered chaotic and mosaic breccias, and heavily fractured host rock. Adjacent to DZ2, the wall rocks are intensely fractured and mineralised with zeolite veins (Figure 3.22a). In addition to this, heavily altered and mineralised chaotic breccias have formed adjacent to the PSZ, and contain sub-rounded basalt clasts in an altered matrix (Figure 3.22b). With increasing distance from DZ2, chaotic breccias fade out into mosaic breccias, which also contain sub-rounded clasts in an altered matrix (Figure 3.22c). 2.2m away from DZ2, breccias are no longer found, and the original morphology of the host rock can be determined. However, the host rock does have an increased level of fracturing, mineralisation and alteration with respect to background levels (Figure 3.22d), e.g. host rock is gray and cohesive, whereas altered basalt within the fault zone is brown and friable.

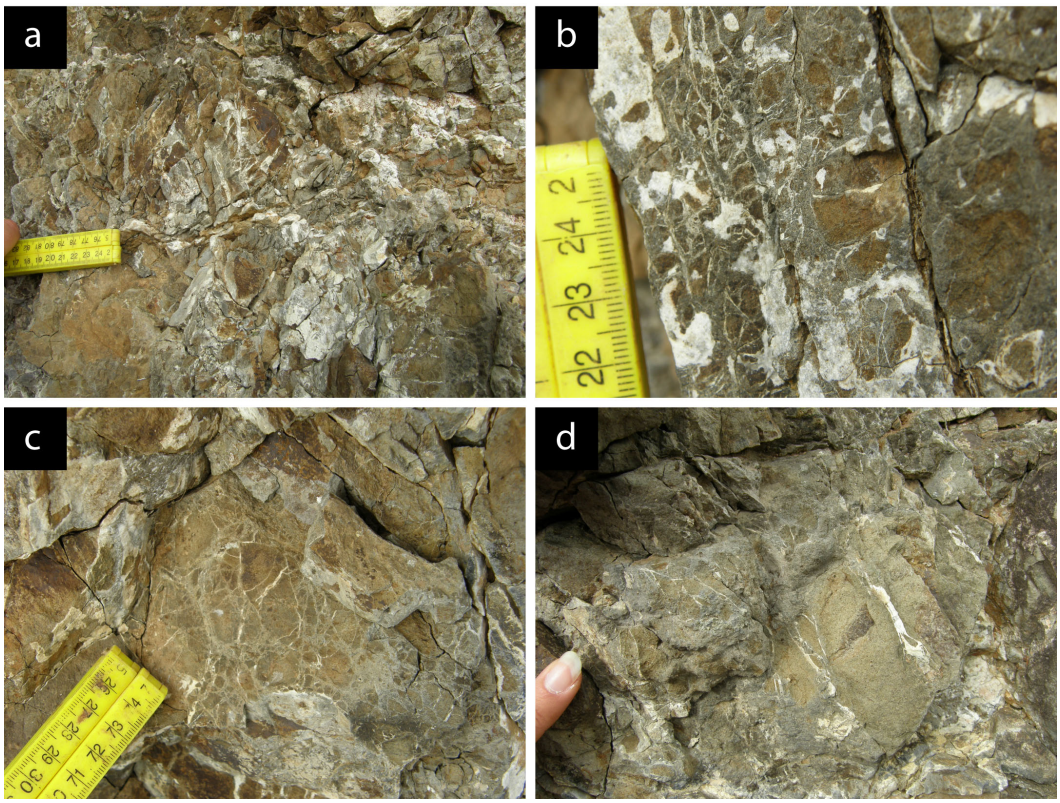

Figure 3.22: Detail of DZ3 in TBF. All photos viewed toward north. a) Intensely fractured, altered and mineralised basalt wall rock adjacent to DZ2. b) Chaotic breccia zone adjacent to PSZ. c) Mosaic breccia zone 1m away from PSZ. d) 2.2m from DZ2, host rock is discernible though still altered with zeolite veins.

Considering the TBF as a whole (taking into account both the 18m displacement fault, 10m displacement fault, and 28m displacement fault where the two faults join at the base of the cliff), it is likely that the dominant, principal faults will have similar fault deformation properties as described above. However, smaller displacement strands (i.e. strands connecting the two split faults) would likely be similar to those of medium displacement non self-juxtaposed faults, or if the faults are self-juxtaposed, similar to medium displacement self-juxtaposed faults. Overall, the principal faults will be clay gouge rich, with clay entrained from inter-lava clay-rich units. Areas between the principal faults will be heavily altered, fractured, brecciated and mineralised, with smaller displacement faults dominated by either gouge/cataclasite mix, or cataclasite and breccia, depending on juxtaposition.

3.4.4. Non self-juxtaposed fault summary from this study

Medium displacement faults (≥1m -10m) in non self-juxtaposed basalt sequences are characterised by mature PSS, where clay-rich gouge (from inter-lava clay-rich units within the basalt sequence) is entrained along the slip surface. The smearing of the gouge results in a narrow zone of localised deformation, developed either on the clay-rich unit side of the fault, or as a clay smear between two basalt lava flows. With increasing displacement, deformation of the basalt wall rocks is dominated by fracturing, alteration, mineralisation and brecciation.

High displacement faults (>10m) have at least one PSS, which may deviate along strike and split into two or more slip surfaces. Subsidiary slip surfaces are common, and form at Y shear and riedel shear orientations to the PSS. Gouge formation (derived from inter-lava clay-rich units) is common along slip surfaces, and forms anastomosing strands surrounding altered survivor clasts. With high displacements, it is more likely multiple clay-rich units will be displaced across a fault, resulting in a complicated fault zone. In this case, incohesive and indurated gouges of differing origins are found within the PSZ. Foliated cataclasites are also found, along with chaotic and mosaic breccias away from the PSS. Heavy fracturing of the fault walls is observed, decreasing in frequency with increasing distance from the fault. These deformation elements present in the above displacement values are summarised in Table 3.2.

Table 3.2: Summary table of deformation elements in non self-juxtaposed faults. (MDF=medium displacement fault, HDF=high displacement fault, MSS=mature slip surface, F=fractures, MB=mosaic breccia, ChB=chaotic breccia, PC=protocataclasites, C=cataclasite, FC=foliated cataclasite, G=gouge, BFS=brittle fault structures, SF=subsidiary faults, Z=zeolite, A=alteration.)

	MSS	F	MB	ChB	PC	C	FC	G	BFS	SF	Z	A
MDF	X	X	X	X	X	X		X	X		X	X
HDF	X	X	X	X		X	X	X	X	X	X	X

Thickness/displacement plots of all non self-juxtaposed faults in this study were generated, to determine if there is a relationship between fault displacement and PSZ thickness. Due to the TBF having multiple slip zones, the total thickness of the deformation zone associated with it was plotted, whereas for the rest of the faults the PSZ variations in thickness were directly measurable, and only contained one PSZ. The results are presented in Figure 3.23. The results do not show an obvious relationship between displacement and thickness, although the maximum thickness in each does increase slightly with increased displacement. Each fault has a large variety of thicknesses within its PSZ, which vary by one order of magnitude.

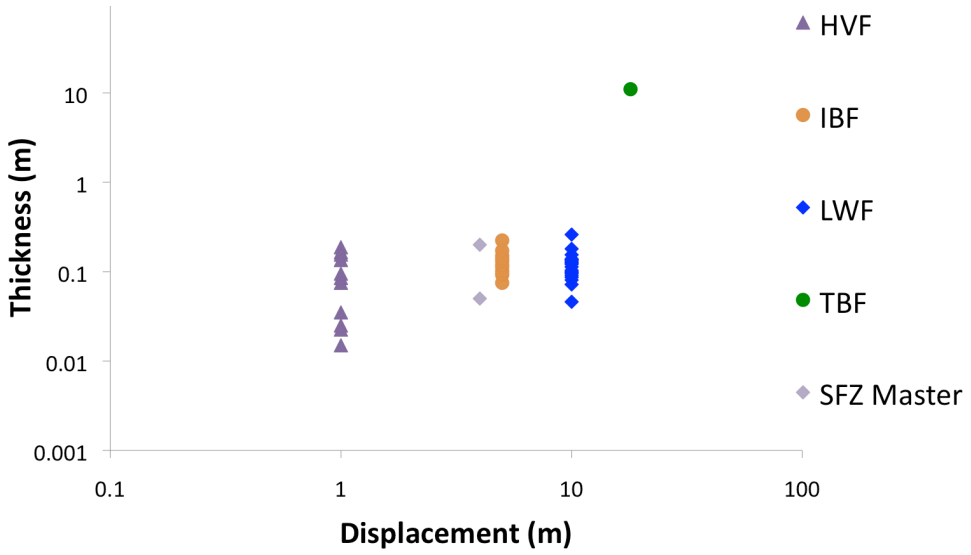

Figure 3.23: Thickness/displacement plot for all non self-juxtaposed faults in this study. Displacements are well constrained within field sites, although the LWF data range could extend to a higher order of magnitude (i.e. 100m) due to uncertainty in its displacement.

3.5. Conceptual model – fault growth and evolution in basalt sequences

By taking into consideration the observations and data from this study, conceptual models of the evolution of the internal structure of faults expected within self- and non self-juxtaposed faults are presented in this section. Before presenting the conceptual models, limitations of the models are as follows:

- No more than two faults were found for each of the displacement types (low-high displacements), and whilst multiple examples of self-juxtaposed and non self-juxtaposed faults were found, only one example of each unique type of juxtaposition (e.g. basalt/peperite, basalt/volcanic conglomerate, basalt/tuff etc) was found. Thus, other fault structures may be possible at the same displacement, and broad juxtaposition type.
- The faults studied are all from slightly different tectonic regimes. Though they are all related to the opening of the North Atlantic in the Palaeogene, local perturbations in the stress field are to be expected. The faults may have undergone slightly different stress histories, though the effect of this should be minimal.
- The faults studied are in basalt sequences of different ages. Background levels of basalt alteration are higher in the BIPIP and FIBG than in the east Iceland basalts, and thus may affect the deformation process.

This model has been modified and tested throughout this study, and the field data gathered supports the proposed fault growth and evolution model presented below. The limitations could be reduced by further field work in faults of similar displacements and juxtapositions in basalt sequences. In the following sections, conceptual models for fault growth and evolution in self- and non self-juxtaposed faults are presented, based on data from this study.

3.5.1. Self-juxtaposed fault growth and evolution model

Fault initiation in self-juxtaposed faults occurs along pre-existing structures in the basalt, or by pre-cursory structure linkage. Figure 3.24 shows the development of a fault in basalt with pre-existing vertical cooling joints. In this scenario, pre-existing structures (such as cooling joints or fractures) are reactivated as shear fractures if optimally orientated (Figure 3.24a). With increased stress, a shear fracture accommodates displacement as an incipient principal slip surface and parallel fractures form surrounding the slip surface (Figure 3.24b). With increasing slip, displacement at low levels is achieved and the slip surface develops into an immature principal slip surface. The increased strain along the slip surface further deforms the surrounding parallel fractures at the margins of the fault into narrow blocks of wall rock (Figure 3.24c). Increasing displacement leads to the development of a mature principal slip surface, and parallel fracture zones are incorporated into the developing principal slip zone as wall rock slabs.

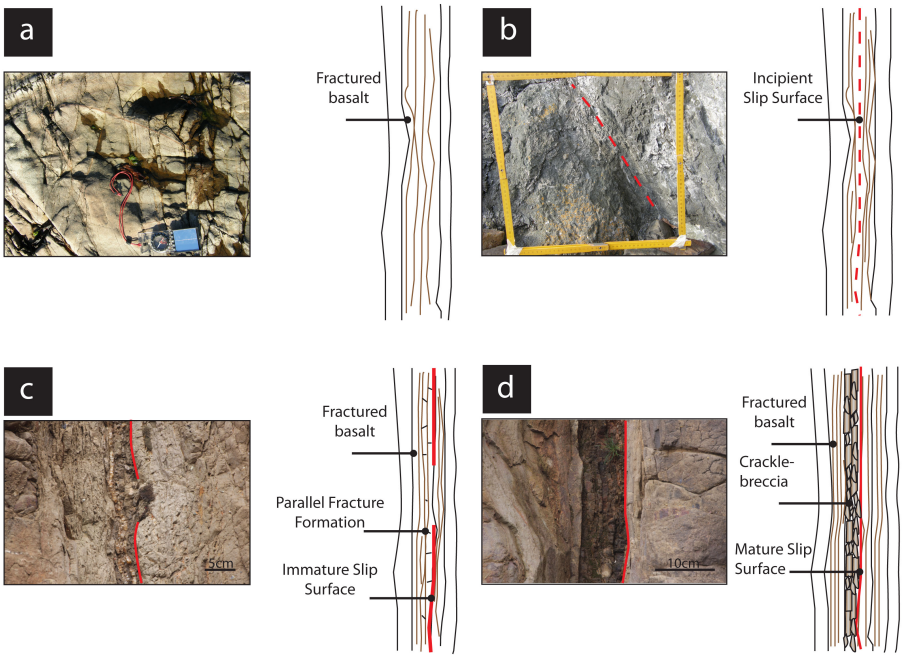

Figure 3.24: Fault evolution conceptual model for low displacement, self-juxtaposed faults forming from pre-existing vertical joints. a) Fault initiation and growth along pre-existing fractures (e.g. Kerrera). b) Development of slip surface along pre-existing structure (e.g. Mull). c) Formation of fault-related fractures surrounding developing slip surface (e.g. VJF). d) Crackle breccia formation within PSZ with increasing displacement (e.g. VPF).

The incorporated parallel fracture zones are deformed into crackle breccias, and rotated and altered within the PSZ (Figure 3.24d). The fault continues to grow in width by this process with increasing displacement, until the PSZ is suitably weak enough that displacement will concentrate along it, and deformation outside the PSZ will not be required. This could be achieved by further brecciation of the crackle breccias into more evolved breccias or cataclasites.

In basalt lavas where pre-existing fractures are absent, a different evolution of faults was found at low displacements. The evolution for this scenario is depicted in Figure 3.25 where, with increasing displacement, pre-cursory fault segments link to form a through-going fault, with fault-bound basalt lenses (Figure 3.25a). The basalt lenses are subject to increased fluid flow and alteration, due to the lenses being internally deformed by fracturing (Figure 3.25a). The fault zone grows by fracturing and brecciation of the basalt lenses (Figure 3.25a), and continued propagation of the slip surface.

With increasing displacement, the fault zone will continue to grow by slip surface propagation and basalt lens incorporation into the PSZ. Continuous incorporation of basalt lenses into the fault zone by asperity removal (with increasing displacement), and by deviation of slip surfaces (along pre-existing structures in basalt, such as cooling joints) results in a relatively wide and distributed zone of brittle deformation. Deformation of the PSZ (particularly slip-surface bound basalt lenses) will continue by further fracturing and increasingly complex brecciation, from mosaic breccias to chaotic breccias due to wear and abrasion (Figure 3.25b).

At high displacements, cataclasites and complex breccias develop along the PSZ, with fault-related fracturing surrounding the breccia and cataclasites zones (Figure 3.25c). Further displacement along newly developed slip surfaces in the fault walls will form multiple cataclasite/breccia zones throughout the fault zone, separated by zones of fracturing.

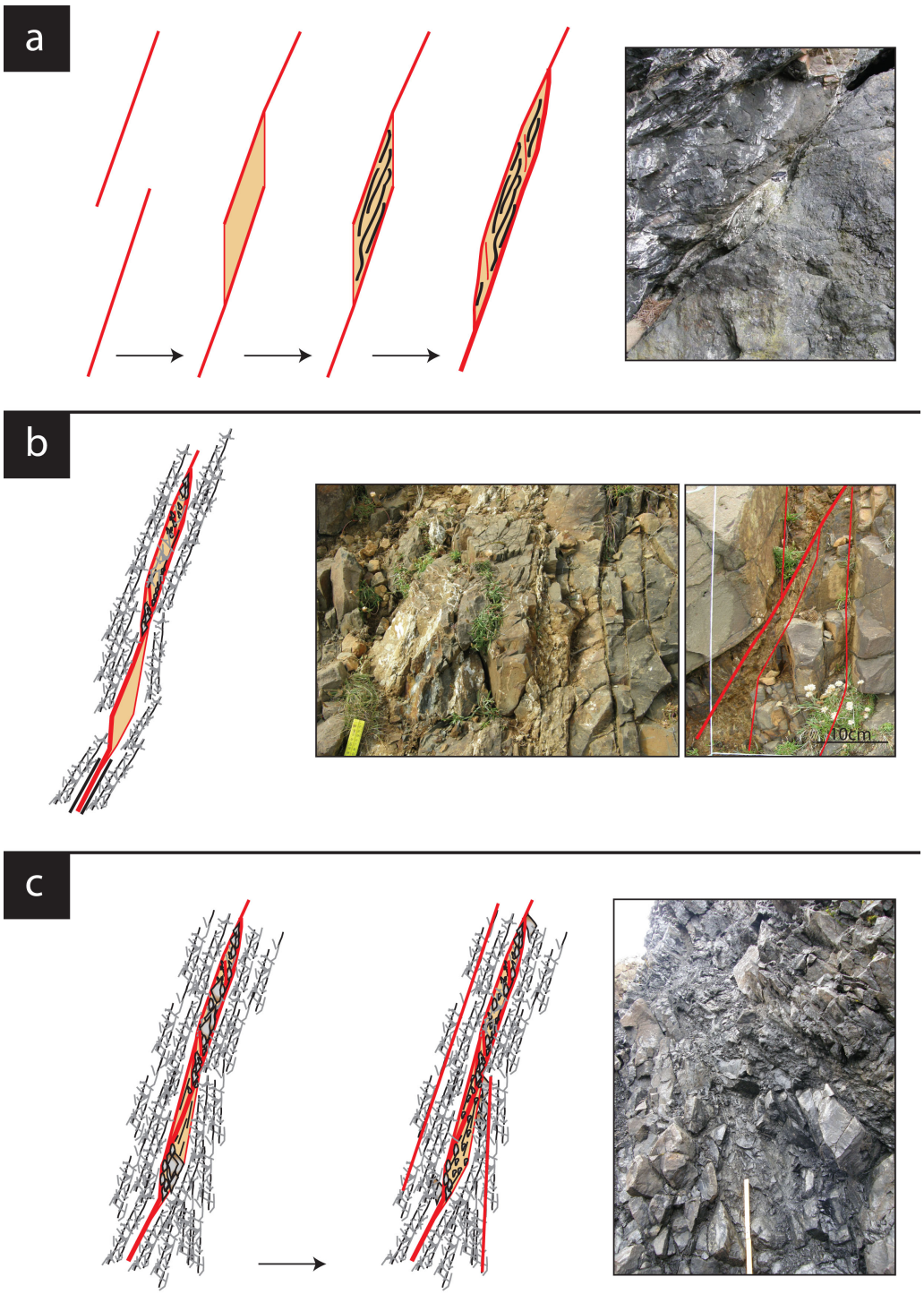

Figure 3.25: Fault zone evolution in lavas without through-going vertical fractures, in self-juxtaposed faults. a) Low displacement evolution (e.g. BNF). b) Medium displacement evolution (e.g. SFZ). c) High displacement evolution (e.g. HBF).

3.5.2. Non self-juxtaposed fault growth and evolution model

In Figure 3.26, the process of non self-juxtaposed fault evolution is shown. With medium and high displacements, the likelihood of faulting a basalt unit against another lithology, such as a clay-rich inter-lava unit, within the basalt sequence is increased. If the fault does cut a clay-rich inter-lava unit, entrainment of clay-rich beds into the fault zone is therefore likely (as has been observed in this study).

At medium displacements, in juxtapositions with clastic clay-rich beds (Figure 3.26a), clay gouge forms at the sediment/fault interface. The matrix of the volcaniclastic bed is entrained into the fault zone preferentially, with clasts within the volcaniclastic bed also being entrained into the zone, and becoming fractured with increasing proximity to the PSS. The fine-grained clay-rich matrix is more easily deformed and smeared, and becomes very fine-grained and comminuted against the PSS. The gouge can be variable in thickness along the zone. Clay-rich units such as tuff may be smeared along the fault (Figure 3.26b). Damage on the basalt side is constrained to a slip surface and some off-fault fracturing. Asperity removal from the basalt wall may incorporate basalt clasts into the smear.

At high displacements (Figure 3.26c), more clay-rich beds are faulted, and the fault evolves to produce multiple gouge strands within the fault zone, derived from smearing of multiple clay-rich beds. Complex fault rocks develop, such as foliated cataclasite and chaotic breccias, which are derived from basalt flows that the fault has moved past. A series of chaotic breccia through to mosaic breccia into fractured zones is seen within the walls of the fault adjacent to the PSZ, a consequence of deformation of the fault walls.

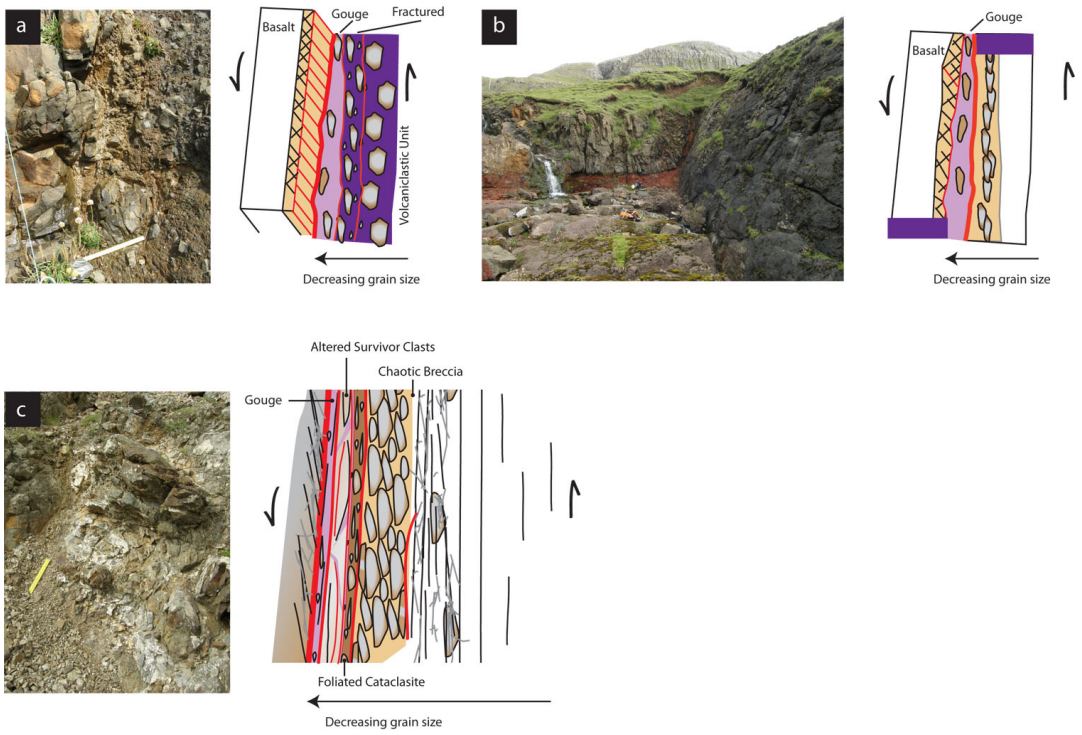

Figure 3.26: Fault evolution model for non self-juxtaposed faults. a) Medium displacement fault with volcaniclastic juxtaposition (e.g. SFZ). b) Medium displacement with clay bed smear (e.g. IBF). c) High displacement fault (e.g. TBF).

3.6. Summary

The data presented in this chapter show that juxtaposition and displacement are primary controlling factors on fault structure and content. Faults initiate in basalt from pre-existing structures (such as cooling joints) or pre-cursory structures, and form fracture meshes. Immature principal slip surfaces develop from these fractures, and develop into through-going slip surfaces. In self-juxtaposed faults, with increasing displacement the content and complexity of fractures, breccias and fault-related deformation increases, with the higher displacement faults containing evolved fault rocks, such as cataclasites and chaotic breccias. However, in pure self-juxtaposition at any displacement (up to 25m in this study), clay gouge is not found. In non self-juxtaposed faults (medium to high displacements), gouge is found entrained along the slip surface, and has a relatively narrow PSZ relative to fault displacement. Gouge is derived from the clay-bearing bed that the fault juxtaposes. With increasing

displacement, gouge strands multiply and anastomose with foliated cataclasites (at high displacements only). In both juxtaposition types, but particularly self-juxtaposed faults, alteration and mineralisation of basalt is distributed throughout the fault zone, particularly at the edges of fractures in low displacements, and throughout the whole fault zone in high displacements.

Fault zone thickness does not necessarily vary with displacement. Self-juxtaposed faults show a weak trend of increasing thickness with increasing displacement, whereas non self-juxtaposed faults do not. A comparison of the thickness/displacement relationship of both self-juxtaposed and non self-juxtaposed faults in this study is presented in Figure 3.27. The results show that non self-juxtaposed faults have relatively low displacement to thickness ratios when compared with self-juxtaposed faults. For example, the 1m displacement non self-juxtaposed fault (HVF) has the same range of thickness values as the VJF self-juxtaposed fault, which only has a displacement of 18cm. Similarly, the ~10m displacement non self-juxtaposed LWF fault has the same thickness variations as the VPF, a 28cm self-juxtaposed fault.

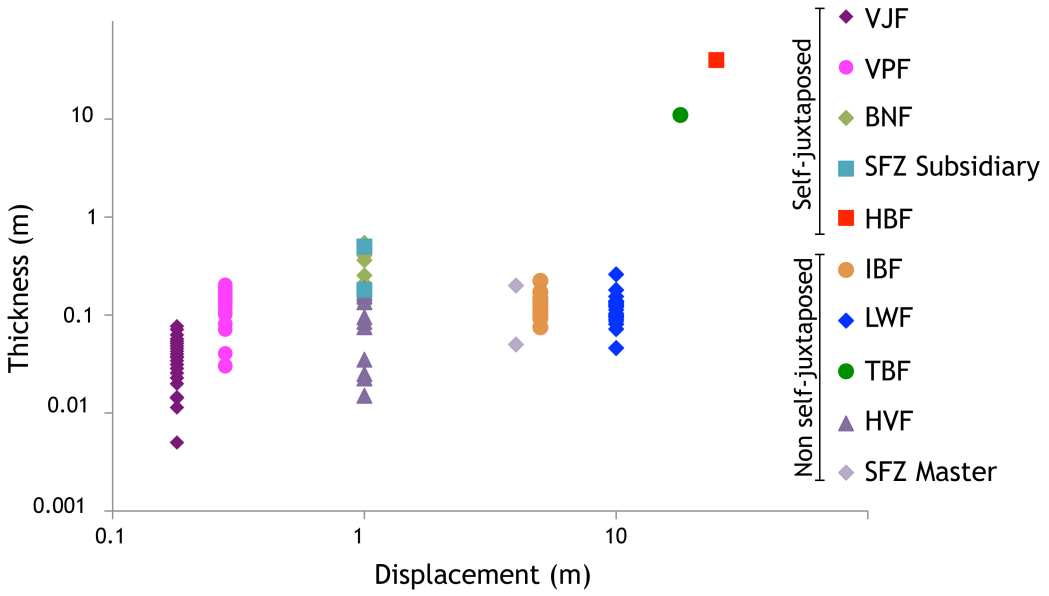

Figure 3.27: Thickness/displacement plot for all faults in this study.

These results suggest non self-juxtaposed faults could have a thinner PSZ relative to self-juxtaposed faults, when basalt is juxtaposed against a clay-bearing unit. As clay gouge is weaker than basalt, it will deform in a ductile fashion, and accommodate displacement more efficiently than a fracture-dominated self-juxtaposed fault. Therefore, clay-bearing rocks juxtaposed against basalt are likely to result in thinner PSZ than self-juxtaposed faults, which will have wider PSZ due to the intense fracturing which must occur in these mechanically strong rocks in order to accommodate deformation.

The orientations of the studied faults vary from vertical to 70º. Vertical faults are encountered in self-juxtaposed faults (e.g. VJF, VPF), where the lava flow they intersect contains vertical, pre-existing through-going cooling joints/fractures. In lava flows where there is a lack of vertical, through-going cooling joints/fractures (e.g. BNF), fault dip is more consistent with the average dip value associated with fault development related to normal principal stresses (i.e. 60-70º). This suggests that in self-juxtaposed faults cutting basalts with no through-going pre-existing structures (such as columnar joints), typical normal fault orientations will be found. In non self-juxtaposed faults, fault orientations vary from 70º to 90º, depending on the mechanical strength of the stratigraphy the fault is cutting (i.e. shallower dips for tuffs and steeper dips for basalt) . Where vertically columnar jointed basalt is juxtaposed against another unit, the fault orientation is sub-vertical (e.g. HVF) suggesting through-going pre-existing structures in basalts exert a strong control upon fault orientation in basalt sequences.

4. Microstructural Analysis of Faulted Basalt

4.1. Introduction

In this chapter, the deformation and alteration of faulted basalt is studied in detail. Prior to this study, alteration of sub-aerially erupted basalts as a result of regional low-grade zeolite metamorphism (e.g. Neuhoff et al., 2006), and alteration related to faults within sub-oceanic erupted basalts at mid-ocean ridge settings (e.g. black smokers; volcanogenic massive sulphide deposits; Hayman and Karson, 2007; Jowitt et al., 2007) have been studied. However, alteration and deformation of sub-aerially erupted basalt as a result of faulting have only briefly been commented on (e.g. Walker et al., 2012a), and therefore the results presented in this chapter are one of the first for faults cutting sub-aerially erupted basalts. Alteration is particularly important, as it changes the strength, permeability and bulk chemistry of the rock it is faulting, and so must be considered when predicting fault behaviour at depth. The results of this will aid in the understanding of the microscopic controls in faults in basalt, and ultimately, overall fault behaviour.

To provide a detailed account of structural and mineralogical changes across each fault zone included in this study, representative orientated samples of the host rock, and of each deformation element within each fault were collected. These deformation elements were defined at the macro-scale in Chapter 3, and include breccias, cataclasites and fault gouge. Other fault-related elements include alteration zones and mineralisation sites. This chapter follows the same format as Chapter 3, where faults are described in order of displacement in two categories: self-juxtaposed and non self-juxtaposed.

The primary aim of studying these samples is to quantify mineralogical, mechanical, geochemical and structural changes within basalt as it is faulted. The observations gathered from this study have allowed the development of a conceptual evolution model for how basalt deforms at micro-scales. A secondary aim of this study is to evaluate porosity and permeability characteristics of fault rocks from basalt sequences, by analysing factors such as clay content and pore space (results of which are applied in Chapter 6 for bulk permeability models). An additional aim is to constrain the maximum temperatures to which the host rocks have been heated. This will allow comparison of temperatures reached in the host rock to those of the fault rock. The temperature data will help constrain burial depth, and therefore possible stress conditions that the faults have experienced.

4.1.1. Primary mineralogy of basalts

It is important to review the original mineralogical and geochemical composition of basalt, in order to facilitate understanding of the composition and chemistry of faulted basalt, particularly when investigating geochemical reactions within the rock and the distribution of elements.

The primary minerals of basalt are plagioclase feldspar, pyroxene, and olivine. **Feldspars** are the most abundant of the primary minerals, forming both groundmass crystals and as phenocrysts. Part of the framework silicates family, the feldspar group form the ternary system: $NaAlSi_3O_8$ (albite)- $KAlSi_3O_8$ (K-feldspar) and $CaAl_2Si_2O_8$ (anorthite) (Deer et al., 1992). **Pyroxenes** belong to the chain silicate family, and are composed of two main series: orthopyroxenes (e.g. enstatite), which have a simple chemistry in the form of $(Mg,Fe)SiO_3$, and clinopyroxenes (e.g. augite), which have a wide range of chemistries from $CaMgSi_2O_6$ to $CaFeSi_2O_6$ to $Mg_2Si_2O_6$ to $Fe_2Si_2O_6$ (Deer et al., 1992). **Olivines** (belonging to the ortho-

silicate family) form a complete solid solution between Mg_2SiO_4 (forsterite) and Fe_2SiO_4 (fayalite).

Accessory minerals commonly found within basalts include Fe-Ti oxides (Fe-Ti spinels and ilmenite), and apatite. Oxides in basalt are typically dominated by ilmenite (Fe_2TiO_3) and the oxide minerals from the spinel group, such as titanomagnetite (Fe_2TiO_4), ulvospinel ($TiFe^{2+}{}_2O_4$) and magnetite (Fe_3O_4) (Haggerty, 1976a).

4.1.2. Secondary mineralogy in basalts

Secondary minerals in basalt most commonly include clay minerals, zeolites, amorphous silica, quartz and calcite.

Clay minerals are sheet silicates. The most common clay groups found in basalts are smectites and chlorites, which are products of hydrothermal alteration and weathering of ferromagnesian minerals (e.g. Dekayir et al., 2005). The smectite group are hydrous aluminosilicates, and have the general formula of $(0.5Ca,Na)_{0.7}(Al,Mg,Fe)_4[(Si,Al)_8O_{20}](OH)_4.nH_20$). The smectite structure allows layers to be composed of other layered silicates (such as chlorite or illite), or water which can be lost from the clays at temperatures as low as 100ºC (Deer et al., 1992).

The chlorite minerals also have a layered structure, with a chemical formula of $(Mg,Fe^{2+},Fe^{3}+,Mn,Al)_{12}[(Si,Al)_8O_{20}](OH)_{16}$. Clays are known to replace minerals within basalt such as olivine, orthopyroxene and plagioclase, as well as filling fractures and lining vesicles (e.g. Kristmannsdottir, 1978; Alt et al., 1998; Neuhoff et al., 2006). Typical ranges of the crystallization temperatures of smectite and chlorite (clay types identified in this study) are provided in Figure 4.1.

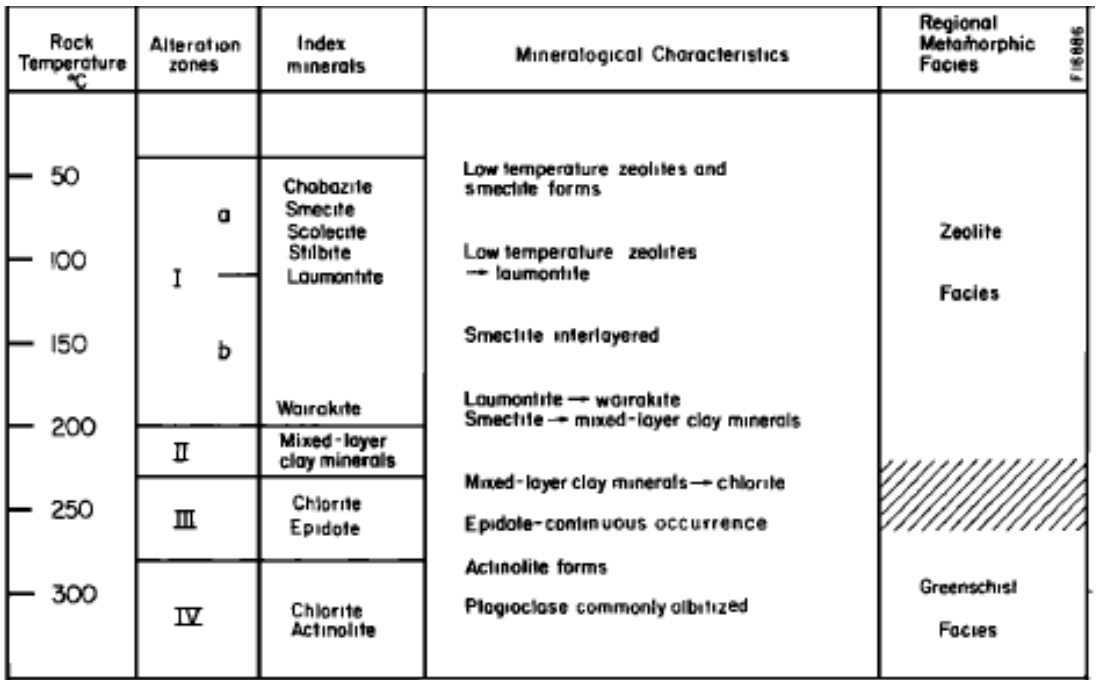

Figure 4.1: Clay minerals and associated temperatures in tholeiitic basalts from Iceland, from Kristmannsdottir (1982).

Zeolites are hydrous aluminosilicates belonging to the framework silicate family, and have the general formula $(Na_2,K_2,Ca,Ba)[(Al,Si)O_2]_n.H_20$. As the zeolite framework is more open and contains larger cavities and channels than in feldspars, zeolites have a greater capacity for ion exchange and molecular absorption, and contain water molecules within structural channels (Deer et al., 1992). As much as 20% of the zeolite structure can be composed of loosely bound water (Mumpton, 1977).

Zeolites are divided into a number of sub groups based on their crystal structures (Deer et al., 1992), including the **natrolite group** (natrolite, mesolite, scolecite, thomsonite), **harmotome group** (phillipsite, gismondine), **chabazite group** (chabazite, erionite), **mordenite group** (mordenite, ferrierite) and **heulandite group** (stilbite and heulandite).

Zeolites are typically found filling vesicles and fractures. They can form as: alteration products of volcanic glass, clays and feldspars (Keith and Staples, 1985; Iijima, 1980); hydrothermal alteration of volcanics (Kristmannsdottir, 1978); diagenetic deposits in sedimentary rocks (Hay and Sheppard, 2001); minerals precipitating from alkaline groundwater in basalts (Walker, 1960);

and as a result of very low temperature regional metamorphism, forming the lower zeolite-facies mineral assemblages (Neuhoff et al., 2006).

Zeolites can be used to assess palaeo-burial depths of lavas, because groundwater alteration leads to zones of zeolite minerals with increasing depth (Jørgensen, 2006; Neuhoff et al., 2000; Walker, 1960). They can form from 50ºC (including chabazite and thomsonite) to >300ºC (including mordenite, laumontite, stilbite). A summary table showing the temperature ranges of zeolites is shown in Figure 4.2.

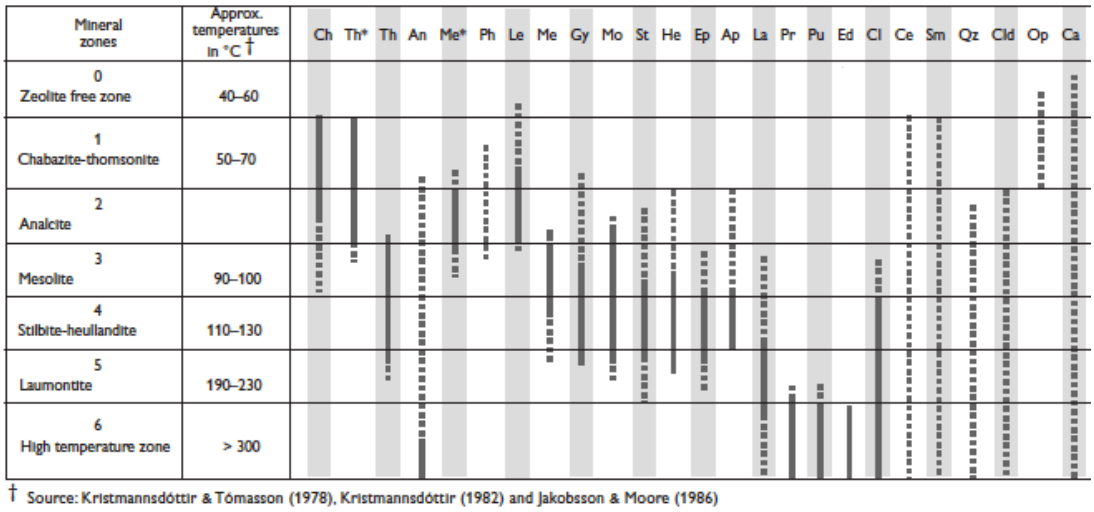

Figure 4.2: Temperature ranges for zeolites and related minerals from Jørgensen (2006). Zeolites and related minerals in this study: Ch - chabazite, Th - thomsonite, He- heulandite, Cl - chlorite, Sm - smectite, Cld - chalcedony, Ca - calcite.

4.1.3. Alteration of basalts unrelated to faulting

Hydrothermal alteration and precipitation of secondary minerals (particularly clays and zeolites) can occur throughout basalt lava piles, as a result of burial and/or metamorphism. Low-grade regional zeolite metamorphism of basalt occurs as basalts are buried and react with groundwater. The deeper the basalts are buried, the hotter the regionally circulating groundwater the basalt encounters. The hotter the groundwater, the higher temperature the precipitating zeolites will be (i.e. laumontite). The same is true for clay minerals, though there are not as many clay as zeolite assemblages. Local hydrothermal systems can also

raise the temperature of circulating groundwater, although effects of this would be seen locally and not regionally. The degree of alteration depends on the groundwater temperature, as well as the original permeability of the basalt - i.e. a permeable basalt will be more prone to alteration to clays and zeolites than a less permeable one. This burial-related alteration can be intensified during faulting, due to the increased permeability of faults channelling flow along them.

Throughout this chapter, burial-related alteration is described as 'background alteration', i.e. alteration of the basalt pile relating to burial and widespread groundwater circulation prior to faulting. As zeolite and clay alteration are commonly found localised and often intensified in and along fault-related rocks, fault-related alteration is simply referred to as 'alteration' throughout the text, i.e. altered host rock refers to the host rock altered by fault processes, and background alteration refers to the host rock altered by burial-related alteration.

4.2. Methodology

The host rock of each fault zone studied was sampled for comparison with its faulted equivalent. Deformation elements from each fault zone were also sampled (i.e. from a breccia zone, altered/mineralised zone etc). Each sample was made into a polished thin section for petrographic and scanning electron microscope (SEM) characterisation, carried out in the Imaging Spectroscopy and Analysis Centre (ISAAC) within the University of Glasgow's School of Geographical and Earth Sciences.

Thin sections were studied initially using a Zeiss Axioplan petrographic microscope, with images captured using a Nikon DS-Fi1 5 Megapixel digital camera. Imaging was carried out using plane polarisers (PPL) and crossed polarisers (XP). A Quanta 200F field-emission environmental SEM (FE-SEM) was used for backscatter electron (BSE) and panchromatic cathodoluminescence (CL) imaging. In BSE images minerals with a lighter greyscale (e.g. Fe-Ti oxides) have a higher mean atomic number than

darker minerals (e.g. Na-zeolites). Qualitative and quantitative chemical compositions were obtained by energy-dispersive X-ray (EDX) analysis using an EDAX Genesis system on the Quanta SEM. Point counting was carried out on all samples to quantify mineralogical content using the FE-SEM, counting 220 points within each sample. This was carried out at 500µm magnification, across an area of 10mm^2, with a space of 500µm between each point counted. The mineral that each point landed on was then counted, and the results are presented in section 4.7.

Quantitative chemical analyses and element maps were acquired using the Zeiss Sigma field-emission analytical SEM (ZS-SEM). The ZS-SEM is equipped with an Oxford Instruments X-Max 80 mm^2 silicon-drift energy-dispersive X-ray (EDX) detector. Spectra were acquired at 15 kV/~2 nA with the electron beam rastered over an area of ~ 5 μm^2 and the counting time was 60 seconds. Spectra were quantified with an Oxford Instruments INCA microanalysis system. Element maps were obtained at resolutions of 1024-800 and 512-400 pixels, at 100,000 counts per second.

Images were analysed using Image J and XT Doc software available on the FE-SEM.

4.2.1. EDX X-ray spectra of mineral phases

Minerals that were not identifiable by their optical characteristics (i.e. via petrographic microscope methods) were identified using their X-ray spectra. X-ray spectra of the dominant minerals found within both the host rock and fault rock were obtained, in particular allowing identification of individual zeolite and clay phases, as well as relative changes in element quantities between reaction phases (i.e. zeolite replacing feldspar). Minerals referred to throughout this chapter have spectra as shown in Figure 4.3, and the reader is referred back to here for spectra of minerals discussed in the text.

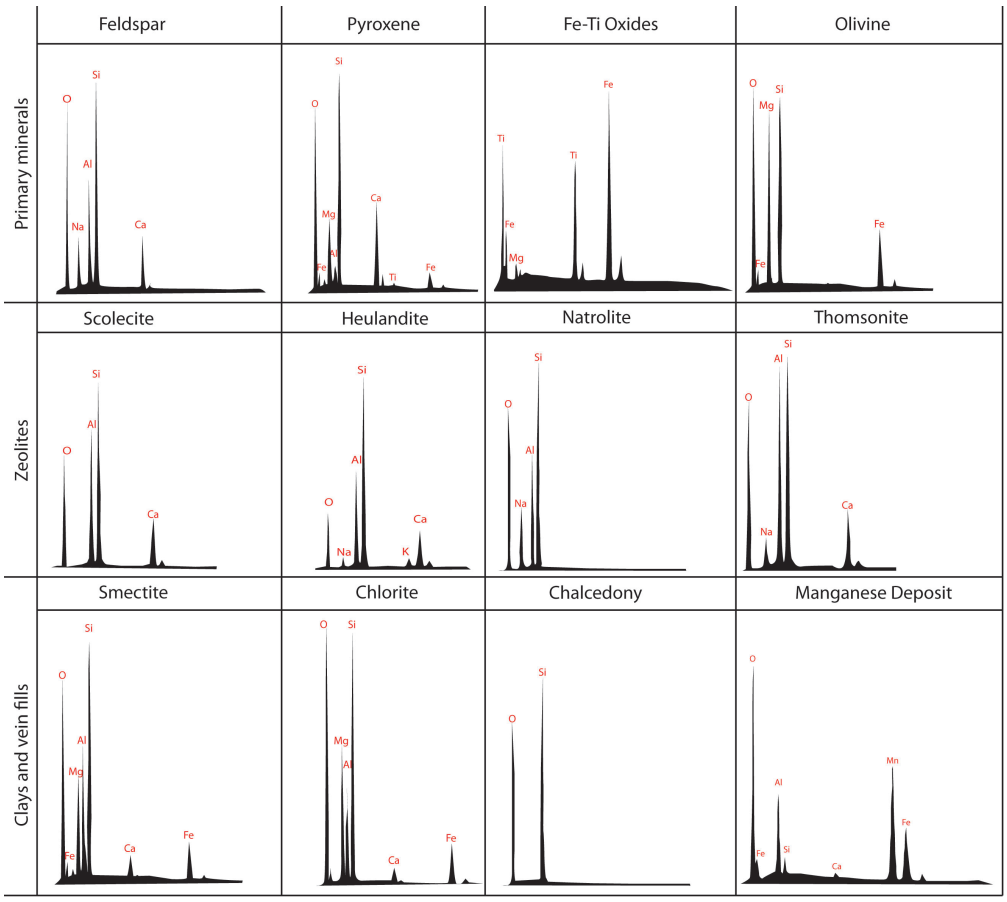

Figure 4.3: Spectra acquired for the major mineral types encountered throughout this study.

4.3. Geochemical and deformation processes

This section provides examples of the geochemical and deformation processes identified from this study. Geochemical processes are found both as background alteration in host rocks and fault alteration in faulted basalt rocks. Deformation processes are only found within fault rocks.

4.3.1. Geochemical processes

Zeolitisation of feldspars: where feldspar minerals retain their original external shape but have been replaced by zeolite minerals, i.e. pseudomorphs. Under the petrographic microscope, this reaction is recognised by a change in birefringence (from low order, uniform interference colours to low order interference colours, with a patchy appearance) and a loss of twinning. Clusters of feldspar minerals that originally had varied optic orientations will often have the same optical orientation when zeolitised i.e. go into extinction at the same point during rotation of the microscope stage (Figure 4.5a). In the SEM, zeolitisation is identified by a change in chemical composition (i.e. from the original feldspar to that of zeolite minerals that are found running as veins throughout the sample). In BSE images the original feldspar had a higher atomic number than the replacive zeolite (Figure 4.5b). In 100% replacement of the feldspar by zeolite (i.e. zeolite pseudomorph after feldspar), dehydration structures (due to heating of the sample during thin section preparation) can be found (Figure 4.5c). Zeolitisation in this study was observed via CL to initiate along fractures or cleavages within the feldspar (Figure 4.4a). As zeolites do not luminesce well, their distribution within luminescent feldspars could be well quantified. Zeolitisation has also been observed to preferentially nucleate in Ca-rich zones before spreading throughout the rest of feldspar (Figure 4.4b).

Clay replacement of primary minerals: where primary minerals (particularly feldspar) are partially replaced by clay, particularly along

cleavages or fractures (Figure 4.5d). Clays replacing primary minerals are greenish/brown under the petrographic microscope in PPL.

Dissolution of minerals: where the original crystal shape can still be determined, but the edges are irregular and indistinct, due to dissolution at the edges of the crystal (Figure 4.5e).

Pseudomorphs: where the original crystal shape of a mineral is retained despite complete replacement by another mineral, e.g. clay (Figure 4.5f).

Interstitial clay: clay filling pore space in the host rock between mineral grains. Interstitial clay appears brown under the petrographic microscope in PPL (Figure 4.5g).

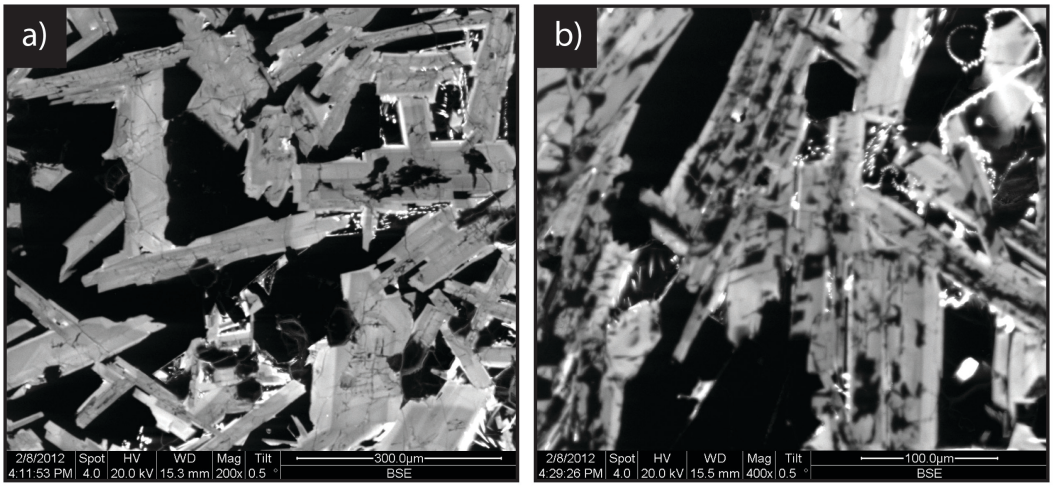

Figure 4.4: CL images of feldspars from Hramaborg Fault, Iceland. a) Host rock feldspars, showing well defined magmatic zoning within luminescing feldspars. b) Zeolitised feldspars, where zeolitised portion does not luminesce well. Zeolite preferentially replaces the core of the mineral, and less so in the Ca rich zone of the feldspar (brighter luminescence at edge of feldspar).

4.3.2. Deformation processes

Cataclasis: where a rock and individual minerals are significantly broken/crushed/reduced in size, as a result of faulting. Mineral clasts (Figure 4.5h,i) and rock clasts (Figure 4.5j) are much reduced from their original size, and may be angular or rounded depending on the degree of deformation and rotation. Cataclastic texture is usually identifiable at the SEM scale, and occasionally under the petrographic microscope.

Rock clasts and mineral clasts: rock clasts are a section of the rock that has been fractured, rotated (rounding of edges), and removed from its original location and entrained into a breccia or cataclasite band; mineral clasts are clasts made of individual minerals from the host rock, rather than clasts of the host rock itself. Mineral clasts can also be derived from zeolite veins.

Dilated grains: where individual mineral clasts have been broken, and dilated in the maximum extensional direction (Figure 4.5k). This process usually occurs along intragranular fractures, and the mineral clast length is increased by extension. Zeolite veins usually fill pore space produced by this extension.

Intragranular fractures: fractures confined within a single mineral grain, usually formed along or at an angle to the cleavage planes (Figure 4.5l) as a result of faulting.

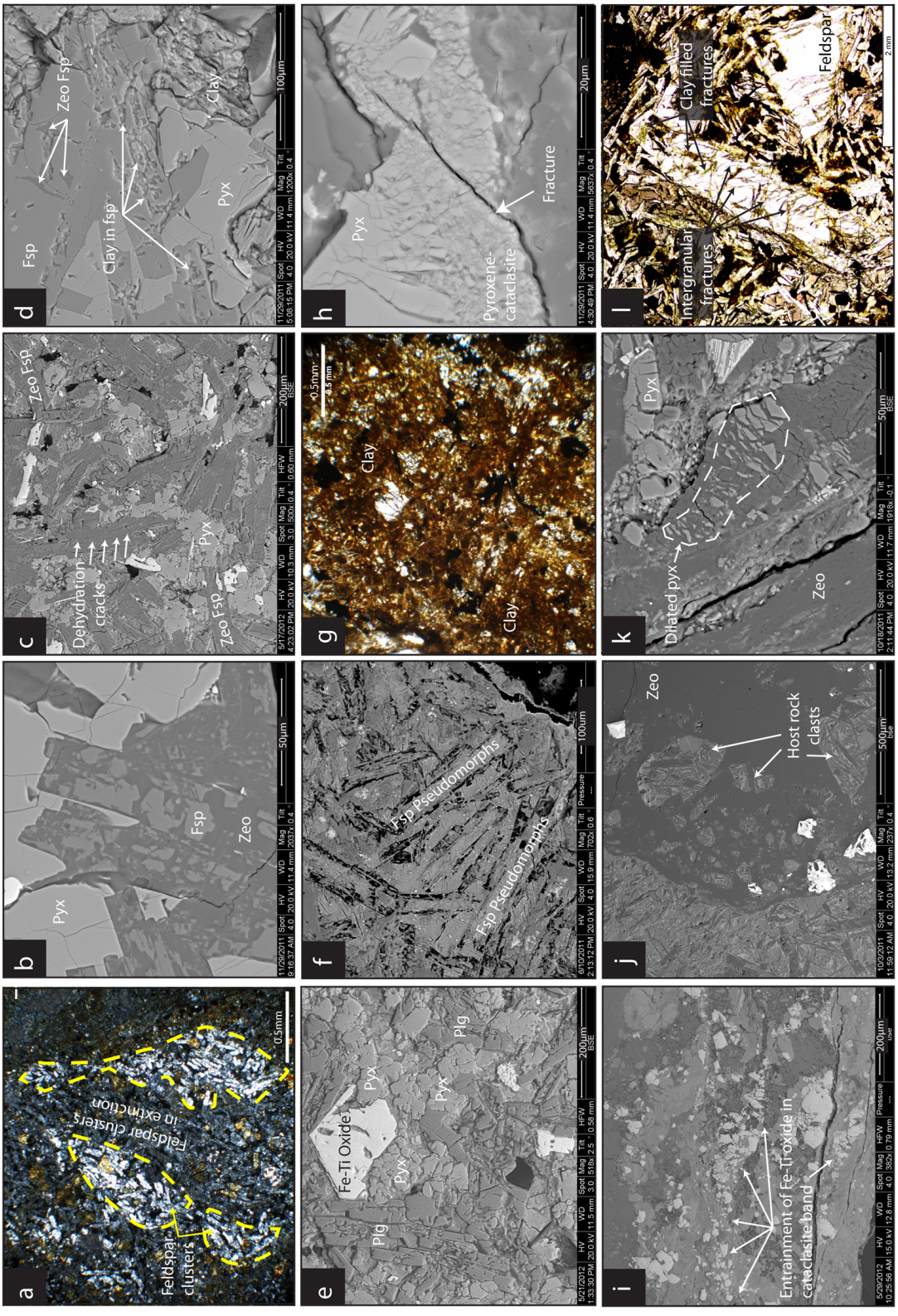

Figure 4.5: Geochemical and deformational processes encountered in faulted basalt. a) Zeolitisation of feldspar in XP, example from IBF. Clusters of feldspar enter extinction simultaneously, and twinning is lost. b) Zeolitisation of feldspar (fsp) in SEM from HBF. Lighter areas are original feldspar, and darker regions are zeolites. Pyroxene labelled pyx. c) Complete zeolitisation of feldspars (zeo fsp) from VJF. Note dehydration structures in zeolites. d) Partial replacement of feldspar by clay, along cleavages and fractures. e) Dissolution of Fe-Ti oxide and

(continued from previous page) pyroxene edges from VPF. f) Clay pseudomorph after feldspar (fsp pseudomorphs) from LWF. g) Extreme example of interstitial clay (brown) from SFZ. h) Cataclasis of pyroxene crystal, with increasing reduction of fragment size toward fracture, from HBF. i) Cataclasite band composed of mineral clasts from TBF. j) Cataclasis of rock clasts from BNF, surrounded by zeolite veins (zeo). k) Dilated pyroxene grain (original morphology outlined), from BNF. l) Intragranular fractures within feldspar, example from HBF.

4.4. Host rock descriptions

The following sections describe host rock mineralogy from each of the field areas. An interpretation of the maximum temperatures that the host rocks have experienced following emplacement are also given, based on estimated temperatures of zeolite and clay formation during host rock alteration. The habit of the four most common minerals in the host rocks (feldspar, pyroxene, olivine and Fe-Ti oxides) is also described, so to help understand how they have changed in response to faulting. Where appropriate, background alteration and amygdale mineralogy are also described.

4.4.1. Bird Nest Fault (BNF), Mull

The host rock of the BNF is composed of two lava flows – a lower amygdaloidal flow (footwall) and an upper massive, blocky flow (hanging wall). The massive blocky flow (Figure 4.6a) was originally porphyritic, but now contains chlorite pseudomorphs after olivine phenocrysts (1mm in size). The groundmass consists of euhedral and finely crystalline (<0.5mm) plagioclase feldspar, clinopyroxene and Fe-Ti oxide. The feldspars have been partially replaced by clays along cleavage planes, and when viewed in XP, have slightly indistinct lamellar twinning. The pyroxenes are comparatively pristine. Chlorite after olivine is fibrous and brownish-green in PPL.

The amygdaloidal flow (Figure 4.6b) is micro-porphyritic, with micro-phenocrysts (<0.5mm) of plagioclase and chlorite after olivine. The groundmass consists of feldspar microliths, with intragranular Fe-Ti oxides and pyroxenes. The plagioclase has been partially replaced by clays, and so has indistinct lamellar twinning. The chlorite is again brownish green in PPL

and fibrous. Amygdales are filled with calcite, zeolites (thomsonite and natrolite) and clays (chlorites and smectites) (Figure 4.6c).

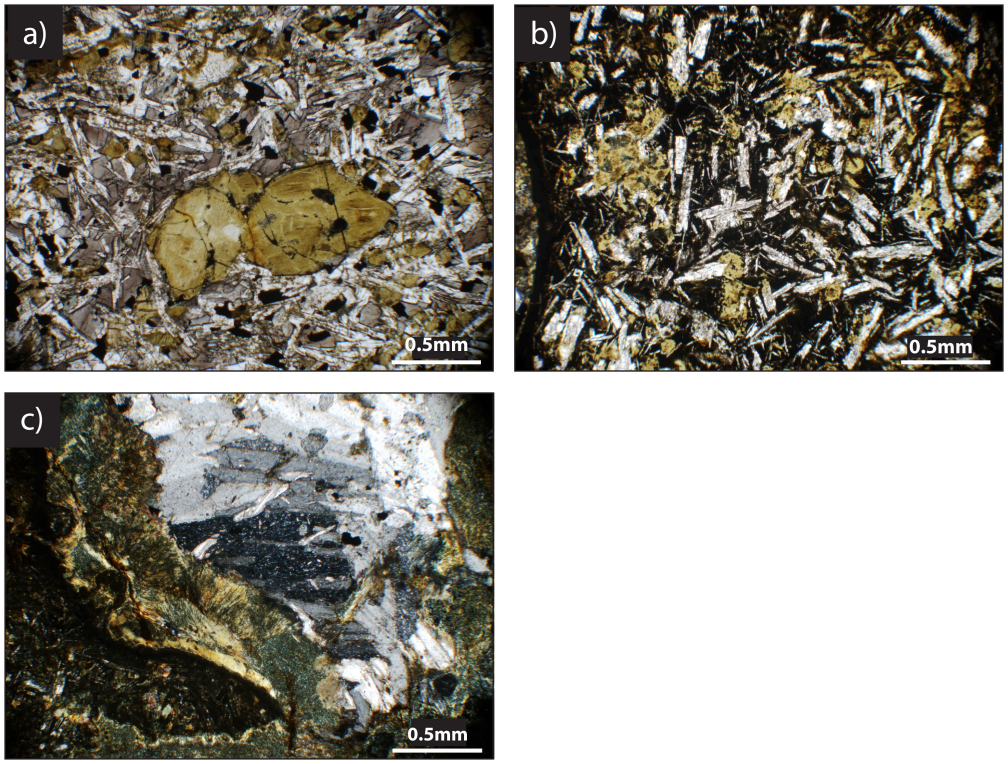

Figure 4.6: BNF host rock. a) PPL view of host rock from the massive blocky flow. Browny pink crystals are pyroxene, white crystals plagioclase feldspar, and large brown crystals are chlorite pseudomorph after olivine. b) PPL view amygdaloidal flow host rock. Black is the fine-grained groundmass of Fe-Ti oxides and pyroxenes, white crystals are plagioclase feldspars, and browny green crystals are chlorite pseudomorphs of olivine. c) An amygdale within the amygdaloidal flow that is filled with calcite (black/white twinkly centre), natrolite (white) and a rim of fibrous clays (chlorite and smectite) in XP.

The amygdaloidal basalt flow may have experienced a greater groundwater flow (and therefore alteration) than the blocky flow due to its high vesicular porosity. However, the presence of chlorite pseudomorphs after olivine, and replacement of some minerals by clay in both basalt flows, shows they have both been altered, probably due to pneumatolysis syn- and post-emplacement of the Mull Central Complex (see Chapter 2). The background alteration temperature of the host rocks can be estimated from amygdale and clay mineralogy. The presence of thomsonite within host rock amygdales suggests temperatures of 50-100ºC during mineralisation (Jørgensen, 2006; Weisenberger and Selbekk, 2009). Chlorite and smectite found in amygdales and as pseudomorphs can form at ~200ºC and 60ºC

respectively (Kristmannsdottir, 1978). Given the presence of thomsonite, and no other higher temperature zeolites in the amygdales, it is more likely background alteration temperatures were <100ºC.

4.4.2. Lawther Fault (LWF), Ardnamurchan

The LWF host rocks are micro-porphyritic tholeiitic olivine basalt (hanging wall) and a fluidal peperite (footwall). The basalt (Figure 4.7a) contains micro-phenocrysts (0.5mm) of plagioclase feldspar (with well developed twinning, fractured in places, and often with a sieve texture) and olivine (heavily fractured and partially replaced by clays). The groundmass consists of plagioclase (<0.25mm), fine feathery pyroxenes and skeletal Fe-Ti oxides. All mineral edges are lined with minor amounts of clay.

The fluidal peperite (Figure 4.7b) is composed of two phases; fine-grained brown mudstone with bulbous margins and brown, highly altered clasts of micro-porphyritic basalt. The sediment comprises clay to silt grade material, locally with fine laminae concordant with margins of the basalt clasts. Plagioclase is the only identifiable mineral within the basalt, with the groundmass being replaced by clays (brown in PPL) or palagonite (yellow in PPL), due to hydrothermal alteration resulting from lava mixing with cold, wet sediment (White et al., 2000; Brown and Bell, 2007). Amygdales are found in the peperite, and contain chlorite and other clays, with a rim of chalcedony (Figure 4.7c).

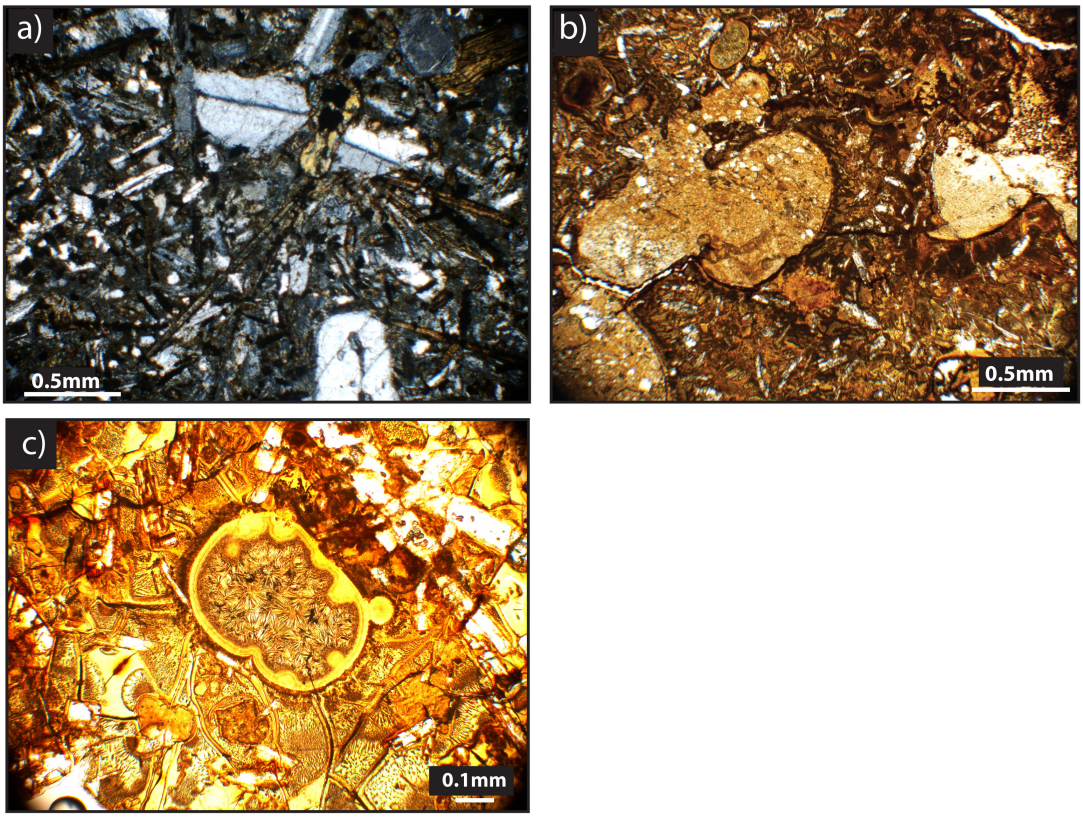

Figure 4.7: LWF host rock. a) XP view of basalt host rock. Large grey/white crystals are plagioclase microphenocrysts, surrounding an olivine microphenocryst. Long, elongated crystals radiating out from these are feathery pyroxenes. The groundmass is composed of laths of feldspars and Fe-Ti-oxides. b) PPL view of host rock from fluidal peperite. Light brown coloured blobs are sediment, surrounded by darker brown basalt. White laths of plagioclase are visible, surrounded by a clay-rich groundmass. c) PPL view of clay-filled amygdale in peperite, rimmed by chalcedony. Surrounding the amygdale is yellow glassy palagonite.

The hanging wall basalt has experienced little alteration, aside from clays rimming crystals. The peperite however contains abundant clay and palagonite. This is a common feature of peperites due to hydrothermal alteration during emplacement, thus suggesting alteration is confined to the peperite, rather than being a common background alteration affecting both lithologies.

The presence of chalcedony in the peperite suggests temperature ranges of 100ºC – 300ºC (White and Corwin, 1961), with a similar range for chlorite and smectite, though this is again likely related to hydrothermal alteration accompanying peperite emplacement. Therefore the background alteration temperature history for these rocks is difficult to estimate. As the lavas are part of the same formation as those found surrounding the Bird Nest Fault,

(Mull Plateau Lava Formation) it is possible that background alteration temperatures could be similar (~100°C).

4.4.3. Talisker Bay Fault (TBF), Skye

Multiple host rock types are cut by this large displacement fault, but only one of them was accessible; a porphyritic mugearite (Figure 4.8a,b). This rock contains phenocrysts of plagioclase feldspar (1mm), microphenocrysts of forsteritic olivine (0.5mm), and a groundmass of flow-aligned plagioclase feldspars, equigranular clinopyroxenes and granular Fe-Ti-oxides.

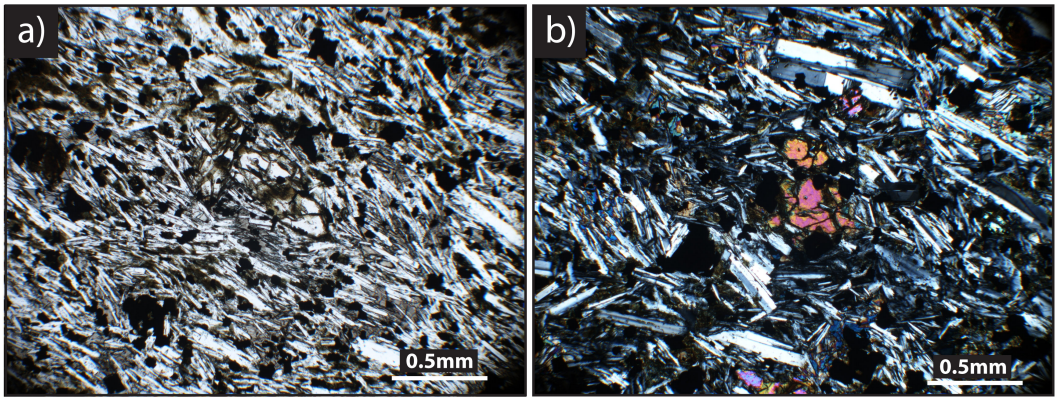

Figure 4.8: TBF host rock. a) PPL of host rock. Flow-aligned feldspars are white lath-shaped crystals, and browny pink crystals of pyroxene. Opaque minerals are Fe-Ti oxides. High relief olivine at centre of image. Pale brown at edge of olivine is clay, also present at edges of other minerals. b) XP view of host rock, with bright olivine in centre.

The olivine phenocrysts are fairly fresh, though are partially altered to serpentine and clay along fractures. There is also a minor volume of interstitial clay. The basalt has therefore experienced little background alteration. Whilst amygdales were absent from this host rock, they occur within the altered wall rock of the fault, where they contain natrolite. This may mean that natrolite mineralisation occurred from fault-related fluids, rather than as a result of background alteration via groundwater circulation. If the natrolite were a result of background alteration, this would suggest amygdale formation at groundwater temperatures of 40-70°C. However, King (1977) and Ferry et al (1987) have identified thomsonite, mesolite, laumontite (high temperature zeolite), heulandite and others from the Talisker Bay area. Through geothermometry

techniques, Ferry et al (1987) estimated that the lavas near Talisker have experienced metamorphism at less than 400ºC (related to emplacement of the gabbroic Palaeogene Cuillin Centre). Therefore, the background alteration temperature of the basalts could be anything from 150ºC to 300ºC, based on zeolite mineralogy.

4.4.4. Hramaborg Fault (HBF), Iceland

The predominant host rock at the HBF is a porphyritic tholeiitic olivine basalt. Ignimbrite and mudstone clasts are absent from the fault zone, and are therefore not described here, as no comparison with a faulted equivalent is available. The basalt is porphyritic with phenocrysts of fresh, zoned plagioclase feldspar (Figure 4.9b) and a groundmass (Figure 4.9a) of plagioclase feldspar, clinopyroxene, Fe-Ti oxide, and forsteritic olivine. Clay within the host rock is restricted to pseudomorphs after olivine.

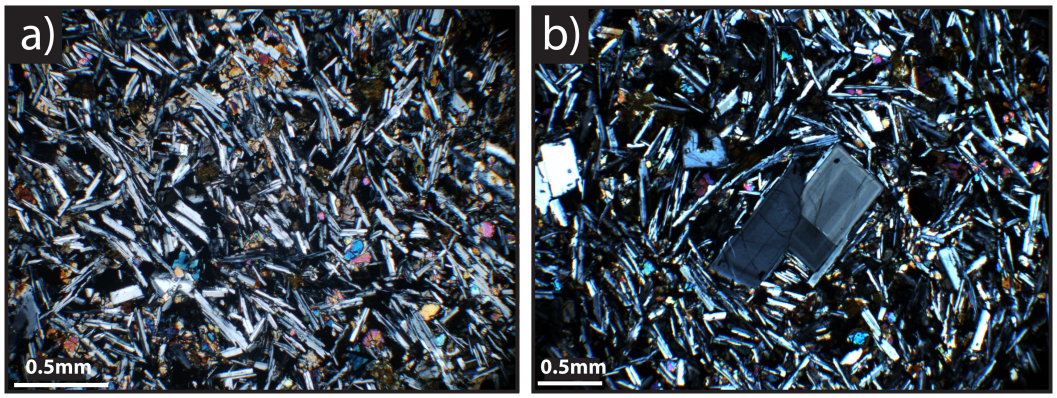

Figure 4.9: HBF host rock. a) XP view of host rock. Long white crystals are plagioclase feldspars displaying lamellar twinning, low BF colours are pyroxenes and bright BF are olivines. Opaque minerals are Fe-Ti oxides. b) XP of feldspar phenocryst. Note well-developed zoning of crystal.

Whilst amygdales are absent from this host rock, Walker (1960) identified zeolites in amygdales in this area of Mull that were predominantly mesolite and scolecite, indicating regional low grade zeolite facies metamorphism at around 50-120ºC, and possibly up to 150ºC from the presence of heulandite in vesicles (also identified by Walker (1960). The lack of clays suggests a low intensity of background alteration of this rock.

4.4.5. Host rocks from the Faroe Islands

The host rocks of the faults studied from the Faroese Island of Suðuroy are all very similar to each other. The host rock is a tholeiitic basalt (Figure 4.10a) with sparse phenocrysts (>1mm) of olivine and plagioclase feldspar (Figure 4.10b). The groundmass is dominated by plagioclase feldspar and Fe-Ti oxide, with very small (<0.05mm) clinopyroxene crystals and interstitial clay. The abundance of amygdales is variable throughout the field sites, and where present the amygdales contain zeolites (Figure 4.10c) and clay (Figure 4.10d).

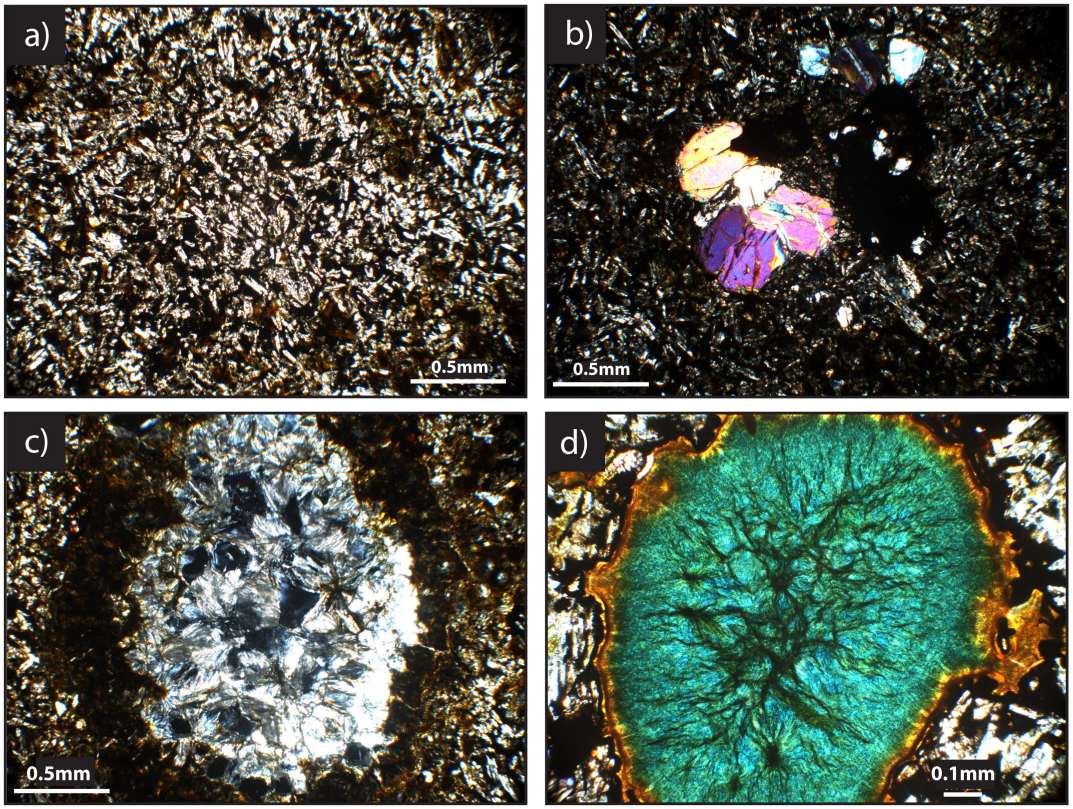

Figure 4.10: Host rock from Vagseiði. a) Aphyric tholeiite, with small laths of white feldspar and opaque Fe-Ti oxides (PPL). Irregular clay patches within the host rock are brown. b) Olivine phenocryst within host rock (XP). c) A heulandite-filled amygdale rimmed with clay (PPL). d) A clay-filled amygdale, probably dominated by chlorite and rimmed by smectite (PPL).

The basalt has been altered to clay in patches, particularly surrounding Fe-Ti oxides and feldspars. This is possibly due to the amygdaloidal nature of the lava enhancing permeability. The presence of heulandite suggests the basalt has undergone low temperature zeolite facies metamorphism, i.e. between 90 - 150°C (Jørgensen, 2006). In fault sites lacking amygdales in

the host rock (Hov, I Botni), a palaeo-temperature estimate is difficult, though Glassley (2006) used zeolite-depth profiles measured from boreholes in Lopra, Suðuroy, to suggest a maximum thermal gradient of 50ºC/km. If <3km has been exhumed (see Chapter 2) from Suðuroy, this suggests the host rocks in this study have experienced a maximum background alteration temperature of <150ºC, which is consistent with the presence of heulandite in amygdales.

Host Rock Description Summary

The majority of the host rocks in this study are tholeiitic basalts. Most contain very little olivine, but the Talisker Bay host rock contains a higher concentration of olivine than most (mineral totals are quantified in section 4.7). Most host rocks contain euhedral minerals, with the exception of the Bird Nest footwall amygdaloidal basalt, which is largely composed of skeletal microliths of rock forming minerals. This chapter will describe and discuss how changes in mineralogy (such as olivine content and mineral habit) influence alteration and deformation characteristics as a result of faulting.

Chapter outline

In the following sections, the detail of each fault rock sample taken from within each fault is described, through a mixture of petrographic and SEM microscope techniques. Where images are shown from the petrographic microscope, they are described in terms of plane polarisers (PPL) and cross-polarisers (XP). Images of the thin sections used for microscopic descriptions are provided at the beginning of each fault section, along with the relevant fault map to illustrate sampling locations. Thin section sizes shown are 76x26mm in the case of thin and long samples and 76x51mm in the case of wider samples. Minerals labelled within the images are given the following abbreviations: plagioclase (plg), feldspar (fsp), zeolitised feldspar/plagioclase (zeo fsp/plg), pyroxene (pyx), Fe-Ti oxide (Fe-TI-Ox), and zeolite vein (zeo).

4.5. Fault-related microstructures - self-juxtaposed faults.

The organisation of this section will follow that of Chapter 3, with descriptions in the order of small to large displacement faults (VJF, VPF, BNF and HBF).

4.5.1. Vagseiði Jetty Fault (VJF) – 18cm displacement

VJF1: altered footwall

The thin section of the altered footwall contains a 5mm thick zeolite vein cutting vertically through the sample, and bounds its edge. A 1cm thick dark brown band of alteration runs parallel to the vein (Figure 4.11a); the other side of the vein is not preserved in the sample. A second 1mm zeolite vein defines the other side of the section. Both veins contain blocky zeolite crystals, radiating out from vein walls (Figure 4.12b). The zeolite was identified as heulandite by EDX.

The mineralogy of the relatively unaltered groundmass is the same as the host rock, but feldspar phenocrysts contain intragranular fractures, and clay pseudomorphs after olivine (Figure 4.12a). Note in Figure 4.13c the dissolution of minerals, particularly pyroxene.

In the zone of alteration next to the thicker vein, feldspars are completely replaced by zeolite (identified as heulandite, also found in the vein) (Figure 4.13c). Sample preparation-related dehydration cracks cut the zeolitised feldspars. At 9.1mm from the vein, the degree of zeolitisation of the feldspar drops rapidly to zero over a distance of 2mm (Figure 4.13d). The smaller vein lacks an equivalent alteration halo.

VJF2: PSZ zeolite lined fracture with clay fill

Sample VJF2 contains altered host rock cut by a vuggy zeolite vein (Figure 4.11b). Structureless clay fills the fracture that the zeolite is growing into. The other side of the vein is not sampled, but from field observations there are no zeolite crystals at the other side of the fracture. The fracture-filling clay post-dates the zeolite crystals, as the clay "drapes" over the euhedral crystals that have precipitated along the fracture walls. The clay fill is homogenous, and appears to post-date faulting as it lacks any fault-related structures.

Mineralogy has changed significantly following alteration of the host rock (Figure 4.12e,f). Whilst there is little in the way of mechanical deformation, and the original mineral grain outlines can still be identified, dissolution of pyroxenes and feldspars, and zeolitisation of feldspars, has occurred (Figure 4.12e,f).

VJF3: altered hanging wall and shear plane

Sample VJF3 contains a network of zeolite veins (Figure 4.11c). The rock mass surrounding the veins hosts partially zeolitised feldspars and all minerals have evidence for dissolution. There is a significant increase of interstitial clay in comparison with the host basalt (Figure 4.12c). In addition, all minerals within the groundmass contain intragranular, clay-lined fractures (Figure 4.13e). Clay also replaces feldspar (Figure 4.13f).

The vein network is composed of foliated and partially crushed zeolite (heulandite) veins (Figure 4.12d). Fine angular clasts of host rock altered to clay occur within the zeolite veins. Other veins and fractures branch off the main network, in riedel shear morphologies. Based on this evidence, the vein network appears to accommodate a component of shear.

Adjacent to the shear vein network, mm-wide zones of grain-size reduction and rotation have affected pyroxenes and Fe-Ti oxides, apparently initiated

along intragranular fractures (Figure 4.13g). However, although feldspars immediately adjacent to this vein have been replaced by heulandite, they are not brecciated or fractured. This sample therefore provides good evidence for mineral-dependent deformational and geochemical processes.

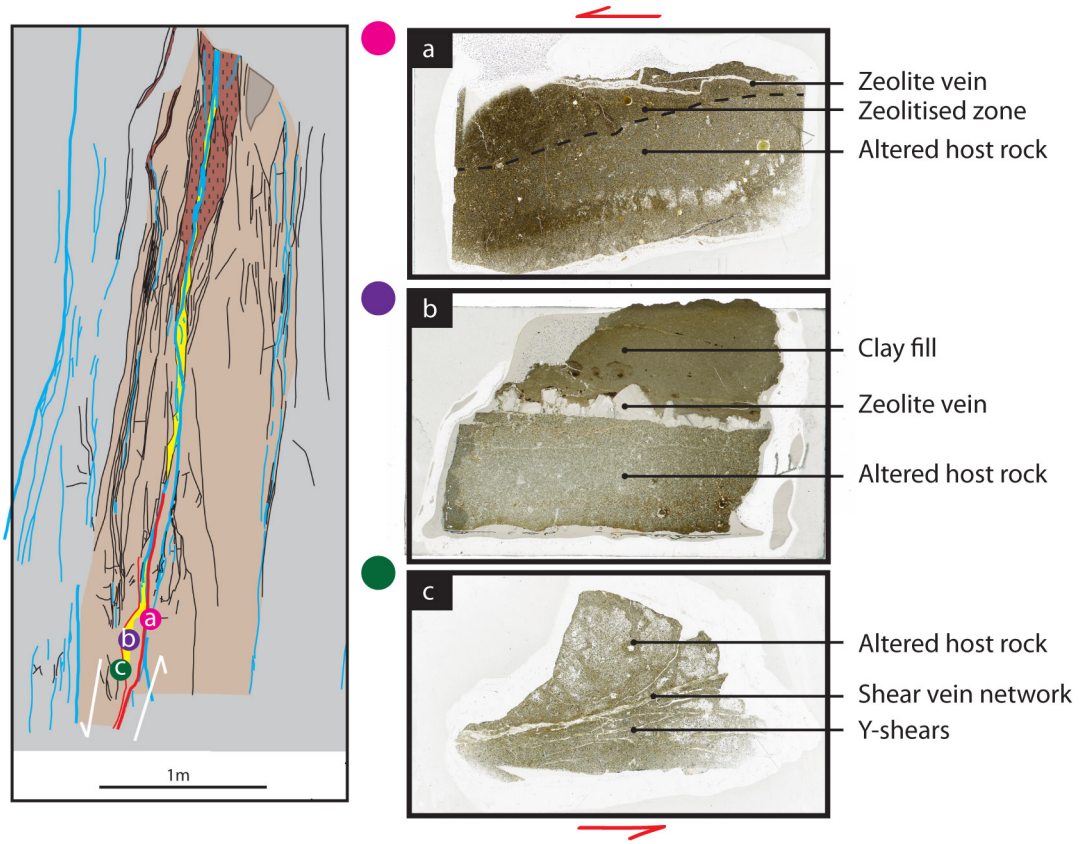

Figure 4.11: VJF fault map marked with sample locations. Scanned images of each thin section given for reference against corresponding coloured dot. Fault movement is marked by red arrows at the side of the scanned sections. Sample ID is in brackets. a) Pink dot = Altered footwall sample, (VJF1). b) Purple dot = sample from PSZ, crackle breccia (VJF2). c) Green dot = Hanging wall shear plane, (VJF3).

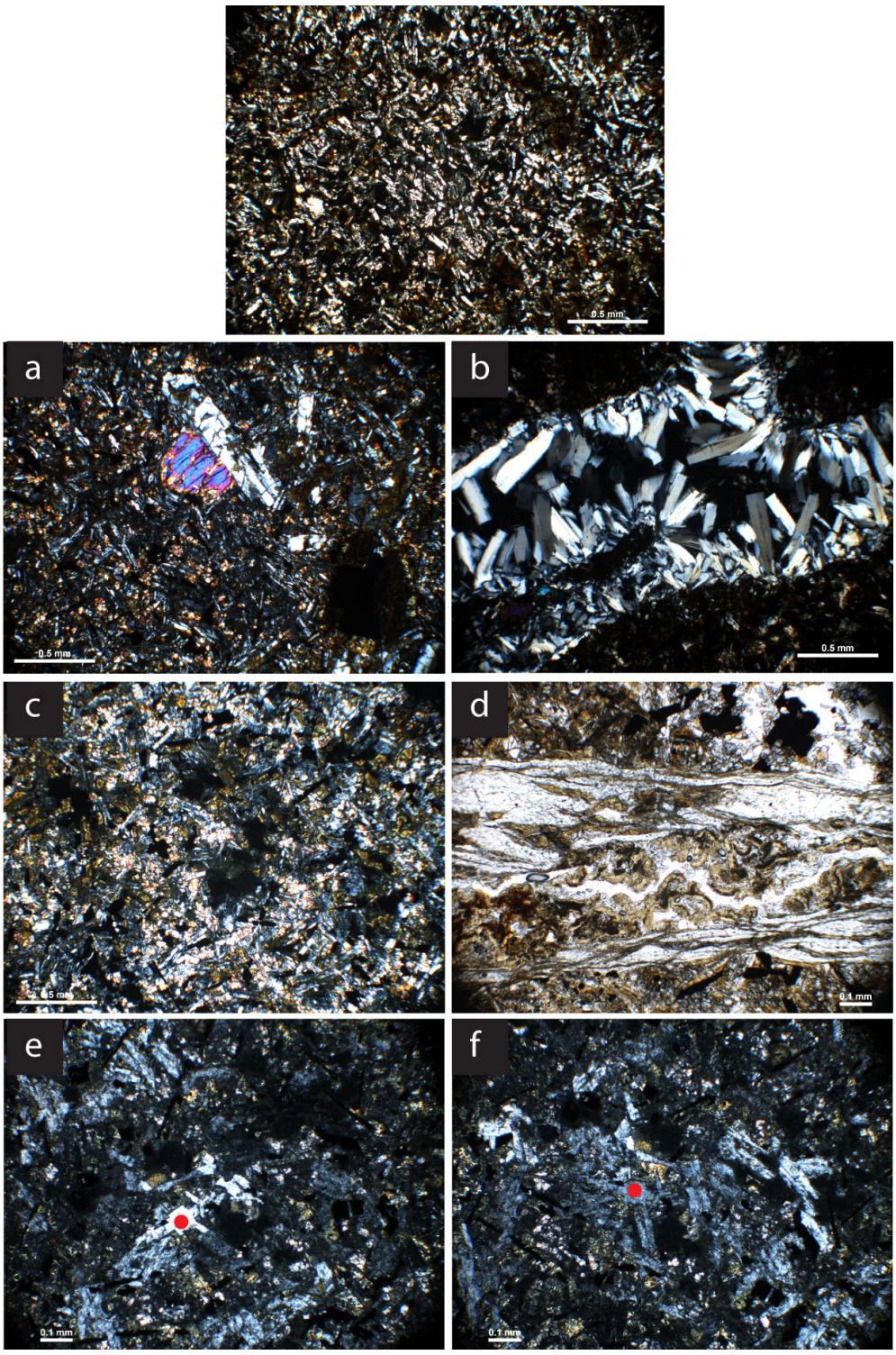

Figure 4.12: Petrographic microscope images from VJF. Host rock (PPL) is shown at the top for reference. a) Fractures in feldspar, and olivine partially replaced by clay in altered footwall (XP). b) Extensional zeolite vein in altered footwall (XP). c) Interstitial clay and zeolitised feldspar from altered hanging wall (XP). d) Crushed zeolite shear plane with altered, brecciated host rock clasts, altered hanging wall (PPL). e & f) Zeolitised feldspars in PSZ, showing a common optical orientation in clusters of feldspar pseudomorphs, a typical characteristic of zeolitisation. The red dots in e) and f) mark the location of a single feldspar crystal used for reference (XP). Figure f) is rotated relative to Figure e).

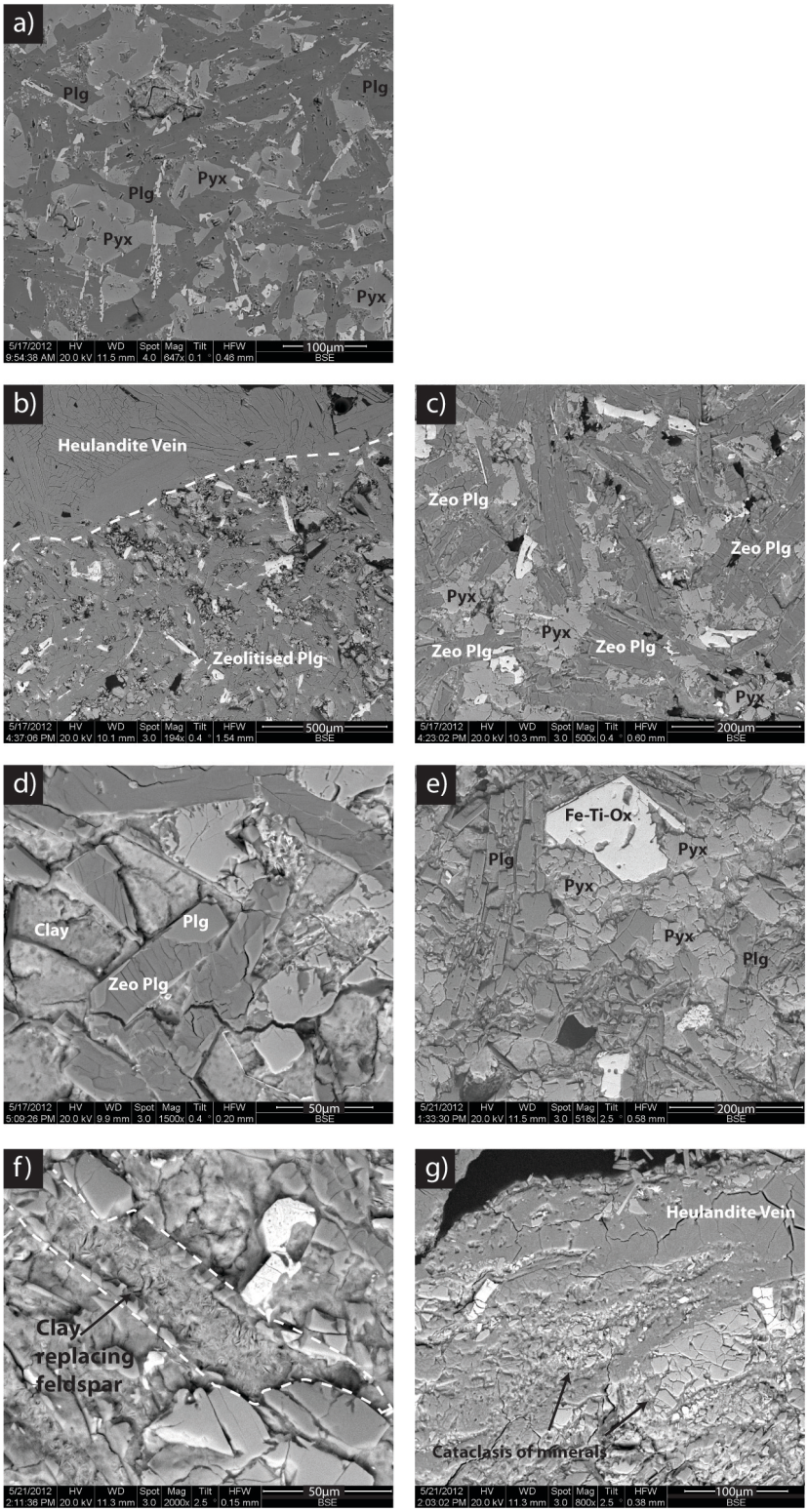

Figure 4.13: BSE images of VJF. a) Host rock, with plagioclase (plg),and pyroxene (pyx) labelled. b) Altered footwall, with heulandite vein and zeolitised plagioclase adjacent to the vein. c) Detail of zeolitised plagioclase (zeo plg) in altered footwall. Note also change in pyx from host rock. d) Close up of zeolite replacing plagioclase in situ in the altered footwall. e) In PSZ. Note rough textures of plagioclase and pyroxenes, with clay forming in newly opened fractures. f) Close up of clay replacing plagioclase in the altered hanging wall. g) Example of mechanical deformation in altered hanging wall, where pyroxene and Fe-Ti oxides are brecciated adjacent to the shear plane (marked by heulandite vein).

4.5.2. Vagseiði Puddle Fault (VPF) – 28cm displacement

VPF1: Altered hanging wall

Sample VPF1 (Figure 4.14b) was taken from the altered host rock edge of an extensional vein. The extensional vein was not sampled. The altered host rock contains zeolitised feldspars. There is also an increase of interstitial clay, and chlorite/smectite are found replacing feldspar phenocrysts (Figure 4.15b).

VPF2: Extensional-shear zone in altered hanging wall

The VPF displays similar alteration and deformation processes to those found in the VJF. Sample VPF2 (Figure 4.14a) was taken ~2.5m from the PSS within the altered host rock, and zeolite shear vein (mm-thick) network.

The altered host rock contains partially zeolitised feldspars throughout the sampled portion (Figure 4.15c). There is also an increase in the abundance of interstitial clay in the altered portion (with respect to the host rock). Chlorite and smectite also form feldspar pseudomorphs.

Zeolites (heulandite) filling mineral veins within the sample are sheared, and the zeolite vein network is therefore considered to have a component of shear. The thicker zeolite veins (~2mm) contain linear trails of fluid inclusions orientated parallel to vein walls, (Figure 4.15d) suggesting crack seal behaviour within these zeolite veins.

VPF3: Fault Plane with zeolite veins

The sample taken from within the PSZ (Figure 4.14c) is very similar in appearance to the PSZ sample from VJF. VPF3 is a clast of crackle breccia (altered basalt), cut by thin (<1mm thick) zeolite veins.

The altered basalt of the crackle breccia clast has evidence for dissolution and fracturing of minerals, and zeolitisation of feldspars. Dissolution of all

types of minerals has occurred (evidenced by irregular mineral edges which are not altered to a secondary phase – in the host rock, mineral edges were well defined), and the pyroxenes and Fe-Ti oxides have also been fractured (Figure 4.16b). An increase in interstitial clay (smectite) compared to the host rock is also found. Feldspars throughout the crackle breccia clast are 50% zeolitised (Figure 4.15e), and in a zone up to ~0.3mm wide adjacent to zeolite veins, feldspars are completely zeolitised (Figure 4.16c). Cutting the altered basalt are zeolite veins (heulandite), radiating out from fracture walls as blocky crystals (Figure 4.15f).

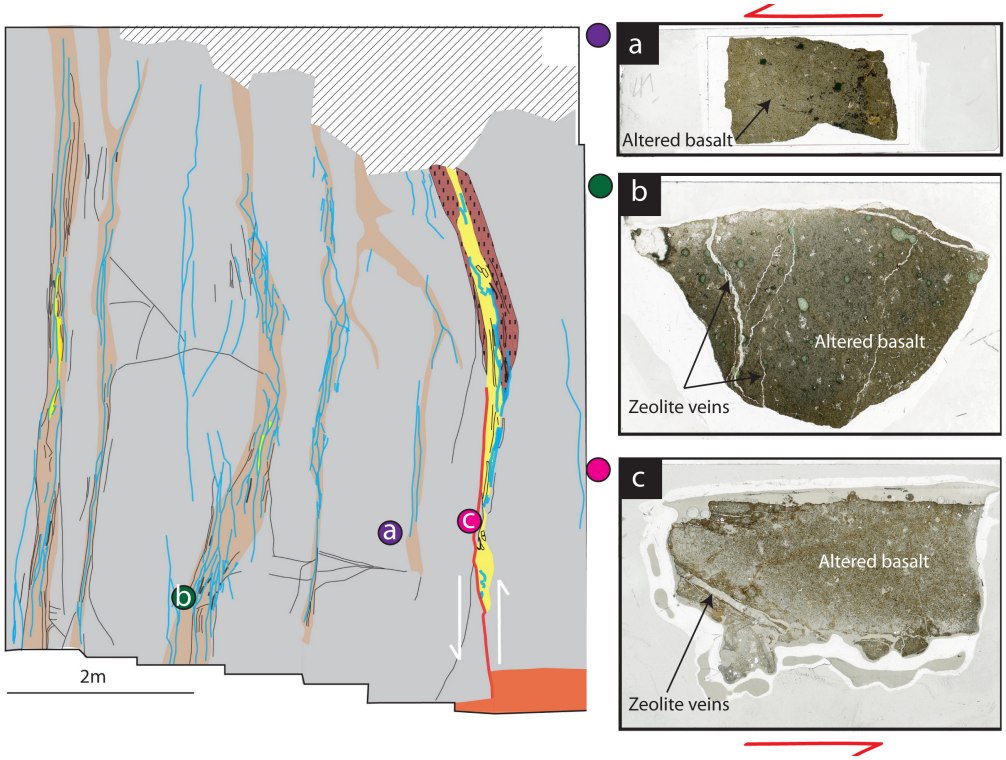

Figure 4.14: Fault map of VPF (section view) with locations of samples marked. a) Purple dot (VPF1) = altered hanging wall. b) Green dot (VPF2) = base of extensional shear. c) Pink dot (VPF3) = crackle breccia clast composed of altered basalt, with zeolite veins from the fault plane.

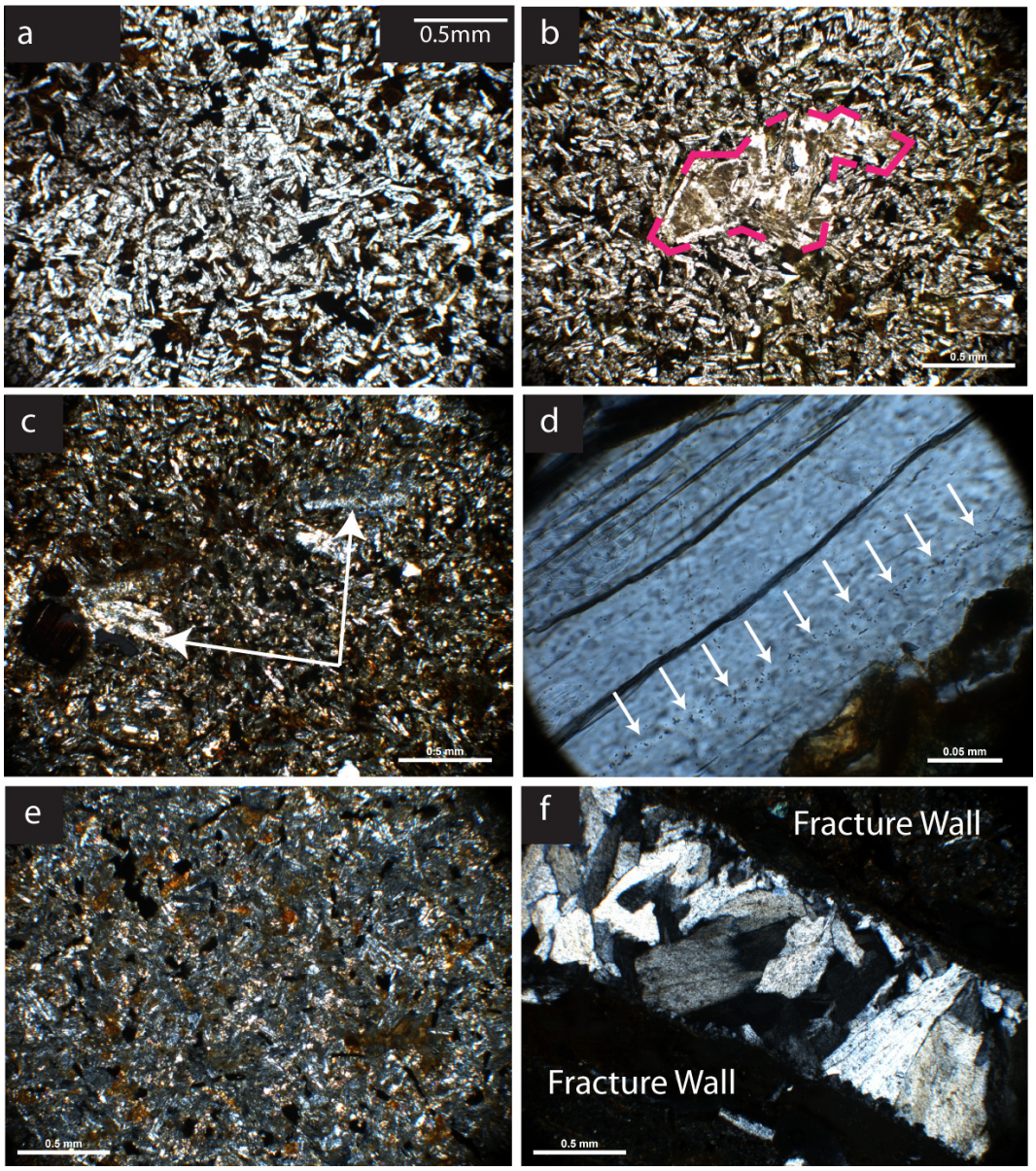

Figure 4.15: Petrographic microscope images of VPF. a) Host rock of VPF for reference (PPL). b) Altered host rock (sample VPF1), with feldspar being partially replaced by clay (outlined) (PPL). c) Altered host rock (sample (VPF2), highlighting partially zeolitised feldspar phenocrysts (arrowed) in XP. Note twinning of feldspars is partially obscured due to zeolitisation. d) Zeolite vein from sample VPF2 with fluid inclusions arrowed (XP). e) Altered host rock within crackle breccia clast from sample VPF3. Twinkly interference colours dominate the feldspars, obscuring feldspar twins (XP). f) Blocky zeolite filling a fracture in VPF3 (XP).

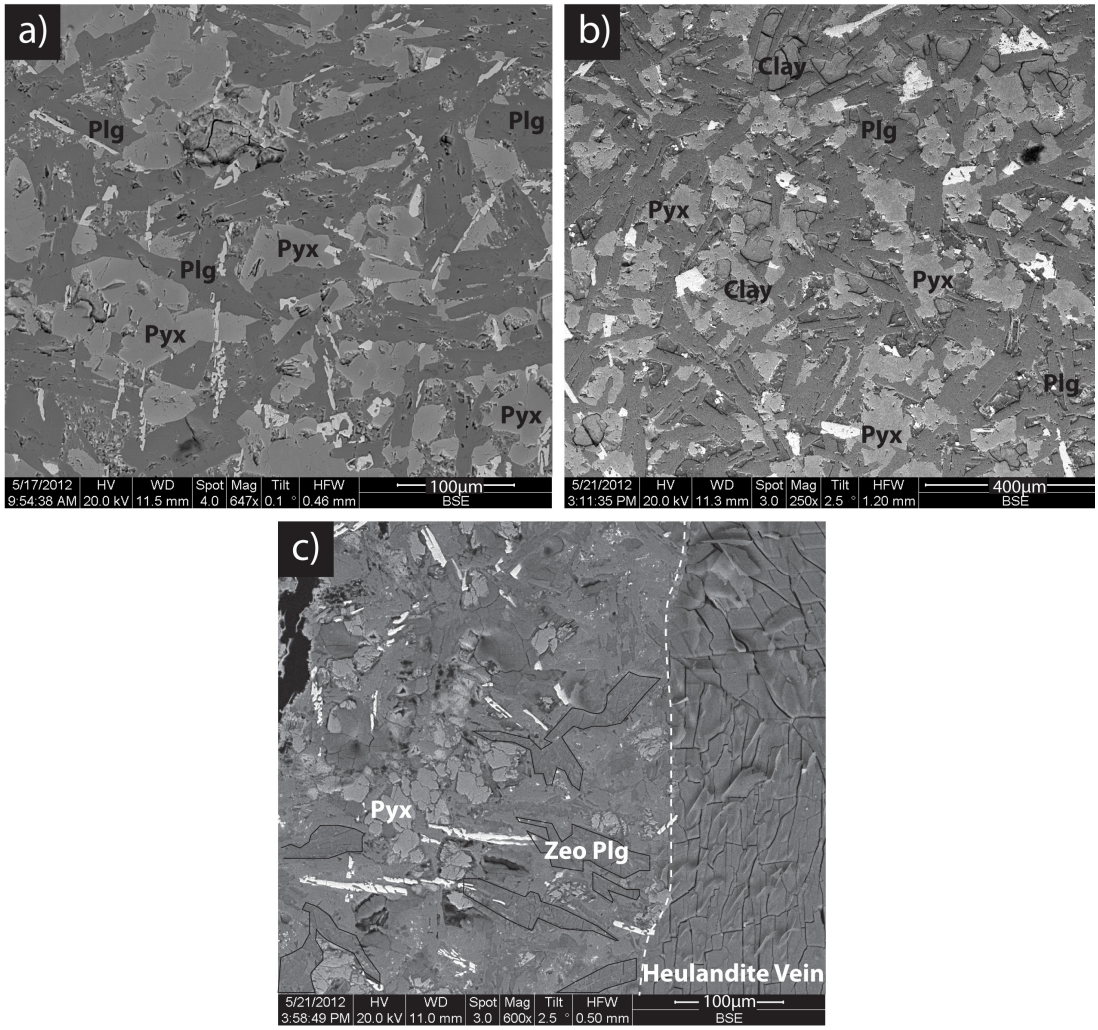

Figure 4.16: BSE images of VPF samples. a) Host rock with minerals labelled. b) Altered host rock showing an increased interstitial clay content, and dissolution of minerals (VPF3), with respect to the host rock. c) Example of zeolitisation of plagioclase adjacent to zeolite vein in the PSZ, outlined in black (VPF3).

4.5.3. Bird Nest Fault (BNF) – 1m displacement

BNF1: Hanging Wall derived PSZ rock phases

Sample BNF1 contains altered (hanging wall-derived) basalt, Y-shears and zeolite veins (Figure 4.17a). The altered basalt mineralogy (Figure 4.18b) is almost indistinguishable from that of the host rock mineralogy. It has a strong yellowish/brown discolouration (in PPL) that is absent in the host rock. This discolouration of the altered host rock coincides with an increase in interstitial clay (chlorite/smectite), and partial alteration of feldspar to clay minerals (with respect to the host rock). Feldspars are also partially zeolitised in this zone (Figure 4.19b). Olivines, present as pseudomorphs in the host rock are absent from the altered basalt. Pyroxenes and Fe-Ti oxides contain more intragranular fractures than in the host rock.

The Y-shear zones within BNF1 (Figure 4.18c) represent shears parallel to that of the PSS. Within the sample, there are at least 5 Y-shear zones, all of which are dominated by fine-grained cataclasite bands. Zeolites in Y-shear orientations have also formed. The cataclastic Y-shears are composed of a very fine-grained cataclasite (clasts <10μm in size), set within a matrix of <10μm thick zeolite (scolecite) veins (Figure 4.19c,d) and/or clay (Figure 4.19f). The cataclasite bands are predominantly composed of pyroxenes, Fe-Ti oxides and zeolite clasts, but not feldspar.

In the zones immediately surrounding the cataclastic bands, grain size reduction is minimal. However, dilation of minerals (in particularly pyroxene) along intragranular fractures occurs in areas surrounding the cataclasite bands. The extra space made as a result of dilation is filled with zeolite, to make intragranular veins (Figure 4.19e,g). Grain dilation is so pervasive in places that the original crystals are very indistinct.

In addition to clays forming the matrix of cataclasite bands, clays within the Y-shear zones are also developed along fractures, and are occasionally foliated (Figure 4.19h). Clays also replace zeolites at crystal margins.

Two generations of zeolite minerals occur, restricted within the Y-shear zone (i.e. they do not continue into the altered host rock). The first generation is parallel to the Y-shears and the later generation crosscuts the first (Figure 4.18d). Zeolite crystals are arranged in radial-fibrous arrays, and both generations have a qualitative chemical composition that is consistent with scolecite.

BNF2: Footwall derived PSZ rock phases altered rock

Sample BNF2 contains footwall-derived altered basalt, and the mineralised PSS of the BNF (Figure 4.17b). In the altered basalt portion (Figure 4.20b), the original mineralogy of the host rock can be determined, albeit with evidence for additional alteration and deformation. Dissolution of all minerals within the altered host rock has occurred, as well as partial zeolitisation of feldspars. Like the altered hanging-wall derived host rock, the altered host rock here is yellow/brown, which coincides with an increase of interstitial clay with respect to the host rock (Figure 4.20b).

Within the mineralised PSS part of the sample, grain size reduction of the rock has occurred. This is different to the grain size reduction in BNF1, where individual minerals rather then the whole rock were brecciated within Y-shears. Altered footwall-derived host rocks are found as clasts within zeolite veins, presumably due to brecciation of the vein walls. Feldspars within these altered host rock clasts are entirely zeolitised (Figure 4.21a). Individual mineral clasts are not found. Wall rock adjacent to zeolite veins also contains 100% zeolitised feldspars, up to at least 2cm away.

Parallel to the mineralised PSS, extensional fractures and two generations of zeolite veins have formed (Figure 4.20c). The zeolites are fibrous and radiate outward from the vein walls (Figure 4.20d). In addition to zeolite mineralisation, equant pyrite crystals also occur within pore space in the zeolite veins (Figure 4.21b). This suggests a late, post-faulting origin for the reducing fluid-bearing H_2S that precipitated the pyrite, as pyrite clasts are absent from the Y-shears and the pyrite-hosted vein is unbrecciated.

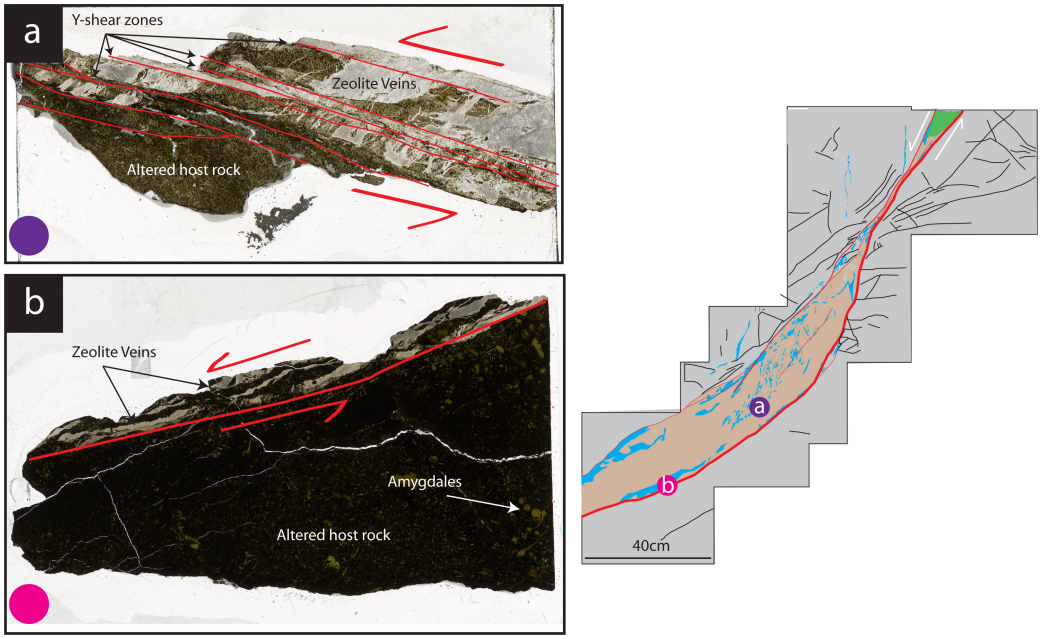

Figure 4.17: Fault map of BNF, with samples located by coloured dots. Fault movement is marked by red arrows next to thin section scans. Images of scanned sections are shown adjacent to corresponding coloured dots. a) Purple dot = hanging wall derived fault rock, with Y-shear zones in red. Note zeolite veins cross-cutting each other. b) Pink dot = footwall fault rock, with PSS highlighted in red.

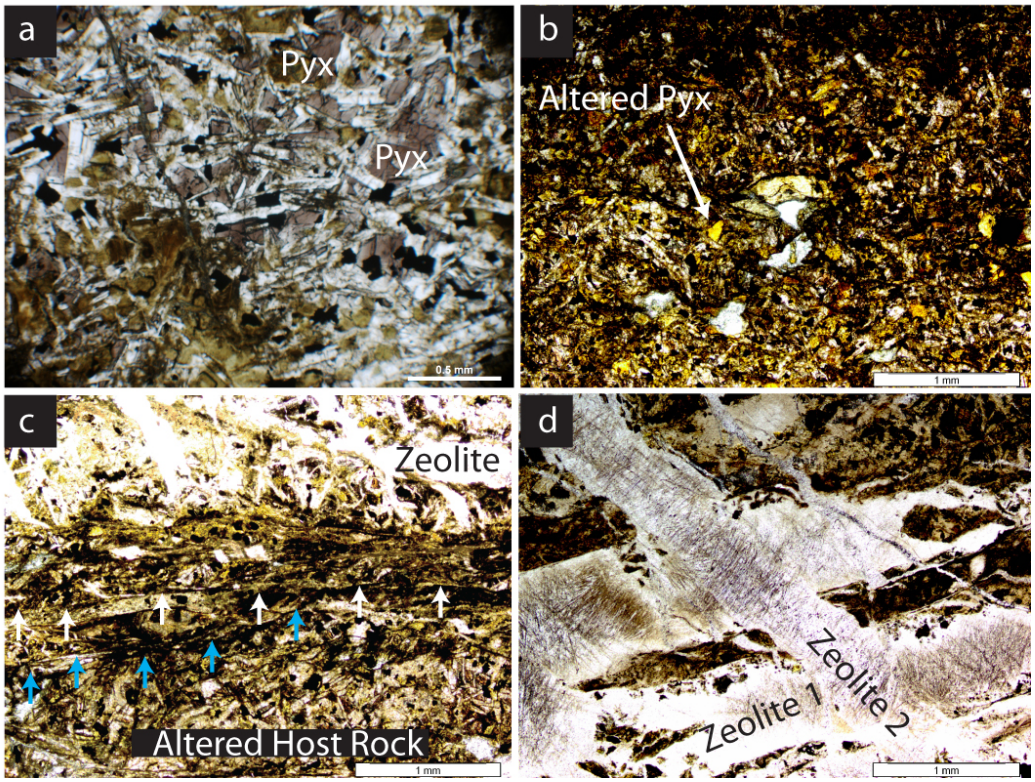

Figure 4.18: Petrographic microscope images of hanging wall component of the BNF. All images in PPL. a) Hanging wall host rock. b) Altered hanging wall host rock, where increased interstitial clay has caused a distinct yellow/brown discolouration of the host rock. c) Y-shears, two of which are arrowed (blue and white). Note opaque Fe-Ti oxides highlight foliations. d) Cross-cutting zeolite veins within the BNF1.

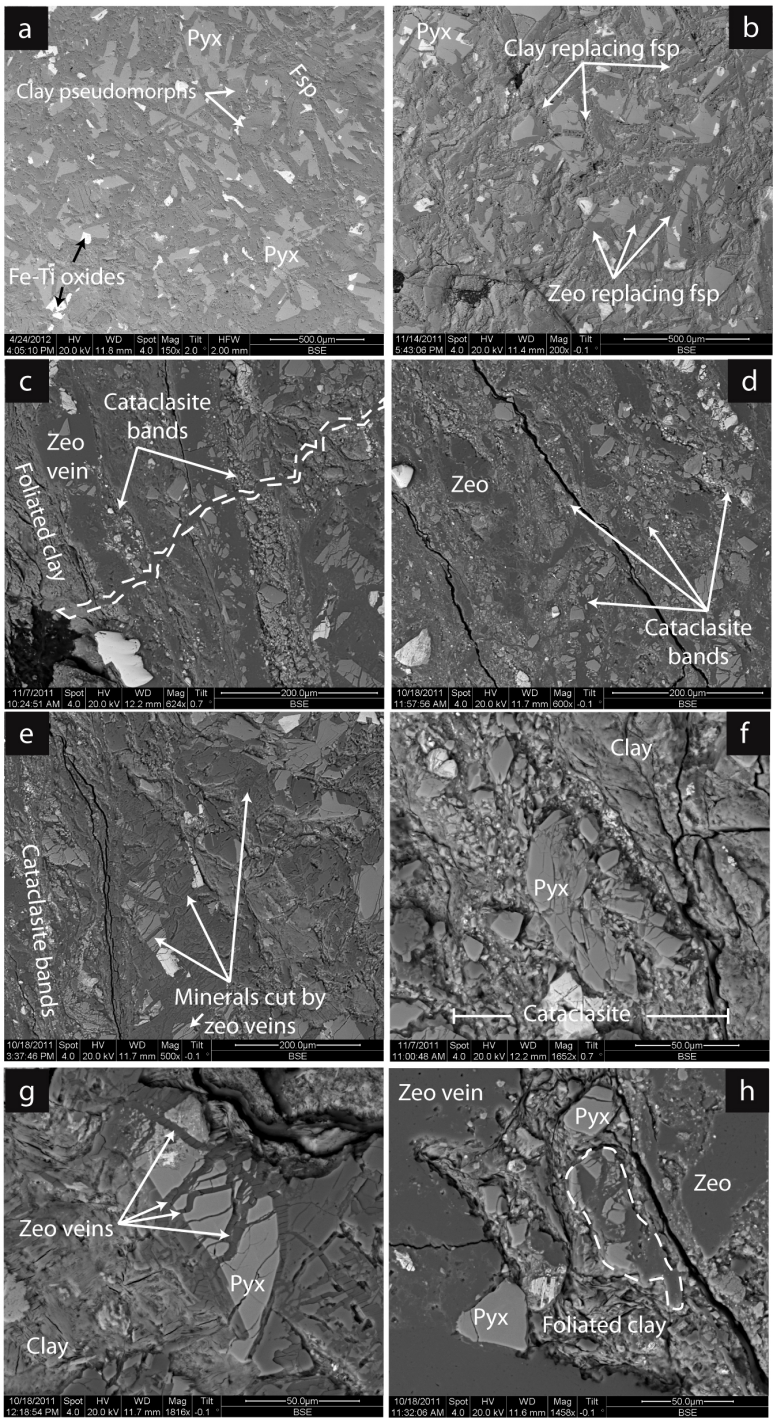

Figure 4.19: BSE images of BNF1, altered basalt and Y-shear zones. a) Host rock image. b) Altered basalt adjacent to Y-shears, showing alteration of feldspar to clay and zeolite. c) Cataclasite bands along Y shears, crosscut in places by zeolite veins (outlined). d) Cataclasite bands with a matrix of zeolite. e) Example of zeolite cross-cutting across minerals within the altered basalt portion. f) Example of pyroxene hosted clay being sheared within cataclasite band, set within a clay matrix. g) Close up of zeolite veins within extensional fractures of pyroxene. h) Example of foliated clay-filled fracture with clasts of zeolite cemented host rock (outlined).

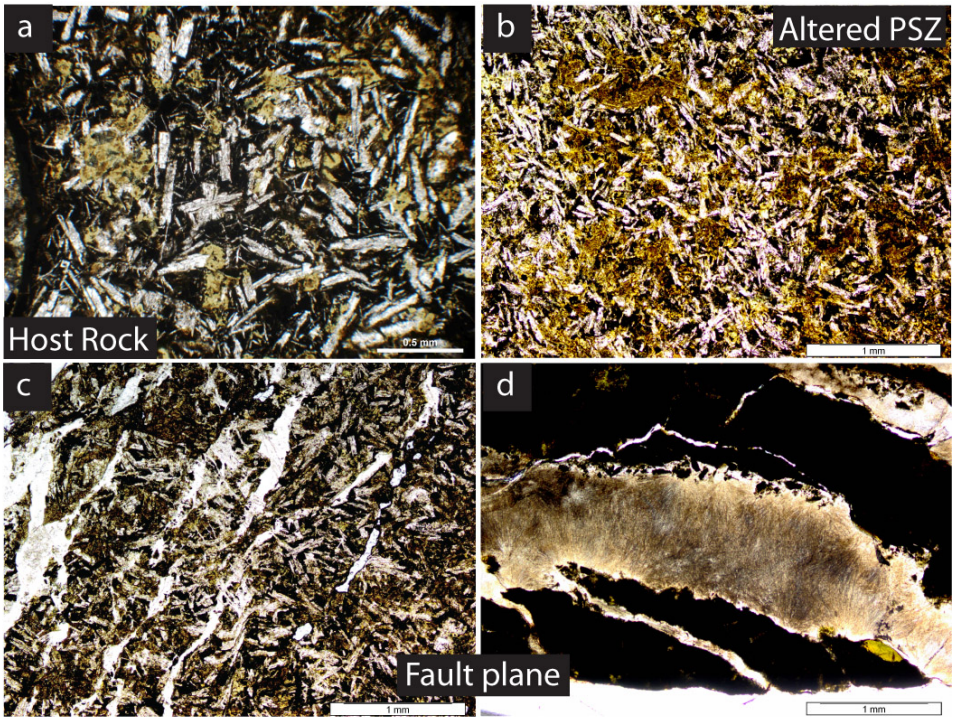

Figure 4.20: Petrographic microscope images of the footwall rock from BNF, in PPL. a) Footwall host rock. b) Footwall host rock in altered PSZ. c) Fractured and mineralised footwall along PSS. Feldspars in host rock clasts are zeolitised. d) Fibrous zeolite vein with brecciation in wall rock.

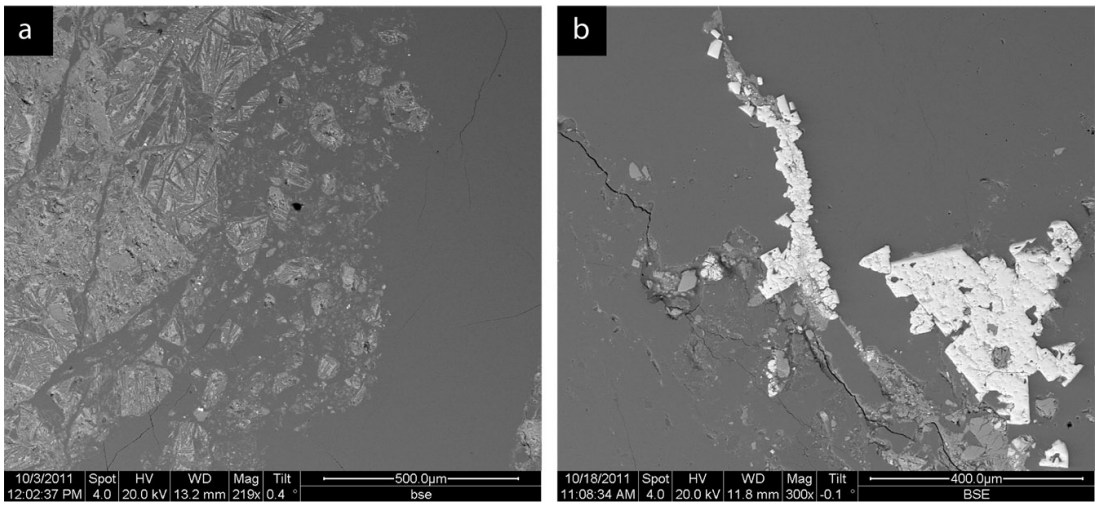

Figure 4.21: Detail of footwall derived fault rock (BNF2) along the PSS. a) Detail of brecciated vein walls, with clasts of host rock. Grey vein is scolecite. b) Pyrite mineralised in scolecite vein.

4.5.4. Hramaborg Fault (HBF) – 25m total displacement

HBF1: Altered host rock

The thin section of HBF1 was made from a fracture bound altered host rock (i.e. the edges of the thin section represent fractures). The thin section is composed of two parts: altered basalt, and altered basalt with zeolitisation. The altered basalt portion (Figure 4.22b), has a higher density of intragranular fractures and greater volume of interstitial clay relative to the host rock, turning the sample a browny/yellow in PPL (Figure 4.23b) from an original (fresh) grey. Clay has also formed along intragranular fractures, and dissolution of all minerals is also noted. Clay has also replaced olivine (Figure 4.24b).

Toward the margins of the section is the altered basalt with zeolitisation. Here, 1-2mm thick fractures are filled with rosettes of green clay (chlorite/smectite) and zeolites (Figure 4.23c). Adjacent to these filled fractures, and the fractures bounding the sample, there is an increase in clay content and intensity of feldspar zeolitisation (Figure 4.24c). Immediately adjacent to these fractures, zeolites have replaced 80% of the feldspar crystal (Figure 4.24d). Moving further away from fracture edges (no more than 1cm), zeolitisation reduces to a zone where euhedral zeolites have replaced interiors of feldspar crystals (Figure 4.24c). Beyond this level, the rock is as described in the altered basalt above.

HBF2: Cataclasite and altered host rock

The sample taken from the protocataclasite zone (Figure 4.22a) is dominated by cataclasite zones and altered host rock with zeolitisation.

In the altered host rock with zeolitisation, interstitial clay is present throughout the whole sample, turning the sample a yellowish/brown colour (in PPL) from its original fresh grey colour. Clay has also replaced pyroxenes and Fe-Ti oxides. Almost all of the feldspar grains are replaced

by zeolites, although it is interesting to note the larger feldspar phenocrysts have suffered zeolitisation only along cleavages and intergranular fractures. This suggests complete zeolitisation of feldspar is a function of size, and probably surface area to volume ratio, i.e. more fluid/time is required to completely replace a larger feldspar. Pyroxene and Fe-Ti oxide grains in the altered host rock contain fractures, and are found entrained along discrete slip surfaces within the altered host rock zone.

Within the cataclasite zone (Figure 4.23d), foliated cataclasites are set in a matrix of clay and/or zeolite and/or SiO_2-veins, made of chalcedony. Clasts within the cataclasite include rounded survivor clasts of altered host rock, containing zeolitised feldspars and pyroxenes altered to clay (Figure 4.24e). The cataclasite is also composed of entrained clasts of pyroxenes and Fe-Ti oxides.

There are three types of grain-size reduction that appear to form an evolution series in HBF2:

1. In-situ grain size reduction is common, where minerals have undergone brittle deformation along intragranular fractures but have not moved relative to surrounding grains.
2. Adjacent to shear fractures within the sample, grain-size reduction along fractures reduces the mineral to very fine-grained clasts (Figure 4.24g). Away from the shear vein, deformation in the mineral is accommodated by wing crack fractures along pre-existing intragranular fractures (Figure 4.24g). Further movement along the shear plane causes entrainment and rotation of the fractured mineral grains. Mineral fragments produced from this type of cataclasis are sub-angular and finely milled in places.
3. The more evolved cataclasite is composed of mixed, broken and sub-rounded clasts of pyroxenes and Fe-Ti oxides (Figure 4.24h). The

original positions and morphologies of these minerals are indiscernible, suggesting greater displacement along fractures where these types of cataclasites are found.

In addition to clays replacing minerals and forming the matrix of cataclasite, clays are also found filling and lining shear fractures within the fault rock and are often foliated (Figure 4.24f). In addition to clay filling fractures, zeolite minerals (thomsonite, natrolite), calcite and chalcedony also form mineral veins.

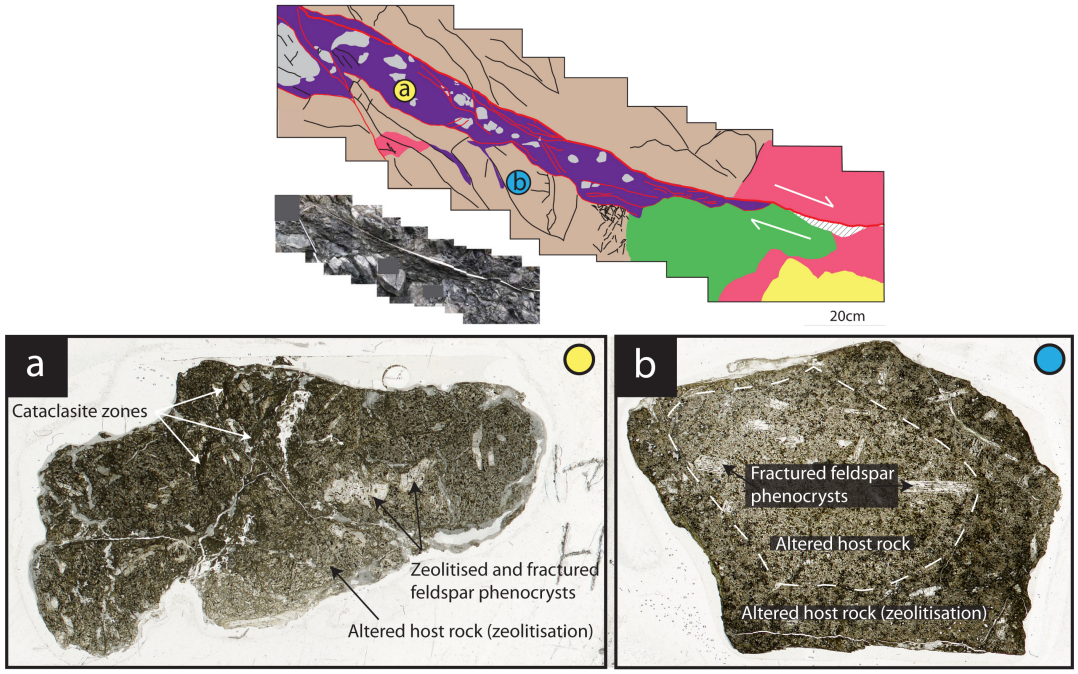

Figure 4.22: Location of samples studied from the HBF. Corresponding thin section images for each sample, with the relevant coloured dot next to thin section image. a) Yellow dot (HBF2)= cataclasite and altered host rock with zeolitisation. b) Blue dot = altered host rock and altered host rock with zeolitisation. The boundary of the altered host rock with zeolitisation is marked by the white dashed line.

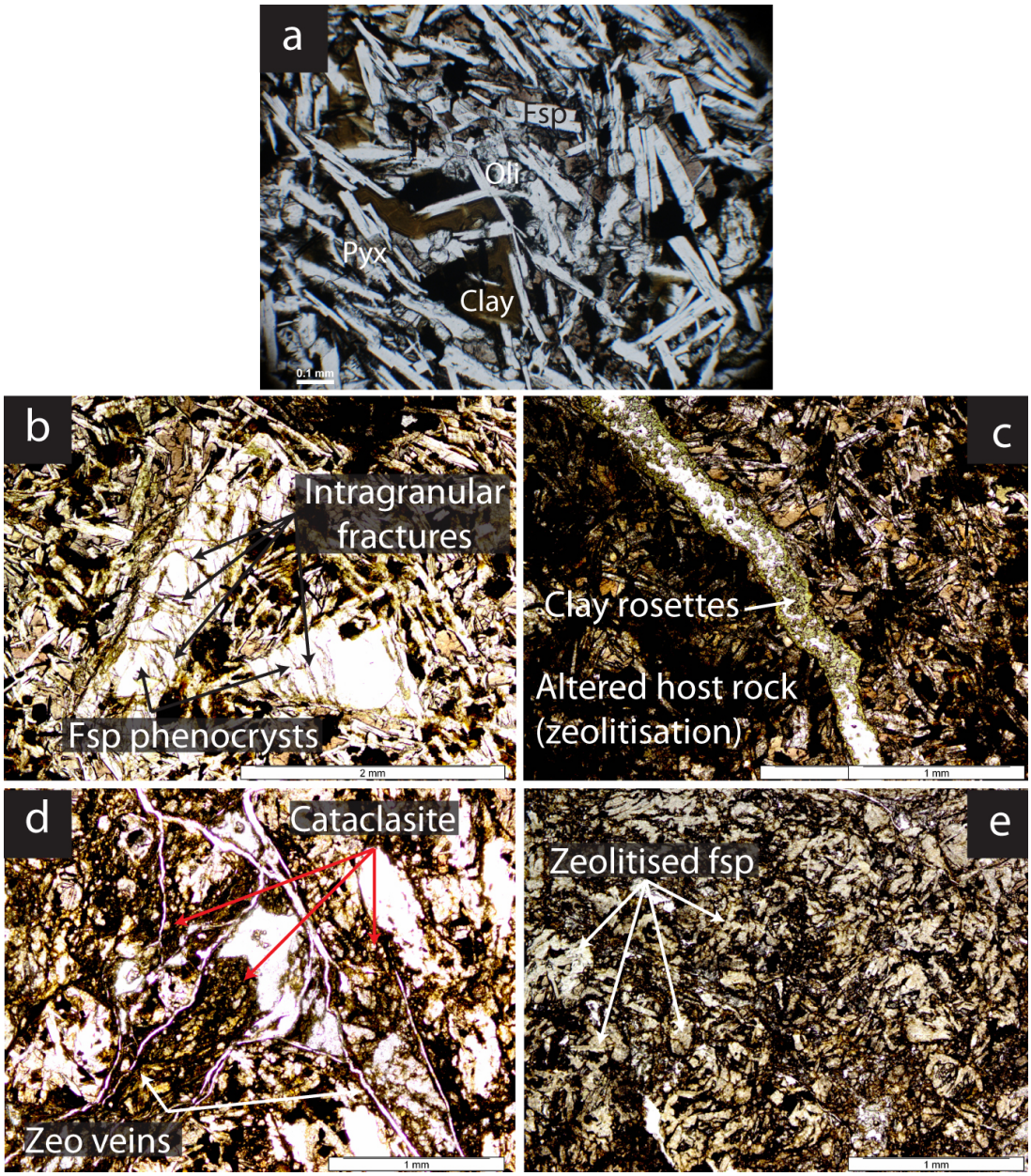

Figure 4.23: Petrographic microscope detail of HBF in PPL. a) Host rock for reference. b) Increased clay content (yellow/brown discolouration) and fracture density (within feldspar phenocrysts) in the altered host rock compared to host rock (HBF1). c) Zeolite and clay veins are also found in the altered host rock (HBF1). d) Cataclasite zones within the protocataclasite are clay-rich and cut by mineral veins (HBF2). e) Altered host rock with zeolitisation surrounding cataclasite zones is altered to clays, and feldspars are completely replaced by zeolites (HBF2).

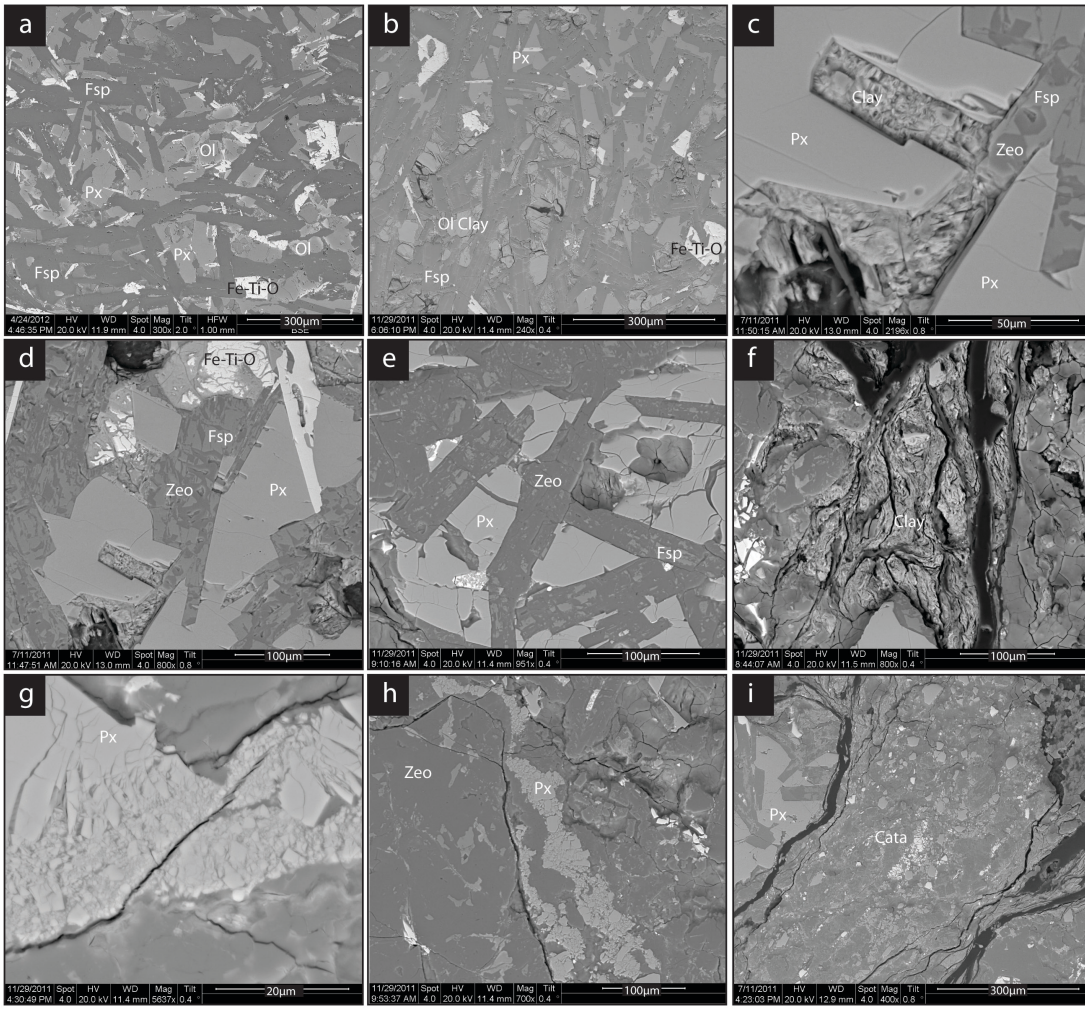

Figure 4.24: BSE images of HBF samples. a) Detail of host rock. b) Detail of altered host rock (HBF1). Note olivines have been replaced by clay. c) From HBF1, examples of host rock alteration. Feldspars are in the process of being replaced by clays, or zeolites (dark grey within feldspar laths). d) From sample edges of HBF1, note the increased replacement of feldspars by zeolites. e) Almost 100% replacement of feldspar laths by zeolites, within a survivor clast from the cataclasite in HBF2. f) Fractures within the fault rock (HBF2) are often lined by foliated clay, surrounding host rock clasts. g) In-situ brecciation of minerals, displaying wing-cracks at fracture tips, and grain-size reduction adjacent to the fracture (HBF2). h) Clasts of pyroxene broken into angular fragments, strung out along minor slip surfaces (HBF2). i) Cataclastic zone, containing clasts of pyroxenes and Fe-Ti oxides that have been fractured (HBF2), presumably in the steps seen in g) & h).

4.5.5. Self-juxtaposed microstructure interpretation

As descriptions of the samples in this study have shown, at the thin section scale, faulting within self-juxtaposed faults is accommodated by deformational and geochemical processes. With increasing displacement, the magnitude of these processes also increases, i.e. cataclasis is minimal in low displacement faults (e.g. VPF), but dominates deformational processes in medium to high displacement faults (e.g. HBF). A cartoon depicting the deformational and geochemical processes accommodating faulting as observed in thin section is shown in Figure 4.25.

Increased intragranular fracturing elevates porosity and permeability, enabling fluids to access mineral grain interiors, particularly feldspars and olivines. With increasing strain, fractures within minerals form and dilate, with this mode of deformation particularly seen in pyroxenes and Fe-Ti oxides. Fracturing of minerals creates a larger surface area for chemical reactions, which release elements and redistribute them in clays/zeolites. The increase in surface area/volume ratio of fractured pyroxenes and Fe-Ti oxides will enhance dissolution and make available more Fe and Mg ions. These may be responsible for the increase in volume of clay with displacement. The replacement of olivine phenocrysts by clay (and other phyllosilicates) early in the faulting history strengthens this hypothesis, with Fe, Mg and Si from the olivine being released into the aqueous fluid system.

Fracturing of the pyroxenes and Fe-Ti oxides in medium to high displacement faults leads to fine-grained cataclasite generated from these minerals along slip surfaces (e.g. Figure 4.24i, HBF). Cataclasite bands may be more susceptible to accommodating further displacement due to their high content of broken grains, which are liable to slip more easily than an unfaulted part of the rock (Fitz Gerald and Stunitz, 1993).

Olivine and feldspar are much more soluble than pyroxene and Fe-Ti oxides in crustal solutions. This makes them more susceptible to replacement by secondary minerals than to deformation by brittle processes. Feldspars, whilst also fractured, tend to be replaced by clays or zeolites from fracture walls, and along other intracrystalline discontinuities such as cleavage planes (e.g. Figure 4.19b). Replacement renders the former feldspar grain more ductile, meaning that fracturing and cataclasis of this mineral is unlikely to occur at the same intensity as pyroxene and Fe-Ti oxides.

Zeolitisation of feldspars is particularly important within medium to high displacement faults, where complete zeolitisation of feldspar is found throughout the PSZ, and in low displacements where complete zeolitisation of feldspar occurs adjacent to zeolite veins. With the zeolitisation of feldspars, it is possible that elements such as Ca and Na are released from feldspar and lost to the fluid, due to replacement of the feldspar by zeolite. Ca may reprecipitate as calcite, and together with Na form new zeolite minerals.

Secondary porosity created during faulting (i.e. fractures), is often found filled by zeolites and clays. The minerals filling secondary porosity (particularly zeolite) may have an increased permeability than the wall rocks, as later episodes of fluid flow within these secondary porosity fills was observed (e.g. pyrite mineralisation in the BNF).

With the presence of fluid, replacement of olivine and feldspars by clay early in fault history may weaken a developing fault further as a result of fluid-rock interactions, promoting slip. With increasing displacement, fluid-rock interactions will continue to replace minerals more susceptible to replacement (i.e. feldspars and olivines) and brittle deformation of pyroxenes and Fe-Ti oxides will occur to accommodate strain.

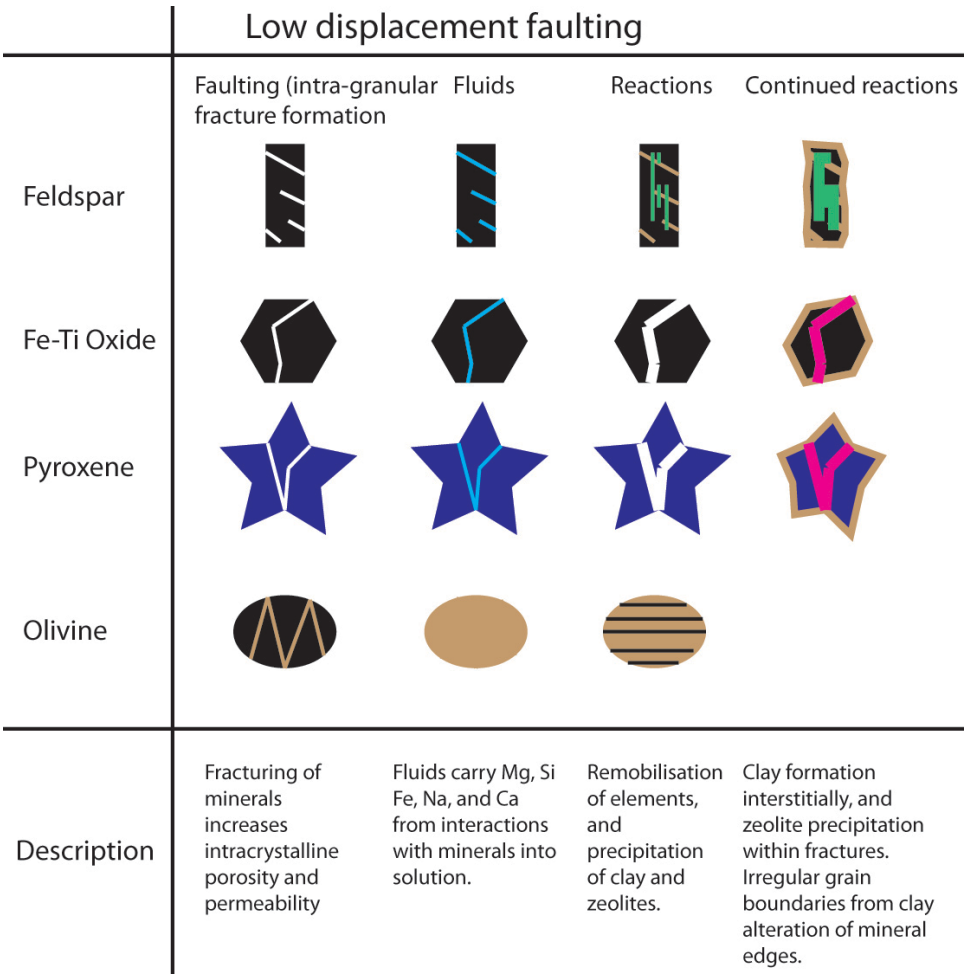

Figure 4.25: Conceptual cartoon of microstructural evolution within self-juxtaposed faults. Cartoons continue over the next page, in order of displacement. Key provided below.

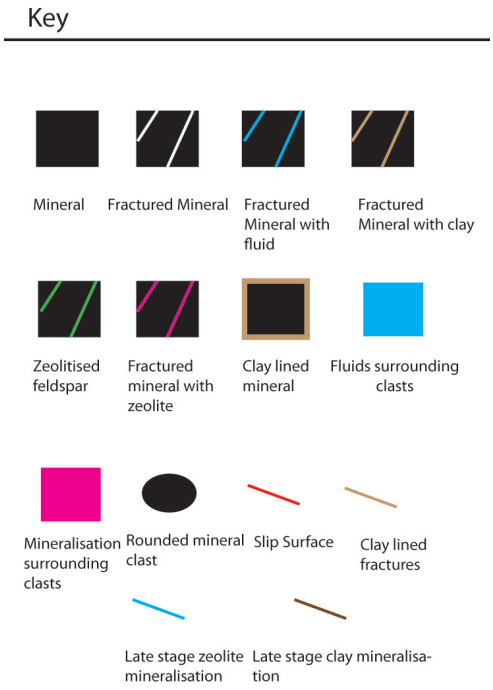

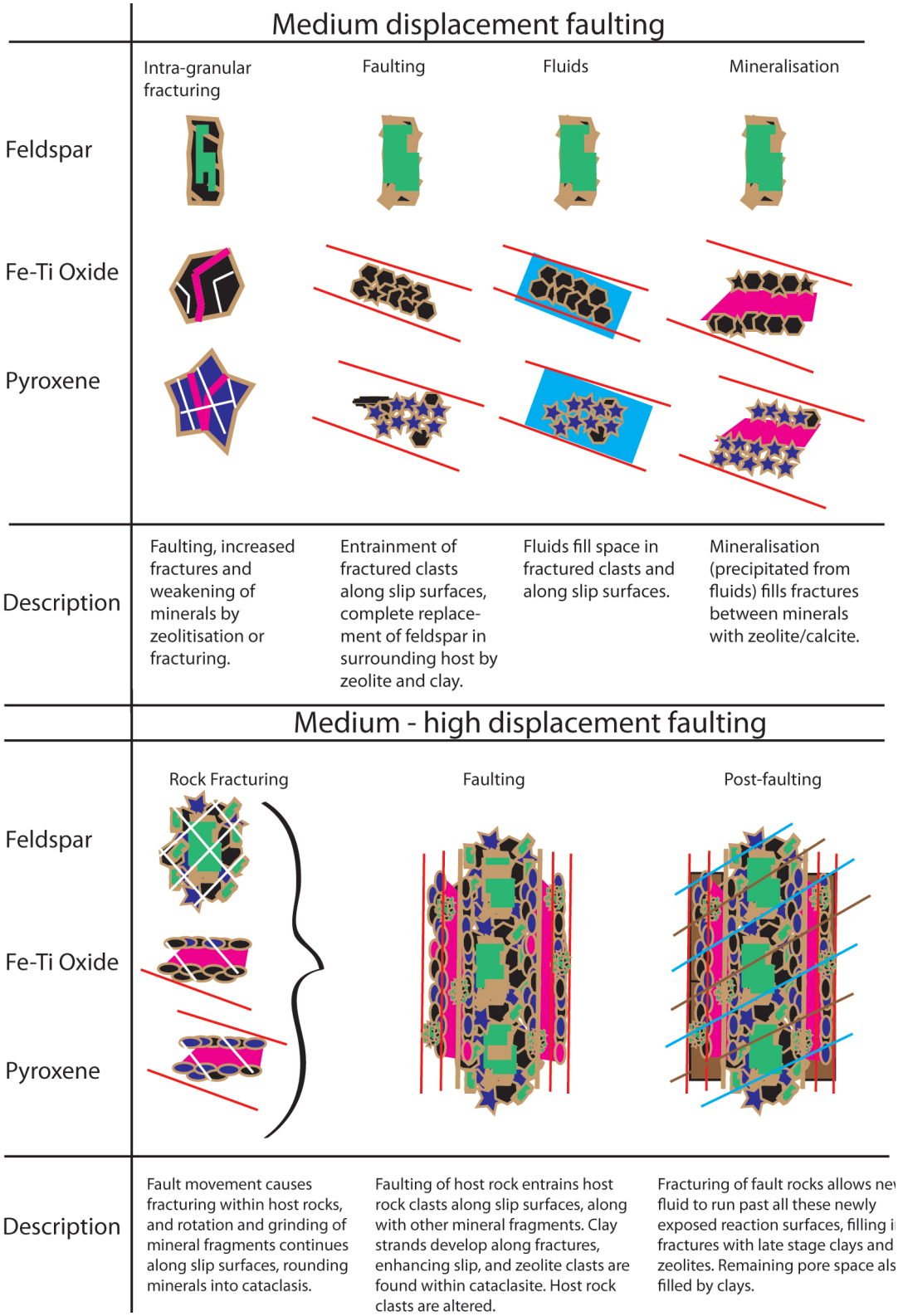
Medium displacement faulting
Intra-granular fracturing
Faulting
Fluids
Mineralisation
Feldspar
Fe-Ti Oxide
Pyroxene
Description
Faulting, increased fractures and weakening of minerals by zeolitisation or fracturing.
Entrainment of fractured clasts along slip surfaces, complete replace-ment of feldspar in surrounding host by zeolite and clay.
Fluids fill space in fractured clasts and along slip surfaces.
Mineralisation (precipitated from fluids) fills fractures between minerals with zeolite/calcite.
Medium - high displacement faulting
Rock Fracturing
Faulting
Post-faulting
Feldspar
Fe-Ti Oxide
Pyroxene
Description
Fault movement causes fracturing within host rocks, and rotation and grinding of mineral fragments continues along slip surfaces, rounding minerals into cataclasis.
Faulting of host rock entrains host rock clasts along slip surfaces, along with other mineral fragments. Clay strands develop along fractures, enhancing slip, and zeolite clasts are found within cataclasite. Host rock clasts are altered.
Fracturing of fault rocks allows ne
fluid to run past all these newly
exposed reaction surfaces, filling i
fractures with late stage clays and
zeolites. Remaining pore space als
filled by clays.

4.5.5.1. Self-juxtaposed discussion

The original mineralogy of the basalt must be considered in order to predict how the rock deforms at microscopic levels. Most of the host rocks are composed of relatively equigranular, euhedral and well-developed crystals of pyroxene and Fe-Ti oxides along with feldspars. These are the minerals that preferentially deform by intragranular fracturing and cataclasis. However, in the case of the footwall host rock in the BNF, only euhedral feldspars have formed, and the groundmass is dominated by very fine-grained pyroxenes Fe-Ti oxides. As this study has shown, feldspars tend to deform by alteration to clays and/or zeolitisation, but cataclasis of feldspars is unlikely. With the grain size of pyroxenes and Fe-Ti oxides also being so small in the footwall BNF host rock, they are unlikely to develop intragranular fractures and cataclasis to the same level as coarser grained basalts. In this scenario, the strongest part of the basalt (and the one more likely to deform by brittle processes) is the whole rock itself, and this is perhaps why, at microscopic levels, the PSS from the footwall from the BNF contains clasts of host rock, and not clasts of minerals.

This hypothesis would need to be tested with other types of basalt (i.e. feldspar-rich vs. feldspar-poor, fine-grained vs. coarse-grained etc) to determine what effect this could have on overall fault architecture. For example, if the basalt was very feldspar rich, it may only deform by shearing owing to prior weakening of the feldspar by zeolitisation and clay replacement, and cataclasis would be uncommon.

4.5.6. Self-juxtaposed summary

A brief summary of the key faulting-related features found within each fault are given below in Table 4.1.

Low displacement (e.g. VPF and VJF): fracturing of individual minerals, increasing surface area available for chemical reactions and increasing clay generation. Intragranular fractures facilitate grain size reduction, thus aiding early cataclasis. Partial zeolitisation of feldspar occurs. Partial replacement of olivine by clay.

Medium to high displacement (e.g. BNF and HBF): intragranular fracturing of mineral fragments, zeolitisation of feldspars, cataclasis, zeolite mineralisation and alteration to clay. Complete replacement of olivine by clay. Fractures within minerals form along shear veins, aiding entrainment and rotation. Cataclasite of mineral and host rock fragments, with zeolitisation of feldspars adjacent to fractures. Foliated clays along fractures. Formation of new zeolite minerals/calcite/Si-veins in fault-related fractures.

Table 4.1: Summary table of fault-related features at microscopic scales within the self-juxtaposed faults.

Fault	Intergranular fractures	Cataclasis	Foliated Cataclasite	Dissolution	Zeolitisation of feldspar	Clay replacement of feldspars	Zeolite Veins	Clay lined fractures	Interstitial Clay	Foliated Clay
VJF (18cm)	●			●	●	●	●	●	●	
VPF (28cm)	●			●	●	●	●	●	●	
BNF (1m)	●	●	●	●	●	●	●	●	●	●
HBF (>25m)	●	●	●	●	●	●	●	●	●	●
	Deformational Processes			Geochemical Processes						

4.6. Fault-related microstructures - non self-juxtaposed faults.

4.6.1. Hov Fault (HVF) – 1m displacement fault

HVF1: Altered basalt and zeolite veins

Sample HVF1 was taken from the altered basalt footwall of the Hov Fault. It is composed of altered basalt and zeolite veins (Figure 4.26a). The altered basalt contains partially zeolitised feldspars, and a minor increase in abundance of interstitial clay with respect to the host rock. Zeolite veins (identified as heulandite) fill the fractures in the sample, along with clay rafts (Figure 4.27d).

HVF2: Mineralised principal slip surface

Sample HVF2 is composed of the mineralised principal slip surface and altered basalt in the fault wall. The mineralised slip surface (Figure 4.26b) is itself composed of two parts – immediately adjacent to the PSS is a zone of altered basalt clasts floating in a zeolite matrix, and further away from the PSS (at the margin of the thin section), is a zone dominated by crack-seal textures and calcite-filled shear veins along the slip surface.

Heulandite and calcite crystals form the matrix to the zone containing floating basalt clasts (Figure 4.27b). PSS parallel mineral veins are present throughout this zone, and some contain a component of shear. This zone contains rounded clasts of altered basalt in a thin breccia band (1-2cm thick), where zeolite minerals line each clast, and radiate out from them. This relationship suggests that brecciation of the wall rocks occurred first, creating pore space, which was rapidly filled by fluids, from which calcite and zeolites crystallized.

In the crack-seal texture zone, host rock clasts are present as long elongated rafts (parallel to the slip direction) surrounded by zeolite veins in crack seal morphology. Occasional breccia clasts are still found on the

edges of these elongated rafts, suggesting minor slip surfaces were present along the edges of the elongated clasts.

Other evidence for minor slip surfaces found within the crack-seal texture zone is apparent by the presence of a zeolite gouge (Figure 4.27e). The gouge is fine-grained (<0.1mm) and foliated (parallel to slip direction). The gouge is composed of elongated, rounded clasts of zeolite minerals, which are set within a fine-grained crushed zeolite matrix. Feldspars within the host rock breccia clasts are zeolitised (Figure 4.27c). Zeolitisation is also seen within the wall rock immediately adjacent to the slip surface.

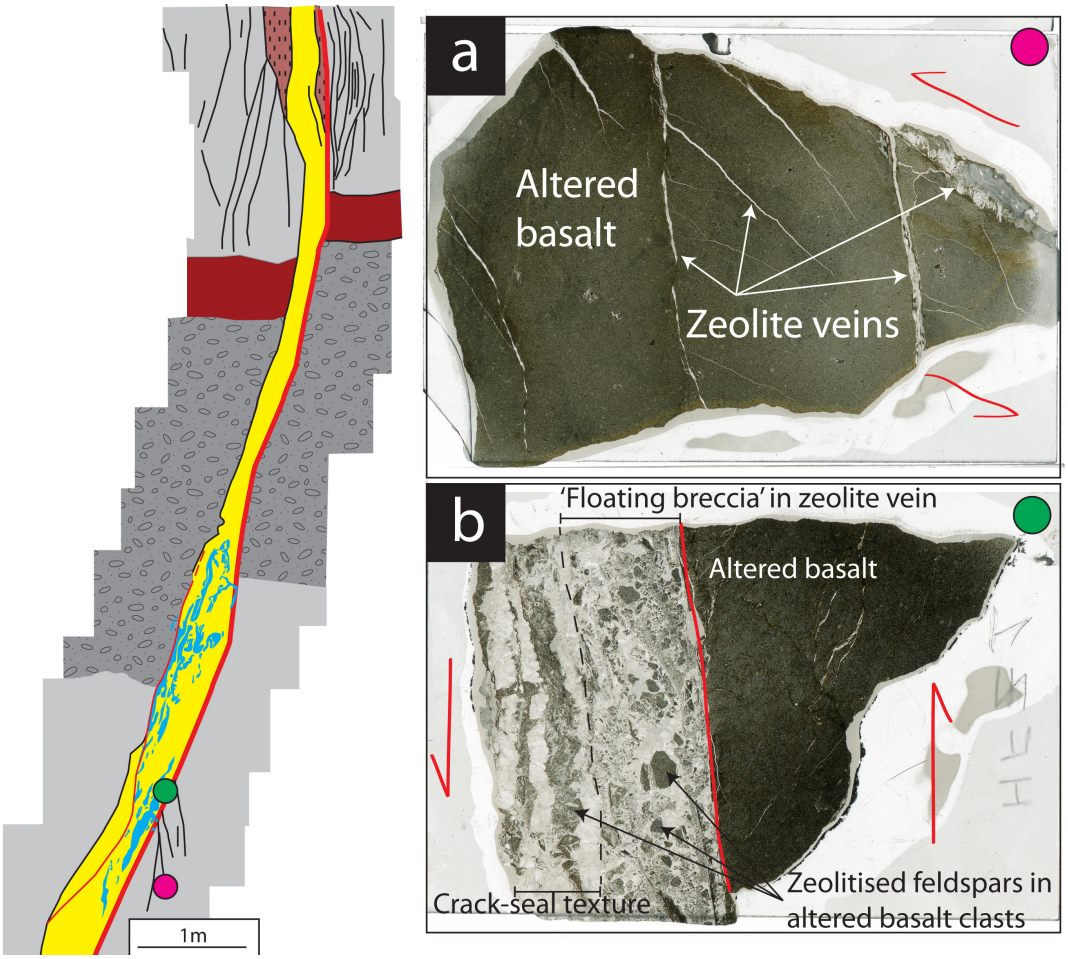

Figure 4.26: Location of samples studied from the HVF. Coloured dots on fault map represent locations of samples. Corresponding thin section images of each sample are given next to coloured dots. Fault movement relative to samples is shown as red arrows. a) Pink dot = HVF1 - altered footwall. b) Green dot = HVF2 - mineralised slip surface, PSS marked as red line.

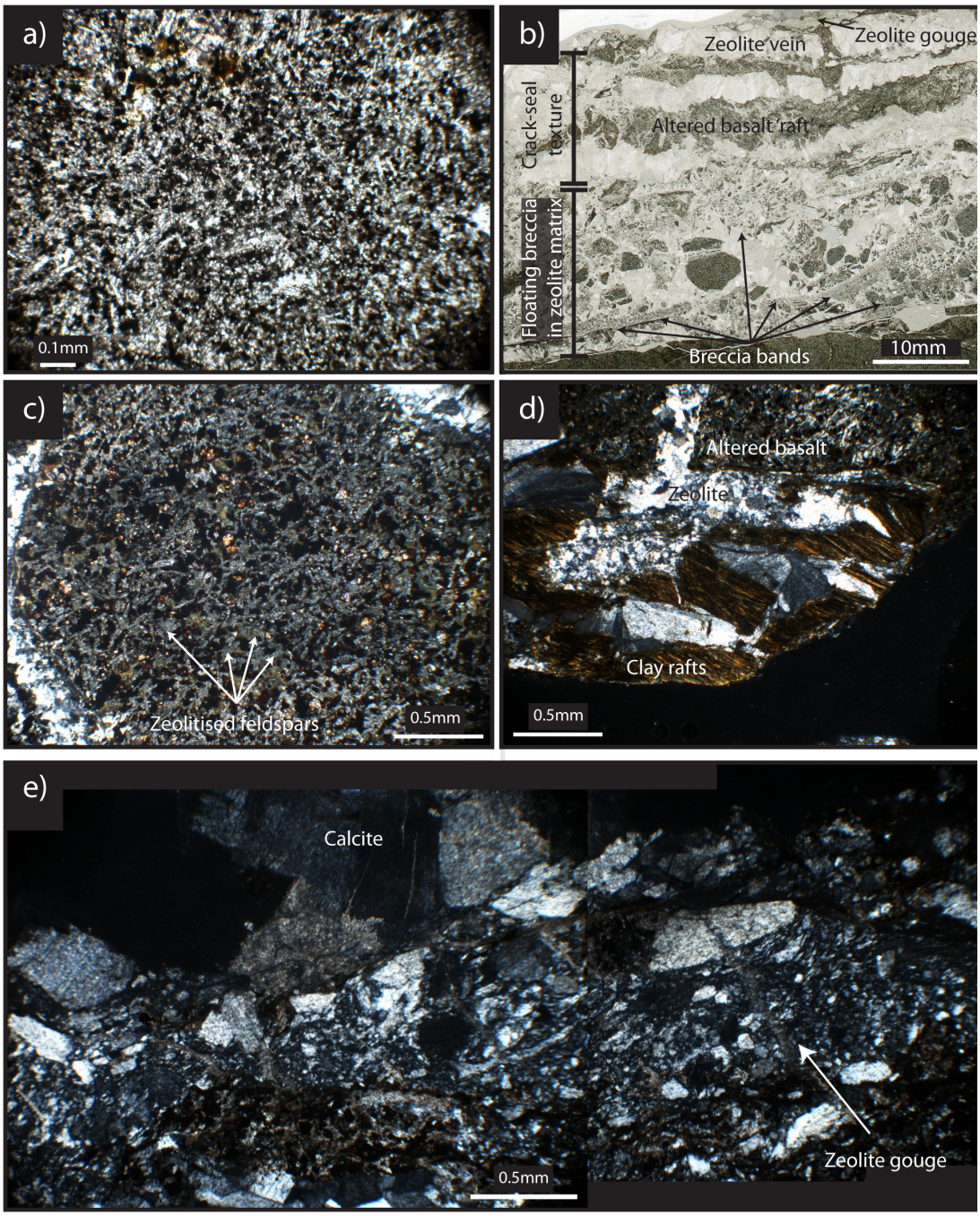

Figure 4.27: Petrographic microscope images of HVF. a) Host rock for reference (PPL). b) HVF2, showing mineralised principal slip surface. The two zones referred to in the text are labelled. c) Altered basalt clast within zeolite veins, showing extensive replacement of feldspar by zeolite (XP). d) HVF1, clay raft making up veins (XP). e) Photomontage of zeolite gouge, location highlighted in b).

4.6.2. Sumba Fault Zone (SFZ) – 5m total displacement

Three samples were taken from the SFZ (Figure 4.28). One sample (SFZ1) contains the PSS of the self-juxtaposed subsidiary fault, and another (SFZ3) from the PSS of the volcanic conglomerate/basalt-juxtaposed master fault. The basalt between the two faults was also sampled (SFZ2).

SFZ1: PSS from subsidiary fault

SFZ1 is composed of shear veins of zeolite and calcite, crosscutting clay-rich altered basalt host rock. The mineral veins contain rounded, altered host rock clasts (Figure 4.29d). Interstitial clay content adjacent to the shear veins increases dramatically with respect to the host rock, obscuring all but the feldspar phenocrysts (Figure 4.29c). The clay is brownish/yellow in PPL.

SFZ2: Altered basalt between faults

The sample taken from between the two faults of the SFZ is more clay-rich than the host rock (Figure 4.28b). Feldspars have been partially replaced by clay and zeolites (Figure 4.29b). Dissolution of minerals has also occurred.

SFZ3: PSS from master fault

Sample SFZ3 is composed of three main components: altered basalt, crack-seal textures, and zeolite veins. The altered basalt is similar to that described in SFZ2. The slip surface is mineralised in a crack-seal style, (Figure 4.29e), with wall-rock parallel rafts of altered basalt separated from their original location by zeolite mineral veins. Basalt clasts found within this slip surface contain zeolitised feldspars. Grain size has been reduced along the wall rocks. Zeolite-derived gouge has formed within the coarser zeolite veins (Figure 4.29f). The gouge is composed of a matrix of finely milled zeolite fibres, with clasts of blocky zeolite crystals. The gouge is finest grained at the edges of remnant zeolite clasts.

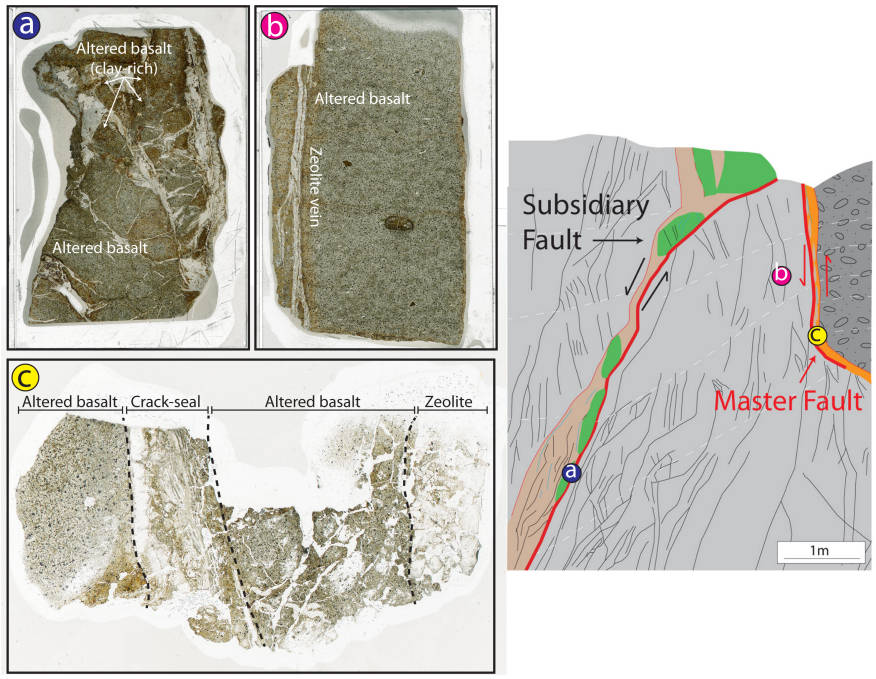

Figure 4.28: Locations of samples from the SFZ, overlain on the fault map of SFZ. a) Blue dot = PSS in basalt (SFZ1). b) Purple dot = fractured sample between the two faults (SFZ2). c) Yellow dot = PSS in basalt/conglomerate fault (SFZ3).

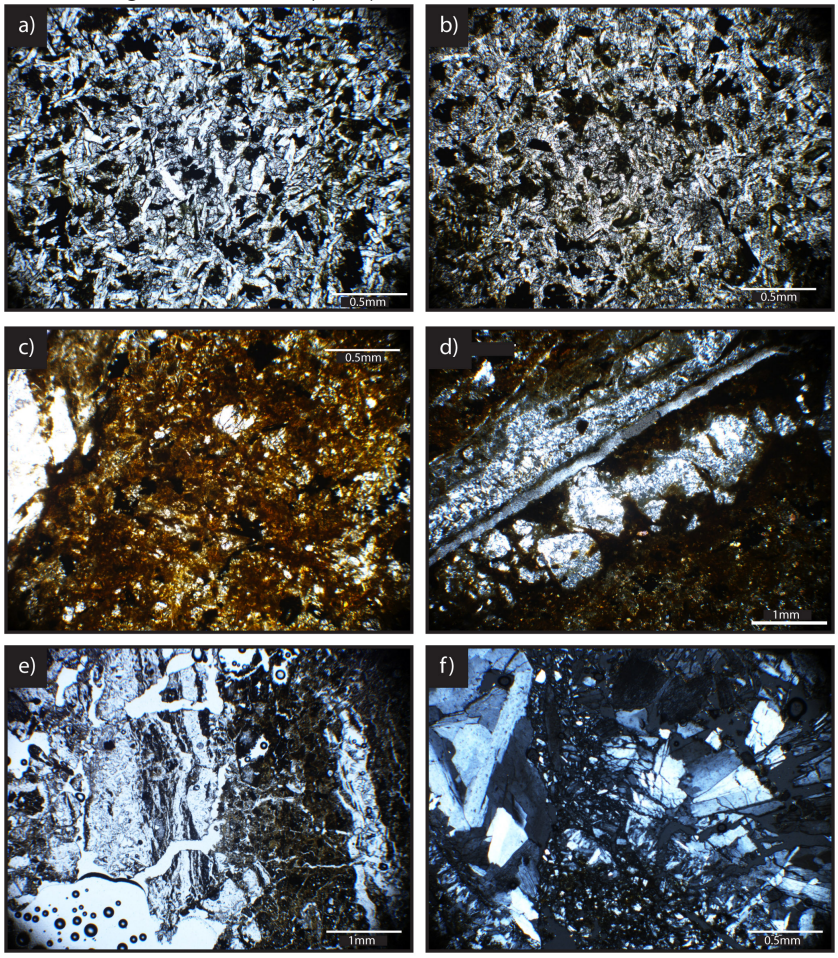

Figure 4.29: (*Previous page*) Petrographic microscope images from SFZ. a) Host rock (PPL). b) Altered host rock (SFZ2) between faults (XP). c) Clay-rich altered basalt from SFZ1. Note sharp increase of clay with respect to host rock (PPL). d) Zeolite veins and clasts surrounding host rock in SFZ1 (XP). e) Crack seal morphologies in SFZ3 (PPL). f) Zeolite derived gouge from SFZ3 (XP).

4.6.3. I Botni Fault (IBF) – 5m displacement

IBF1: Tuff gouge and altered basalt clast within PSZ

Sample IBF1 (Figure 4.30a) was taken from a basalt host rock clast surrounded by tuff gouge, from within the PSZ. The sample contains altered host rock clasts of basalt within a tuff-derived gouge (Figure 4.31a,b), with crosscutting zeolite veins.

Feldspars in the altered host rock clasts have been zeolitised (Figure 4.31a). In some areas, sub-angular clasts of breccia are contained within clasts (Figure 4.31b), demonstrating multiple stages of deformation. The matrix to these sub-angular clasts is altered basalt, which is richer in interstitial clay in comparison to the rest of the altered basalt encountered within the sample.

The tuff gouge is composed of very fine-grained (<0.1mm), angular tuff and zeolite fragments (Figure 4.31c). Clasts of altered basalt 1mm across (Figure 4.31d) occur within the tuff gouge, the feldspars of which are also zeolitised. Zeolite (heulandite) and calcite fills fractures, and crosscuts altered basalt clasts and tuff gouge.

IBF2: PSS cataclasite and breccia

The PSS was sampled (Figure 4.30b), and it contains cataclasite, which makes up the PSS. The sample is also composed of an altered basalt clast-rich breccia.

The cataclasite is fine-grained and composed of shattered mineral clasts (Figure 4.31e), less than 0.25mm in size. The matrix to the cataclasite is

clay-rich. Within the cataclasite in the sample are large clasts of altered basalt, which contain zeolitised feldspars.

In the breccia immediately adjacent to the cataclasite, altered basalt clasts (with zeolitised feldspars) are surrounded by fine-grained cataclasites, and clay minerals occur in both the clasts and matrix (Figure 4.31f). Clasts within the breccia are <5mm in size (Figure 4.31h), and are set within a matrix of cataclasite (dark areas within Figure 4.31h) or clay-rich altered basalt.

Within the zeolite veins that pervade the sample are clasts of cataclasite (Figure 4.31g), suggesting that the cataclasite had formed prior to mineralisation. In other areas within the fault, breccia clasts are surrounded by zeolite, and have a zeolite fringe, suggesting that rapid mineralisation took place following faulting. These relationships shows that mineralisation of the fault zone occurred after faulting.

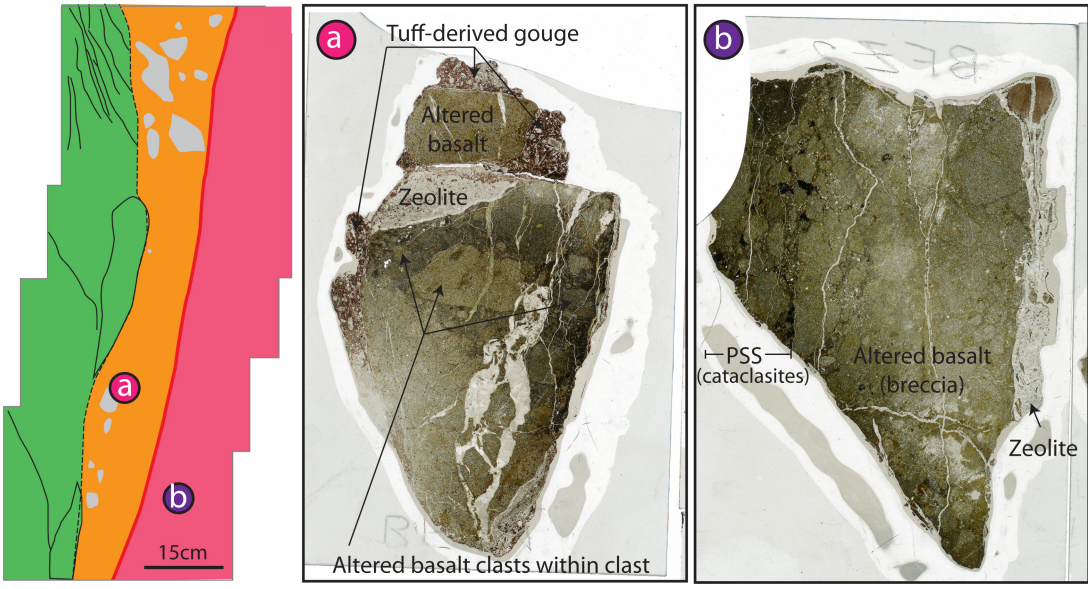

Figure 4.30: Location of samples from within the IBF. Coloured dots represent locations of where samples were taken, with the pink dot = tuff smear, and the purple dot = basalt slip surface. Corresponding thin section images adjacent to coloured dots.

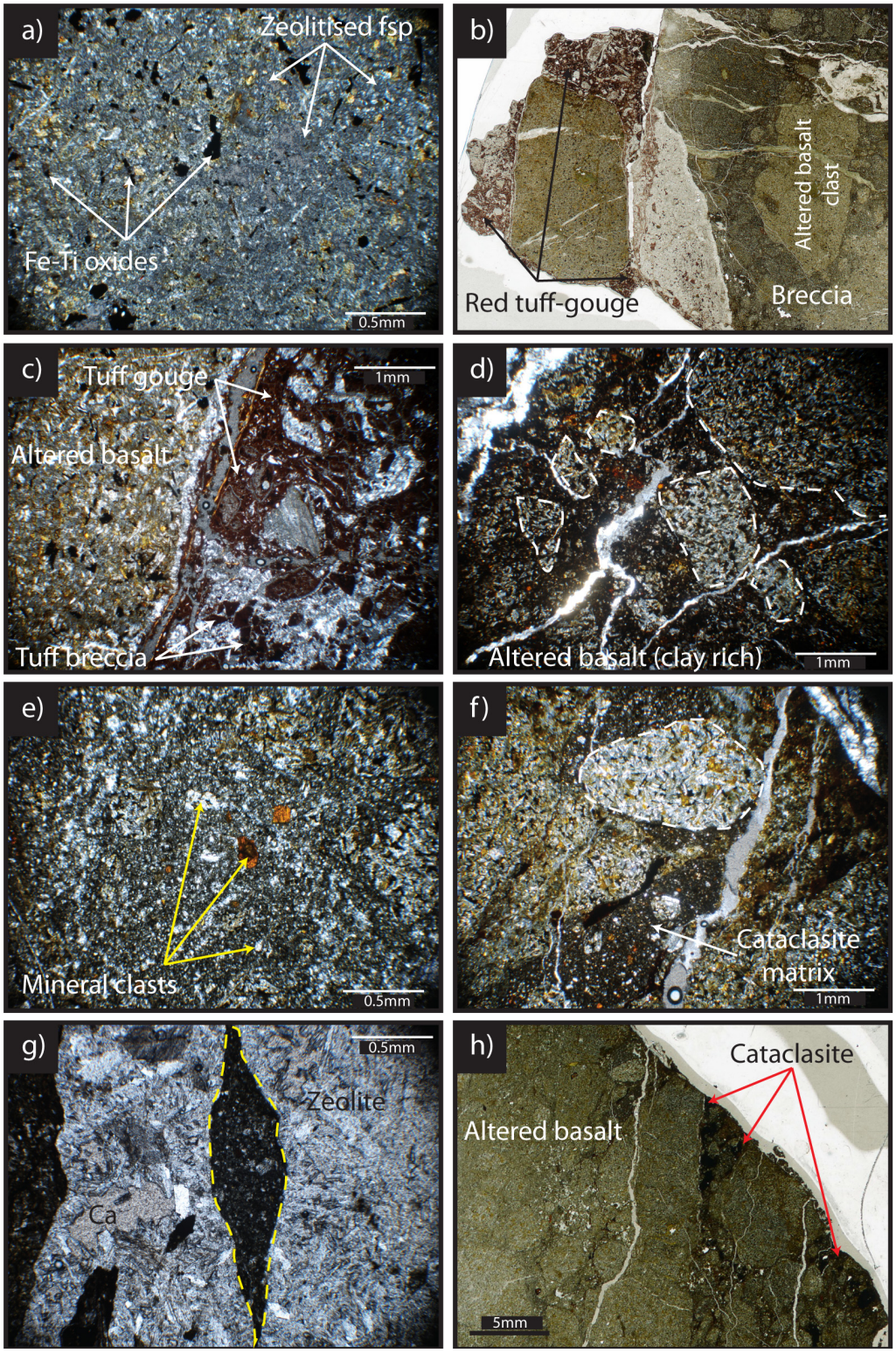

Figure 4.31: Petrographic microscope images from IBF. a) Altered basalt clast in fault rock lens (IBF1) from tuff smear. Note lack of internal structure in feldspars (XP). b) Thin section view of fault rock in tuff smear (IBF1). Note red tuff gouge and breccia. c) Detail of red tuff gouge from IBF1 (XP). d) Altered basalt clasts (outlined) within breccia clast (IBF1), set in a matrix of clay-altered basalt (PPL). e) Cataclasite from PSS (IBF2). f) Altered basalt clasts (outlined) within the breccia of IBF2 have a cataclasite matrix (PPL). g) Zeolite vein with clast of cataclasite (outlined) (IBF2, XP). h) Thin section view of slip surface (IBF2). Note altered basalt clasts and darker cataclasites.

4.6.4. Lawther Fault (LWF) - >10m displacement

Four samples were taken from the LWF – two from 0.5m away from the fault in both walls (i.e. basalt and peperite), one from a black gouge filled fracture, and the remainder from the altered basalt zone of the PSS.

LWF1: Altered peperite with minor slip surfaces, footwall

Sample LWF1 is composed of two main parts: altered peperite, and minor slip surfaces that cut it (Figure 4.32a).

In the altered peperite, interstitial clay content increases with respect to the peperite host rock, turning the rock (in PPL) to a stronger yellow from an original brownish/yellow colour (Figure 4.33b). Clasts of basalt within the peperite are preserved, as are bulbous margins (an original feature of the peperite host rock).

The peperite surrounding the slip surfaces within the sample is further altered, with an increase in clay content found, particularly filling pore space. The basalt component of the peperite is completely replaced by clay here, with only a few clay pseudomorphs of feldspar being recognised (Figure 4.34c). The sedimentary component of the peperite was very clay-rich in the host rock, and remains so here. The minor slip surfaces are branching in nature, cross-cutting the altered peperite (Figure 4.33c). Along the slip surfaces are thin (0.5mm) clay gouges and chalcedony veins. Where the slip surfaces branch, the altered peperite between them is deformed into a foliated cataclasite (Figure 4.33c). The clasts within these cataclasites are rounded, and set in a very fine-grained clay-rich matrix.

LWF2: Altered basalt, hanging wall

LWF2 is composed of altered basalt (Figure 4.32b). Interstitial clay content within the altered basalt has increased with respect to the original host rock (Figure 4.33e), along with evidence for dissolution of minerals (Fe-Ti

oxides). Feldspars are completely pseudomorphed by clay minerals (Figure 4.34b), and the groundmass is also completely replaced by clay minerals.

LWF3: Black gouge filled fracture in hanging wall

The black gouge filled fracture contains chalcedony, calcite and dendritic manganese deposits (Figure 4.32c). The fracture is partially mineralised by calcite and chalcedony. The black gouges identified in the field are actually dendritic manganese deposits, which partially fill pore space within the mineralised fracture (Figure 4.34d). It is therefore likely that these dendritic deposits formed after faulting, as their delicate branching is preserved, and it fills the pore space left by calcite and chalcedony, the latter of which is sealing fault gouge in sample LWF4.

LWF4: PSS and altered basalt fault rock

Sample LWF4 (Figure 4.32d) is composed of four distinct zones – the PSS is composed of clay-rich gouge, and chalcedony veins sealing gouge. Cataclasite with chalcedony veins and clay-rich altered basalt compose the remainder of the sample (Figure 4.34f).

The clay-rich nature of the zones composing the PSS renders the fault rock a distinct yellow/green colour (Figure 4.33f). The gouge is composed of very fine-grained clay (<10μm), and is foliated. At the edge of the thin section, a Fe-rich clay-rich gouge layer is found, below which lies a foliated clay gouge with rounded clay clasts.

The chalcedony veins sealing the gouge lie below the clay-rich gouge zone in the thin section (Figure 4.34e). The PSS is itself composed of foliated cataclasites and clay gouges (Figure 4.33g). Riedel shears off the PSS are highlighted by highly comminuted altered basalt and chalcedony veins (Figure 4.33g). The chalcedony forms a dense network of thin (<0.1mm) veins, which fill the slip surfaces and pore space within the clay gouge, suggesting the pore space was filled after faulting. Clasts of quartz within the foliated cataclasites are found in riedel shear orientations.

Below these zones of intense mechanical deformation is a ~500µm wide zone of cataclasite with chalcedony veins, which is composed of comminuted clasts of Fe-Ti oxides set in a very fine-grained clay-rich matrix. Other minerals have been replaced by clay to an extent that their original identity is difficult to determine.

At the base of the thin section are extensive clay domains, which are large areas of clay sheets (<2cm thick). This clay fills the matrix to a breccia composed of altered basalt clasts. The host rock clasts are also very clay-rich, and occasional clay pseudomorphs of feldspar laths are visible. Also interspersed throughout this zone are chalcedony veins, which fill pore space and fractures. Occasionally, pore space within this sample is partially filled by dendritic manganese deposits, a result of late groundwater precipitation.

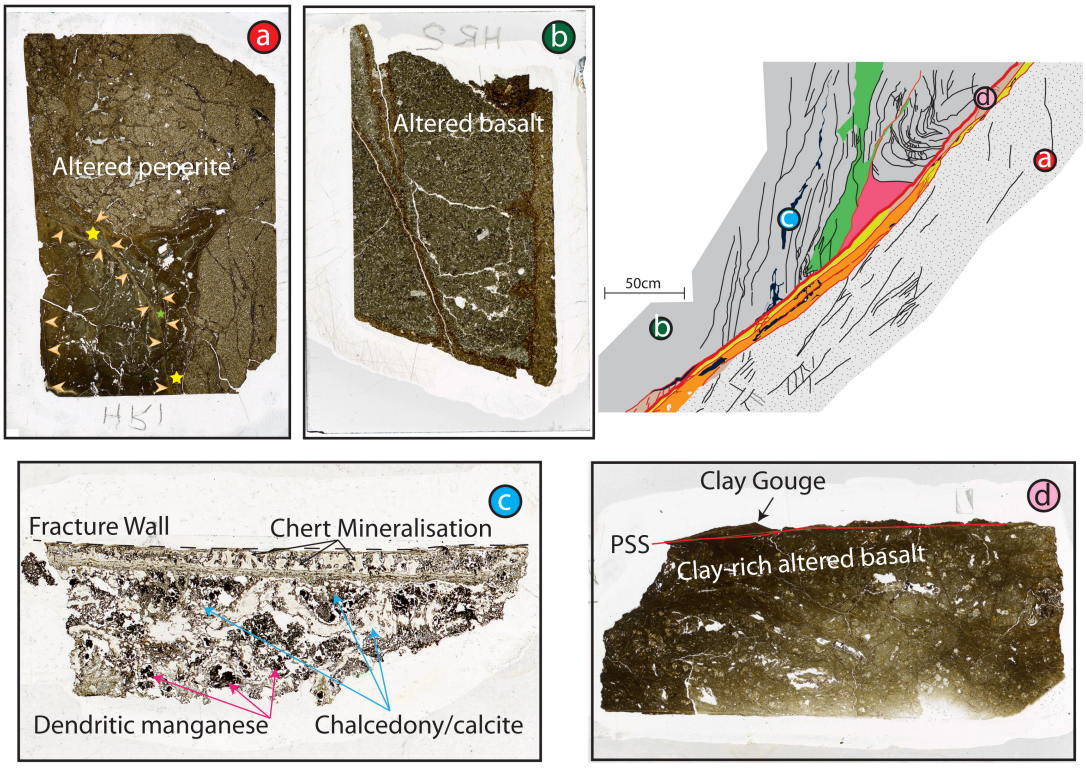

Figure 4.32: Locations of samples taken from the LWF. Sample locations are marked on map. a) Altered peperite sample (LWF1, red dot) with minor slip surfaces marked by orange arrows, cataclasite by yellow stars, and gouge by green star. b) Green dot = altered basalt sample (LWF2). Fractures are sample preparation derived. c) Blue dot = black gouge filled fracture (LWF3), with mineralisation labelled gouge and mineralised fracture. d) Pink dot = PSS and altered basalt. PSS is marked by red line.

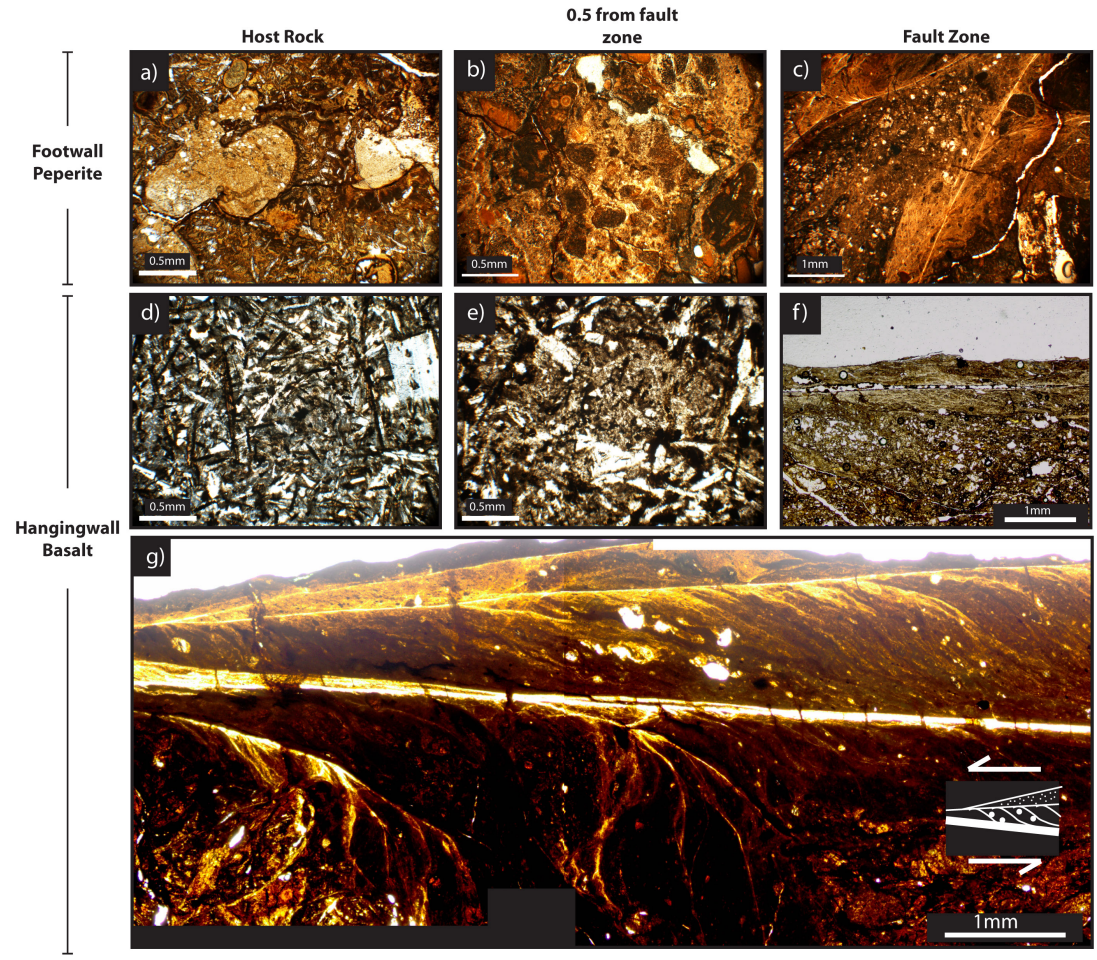

Figure 4.33: Petrographic microscope images of LWF. a) Host rock peperite. b) Peperite 0.5m from fault zone. Note stronger yellow colouration. c) Peperite in fault zone. Grain size reduction, development of minor slip surfaces, and alignment of clays. d) Host rock basalt. e) Altered basalt 0.5m from fault, note increased clay replacement in groundmass compared to host rock. f) Basalt in fault zone. Note grain size reduction and discolouration. g) PSS of LWF, adjacent to basalt HW. Note slip surfaces and riedel shears branching from them, gouge development and grain entrainment and reduction. Shear sense is given on the mini cartoon in the figure (normal sense of shear).

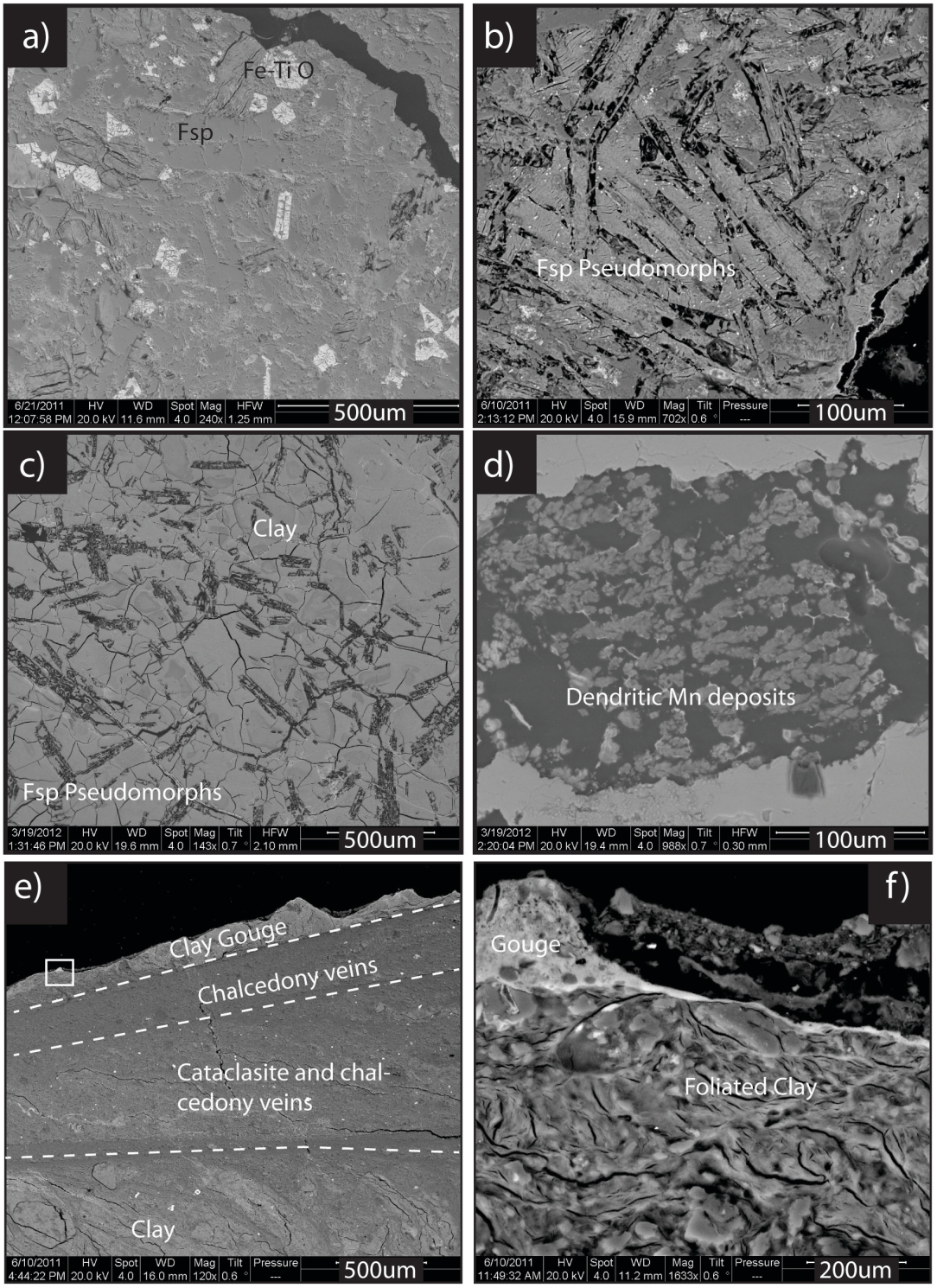

Figure 4.34: BSE images of LWF. a) Host rock for reference. b) 50cm from fault plane, note clay pseudomorphs of feldspars. c) Igneous clast within peperite completely replaced by clays. d) Dendritic manganese deposits within a fracture adjacent to mineral veins. e) Slip surface detail of LWF4, white dashed lines represent mineralised Y-shears. White box shows the location of f). Zones discussed in the text are labelled. f) Detail of clay gouge, where foliated clay gouge is composed of a matrix of clay with clay clasts.

4.6.5. Talisker Bay Fault (TBF) – 18m fault strand

TBF1: Altered basalt (footwall)

TBF1 was sampled 25cm from the fault in the altered footwall (Figure 4.35a). The altered basalt mineralogy in this sample is similar to that of the host rock, but with an increase in interstitial clay (Figure 4.37b). There is also evidence for partial dissolution of minerals, and olivine phenocrysts (relatively fresh in the host rock) have been completely replaced by clays, and the feldspars have been replaced by clay in their cores (Figure 4.38b).

TBF2: Cataclasite from PSZ

The cataclasite was sampled from within the PSZ (Figure 4.35b). The thin section contains fine-grained, foliated cataclasites (Figure 4.36a), with rounded clasts of altered basalt and mineral clasts set within a fine-grained matrix.

Rounded clasts of altered basalt (Figure 4.36b) with pyroxenes and zeolitised feldspars occur in the cataclasite. The cataclasite is also composed of clasts of sub-rounded pyroxenes and Fe-Ti oxides, with a matrix of clay and zeolite (Figure 4.39c). Zeolite needles extend into the altered basalt clasts in places, suggesting they formed after cataclasis of the rock occurred. There are also clasts of zeolite within the cataclasite, demonstrating mineralisation of the fault prior to cataclasis.

Figure 4.39a shows the cataclasite matrix surrounding altered basalt clasts. This matrix is composed of extremely fine-grained mineral clasts, clay and zeolite fibres. At the margins of larger altered basalt clasts (i.e. ~1cm in size), very fine-grained cataclasites are found (Figure 4.39b). Also at the margins of these clasts are zeolitised feldspars, but with increasing distance from the clast edge the feldspars are replaced by clay. This gradation in alteration suggests that zeolite-bearing fluids alter the margin of the clast first, before continuing to the centre of the clast.

Weathering-related iron staining highlights riedel shears within the cataclasite. This iron staining has also infiltrated the matrix of the cataclasite in places (Figure 4.36d). The foliated nature of the cataclasite is also highlighted by entrainment of mineral clasts (Figure 4.39d), with Y-shears being particularly well distinguished (Figure 4.36c). Running parallel to the Y-shears are small, light green flakes of chlorite.

As well as forming the matrix to the cataclasite and occurring as mineral clasts within the cataclasite, zeolites form veins throughout the sample. These zeolites are natrolite and chabazite and crosscut the host rock clasts and the cataclasite, suggesting that cementation of the cataclasite was prior to zeolite veining.

TBF3: Altered basalt lens within PSZ

Sample TBF3 was taken from the altered basalt lenses within the PSZ (Figure 4.35c). This altered basalt is rich in interstitial clay (Figure 4.37d) when compared with the host rock, contains localised bands of cataclasite, and is crosscut by zeolite veins.

Within the altered basalt, feldspar grains have been altered by one of four types of reaction: a) partial/complete zeolitisation of feldspars; b) replacement by clay along intragranular fractures, and by an irregular low mean atomic number zeolite mineral along cleavage planes (Figure 4.39j); c) a more extreme example of b), where very little feldspar has survived replacement by zeolites and clays along intragranular fractures (Figure 4.39i); and d), complete replacement of feldspar by clays. These different feldspar replacement types are irregularly distributed throughout the rock, and so presumably represent a temporal evolution of geochemical reactions.

At the edge of the sample cataclasite is found (Figure 4.39k), composed of clasts of zeolite, altered basalt, Fe-Ti oxides and pyroxenes, with a matrix of clay and zeolite (as found in sample TBF2).

Multiple generations of zeolite veins (at least three) crosscut the sample. In these veins, a complex history of clay and zeolite relations can be observed. In Figure 4.39l, clays are found to be replacing zeolite veins, suggesting clay formation after zeolite veining. As the zeolite veins crosscut the fault rock, this suggests that clay replacement of zeolite must be a very late stage process. However, later generations of euhedral zeolites are also found growing in pore space within clay-rich areas (Figure 4.39m). This suggests that these particular clay and zeolite formations occurred after cataclasis of the rock, but formed at different times following cataclasis in different parts of the sample.

Foliated clays along fractures also occur within the sample, and contain rounded clasts of mineral fragments, set within a clay matrix (Figure 4.39n).

TBF4: PSS and altered basalt

The sample taken from the PSS contains the heavily deformed slip surface and altered basalt clasts, surrounded by zeolite minerals (Figure 4.35d).

The altered basalt contains a much greater volume of brownish/yellow clays in PPL (Figure 4.37c), relative to the host rock. Fe-Ti oxides can still be identified, but laths of feldspar and detail of the pyroxene grains are lost. Clasts of altered basalt contain pyroxenes partially replaced by clay, as well as feldspars replaced by both zeolite and clay (Figure 4.39e).

At the base of sample is the PSS, dominated by foliated cataclasite (Figure 4.39f). The foliated cataclasite is largely composed of entrained mineral clasts of pyroxene and Fe-Ti oxides (Figure 4.39h), and sigmoidal clasts of broken Fe-Ti oxides are also found. The cataclasite matrix is clay-rich.

Zeolite minerals (identified as chabazite and thomsonite from their compositions) crosscut the host rock. High magnification images of the zeolite veins (Figure 4.39g) reveals three generations of zeolites, namely a core of natrolite that is cross-cut or surrounded by chabazite. Within pore space of these zeolites, equant crystals of an unidentified zeolite have

grown, suggesting that multiple phases of fluids flowed along the slip surface.

TBF5: Mineralised and altered basalt (hanging wall)

The sample taken from the altered hanging wall contains altered basalt cut by mineral veins (Figure 4.35e).

The altered basalt has a greater abundance of clay (Figure 4.37e) than the host rock, though not to the same extent as was found within the altered basalt in TBF4 and TBF3. Throughout the sample, feldspars have been partially zeolitised, within grain cores and along fracture walls (Figure 4.38d), and replaced by clay along mineral cleavages (Figure 4.38c). Feldspars have also been almost completely zeolitised adjacent to zeolite veins that crosscut the rock (Figure 4.38e). The intensity of zeolitisation varies irregularly with distance from the zeolite veins. Where zeolitisation decreases, clay alteration of feldspars becomes dominant. Clay pseudomorphs of olivine also occur, and partial replacement of pyroxene by clay is noted.

Within this sample are more highly altered ‘clasts’ of basalt (Figure 4.37f), although the ‘clasts’ are unbroken. They are recognised by localised zones of more intense alteration to clay and as the flow orientation of the feldspars remains constant between ‘clasts’, they have not been rotated relative to each other. The altered basalt surrounding these ‘clasts’ contains zeolitised feldspars, which are absent in the ‘clasts’.

Clays and zeolites fill fractures in the sample. In the clay-filled fractures, new growths of zeolite are present within pores in the clay (Figure 4.38f). At the margins of the zeolite veins, zeolite-derived breccias are present (Figure 4.38g). As in previous samples, multiple generations of zeolite minerals crosscut the sample, with the same zeolite minerals identified (natrolite, thomsonite and chabazite).

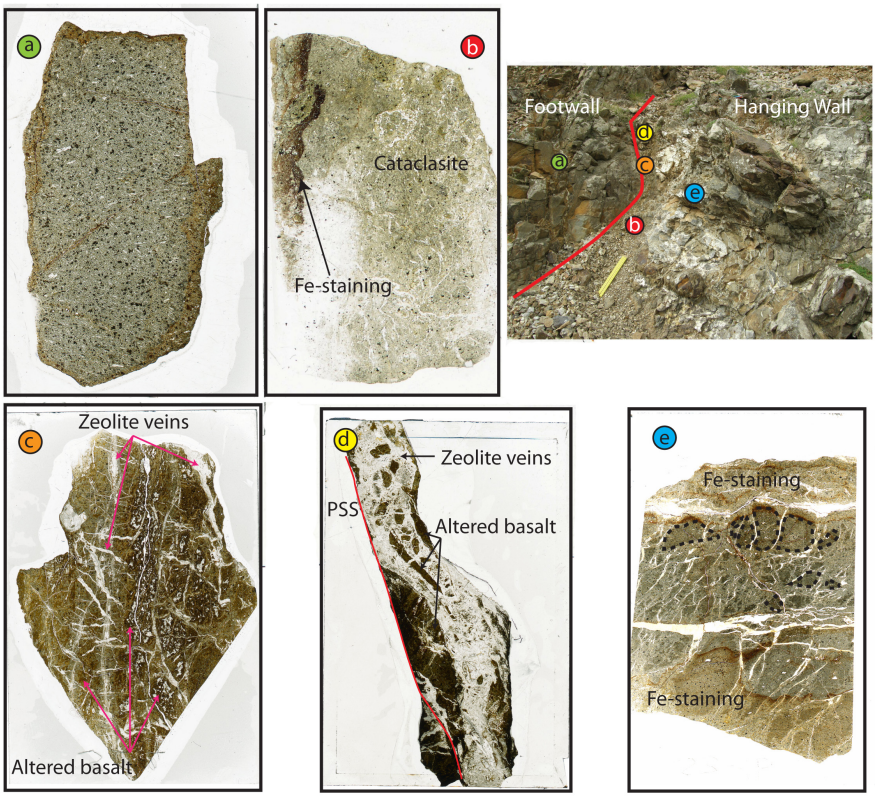

Figure 4.35: Sample locations from the TBF, overlain on a photograph of the fault zone. a) Green dot = footwall altered basalt (TBF1). b) Red dot = PSZ cataclasite, weathering related Fe-staining labelled (TBF2). c) Orange dot = altered basalt lens from PSZ, crosscut by zeolite veins (TBF3). d) Yellow dot = PSS and altered basalt clasts, PSS is marked by red line (TBF4). e) Blue dot = hanging wall mineralised and altered basalt (TBF5). 'Clasts' of basalt are outlined with dotted lines.

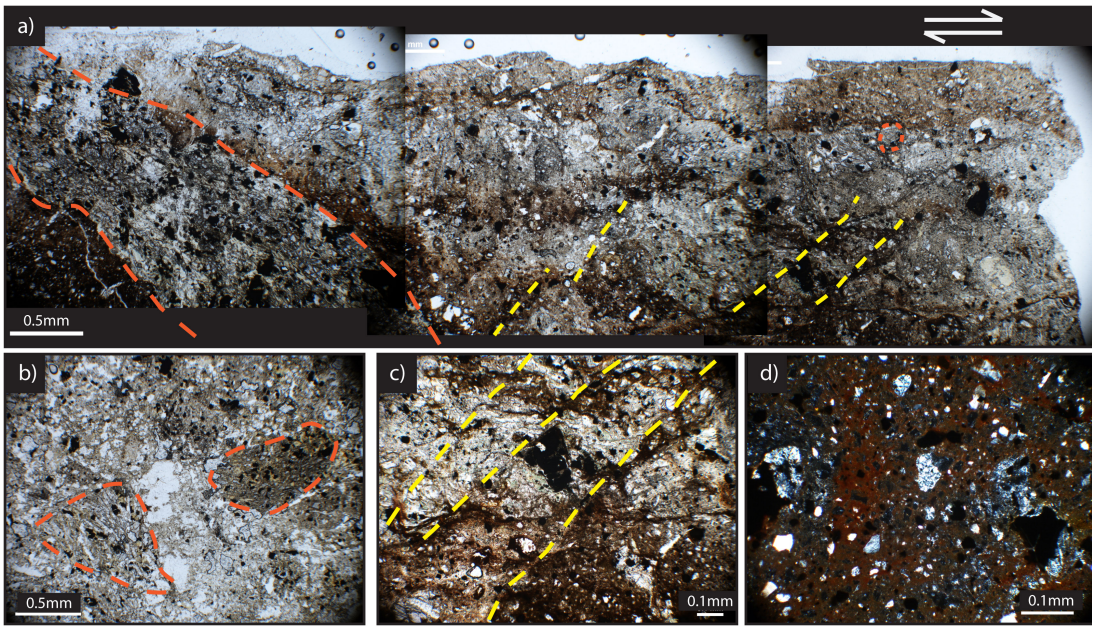

Figure 4.36: Petrographic images (PPL) cataclasite (sample TBF2). a) Photomontage of cataclasite. Yellow dotted lines highlight S fabric within cataclasite, and orange dotted lines outline altered basalt clasts. b) Altered basalt clasts (outlined) in a matrix of cataclasite contain zeolitised feldspars. c) S fabric within cataclasite (highlighted), defined by individual mineral clasts. d) Clasts of zeolite also compose the cataclasite.

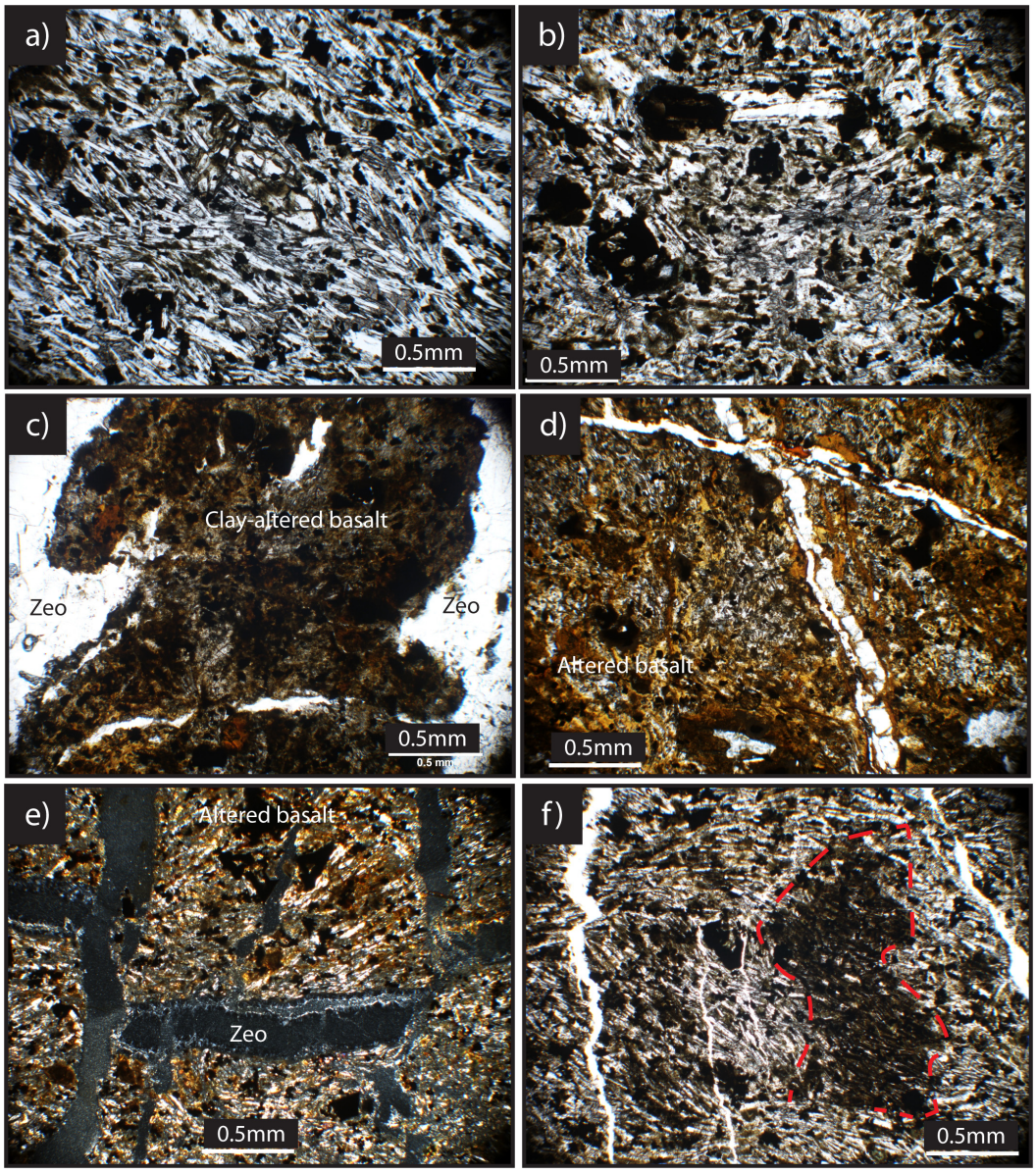

Figure 4.37: Petrographic image of TBF. a) Host rock (PPL) with flow aligned feldspars and olivine phenocryst (centre). b) Altered basalt from sample TBF1 (XP), with an increase in interstitial clay content relative to the host. c) Survivor clast in slip surface (PPL, TBF4). Note obscuring of original features by increased clay content with respect to host rock. d) Detail of an altered basalt clast lens (XP) from within TBF3. Original mineralogy and textures from the host rock are preserved but it is much more clay-rich (brown). Zeolite veins crosscut the sample. e) Altered basalt from TBF5, with preserved host rock features but an increase in interstitial clay with respect to the host rock. Zeolite veins crosscut the basalt (XP). f) Altered basalt also from sample TBF5, with 'clast' of more clay-rich basalt outlined, surrounded by less clay-rich altered basalt (PPL).

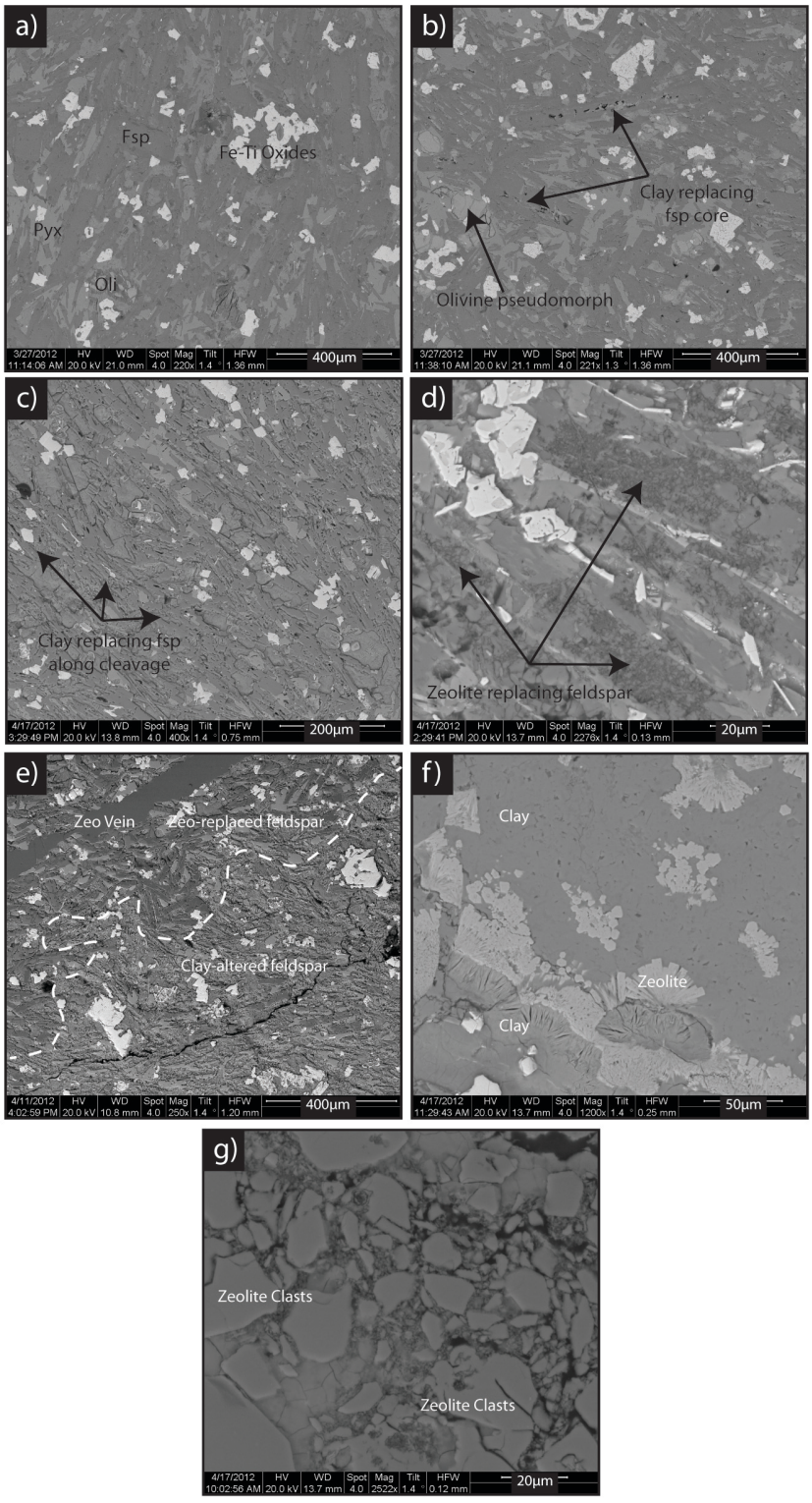

Figure 4.38: BSE images of altered and mineralised rocks from the TBF fault zone. a) Host rock for references. b) TBF1, where feldspars are being replaced by clays in their cores. c) TBF5 with extensive clay replacement of feldspar along cleavages. d) Zeolitisation of feldspars in TBF5. e) Zeolite veins (TBF5) crosscutting altered basalt. The zeolite veins are surrounded by zeolitised feldspars, with an irregular boundary between them and a 'clast' of clay-altered feldspar. f) Clay filled fracture, with zeolite growing in clay pore space. g) Zeolite breccia formed along the edges of a zeolite vein.

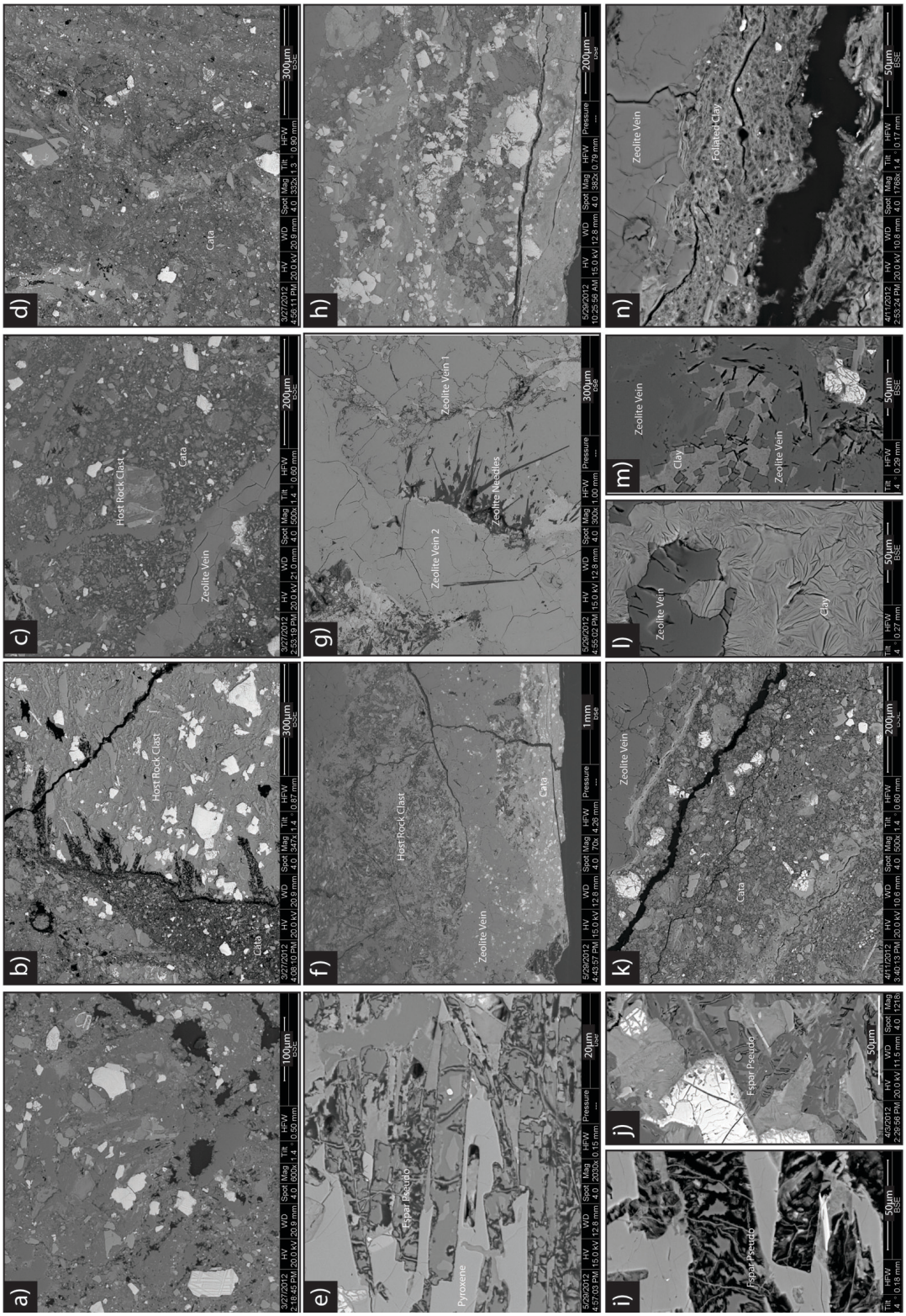

Figure 4.39: BSE images of fault-related rocks from the TBF fault. a) Cataclasite and host rock clasts (TBF2). b) Altered basalt clast with cataclastic margin, and zeolitised feldspars at contact (TBF2). c) Cataclasite with rounded clasts of host rock and zeolite veins (TBF2). d) Foliated cataclasite (TBF2). e) Feldspar pseudomorphs, zeolitised and replaced by clay (TBF4). f) Cataclasite and altered basalt clasts filled with clays, crosscut by zeolite veins (TBF4). g) Multiple generations of zeolite veins within TBF4. h) Sigmoidal clast within slip surface composed of Fe-Ti oxides (TBF4). i) Clay and zeolite pseudomorphs of feldspars (TBF3), j)

(continued from previous page) Zeolitised feldspar (TBF3). k) Cataclastic edges within fault rock (TBF3). l) Clay replacing zeolite (TBF3). m) Zeolite crystals growing in clay (TBF3). n) Foliated clay along fractures (TBF3).

4.6.6. Non self-juxtaposed interpretation

As this study has shown, juxtapositions of basalt against other clay-poor lithologies results in microscopic deformation similar to that found in self-juxtaposed faults, at low and medium displacements. Intragranular fracturing, entrainment and cataclasis of minerals, replacement of feldspars by zeolite and clay minerals, and increased contents of interstitial clay (with respect to the host rock) dominate deformation (i.e. SFZ).

However, different deformation styles are found where basalt is juxtaposed against clay-rich lithologies, in particular against peperite (i.e. LWF). The abundant clay in the host rock peperite has been well mixed and entrained along the fault zone. Further alteration to clay of basalt clasts within the peperite accompanying faulting also increases the clay content of the fault zone. This may be due to the lack of zeolite mineralisation in the LWF, and so feldspar has not been replaced by zeolite. Therefore, feldspars are more susceptible to clay replacement, and as they comprise a considerable portion of the basalt and peperite fault walls, the replacement of feldspar to clay is likely to be intense. This increase in clay content within the fault zone causes the fault rock to deform by ductile processes (i.e. smearing) rather than brittle processes (i.e. cataclasis of individual mineral clasts), allowing complex fault rocks to form, such as clay gouges with well developed riedel shears.

Within the largest displacement fault of the non self-juxtaposed faults, the TBF microstructures are similar to those of the HBF self-juxtaposed faults with cataclasites composed of mineral and host rock clasts. However, unlike the HBF, very fine-grained clays and zeolite minerals dominate the matrix of the TBF cataclasite, and host rock clasts within the cataclasite are mostly altered to clays. Clays are also more widespread throughout the fault wall rocks than the HBF.

A conceptual cartoon of the microstructural evolution of basalt juxtaposed with clay-rich lithologies is shown in Figure 4.40. As deformation is similar at lower displacement levels, a conceptual model is shown only for medium-high displacement faults.

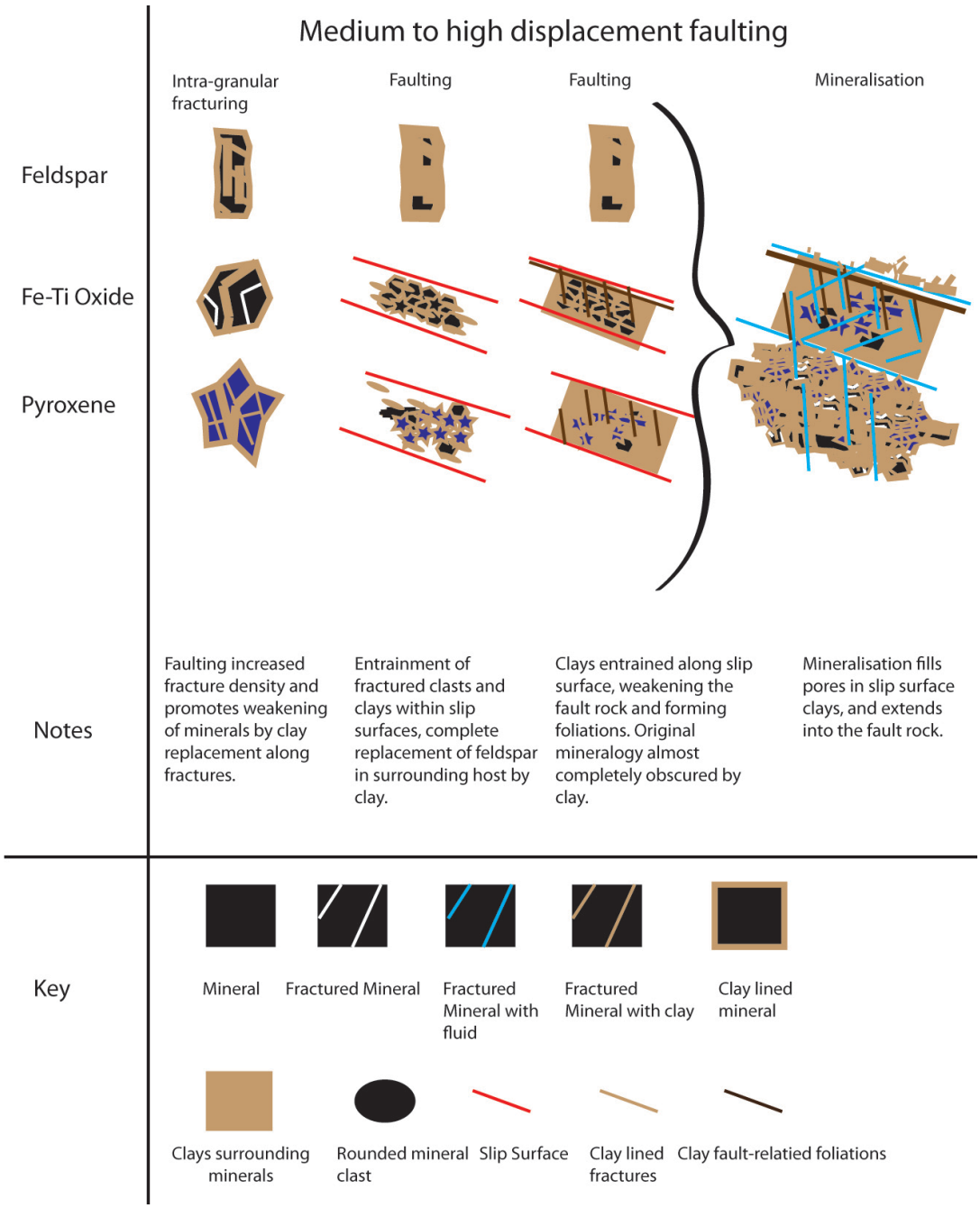

Figure 4.40: Conceptual model for medium to high displacement non self-juxtaposed faults at thin section scale. Low displacement microstructures are similar to that of self-juxtaposed faults.

4.6.7. Non self-juxtaposed summary

A brief summary of the key observations from each fault is below, and these observations are also summarised in Table 4.2.

Medium Displacement (e.g. HVF, SFZ, IBF): all faults are deformed through intragranular fractures, grain size reduction, gouge formation, replacement of feldspar by zeolite and clay, and interstitial formation of clay.

High Displacement (e.g. LWF, TBF): all faults contain deformation elements of intragranular fractures, interstitial clay, grain size reduction, cataclasis and gouge. Zeolitisation of feldspar does not occur in clay-rich faults, and feldspars are free of clay in the heavily zeolitised faults, particularly adjacent to zeolite veins.

Table 4.2: Summary table of microstructural features within non self-juxtaposed faults.

	Intergranular fractures	Cataclasis	Foliated Cataclasite	Dissolution	Zeolitisation of feldspar	Clay replace-ment of feldspars	Zeolite Veins	Clay lined fractures	Interstitial Clay	Foliated Clay
HBF (1m)	●			●	●	●	●		●	●
SBF (5m)	●	●		●	●	●	●	●	●	
IBF (5m)	●	●	●	●	●	●	●	●	●	
LWF (<10m)	●	●	●	●		●		●	●	●
TBF (18m strand)	●	●	●	●	●		●	●	●	●
	Deformational Processes			Geochemical Processes						

4.7. Mineralogical changes as a result of faulting

Point counting was used to identify mineralogical changes as a result of faulting in basalt-hosted fault zones (methodology is described in section 4.2). Samples were studied from the VJF, BNF, HBF, and TBF, as these faults provide the best exposure of host rock through to fault rock, to evaluate mineralogical changes related to faulting. Point counting was carried out at a magnification of 500μm in all samples. Porosity values in all samples are maximum estimates because although original porosity can in some cases be confirmed (i.e. pore space rimmed by zeolite minerals), other pores may have formed during sampling and thin section preparation. In future, original porosity could be more accurately determined by dye-staining samples prior to thin-section making.

4.7.1. Vagseiði Jetty Fault (VJF)

Figure 4.41 shows changes in mineralogy from the host rock through to samples from the PSZ. Proportions of feldspar and pyroxene decrease toward the fault zone, but the Fe-Ti oxide content does not change. Clay content, zeolite mineralisation and porosity all increase toward the fault zone. This would suggest that feldspars and pyroxenes are increasingly replaced by clays and zeolites toward the fault zone, and/or dissolved, leaving pore space. However, given that feldspar content drops by 23% from host rock to fault rock, and that clay rises by 20%, it is reasonable to assume that feldspar loss can mostly be attributed to replacement by clay (a feature also noted in the microscopic observations). It is therefore likely that the 8% drop in pyroxenes could be attributed to dissolution, and possibly explain the 8% rise in porosity from host rock to fault rock. However, this increase in porosity toward the PSZ may be inaccurate due to sampling and thin section making processes, which may have artificially increased the amount of pore space. Porosity varies throughout the sample, e.g. at the edge of the extensional vein with zeolitised feldspars (within the altered sample) porosity was 6%, and 9.1mm away (where zeolitisation of feldspars became <100%) porosity was as 1.9%.

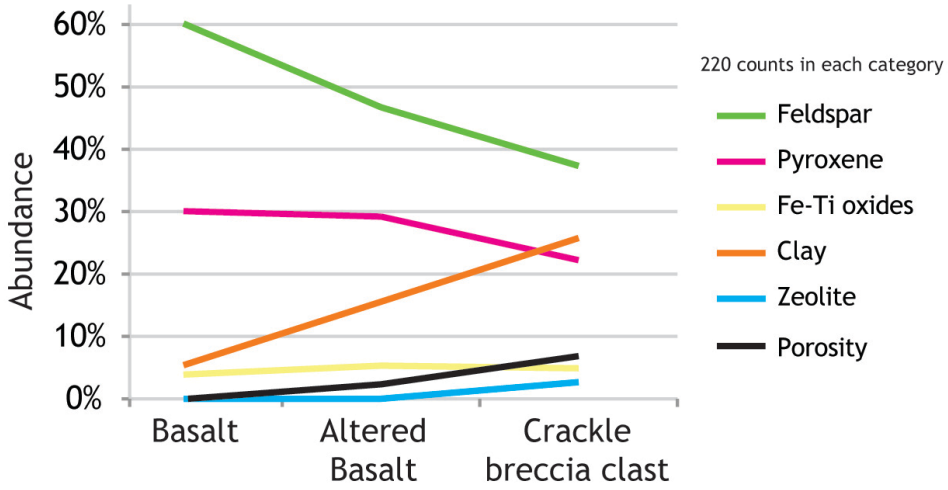

Figure 4.41: Mineralogy and porosity of samples from VJF, determined by SEM point counting.

4.7.2. Bird Nest Fault (BNF)

Clay, pyroxene and Fe-Ti oxide abundance decrease slightly from the host rock to the PSZ , suggesting little in the way of replacement or dissolution of these minerals. Feldspar content falls to zero from 35% in the PSZ, whilst feldspar pseudomorphs (classed together as feldspar pseudomorphs after zeolite and clay replacement) and zeolite all increase toward it (Figure 4.42). This suggests that with increasing proximity to the fault zone, feldspar is increasingly replaced by zeolite and clay until only feldspar pseudomorphs remain. Porosity also increases slightly toward the PSZ.

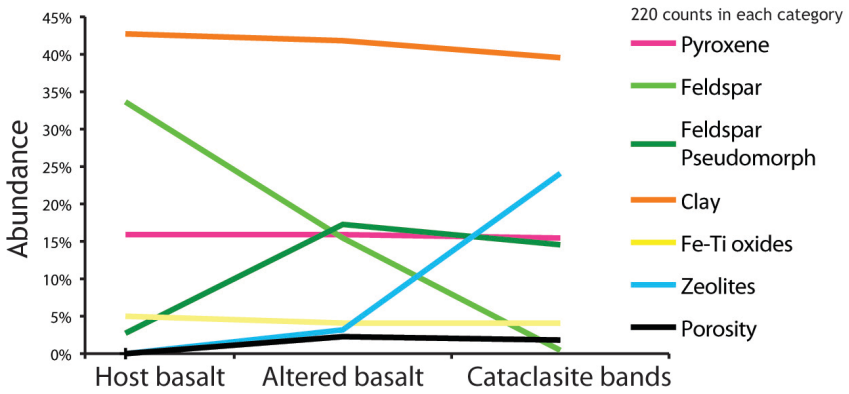

Figure 4.42: Mineralogy and porosity of samples from the hanging wall host rock and hanging wall derived fault rock from the BNF, determined by SEM point counting.

4.7.3. Hramaborg Fault (HBF)

Pyroxene and Fe-Ti oxide abundances vary little across the samples, but olivine abundance falls from 10% in the host rock to zero in fault-related samples (Figure 4.43). Clay abundance rises by ~20% from host basalt to altered basalt, where combined olivine and feldspar abundances decrease by around 20%. This suggests clay content is increasing as a result of it replacing feldspar and olivine, which was noted in microscopic observations. Closer to the fault zone, feldspar content continues to fall sharply toward the fault, suggesting feldspar is being replaced by other minerals. This is confirmed by the increase in feldspar pseudomorphs (zeolites and clays), which rise in content toward the fault zone. Clay content, zeolite mineralisation and porosity all increase relative to the host rock within the cataclasite domain of the fault zone, suggesting enhanced fluid flow and precipitation have taken place within this zone.

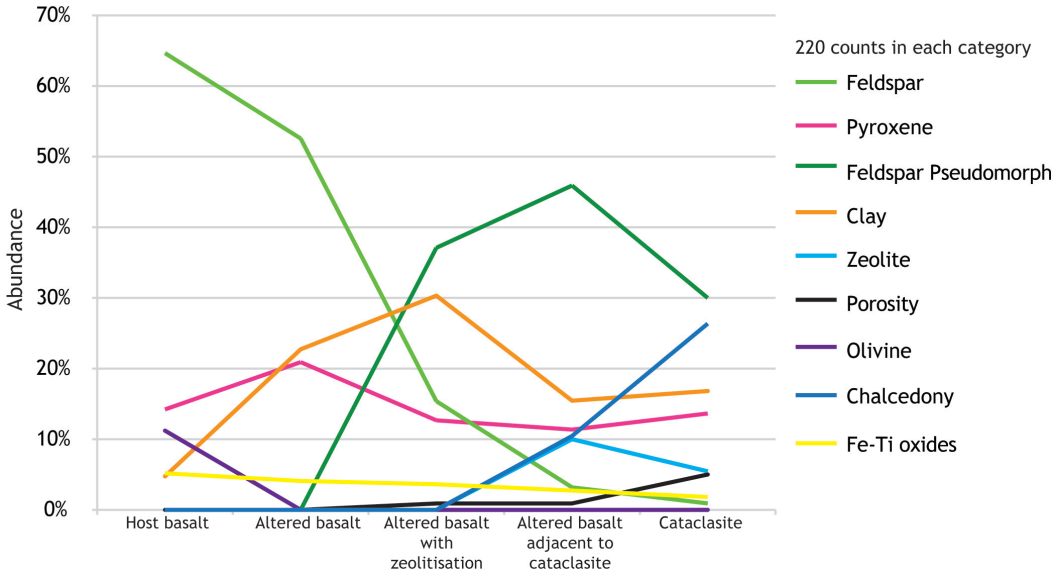

Figure 4.43: Mineralogy and porosity of samples from the HBF determined by SEM point counting.

4.7.4. Talisker Bay Fault (TBF)

The mineralogy of the TBF was described from samples of the altered footwall (TBF1), PSZ fault rocks (TBF2, 3 and 4) and altered rock from the hanging wall (TBF5). In the altered footwall, feldspar content decreases

relative to the host rock, and clay and feldspar pseudomorphs and porosity all increase relative to the host rock (Figure 4.44). As in the previous point count results, this suggests feldspar is being replaced by clays with increasing proximity to the fault zone. The PSZ cataclasite is dominated by a new mineralogy, (a clay/zeolite matrix between rock clasts), and thus other minerals are correspondingly scarce. This suggests the cataclasite zone acted as a fluid conduit, allowing new minerals to precipitate in pore space generated by faulting. The porosity also increases. In the PSZ fault rock, feldspars are again absent but feldspar pseudomorphs are more abundant as is clay mineralisation. In the altered basalt PSZ breccia, clay content and feldspar pseudomorphs increase relative to fault rock lenses, but zeolite mineralisation decreases. Porosity remains constant. In the altered hanging wall, an increase in feldspars is seen with respect to PSZ breccias, and a decrease in clay and porosity. Throughout the samples, pyroxenes and Fe-Ti oxides abundances remain constant.

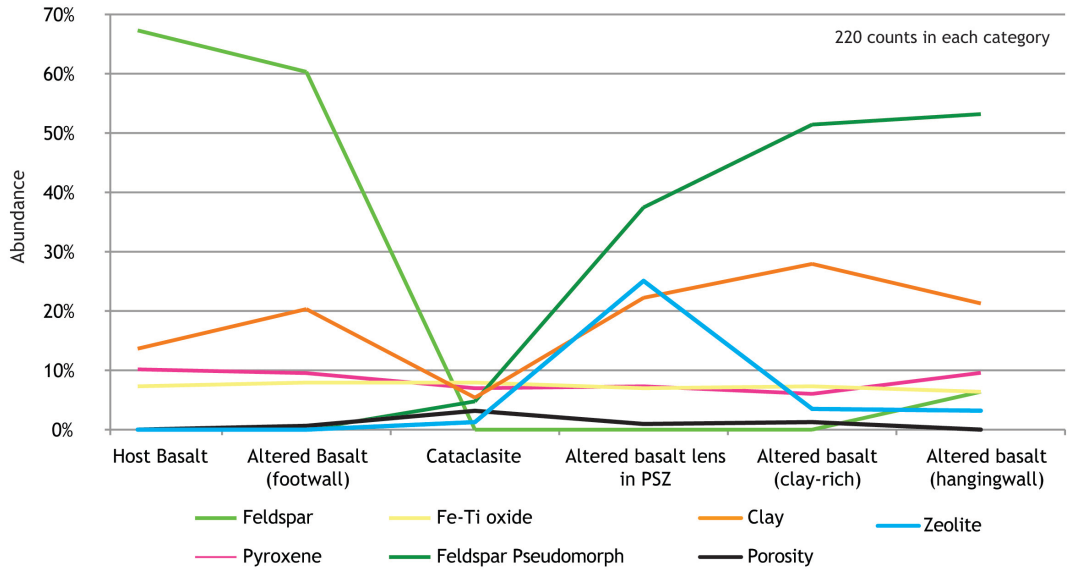

Figure 4.44: Mineralogy and porosity of samples from TBF determined by SEM point counting.

4.7.5. Element mapping of fault rocks

Element maps were also carried out to study the element distribution in selected fault rocks from the BNF, HBF and TBF, and to understand chemical changes as a result of zeolitisation of feldspars.

A large area scan of the fault rock from the BNF is shown in Figure 4.45. To illustrate how an individual element can dominate a sample due to its distribution in a particular mineral, Figure 4.45 shows Al distribution is concentrated within zeolite veins and feldspars. Whilst Ca is not shown here, the zeolite vein is scolecite, which is a Ca-rich zeolite. In this particular example therefore, it may be expected that bulk chemistries of the fault rock would be rich in Al and Ca (with respect to the host rock), due to the dominating presence of scolecite.

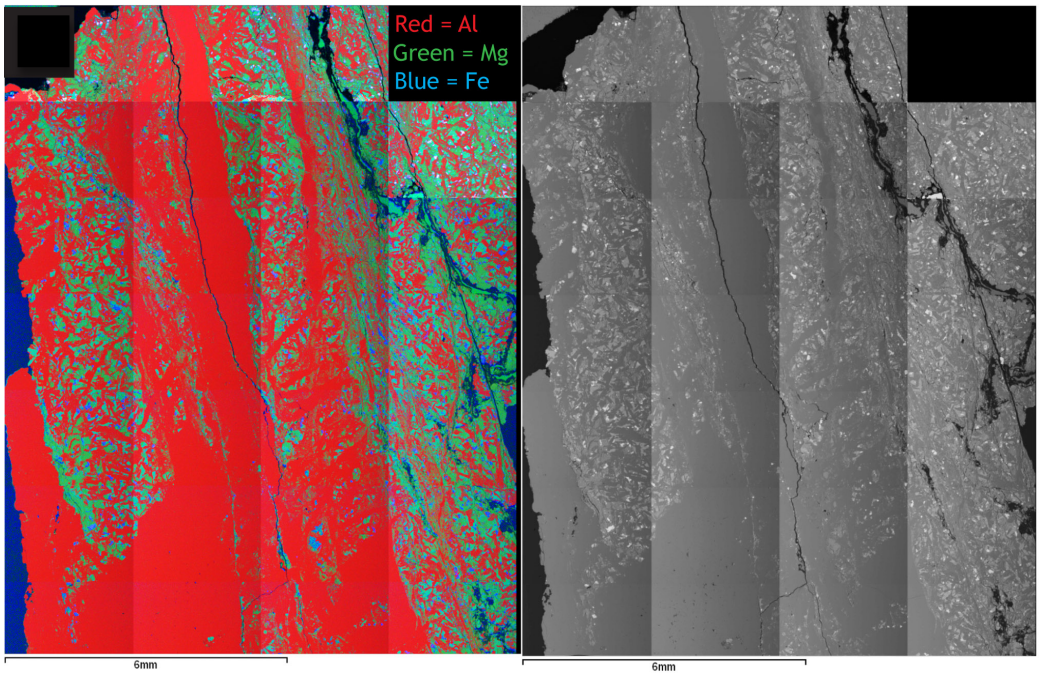

Figure 4.45: Element mapping from ZS-SEM of the BNF fault rock. Large area scan. Original image is shown for reference on right. In general, red represents zeolite veins or feldspars, green pyroxenes or clays, and blue Fe-Ti-oxides.

In Figure 4.46, element maps from the HBF are shown. In Figure 4.46a, clasts within the fault rock are dominated by Ca and Fe (pyroxenes and Fe-Ti oxides). The matrix is dominated by Al and Si, a result of zeolite and SiO_2 vein mineralisation. As in the example from the BNF, bulk chemistries of

the fault rock from the HBF might be expected to be rich in Al and Si (with respect to the host rock) due to the mineralisation of zeolite dispersed throughout the fault rock. In Figure 4.46b, zeolitisation of feldspar can be seen clearly, due to the original feldspar containing a higher Al content than the zeolitised portion. This suggests that as the feldspar is replaced by zeolite, in this example, the Al content of the original feldspar is reduced. The lost Al is likely to be redistributed by groundwater, and re-precipitated in zeolite minerals.

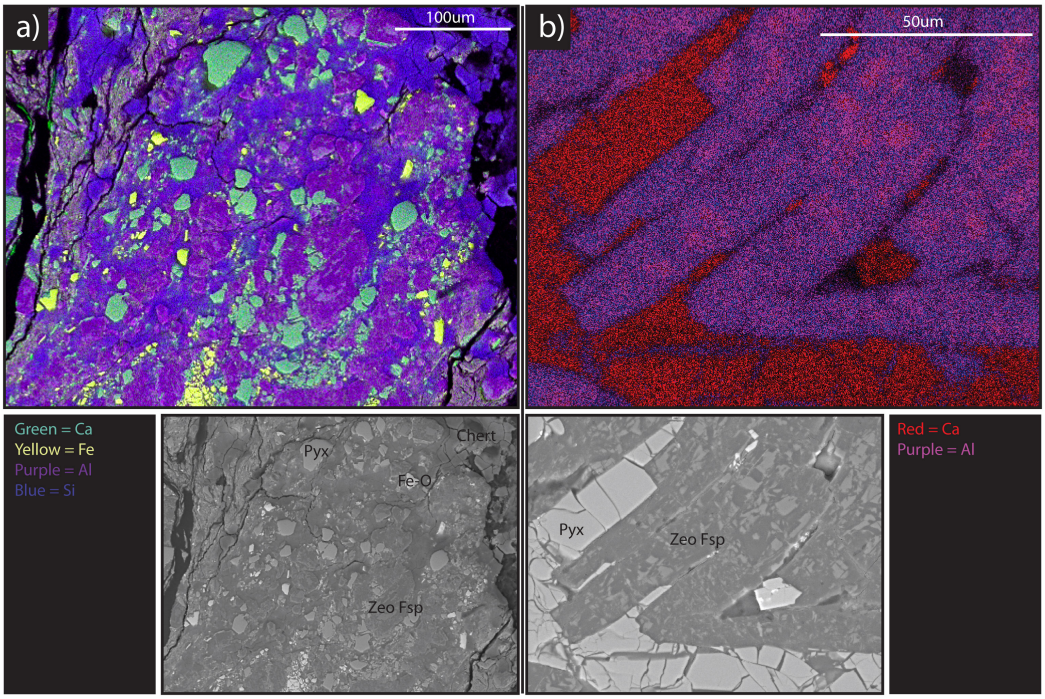

Figure 4.46: Element mapping from ZS-SEM of the HBF fault rock. a) Element map within cataclasite from HBF, highlighting entrained Fe-Ti oxides (yellow) and pyroxenes (green) well. These clasts sit in a matrix rich in Si and Al (zeolite and SiO_2 veins) and occasional feldspars (purple). b) Element map of zeolitised feldspars, highlighting original feldspar (bright purple) had a higher Al content than the zeolitised portion (dark purple).

Element maps from the TBF are presented in Figure 4.47. In Figure 4.47, the distribution of Fe and Ca shows the entrainment of Fe-Ti oxides and pyroxenes within the cataclasite, which is set in a matrix rich in Al (zeolite). As in the previous examples, this could suggest that zeolite mineralogy dominates the chemistry of the fault rock.

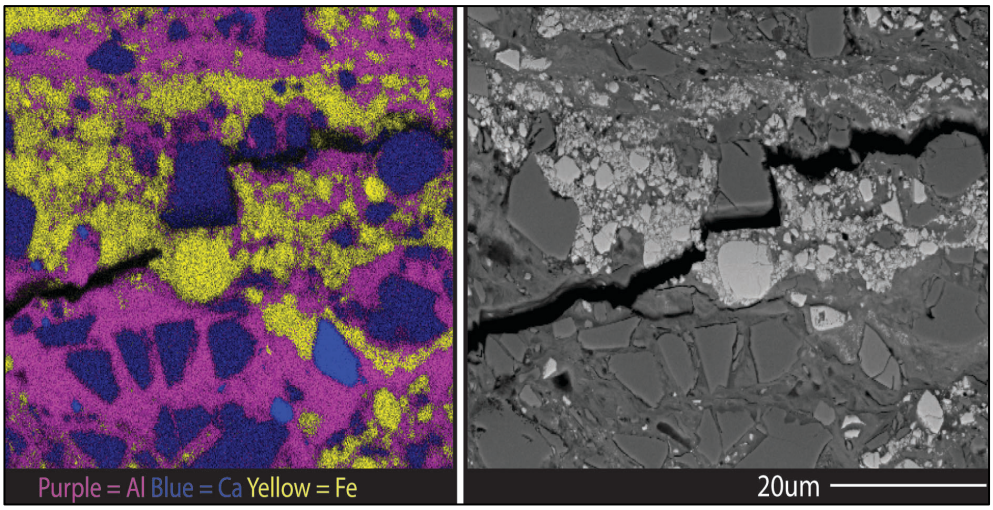

Figure 4.47: Element mapping from ZS-SEM of the TBF fault rock. This image shows a cataclasite, where yellow (Fe) represent Fe-Ti oxides, blues (Ca) pyroxenes, and purple (Al) zeolites. BSE image of mapped area is shown on the right.

4.7.6. Mineralogical changes - interpretation

In general, an increase in present-day porosity, clay and zeolite mineralisation is seen within the PSZ fault rocks (i.e. zones of alteration and cataclasis), with respect to the host rock, suggesting that fluid flow was concentrated in this zone. With a fall in the abundance of feldspar there is a reciprocal increase in abundance of feldspar pseudomorphs and clay. This suggests that the breakdown of feldspars contributes to clay formation, and that they are more susceptible to being replaced (pseudomorphed), rather than mechanically dispersed throughout the fault zone. Pyroxene and Fe-Ti oxides content are relatively invariant suggesting that these minerals are preferentially fractured and dispersed rather than chemically altered. It is likely that the replacement of feldspar by clays/zeolite will alter the chemistry of the fault rocks with respect to the host rock, as will precipitation of new minerals within increased pore space (i.e. zeolite veins and clay minerals). Thus, the introduction of fluids via the fault zone will alter the host rock basalt, and result in a fault rock basalt with increased volumes of clay and zeolites. This mineralogical change could have a profound effect on the bulk chemistry of the fault zone, and the implications for this are discussed in the Discussion chapter.

4.8. Conclusions

Deformational and geochemical processes control faulting of basalts at the grain scale. Certain minerals are affected by cataclastic deformation, resulting in a reduced grain size, which increases the likelihood of slip. Minerals are also partially or fully replaced (as a result of fluid-rock interaction) by secondary mineral phases, changing the properties of the original phase, and thus the region affected by faulting. This study has found that Fe-Ti oxides and pyroxenes preferentially deform by intragranular fracturing and grain size reduction, whereas olivines and feldspars are susceptible to replacement by phyllosilicates and zeolites. The implications of this are discussed in the Discussion chapter.

Fault rocks are typically composed of entrained broken mineral clasts of pyroxene and Fe-Ti oxides in cataclasite zones, set in a zeolite- or clay-rich matrix. Cataclasites are also composed of host rock clasts with clay/zeolite pseudomorphs after feldspar. The fault rocks of non self-juxtaposed faults are similar to those of self-juxtaposed faults, but with the addition of more clay in the fault rocks due to entrainment of clay-rich sedimentary rocks (by fault drag of clay-rich units), and alteration of feldspars to clay in the absence of zeolite mineralisation.

Secondary mineralisation of faults in basalt is also important. Zeolite mineralisation and clay precipitation is present throughout most of the fault zones, replacing feldspars and filling pore space. Clay minerals are also found along fractures (neoformed), and dispersed throughout pore space.

Fault rock bulk chemistries are likely to be controlled by secondary mineral formation, as a result of replacement of minerals (e.g. feldspars and olivines) and/or a result of new minerals formed within pore space generated by faulting (e.g. zeolite and clay minerals). These results have implications for fault strength, permeability and bulk chemistry estimates for CO_2 storage, which are explored further in the Discussion chapter.

5. Seismic-scale Faults in Basalt: Fault Zone Evolution and Fluid Flow

5.1. Introduction

In the previous chapters of this thesis, detailed descriptions of the macro- and micro-morphologies of sub-seismic fault zones (<25m displacement) in basalt have been presented. Sub-seismic faults fall below the maximum resolution of seismic imaging, and can therefore go undetected, and un-modelled, when it comes to assessing the fluid flow and sealing potential of a hydrocarbon basin. Instead, very high displacement faults that are easily picked in seismic images are usually considered for assessing the sealing potential of a reservoir. Therefore, determining the internal structure of seismic-scale faults in basalt sequences is very important. By studying seismic-scale displacement faults, a further understanding of the evolution of faults in basalt sequences can be achieved, particularly by considering the role clay-rich units between basalt flows have on overall fault architecture.

Due to poor exposures of seismic-scale faults in the North Atlantic Igneous Province basalt sequences (i.e. typically covered in vegetation or water), faults within basalts of Palaeogene age were not studied. However, an excellently exposed seismic-scale fault in the ~420 Ma Lorn Plateau Lava Formation basalt sequence on the west coast of Scotland was studied, and is described in this chapter. The exposures of this fault on Kerrera provide a rare opportunity to study an exhumed large offset fault zone in Scotland, and also to describe in detail the broad fault zone architecture associated with a seismic-scale fault zone in a basalt sequence.

An exhumed fault zone (with 125m total dip-slip displacement, determined from lithostratigraphic markers) cutting a Devonian basalt sequence is exposed on the island of Kerrera (the geology and geological history of which is described in Chapter 2). The fault zone forms part of the graben

structure that trends NE-SW across the SE coast of Kerrera. A narrow strip of exposed Lorn Plateau Lava Formation is bound by the Kerrera Graben (Figure 5.1). The graben's bounding faults are referred to as the NW and the SE bounding faults in this study. Two key localities are exposed in the Kerrera Graben – the first is a set of exposures of the SE bounding fault, with a total of 125m displacement accommodated along it (Location 1 on Figure 5.1). The second outcrops 1.8 miles away (Location 2 on Figure 5.1), at the SW edge of the island, exposing a 40m wide deformation zone associated with the NW bounding fault (not exposed). This deformation zone contains dip slip (sometimes reversed) and strike-slip faults. At both localities, the fault cuts a sequence of basaltic lava flows, volcaniclastic sedimentary rocks and Lower Old Red Sandstone (LORS) sandstones and conglomerates. At Location 2, the fault also cuts into the Dalradian basement of pelites.

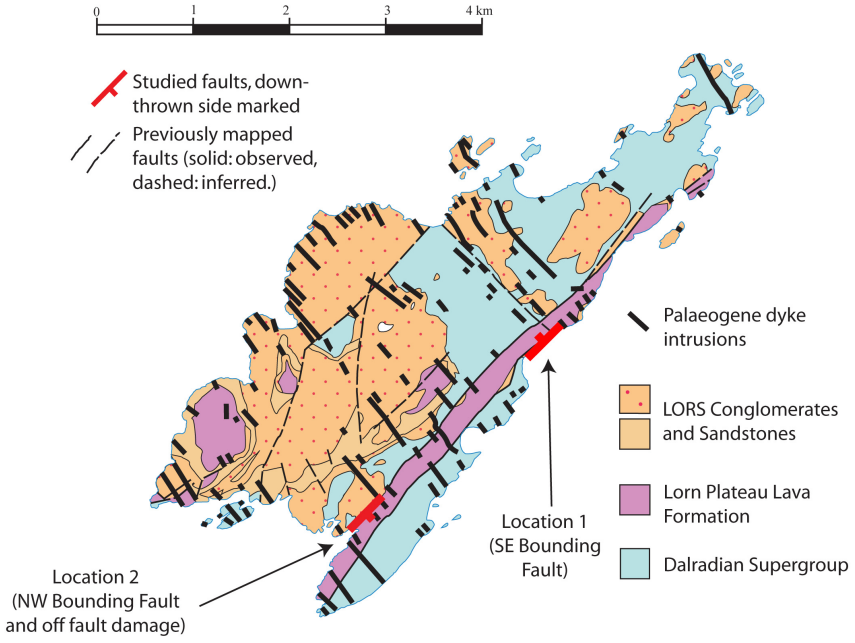

Figure 5.1: Geological map of Kerrera (after BGS, 1992). Key localities are indicated, and marked in red.

5.2. Methods

Preliminary mapping of the exposure of the SE bounding fault was carried out at a scale of 1:25 across a 10m exposure of the bounding fault during the author's undergraduate degree. The baseline mapping method was

used, where a baseline parallel to the exposure was constructed. At 1m intervals, the distance from the baseline to different domains of the exposure (e.g. footwall units) was measured, and mapped. At the time of mapping, the author identified five fault zone components. For this doctorate study, the fault exposure was revisited and these five fault zone components were described in fuller detail, and additional exposures of the same bounding fault were mapped to the north and south of the original site. The full detail of the fault components from both of these exposures of the SE bounding fault will be described in this chapter, and aside from the base map produced from the undergraduate study, and some microstructural work (which will be acknowledged in the text), work described from now on is original work derived from this doctorate study. Using the pace and compass technique, mapping at a scale of approximately 1:100 was carried out along the 40m deformed zone associated with the NW bounding fault, mapping boundaries between different lithologies and large scale structures (faults/fractures). This allowed identification of the broad scale fault zone architecture.

Thin-section analysis was carried out using the methods described in Chapter 4 for petrographic and SEM analysis. In addition to these instruments, cathodoluminescence (CL) of luminescent minerals (calcite) were studied using a Cambridge Image Technology Limited luminoscope mounted on a Zeiss Axioplan microscope. Images were captured using a Nikon DS-Fi1 5 Megapixel digital camera. Isotope analysis of calcite from the samples was also carried out, and the procedures for this are explained in Section 5.6. Whilst the faults described in Chapter 4 were rich in zeolites but poor in calcite, the calcite rich nature of the samples from Kerrera makes them ideal for CL and isotopic analyses.

5.3. SE bounding fault – field description

The SE bounding fault is observed in four key localities (locality i, ii, iii and iv) along the SE facing shore of Kerrera. These localities are found along the coast, between the ferry pier (NM 830,287) and Horse Shoe bay (NM

824,281). A transect between these locations was carried out to map the local geology along the shore, where a sequence of basalts and volcaniclastic sediments dip gently to the NE (Figure 5.2a). Toward the base of the section, the Strontian Felsite (potentially intruding along the SE bounding fault) was mapped, following a mapped unit of LORS breccia. A schematic block diagram (not to scale) of the geology along this transect is presented in Figure 5.2b, which includes the trace of the SE bounding fault. Note the gently dipping beds toward the NE, and the drag of the beds toward the fault plane (Figure 5.2c). Adjacent to the fault plane the geological units have a dip of 60-80° toward the NW, but along the rest of the transect have a dip of ~10° toward the NE. Due to the gentle dip of the beds, and uneven erosional surfaces along the coast, juxtapositions of some of the individual geological units against the fault are found as cross sections within the present day topography. This relationship is explained in Figure 5.2c where present day erosional surfaces are shown as dashed lines. Each of the key localities are described in the following sections.

5.3.1. Locality i – LORS sheared breccia

Locality i (Figure 5.2d, i) is located within LORS breccia, which forms the lowest of the geological units exposed in the footwall. The breccia dips 60° toward the NW, and clasts are imbricated in a strong NW orientation. This is interpreted as shearing of LORS breccia adjacent to the SE bounding fault. LORS are generally gently dipping, and so this steep dip is uncharacteristic of the unit, and is therefore likely to be related to the adjacent fault. This outcrop also contains pyrite cubes, situated in the LORS breccia matrix. This pyrite mineralisation may be fault-related – whilst pyrite is widespread within the underlying Dalradian slates, pyrite in the LORS is only found in outcrops adjacent to the SE bounding fault. The pyrite mineralisation of the LORS could have resulted from reducing, H_2S-bearing fluids percolating through Dalradian rocks, and travelling along the fault to leach into available pore space (matrix of LORS breccia), and precipitating pyrite cubes.

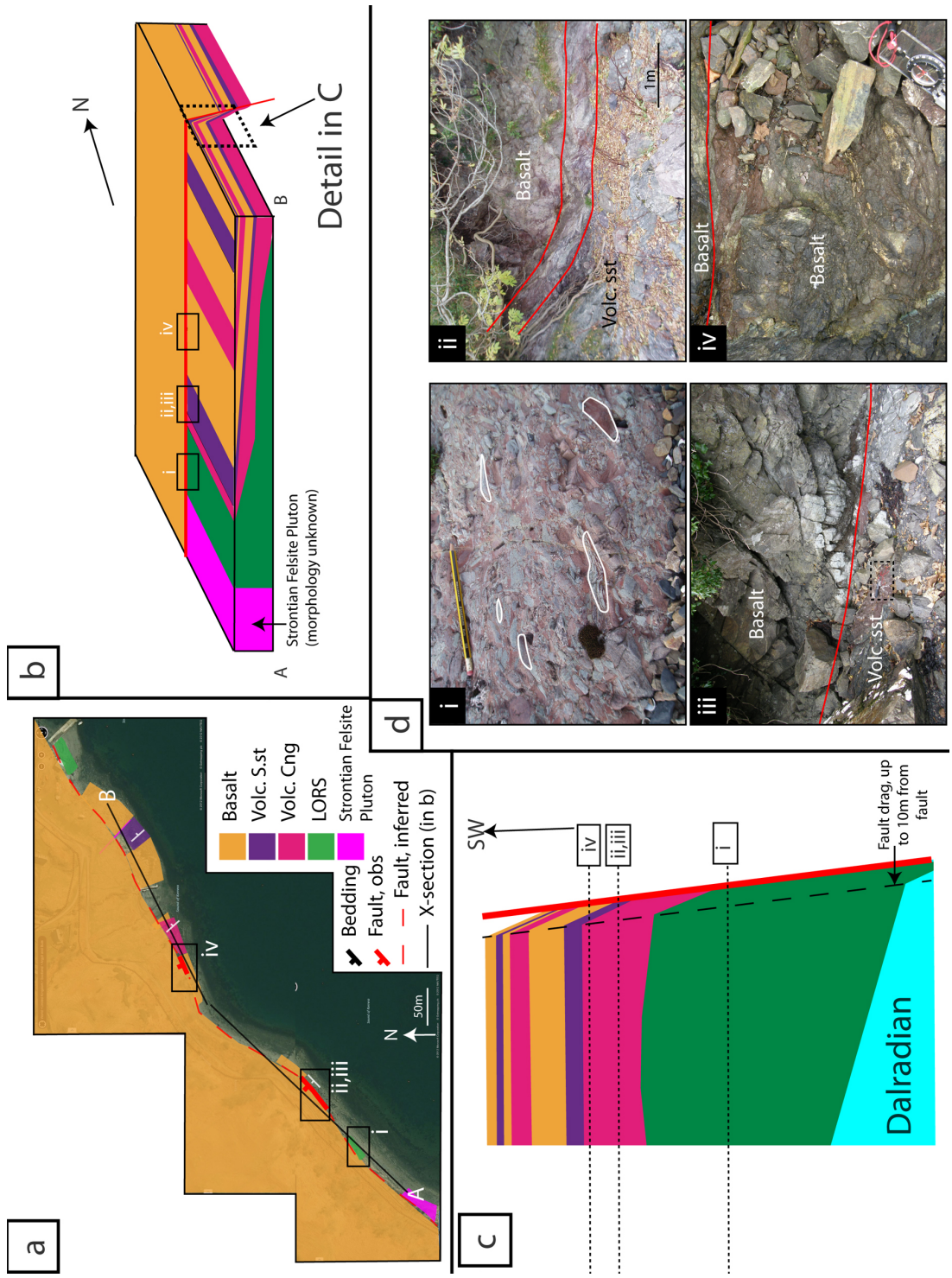

Figure 5.2: SE Bounding fault, Kerrera. a) Geological map of SW facing coast. Red dashed line represents trace of SE bounding fault. Boxes show locations of key localities. b) Schematic block diagram showing gently dipping nature of geology, and juxtaposition relationships with the SE bounding fault (red). c) Detail of geological relationships to the SE bounding fault. Note increased dip adjacent to fault plane (fault drag). Dashed lines represent present day erosional surfaces across different parts of the fault. d) Photo overviews of the key localities, red lines on each diagram represent SE-bounding fault trace. i: imbricated LORS breccia, orientation of clasts highlighted in white. ii: Fault zone between downthrown basalt and volcaniclastic sedimentary rocks & volcanic conglomerate. iii: Fault zone between downthrown basalt and volcaniclastic sedimentary rocks. iv: Fault zone between downthrown basalt and basalt.

5.3.2. Localities ii and iii – fault zone with volcaniclastics and basalt

Localities ii and iii are located at the base of the Lorn Lava Formation, where interbedded volcaniclastic breccias and sandstones are juxtaposed against the downthrown Lorn Lava in the graben. These rocks are found adjacent to the SE bounding fault, dipping at 80º with a NW orientation, and are continuous along strike.

Figure 5.3 shows the base map for locality ii and the SE bounding fault. The footwall is exposed in an approximately horizontal exposure, whereas at the PSS, the hanging wall basalt forms a low overhanging cliff. All lithological units within the footwall are steeply inclined to the NW at ~80º, whereas across the rest of the island, all have a slight dip but none are vertically bedded (with the exception of parts of the Dalradian basement). Starting with the unit exposed furthest from the PSS in the footwall, a 2m thick bed of volcanic conglomerate contains clasts of amygdaloidal basalt, quartz, jasper and veins of calcite. Separating this volcanic conglomerate from the adjacent sandstone unit is a thin (1-5cm) slip surface filled with calcite along the thinnest part, or fault breccia where thicker. The sandstone is red/purple, fine grained and micaceous. Closer toward the PSS, these beds are a mix of sandstones and mudstones with areas of green reduction within the red sandstone. Gray mudstones are also present. The sedimentary rocks adjacent to the PSS are much more friable than those away from it, and are softer to the touch.

In the hanging wall, the basalt is extremely friable and brecciated in areas, as well as cross cut by calcite veins. 4m above this exposure is a road cut, where fresh basalt is exposed.

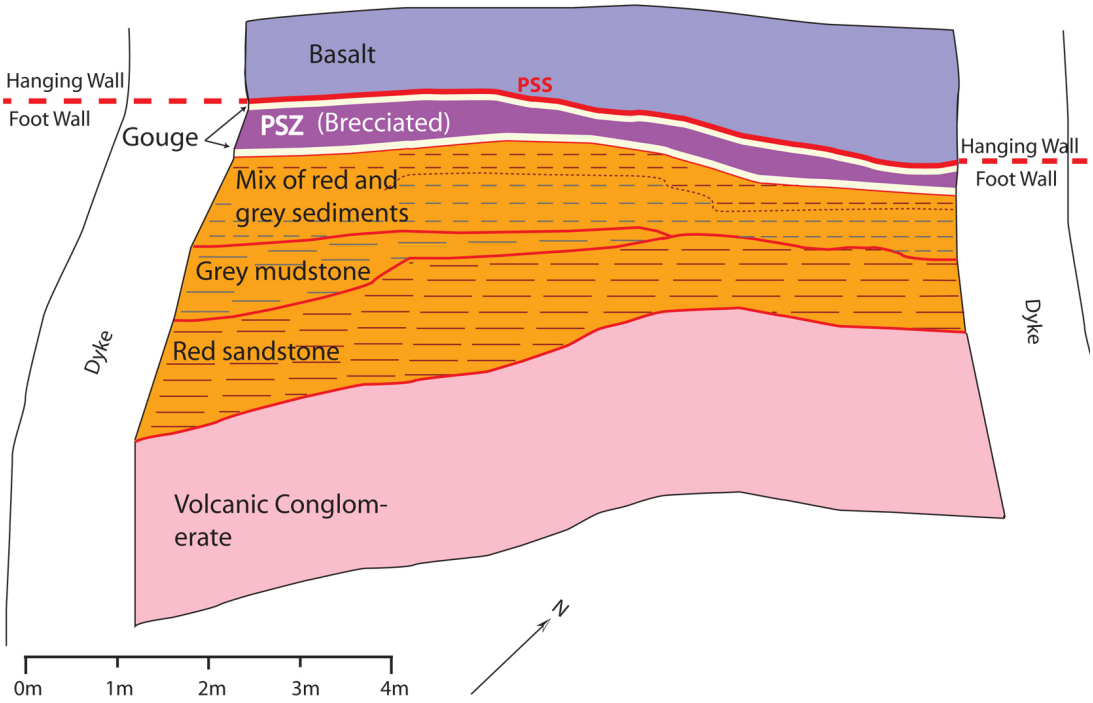

Figure 5.3: Base map of SE bounding fault from locality ii, Kerrera. The detail of the fault rock is very complex, and has been summarised in this figure with photographs of the detail of the SE bounding fault in Figure 5.4. The exposure is bound by Palaeogene dykes at either side, and is composed of a metre thick principal slip zone. Details of each zone are given in the text. Base map made during undergraduate study.

The detail of the principal slip zone is shown in Figure 5.4a. The principal slip zone is very complex, with steeply dipping units within this zone being composed of a mix of fault rock and protolith. There are at least two high strain zones with well-developed, highly foliated clay gouges, typically between 1cm and 20cm thick (Figure 5.4 d, g, h, i). The clay gouge varies in colour from creamy white to brown to red, and contains fragments of host rock. The thicker gouge (creamy white) is continuous along the length of the fault exposure parallel to the principal slip surface, and has the same dip and strike as the fault zone. Other fault rocks and protolith lenses within this fault zone also have the same dip and strike as the fault zone (Figure 5.4c). Thinner gouges are localised along fault-related fabrics, such as riedel shears (Figure 5.4f). Between fault gouge strands, less strained rocks include lenses of protolith and zones of cataclasis. Protolith lenses are surrounded by clay gouge, and deformation within the lenses is dominated by fracturing and brecciation. Microstructural evidence suggests that the red/gray fault rocks are generated from volcaniclastic

sandstones (due to similar levels of mica and other mineralogical content), and the large protolith lens from basalt (due to the presence of clay-replaced feldspars). Identification of the protolith that generated the creamy white gouge was not possible, but from XRD the dominant clay is smectite (from the author's undergraduate work). The hanging wall basalt (adjacent to the slip surface) is highly altered to clays, is brecciated (Figure 5.4e), and displays well-defined slickenlines, with a slightly sinistral dip slip orientation. This sinistral motion is also defined by the brittle rock fabric highlighted by the gouge (Figure 5.4f). The SE bounding fault therefore has some component of strike-slip associated with it. Calcite mineralisation (Figure 5.4j) is common throughout the fault zone, with veins forming both parallel (i.e. along-fault) and perpendicular to (i.e. across-fault) the fault zone.

The highly foliated nature of the gouge bands suggests high strain localisation. The presence of red gouge within the fault zone suggests, at least partially, these gouges may have formed as a result of shearing of sedimentary rocks within the fault zone. In the other faults in basalt studied in this study, gouge was only found when clay-bearing rocks had also been faulted. This is further evidence that the gouges are derived from sedimentary/inter-lava rocks rather than from the basalt itself. The fault may have preferentially localised along the weaker sedimentary rocks that have been dragged into the fault and rotated to a fault parallel orientation. Basalt is likely to have deformed by fracturing and alteration and that is why it is preserved as lenses within the fault zone, rather than being smeared out within the high strain zones. With decreasing distance from the fault, the red and gray volcanic sandstone become softer and friable. This suggests that fluids from the fault zone leached out into the wall rocks, altering them to clay. This alteration may have reduced their strength making them susceptible to shearing and entrainment into the fault zone.

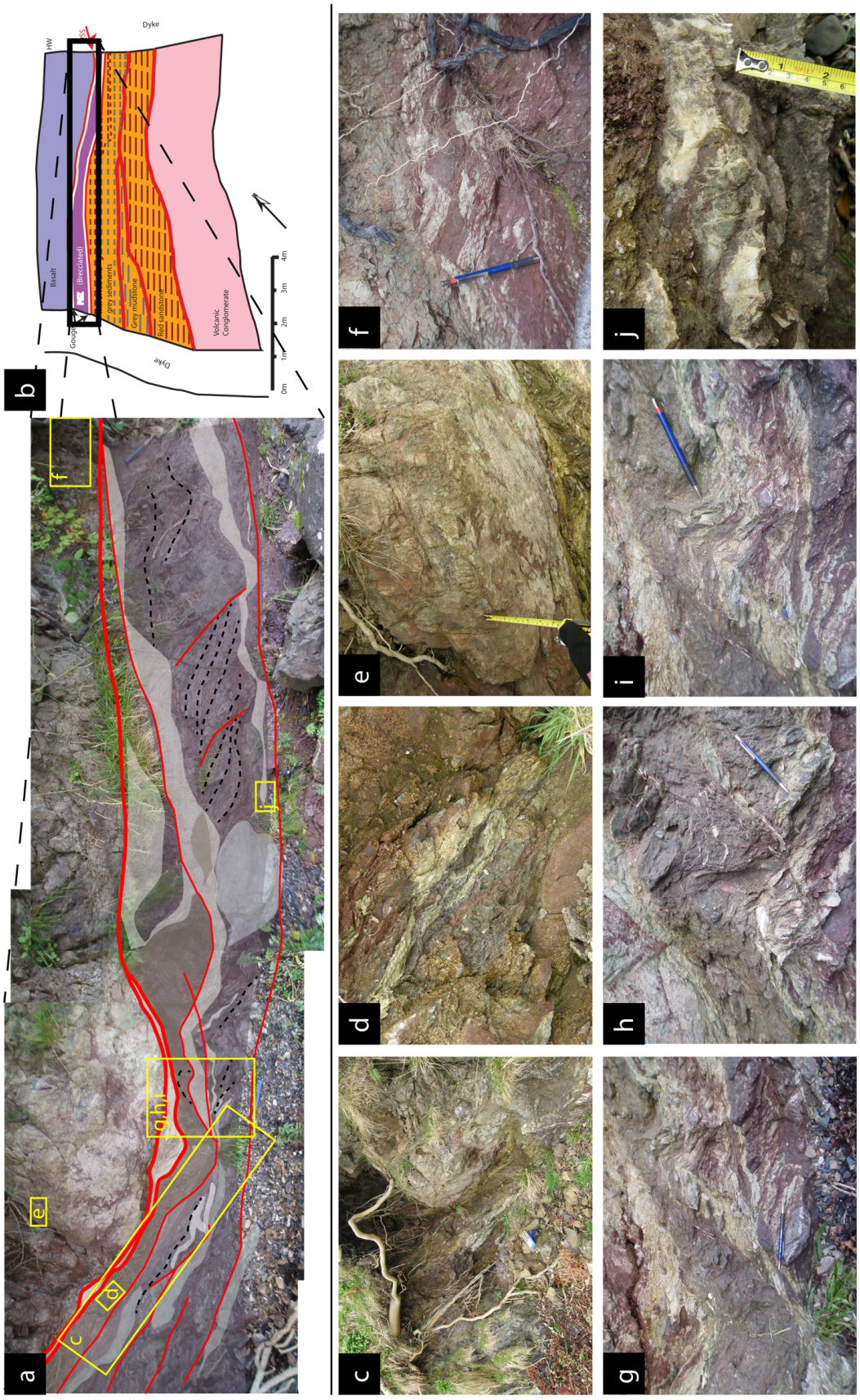
a
b
c
d
e
f
g
h
i
j
Dyke
HW
Basalt
(Brecciated)
Grey sediments
Grey mudstone
Red sandstone
Volcanic Conglomerate
Dyke
0m
1m
2m
3m
4m

Figure 5.4: (Previous Page) Structure of the SE bounding fault, Kerrera. a) Key fault features mapped on stitched photographs. Red = slip surfaces, black = foliations, white = gouge, brown = brown gouge, gray = protolith clast, purple/gray = cataclasite. Yellow boxes mark where detailed photographs c-j were taken. b) Base map for reference. c) General photo, highlighting dip of lithological and fault units toward the fault plane. d) Detail of clay gouge strand (white cream) within c. e) Detail of hanging wall basalt, very altered and brecciated. f) Riedel shears found in hanging wall in clay gouge, suggesting sinistral motion on this fault. g&h) Detail of main gouge zone, showing complex interactions between gouges of different types (red and white), which are entrained along discrete slip surfaces. i) Clay gouge developed folding within fault zone, suggesting weakening within fault gouge. j) Calcite mineralisation cross cutting protolith lenses within fault zone.

5.3.3. Locality iii – fault zone with volcaniclastics

Locality iii is five metres north from Locality ii. However, the fault zone here is not as complex as in Locality ii, and is narrow (10cm) compared to the 1m wide fault zone seen at the previous locality. The fault zone is composed of a narrow, 5cm, red fault gouge, which is foliated and continuous along strike (Figure 5.5), containing protolith lenses. The footwall sandstone is highly fractured and mineralised adjacent to the fault, with bedding in the same orientation as the fault zone. The hanging wall basalt is highly fractured and altered, as it was in locality ii. The main difference between localities ii and iii is the thickness and content of the principal fault zone. Locality ii was 1m thick at its widest point, and consisted of multiple gouge strands, with an altered, partially mineralised footwall and an altered brecciated hanging wall. Locality iii is 10cm thick at its widest point, with one gouge strand, with a highly fractured and mineralised footwall, and an altered brecciated hanging wall.

This difference in style could be due to a change in juxtaposition – the footwall red sandstone at Locality iii behaves in a similar fashion to Locality ii (softer and more altered toward PSS) but the sandstone has a slightly higher volcanic component to it, and is therefore harder and more susceptible to fracturing rather than alteration to clay in the presence of fluid. This results in a narrowing of the PSZ, as soft, footwall rocks are not available for smearing along the fault as clay gouge, and so deformation is taken up in the fault walls as fractures and brecciation.

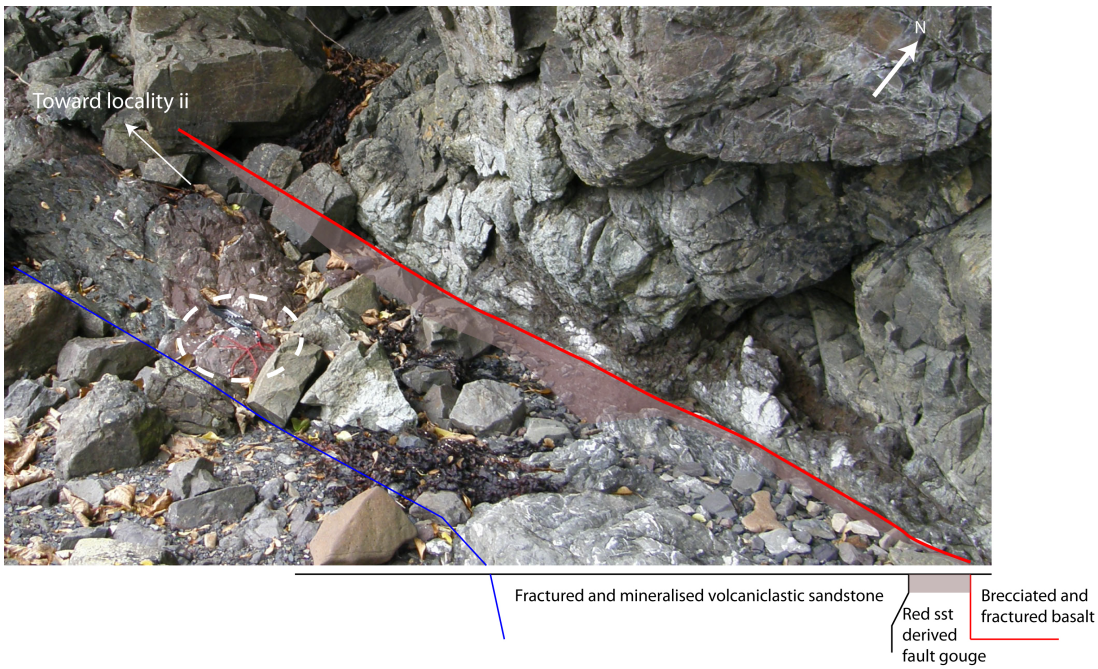

Figure 5.5: Photograph of PSZ and deformation zone in locality iii. Red line marks the SE bounding fault position, and the blue line the extent of the mineralised and fractured footwall. A pale red overlay marks the distribution of the red clay gouge along the slip surface. Photo taken in same orientation as Figure 5.4a. Note compass for scale.

5.3.4. Locality iv – fault zone with basalts

Locality iv is bound by two Palaeogene dykes, at the point where the SE bounding fault of the Kerrera Graben cuts sequences belonging to the Lorn Plateau Lava Formation (Figure 5.6a). The footwall of the fault contains volcanic breccia, volcaniclastic sandstone and basalt, dipping steeply (70°) toward the fault plane. As in all the previous localities, the Lorn Plateau Lava basalts are found in the hanging wall, although with much less alteration and brecciation than in previous sites. In this site therefore, the Lorn Plateau Lava Formation is juxtaposed against itself (refer to Figure 5.2 for cross-section). Adjacent to the fault plane are brecciated basalts and sheared sandstone layers within volcanic conglomerates (Figure 5.6b). The sheared sandstone layers again dip at a steep angle toward the fault. At the fault interface (Figure 5.6c), basalt (from a lower level in the Lorn Lava sequence) is juxtaposed against basalt (from a higher level in the Lorn Lava sequence). In the lower basalt sequence, the basalt is intercalated with

sandstones and weathering horizons, which appear to act as high strain zones within the fractured and sheared basalt, as these zones contain gouges. Along the SE boundary fault itself, a high strain zone following the slip surface is composed of red and cream coloured gouge, with clasts of rounded basalt (Figure 5.6d). This red and cream gouge is very similar to that found at previous localities. If it has the same source as at other sites, it appears to be continuous along the fault for at least 170m along strike (from locality ii to this locality).

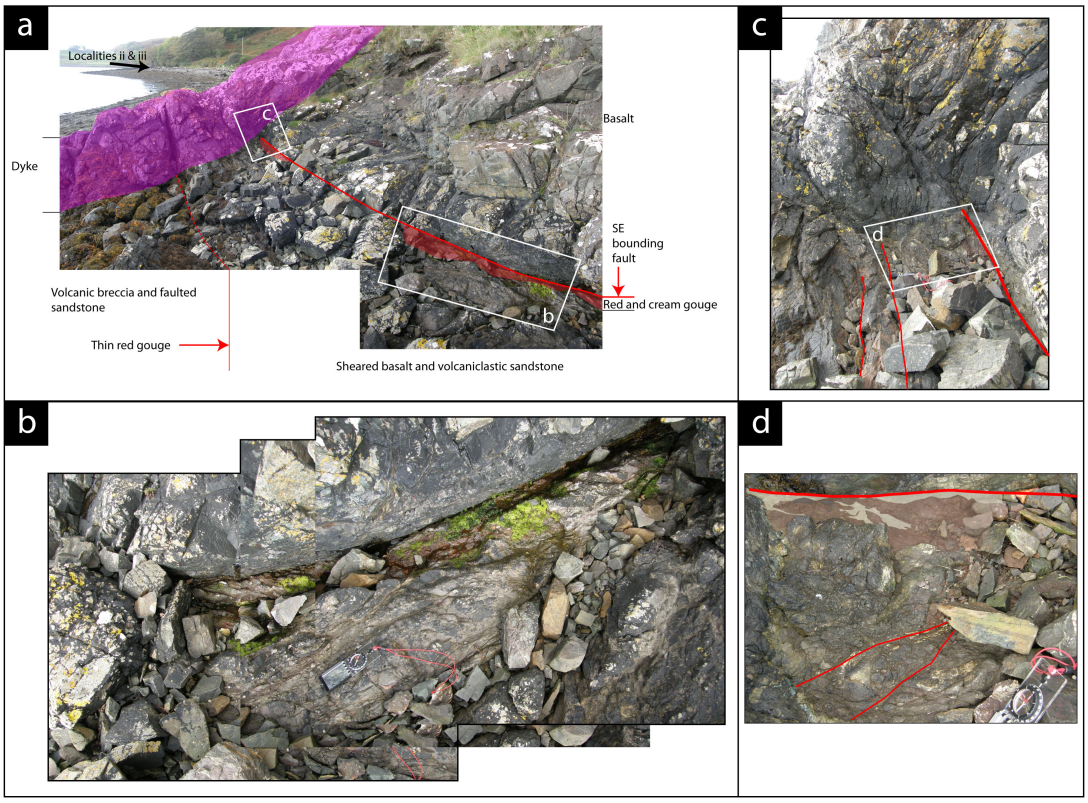

Figure 5.6: Detail of locality iv. a) Photomontage of exposure of SE bounding fault with Lorn Lava sequence juxtaposed against basalt. SE bounding fault is marked, as well as observed principal slip zone thickness. Thickness is covered in middle of image due to rock fall. A secondary slip surface below the zone of sheared basalts and volcaniclastic sandstones is marked by a thin (2cm) layer of fault gouge. Locations of b&c are highlighted in white boxes. b) Plan view. Detail of sheared volcaniclastic sandstones and basalt (underneath compass) below principal slip surface (marked with green moss). Hanging wall basalt at top of the image. c&d) Section and plan view. Detail of SE bounding fault (thick red line), with high strain zone marked by red and cream gouge. Riedel shears within the sheared basalt are marked by thin red lines.

The style of deformation in the footwall is different to the previous localities, due to the difference in lithology. The mix of basalt and sandstone interbeds has led to strain being preferentially taken up along the weaker sandstone, causing shearing and fracturing of the basalt

surrounding the weaker sandstone beds. Some mineralisation is found within the footwall, but not as extensive as in locality iii. The hanging wall deformation is similar, though with a lesser extent of brecciation and only a veneer of alteration along the fault plane, and slickenlined mineral fibres.

5.3.5. Microstructural observations

Samples of clay gouge were taken from the SE bounding fault. Gouge (Figure 5.7a) is composed of foliated clays with a smectite signature (from XRD work in undergraduate). Fractures within the gouge are filled with calcite. Cataclasite (Figure 5.7b) from the SE bounding fault is composed of rounded clasts of quartz and elongated mica grains set in a clay rich matrix, with grain size reducing toward mineral veins, suggesting mineralisation has occurred along slip surfaces. The cataclasite contains S-C fabrics, and foliation of micas parallel to faulting. The host rock clasts of basalt have a very similar microstructure to that of the LWF in Chapter 4, with the main minerals completely replaced by clays. However, here, calcite precipitation has occurred, filling porosity within the clay, unlike in LWF.

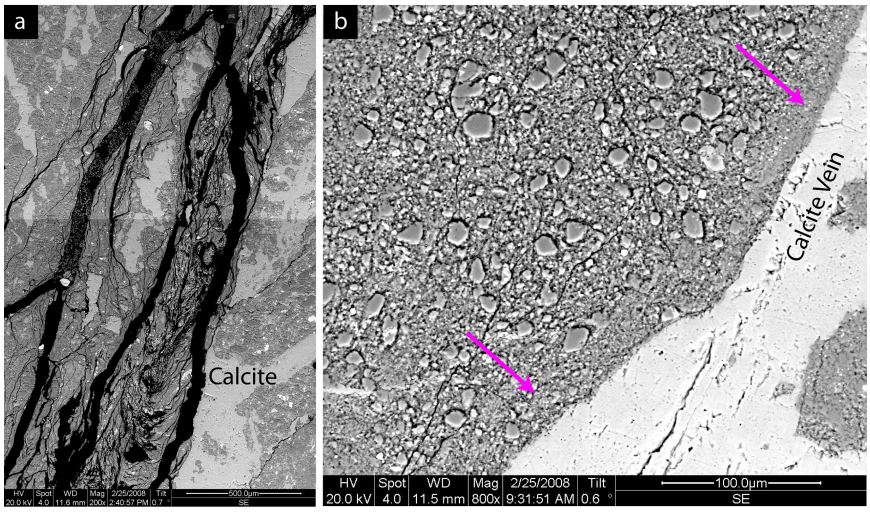

Figure 5.7: SEM images of fault rocks from the SE bounding fault. a) BSE image of fault gouge. Note foliations within gouge running top left to bottom right across the photo, lighter shades are calcite veins. b) Cataclasite from SE bounding fault. Grain size decreases further adjacent to the calcite vein (arrowed).

5.4. NW bounding fault deformation zone – field description

At the south of the island, the NW edge of the graben is exposed on the coast. Beach deposits and grass cover the NW bounding fault itself, and therefore the exact location of the fault is difficult to pinpoint. However, the deformation zone associated with it is partially exposed along a raised rock platform. The observed deformation zone is at least 40m wide, but exposure past this point is poor. The NW fault zone accommodates a total displacement of 125m, with individual structures within the zone accommodating significantly less. The broad geology and structure of this zone is presented in map form in Figure 5.8a, and a cross-sectional interpretation based on field evidence in Figure 5.8b.

The Lorn Plateau Lava Formation basalt and volcaniclastic rocks, and LORS conglomerate are dipping at 40º to the east within the deformation zone, whereas to the NW of the graben (unfaulted) the units are horizontal. This tilting of beds could be the early expressions of fault drag of lithological units toward the NW bounding fault. Dips of 80º in the lithological units (seen in Localities i-iv in the SE bounding fault) are not found, though this is possibly due to there being no exposure of units within 10m of the NW bounding fault being available.

Within the deformation area, the stratigraphy is repeatedly cut by faults, causing repetition of the sequence (Figure 5.8a and b). All faults trend in a similar orientation to the NW bounding fault, and appear to accommodate the majority of strain along these structures, with less in inter-fault lenses.

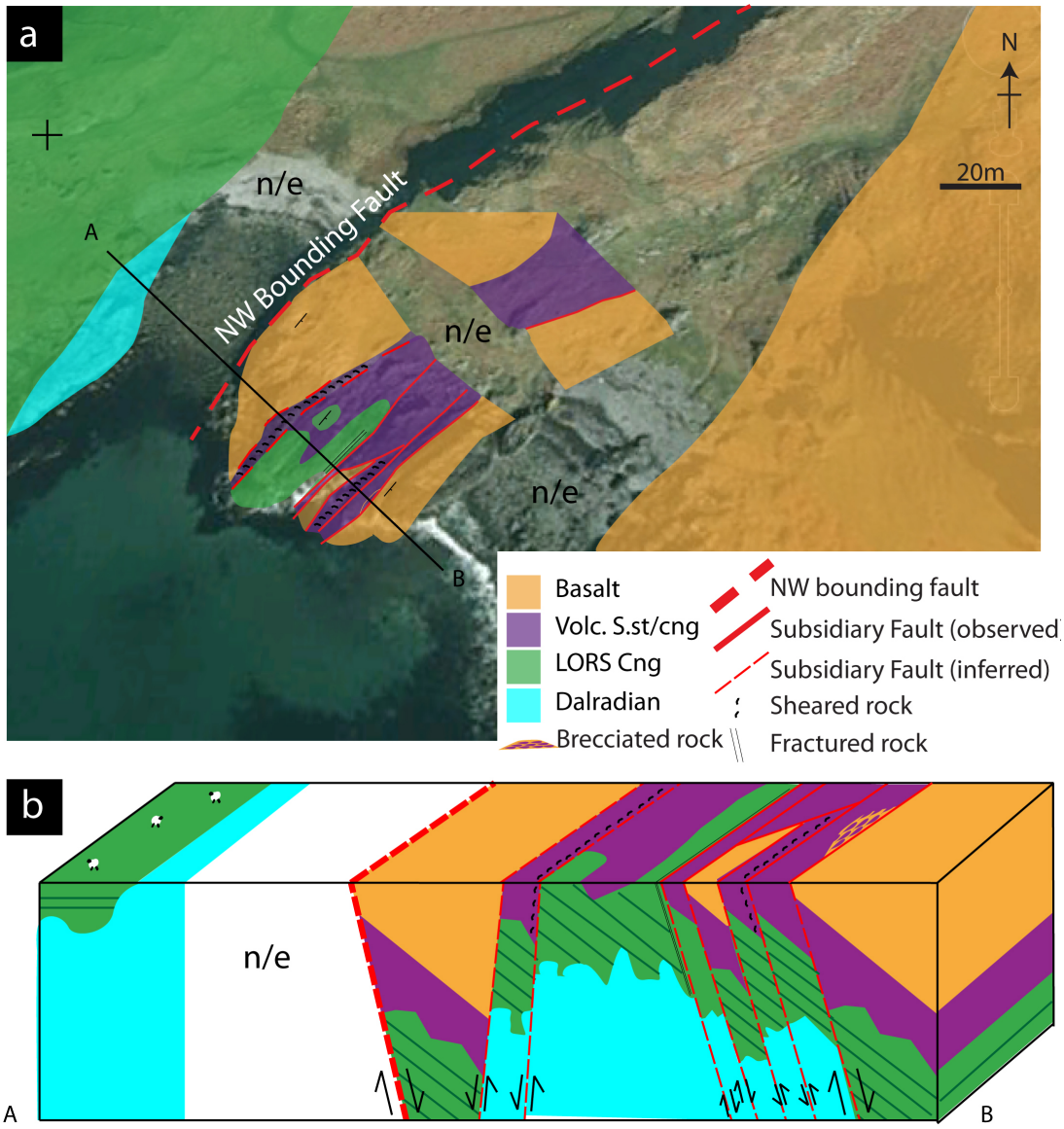

Figure 5.8: Geological map of deformation zone relating to the NW bounding fault on Kerrera. Structures are overlain on Google Earth image. Line of cross section A-B traverses the deformation zone. b) Cross section along A-B, showing dip in lithological units to the SE of the fault, and interpretation of the structures. Note horizontal dip of LORS to the NW of the bounding fault.

Smaller faults with less than 10m strike-slip (defined from rakes of slickenlines) displacement faults also formed along lithological boundaries, connecting major trending NE-SW trending faults in the sedimentary rocks. The style of deformation along and between these NE-SW trending faults and strike-slip faults varies depending on lithology. The NE-SW faults are always formed within the mechanically softer volcaniclastic sedimentary rocks, which are composed of sandstones, and mudstones. Along these faults, the sedimentary rocks are sheared along slip surfaces as red/cream

gouge (Figure 5.9b, c), similar to that seen along the SE bounding fault. The deformation associated with individual faults is up to 1m wide. Lenses of deformed basalt are occasionally found along these dominant faults, and are sheared in situ with intense brecciation and alteration (Figure 5.9d). Strike-slip faults form along boundaries between basalt and volcaniclastic sediment, using the weak contact as a slip plane (i.e. Faults A and B, Figure 5.9e and f respectively) and link the major NE-SW trending faults. These faults are dominated by brittle fault rocks, with cemented gouges and foliated cataclasites common. Alteration of basalt is also observed in a similar style of deformation to non self-juxtaposed faults described in Chapter 3. The faults are mineralised with calcite along slip surfaces and along fractures within the wall rocks.

As well as localised strain accommodated along fault planes within the deformation zone (as smeared sedimentary rocks or fault rocks), distributed strain is observed particularly well within the mechanically harder rocks of basalt and LORS cemented conglomerates. The basalts are very fractured and sheared across large (~5m) areas, with minor faults running throughout them (Figure 5.9g). The LORS conglomerates are intensely fractured adjacent to one of the normal faults cutting them (Figure 5.9h).

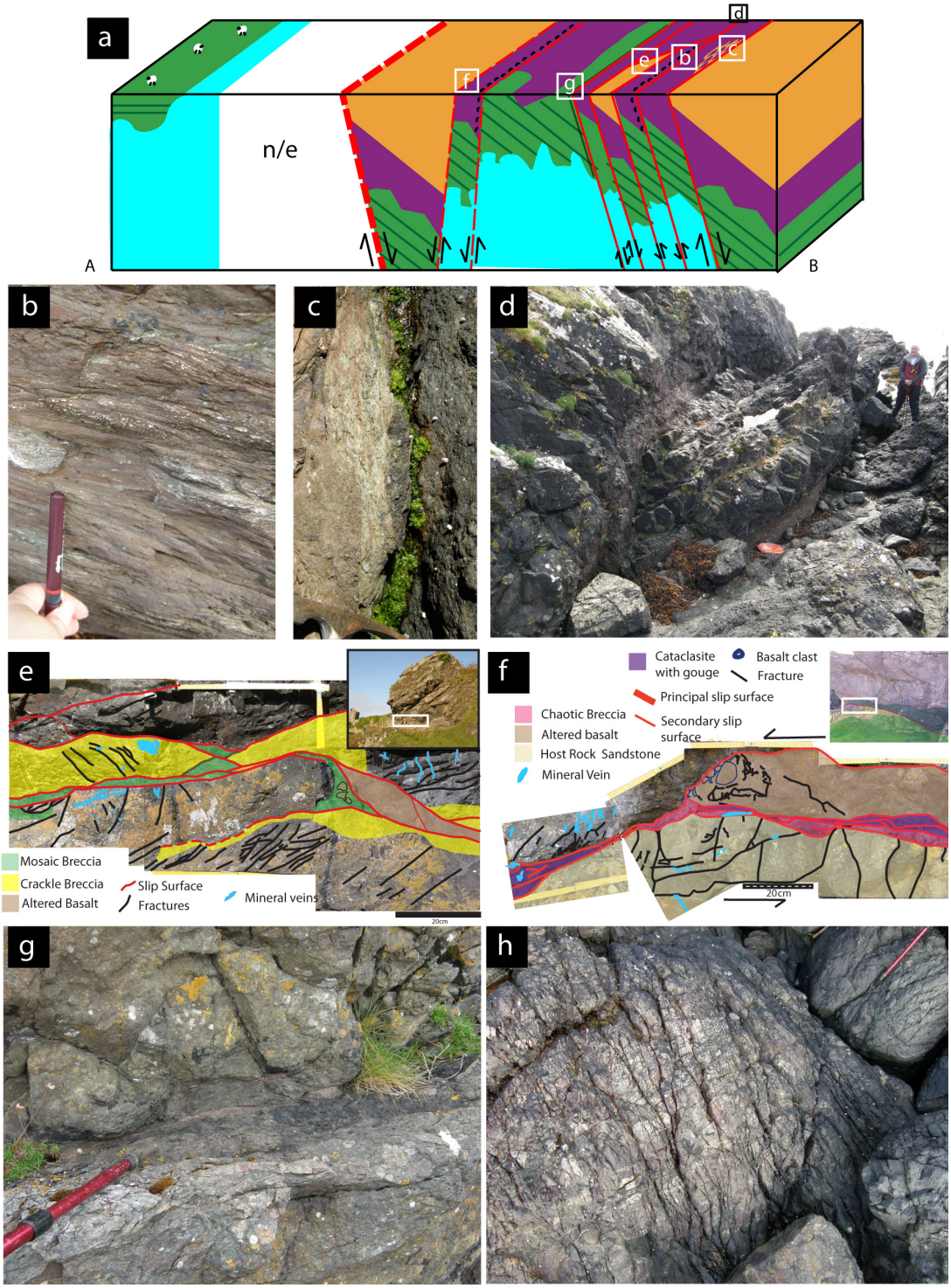

Figure 5.9: Detail of the deformation zone related to the NW bounding fault, Kerrera. a) Cross sectional view of deformation zone, with locations of photographs labelled. b) Sheared volcaniclastic mudstone along NE-SW trending structures. c) White fault gouge within sheared mudstone along NE-SW trending faults. d) Sheared and brecciated basalt lens along NE-SW trending fault. e) Fault zone detail of strike-slip fault, showing zones of individual deformation within the larger deformation zone. f) Another example of a strike-slip fault (section view). g) Sheared and fractured basalt within basalt block to the SE of the NW bounding fault. Walking pole for scale (1m). h) Fracturing of LORS conglomerate adjacent to NE-SW trending fault, walking pole for scale (1m).

5.4.1. Microstructural observations

Fault rocks from the NW bounding fault deformation zone show calcite filling fractures as veins, or in pore space between breccias. The calcite has thick (1-2 micron thick) twins (Figure 5.10c), which are in places offset suggesting continued deformation after vein filling. Pyroxenes and Fe-Ti oxides within the basalts in the deformation zone are largely replaced by chlorites (Figure 5.10b). Chlorite veins are also common throughout the deformation zone. The basalt is typically fractured and mineralised, with little in the way of mechanical deformation. On the other hand, sedimentary units along the dominant faults within the deformation zone have seen intense grain size reduction and formation of gouges and brittle fault rock fabrics including riedel shears (Figure 5.10a). Clays within these sedimentary units are foliated along the riedel shears, with clasts of quartz or feldspar shattered and entrained along shear bands. This microstructural evidence strengthens the hypothesis that faulting focuses along sedimentary beds within a basalt sequence. The sedimentary beds are softer and easier to deform due to their higher phyllosilicate content than basalts.

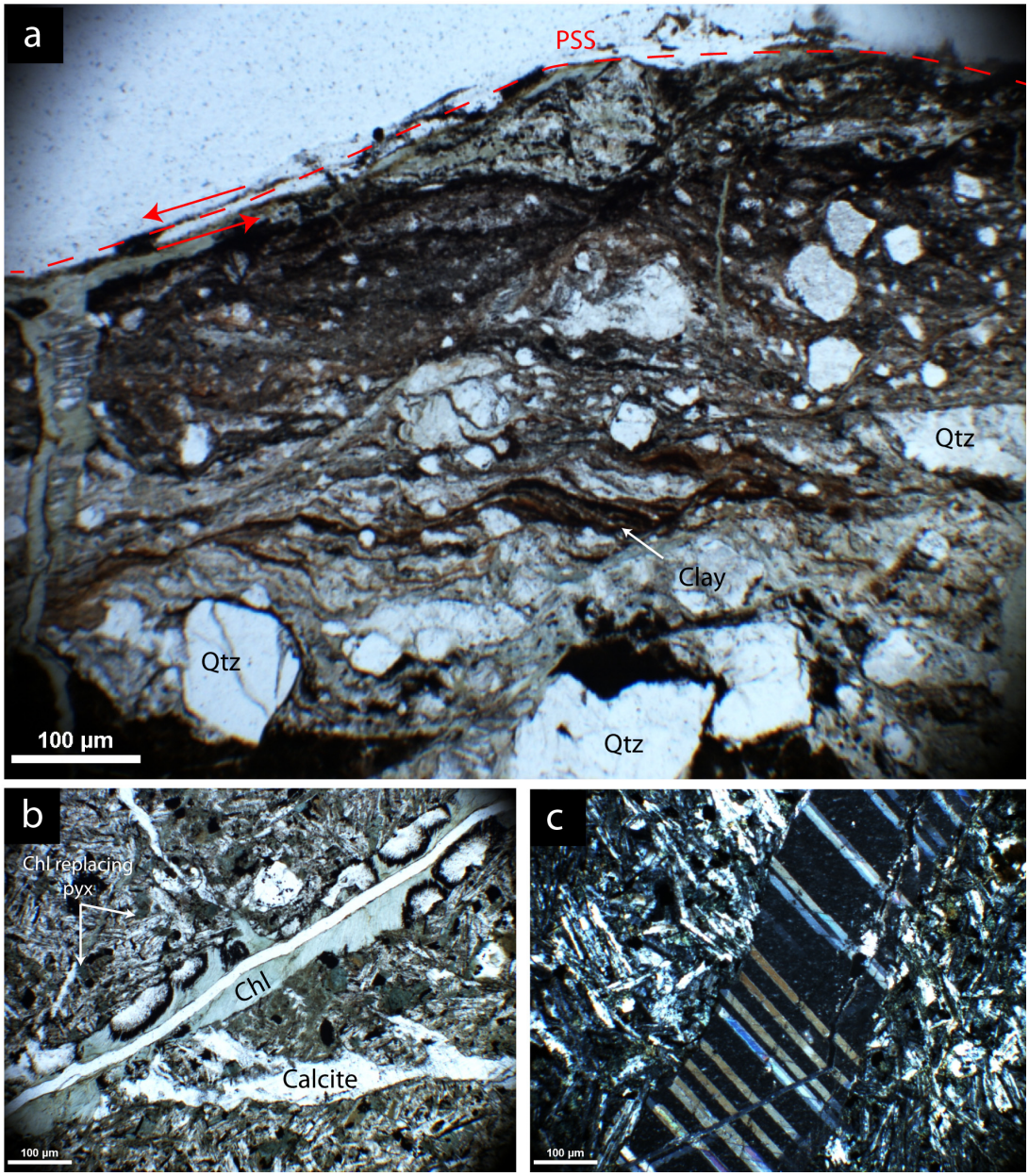

Figure 5.10: Petrographic microscope images from fault rocks in NW bounding fault deformation zone. a) Faulted sandstone. Dark patches are clays, and light clasts are quartz. Note preferential entrainment of clays into shear surfaces (R and Y), and increasing grain size reduction of quartz clasts toward the principal slip surface (top of section). b) Chlorite vein along fractured basalt. Note replacement of pyroxenes and Fe-oxides to chlorite, and lack of mechanical breakdown but increase in fracturing and calcite infill compared to a). c) Calcite mineralisation in basalt from the NW bounding fault deformation zone. Note thickness of twins, and local displacement within vein.

5.5. Cathodoluminescence characteristics of fault-related calcite veins

The study of the cathodoluminescence (CL) characteristics of the fault-related calcite veins determined if mineralisation of the fault zone happened as a single fluid event, or if multiple fluid events (and therefore potentially sources) were involved with precipitation. CL-colours reflect differences in trace element compositions (e.g. Mn and Fe) of the fluids that precipitated the calcite, and may also reveal different growth rates and types of the calcite.

The most abundant calcite mineralisation was found in strike-slip Fault A, and a detailed account of the fluid history within these veins could be discerned (Figure 5.11). Fault rocks show bright luminescence in soft linked calcite fractures within the basalt matrix (Figure 5.11a, b). Similar brightly luminescent calcite veins form through-going, crack seal morphologies throughout the fault rock (Figure 5.11c, d). In those areas where two calcite veins are observed cross cutting one another (Figure 5.11e, f), younger veins display slightly lighter luminescence compared to the older veins. Calcite veins with two distinct episodes of calcite precipitation are distinguishable (Figure 5.11g, h). An older, dark luminescent calcite fills a fracture along the top part of Figure 5.11g, and also appears as isolated crystals of calcite surrounded by the younger (brightly luminescent) calcite. The younger calcite is also precipitated at the edges of the fracture infilled by older (dark) calcite. Finally, crack seal morphologies within calcite veins themselves (that appear as single event veins in PPL) are observed (Figure 5.11i, j), where older (dark) calcite has been cracked in situ, and resealed by newer (bright) calcite.

This sequence of events described from the CL suggest that two mineralising phases occurred throughout the faulting history – the first, a minor dark luminescing calcite that filled fractures calcite veins, and the

second, a more abundant, brightly luminescing young calcite which fills fractures (both isolated and crack seal) as veins in the rock and fractures formed in original calcite veins (crack seal within an apparently one generation vein). Similar CL characteristics are found within Fault B of the NW bounding fault deformation zone, where multiple examples of the young, bright luminescent calcite are found filling pore space and fractures (Figure 5.12a, b), and also where older calcite is found partially filling fractures and surrounded by young calcite (Figure 5.12c, d). This relationship is also found within calcite samples from the SE bounding fault site (Figure 5.12e, f) but, in addition to vein fill, the brightly luminescing calcite is also found as cement within host rock lenses deformed by cataclasis (Figure 5.12g, h).

Based on this evidence, at least two mineralisation events have occurred within the Kerrera Graben. The first event sealed fault-related fractures. The second event resulted in fluids of a slightly different composition flowing within new fault-related fractures, which sealed those fractures (formed both in the rock and within original calcite veins).

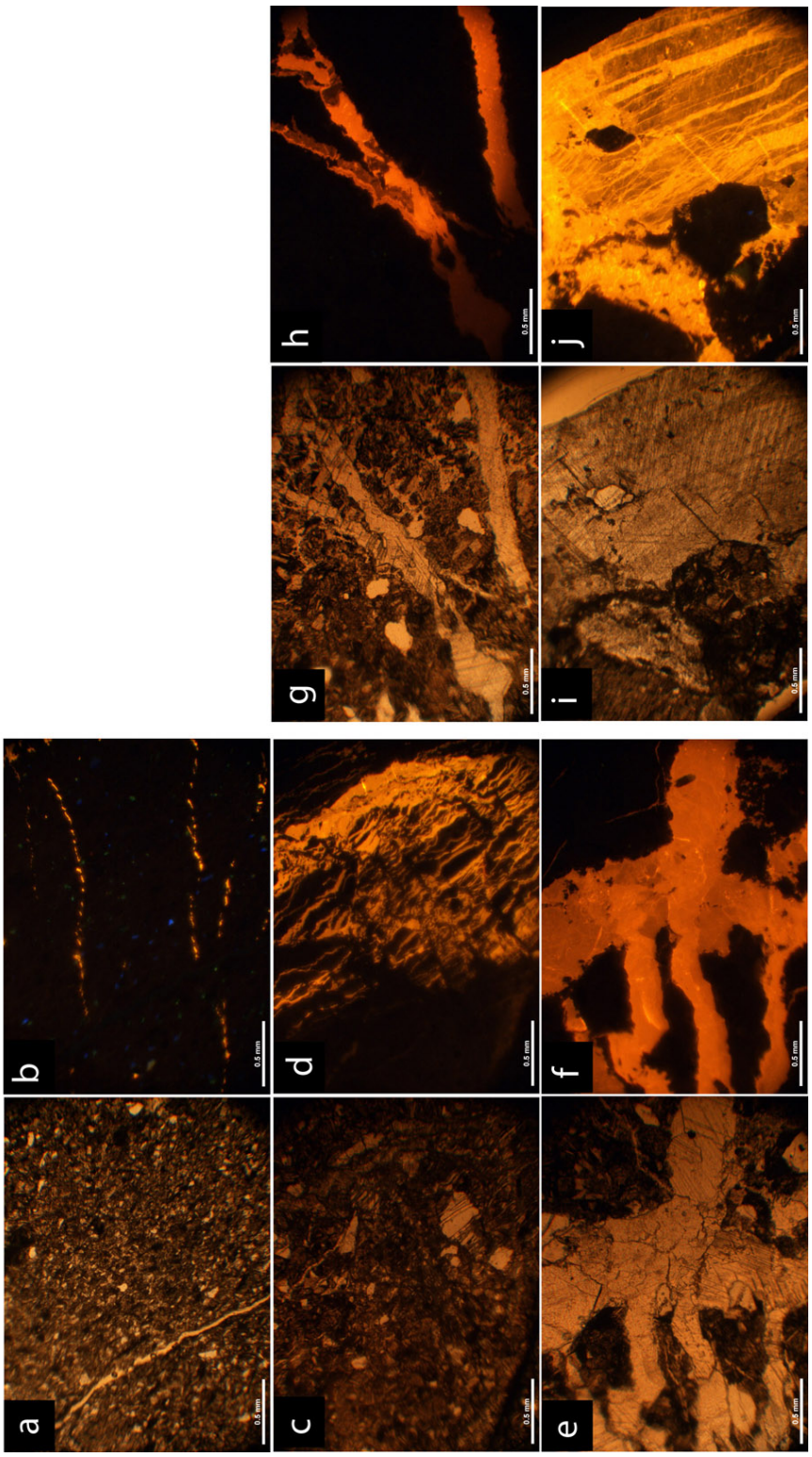

Figure 5.11: Photomicrographs of calcite mineralisation in fault rocks under PPL (a,c,e,g and i) and CL photographs of the same area in b,d,f,h and j. a,b) Bright, young calcite filling soft linked propagating fractures. c,d) Bright calcite filling crack seal fractures. e,f) Cross cutting calcite veins with very similar CL characteristics. g,h) Distinct episodes of calcite precipitation along fractures, with dark, old calcite partially filling fractures and bright, young calcite filling surrounding space. i,j) Crack seal morphology within single calcite vein, with younger bright calcite sealing cracks in older, dark calcite.

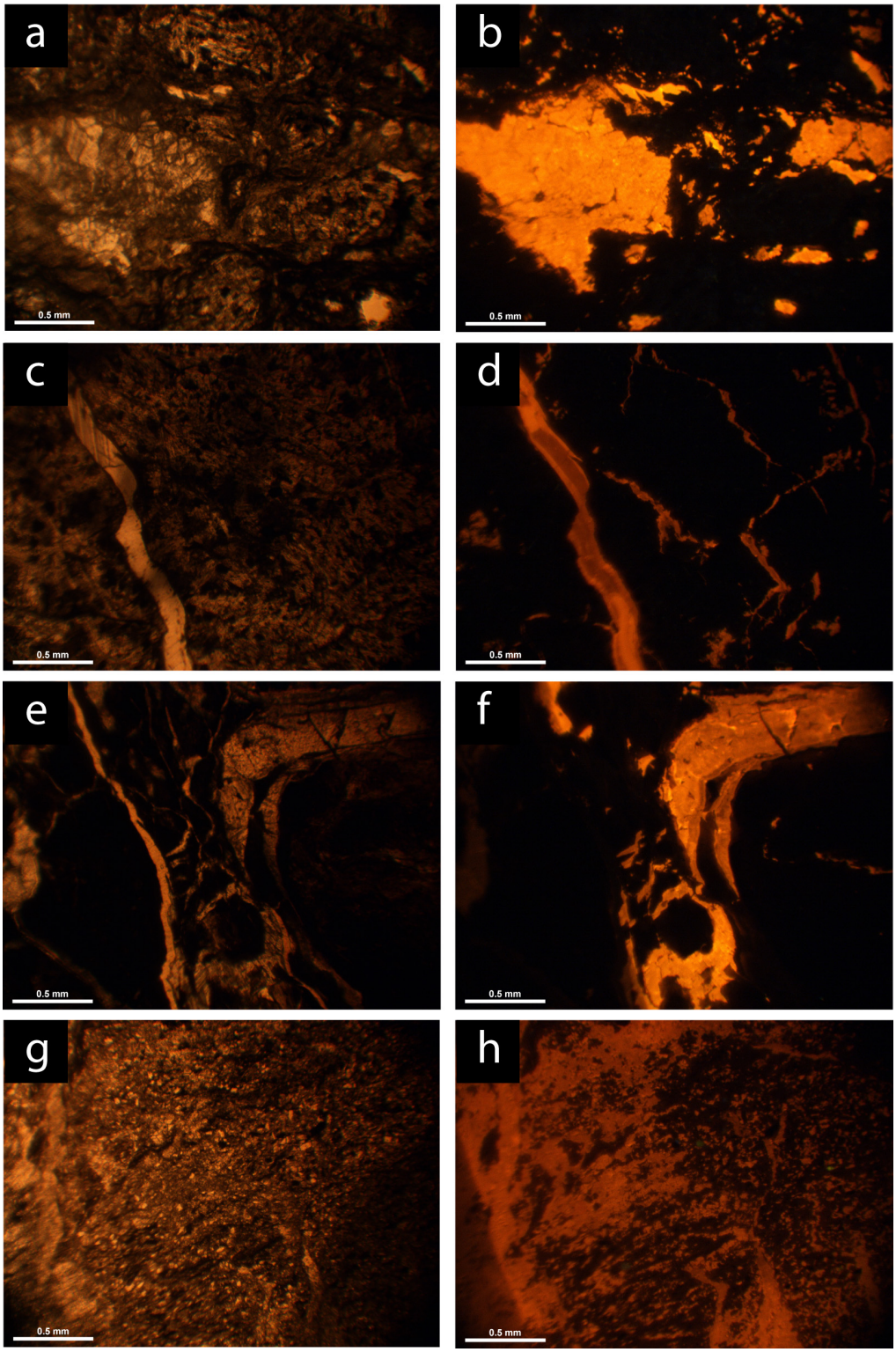

Figure 5.12: Photomicrographs of fault-related calcite veins from Fault B (a-d) and SE bounding fault (e-h). PPL images in left, and CL images on right. a,b) Young, bright calcite filling pore space. c,d) Two episodes of calcite precipitation, dark = old, bright = young. e,f) Example of two-phase mineralisation within SE bounding fault. g,h) Calcite mineralisation filled pore space within cataclasite.

5.6. Stable isotope analysis of calcite veins

Fault-related calcite veins from the NW bounding fault deformation zone in Kerrera were collected for stable isotope analysis at the Scottish Universities Environmental Research Centre (SUERC). The samples were collected from two mineralized strike-slip faults (30m apart) within the deformation zone, and were selected for stable isotope work to:

a) Identify the source of fluid which mineralised these faults;

b) Help understand the fluid flow history within a large displacement fault in basalt.

5.6.1. Methods

Twelve samples were collected from the two strike-slip faults (Faults A and B – location in Figure 5.13) in the deformation zone, and six were selected for stable isotope work, due to the high content of calcite veins within fault in the fault rock samples. Through-going NE-SW trending faults were not mineralised (potentially due to smearing of sandstones and mudstones along them) and therefore not sampled for isotope work. Fractures in host rocks between faults are also filled with calcite, but the relationship to faulting is not certain (e.g. fractures in lava are likely to be cooling-related). Therefore, these were also not selected for isotope work, as confirmed fault-related calcite is required for determining fault fluid-flow history. Calcite veins within each sample (from Fault A and B) were milled using a computer-controlled micromill with a 3mm drill bit (Figure 5.13b). Powdered samples generated from this milling process were collected on aluminium foil and transferred to glass buckets prior to analysis. All of the samples collected weighed between 4 and 20 mg.

Stable isotope analysis of the calcite samples was carried out using the ‘gold standard’ acid digestion and gas line purification method, prior to

analysis on a VG SIRA10 isotope ratio mass spectrometre (IRMS). This method for generating CO_2 from calcite relies upon samples being reacted overnight, in sealed tubes, with 103% phosphoric acid (H_3PO_4) at 25°C (optimum temperature for calcite/acid reaction). When this reaction reached completion, the sample tubes were transferred to a manual purification line (at SUERC) where H_2O generated during the reaction was removed using an acetone/dry ice 'slush trap' at 81°C. The remaining CO_2 was collected in a sample tube using liquid nitrogen and transferred to the manifold of the IRMS. Along with the samples a series of 'in-house' calcite standards, of known isotopic signature, were also analysed. The in-house laboratory standard used for carbonate work is a marble (MAB). The precision of the isotopic results generated is +/- 0.2‰.

Results were corrected relative to the standards VSMOW (Vienna Standard Mean Ocean Water) and VPDB (Vienna Pee Dee Belemnite) using in-house standards, and with the Craig correction applied (Brand et al., 2010) for calcite samples reacted at 25°C. Results from the standards (MAB) are provided for reference (Table 5.1). Note that the standard deviation is small (0.1), showing high accuracy and minimum variation in results.

Table 5.1: MAB Standard Data

Standard ID	$\delta\,^{18}O_{VPDB}$	$\delta\,^{18}O_{VSMOW}$
MAB 2C	-2.8	28
MAB 2C	-2.8	28
MAB 2C	-2.6	28.2
MAB 2C	-2.6	28.2
Average	-2.7	28.1
St Dev.	0.1	0.1

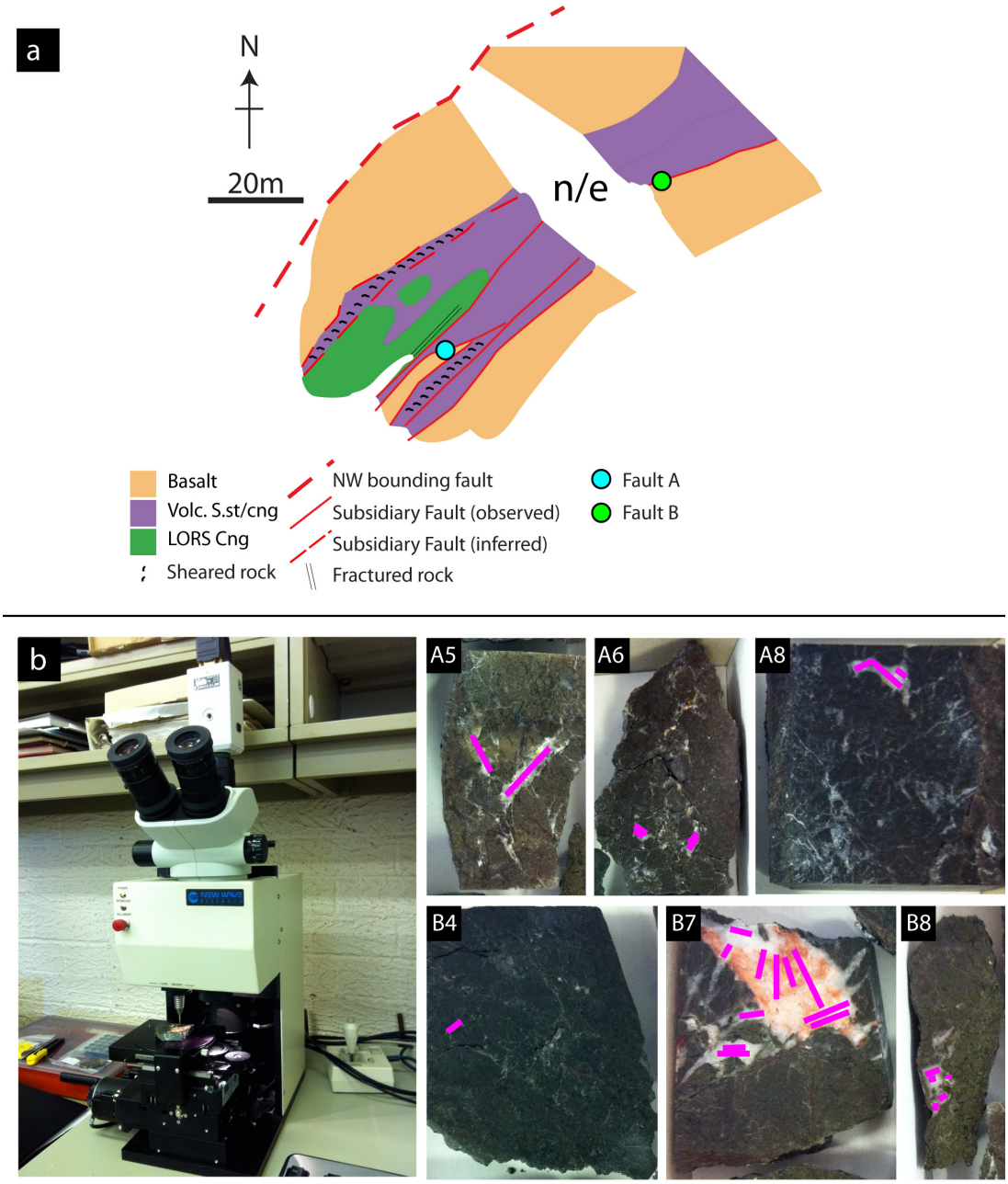

Figure 5.13: a) Location map of NW bounding fault deformation zone on Kerrera. Faults sampled for stable isotope work marked by coloured dots, blue for Fault A, and green for Fault B. b) Micromill used for drilling, with sample B7 loaded for drilling. Each sample drilled is shown adjacent to this, with labels corresponding to which fault it came from and sample number. Pink lines represent locations where calcite was drilled.

5.6.2. Stable isotope results

The measured $\delta^{18}O$ values from the six carbonate samples used in this study are presented in Table 5.2. Results show that the isotopic composition of the veins varies for $\delta^{18}O_{VSMOW}$ from 15‰ to 16.5‰, with an average of

15.7‰. The values for both faults within the NW bounding fault deformation zone show minimal difference (i.e. small standard deviation), suggesting that the calcite veins formed from the same fluid source within both faults.

Table 5.2: Isotope ratios ($\delta^{18}O$) results of fault-related calcite veins from the Kerrera Fault Zone.

Sample ID	$\delta\,^{18}O_{VPDB}$	$\delta\,^{18}O_{VSMOW}$
A5	-15.3	15.1
A6	-14.4	16.0
A8	-14.7	15.8
B4	-15.4	15.0
B7	-14.6	15.8
B8	-14.0	16.5
Average	-14.7	15.7
St Dev.	0.53	0.54

Expected equilibrium values were converted from VSMOW to VPDB scale using the conversion equation from Sharp, (2006):

$$\delta^{18}O_{carb}VSMOW=1.03091(\delta^{18}O_{carb}\ VDPB)+30.91$$

Using the measured $\delta^{18}O$ values from the calcite veins, it is possible to estimate the temperature and $\delta^{18}O$ values of the host water from which precipitation occurred. These results can be calculated using the oxygen isotope fractionation between calcite and water at high temperatures equation (O'Neil et al., 1969):

$$\delta^{18}O\ carbonate - \delta^{18}O\ Water = (2780000/T\text{^}2)-2.89$$

where 2780000 and -2.89 are constants, while T is the temperature in degrees Kelvin, and $\delta^{18}O$ carbonate and $\delta^{18}O$ water are reported with respect to VSMOW.

Using this equation, a range of host water temperatures and $\delta^{18}O$ values for the water which precipitated the calcite can be determined. The value of

'$\delta^{18}O$ carbonate - $\delta^{18}O$ Water' was determined in this study using a range of T, from 273.15 to 573.15 K. By taking the measured minimum and maximum $\delta^{18}O$ (relative to SMOW) carbonate values from Table 5.1, the '$\delta^{18}O$ carbonate - $\delta^{18}O$ Water' values were subtracted from these $\delta^{18}O$ carbonate values. These results were then plotted with respect to temperature in degrees Celsius (equivalent temperatures to the degrees Kelvin temperatures used to determine '$\delta^{18}O$ carbonate - $\delta^{18}O$ Water'), and the results plotted in Figure 5.14. The blue curve represents the plotted results obtained from a minimum $\delta^{18}O$ value of 15, and the red curve represents the plotted results obtained from a maximum $\delta^{18}O$ value of 16.5.

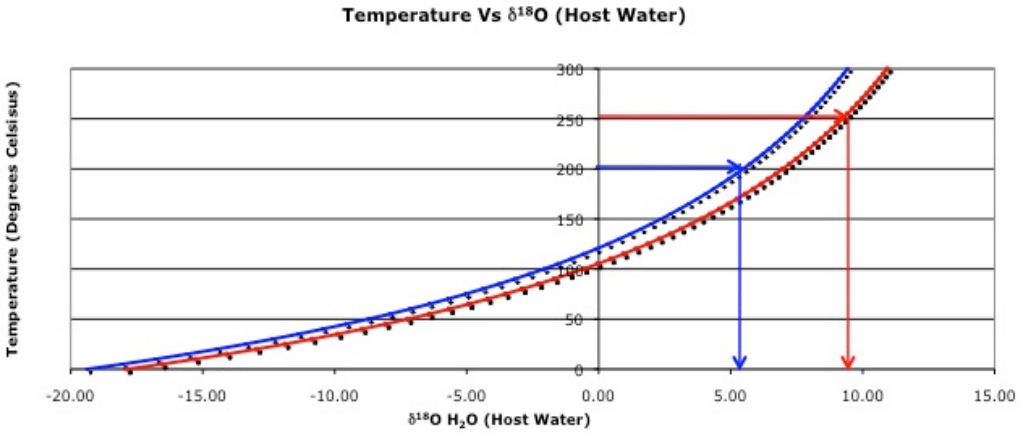

Figure 5.14: $\delta^{18}O$ temperature plot for fault-related calcite veins. The curves represent isotopic composition of the samples in equilibrium of fluid from which the veins were precipitated. Blue curve generated from the minimum $\delta^{18}O$ value obtained from the samples, and red curve generated from the maximum $\delta^{18}O$ value. Arrows represent the $\delta^{18}O$ ranges of the host water derived from likely calcite-precipitation temperature ranges (discussed in section 5.6.3).

5.6.3. Isotope results - discussion

Now that the maximum and minimum $\delta^{18}O$ values of the samples are known, the $\delta^{18}O$ of the host water can be estimated, using the fractionation relationship between host water and calcite given in Figure 5.14.

Microstructural evidence suggests the likely range of formation temperatures for the calcite in the fault rocks is between ~200-320°C. This estimate is based upon mineral replacement relationships in the fault

zones, and temperature depth estimates based on brittle fault rocks and lava thickness. The lava pile in which the fault is contained is exposed near the base of its onshore exposure, as evidenced by local interfingering with the Old Red Sandstone (ORS). The lava pile has been estimated at 800m thick (Browne et al., 2002), therefore the base of the lavas must have been at least 800m below the surface during its existence. Calcite veins are found within fault-related rocks in the lava, and this faulting occurred at a maximum of 5km depth based on cohesive fault rocks (gouges and cataclasites) found throughout the fault zone (Sibson, 1977). Assuming a normal geothermal gradient, (~50ºC per km) the temperature range the fault formed at is ~250ºC, based on 5km depth. However, given that Kerrera was volcanically active during emplacement of the lavas, an elevated geothermal gradient could also be assumed, due to volcanism (which could be 100º per km). If this were the case, based on 5km depth, this would suggest the fault has seen temperatures of 500ºC, which is unrealistic due to metamorphic mineral assemblages resulting from these high temperatures not being present. If an elevated geothermal gradient were in place, it would be more likely that the fault formed between 2-3km, resulting in temperatures of 200-300ºC, which is more in keeping with metamorphic minerals found throughout the basalt. The microstructural study found chlorite partially replacing pyroxene in host rock basalt, indicating medium temperature regional metamorphism in the host rocks to a maximum of 320ºC, and a minimum of 200ºC. There is no microstructural evidence for higher temperature mineral reactions on the vein walls. In addition to this, twin widths within fault-related calcite veins are 1-2 microns thick, typical of Type II twins (Ferrill et al., 2004). Type II twins within calcite veins suggest temperatures (post-precipitation) were between 200-250ºC, equivalent to 4-5km depth, assuming a normal geothermal gradient, or 2-3km depth assuming an elevated geothermal gradient. This microstructural evidence could therefore suggest the fluid which precipitated the calcite veins was 200-250ºC.

Using this range (200-250°C), it is possible to estimate the $\delta^{18}O$ value of the host water, and determine if the fluid source is meteoric, magmatic, or metamorphic (Figure 5.15). Meteoric waters originate from rain and snow fall, and generally have $\delta^{18}O$ values of >0‰, relative to VSMOW (Sheppard, 1986). Magmatic waters have equilibrated with magma at some point during their formation history and have travelled with magma from depth, and have $\delta^{18}O$ values generally between +5.5 and +10‰, with respect to VSMOW (Sheppard et al., 1969). Metamorphic waters are equilibrated with or released from dehydration of metamorphic rocks, and generally have $\delta^{18}O$ values of between +3 and +20‰ (Sheppard, 1986).

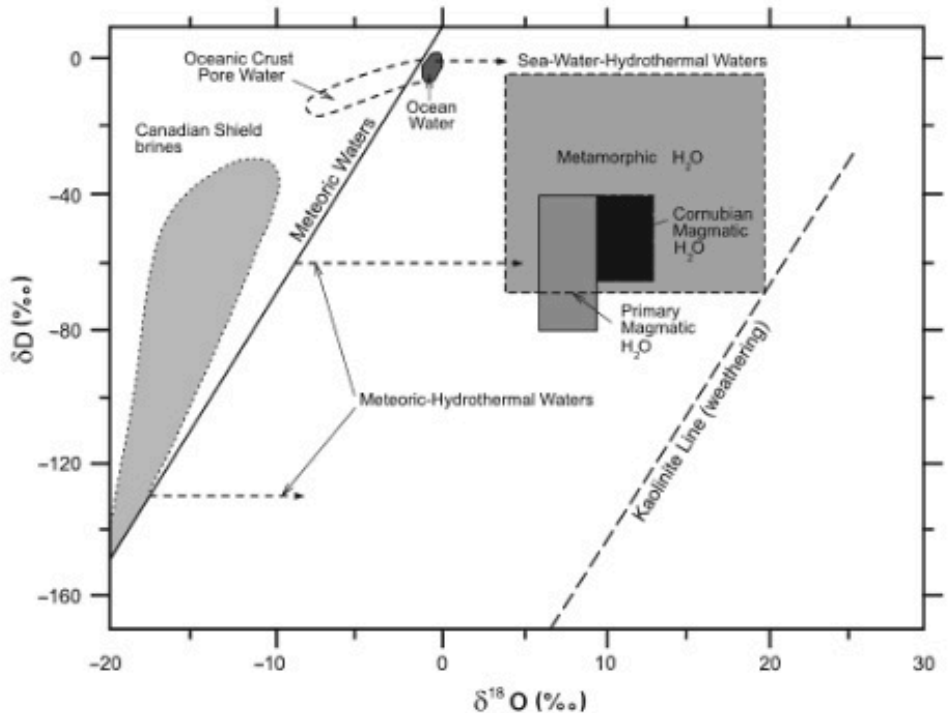

Figure 5.15: Isotopic compositions and fields of natural waters. Note in particular meteoric, magmatic and metamorphic waters - these are discussed in the text. From Sheppard (1986).

If the calcite mineralising fluid were meteoric in origin (i.e. with a $\delta^{18}O$ value from 0% and less), using the known fractionation curves of measured samples in Figure 5.14, temperatures of the fluid would range from an absolute maximum of 100°C through to temperatures well below 0°C. At these $\delta^{18}O$ levels, meteoric signatures would come from marine waters (Sheppard, 1986). There is no evidence to suggest marine waters were in

the area throughout the geological history of the study area (i.e. lack of marine derived rocks), therefore it is highly unlikely the calcite in these faults was deposited from cool, marine waters. In addition to this, microstructural evidence from the samples shows a likely minimum fluid temperature of 200ºC, again making it unlikely that cold fluids (<100ºC) precipitated the calcite.

Based upon microstructural evidence, and the unlikeliness of meteoric-derived fluids precipitating calcite in the samples, magmatic and metamorphic sources must be considered. Assuming a minimum temperature of 200ºC and a maximum temperature of 250ºC of calcite-bearing fluid within the veins (from microstructural evidence), the water from which the calcite has precipitated has $\delta^{18}O$ values between 7‰ and 9‰ (from the red curve on Figure 5.14) and 5‰ and 7‰ (from the blue curve on Figure 5.14). This signature can therefore be bracketed at 5-9‰ $\delta^{18}O_{H2O}$, which when compared with Figure 5.15, suggests a magmatic source for the fluids. A metamorphic source is unlikely, as there is no microstructural evidence to support higher temperature phases, and high (up to 20%) $\delta^{18}O$ values are not obtainable based on the available microstructure evidence for temperatures.

This magmatic source of fluid may have been derived from isotopes in meteoric waters, which equilibrated with igneous rocks as they circulated within the lava pile over time. Alternatively, it is possibly from the Late Caledonian magmatism (~430Ma, following the subduction of Avalonia beneath Laurentia) responsible for the emplacement of the Lorn Lavas in the Kerrera area (Thirlwall, 1988). This would suggest the mineralisation of the deformation associated with the NW bounding fault in Kerrera occurred post-lava emplacement (it could not have occurred during lava emplacement as the depth of faulting was not reached at that time). Lava emplacement occurred over 22Ma (Groome and Hall, 1974), and so the mineralisation is potentially 430 to 410 million years old, a similar age to

the formation of the nearby, similarly NE-SW orientated Great Glen Fault (Jolivet, 2007). A second pulse of magmatic activity is also found in Kerrera, in the form of Palaeogene dyke intrusions (linked to the Mull Central Complex (Emeleus and Bell, 2005)). It is therefore also possible that the Kerrera Fault Zone mineralisation is associated with Palaeogene igneous activity. However, throughout the fault zone, calcite veins are cross cut by Palaeogene dykes, and therefore the veins predate the dykes. Based on this evidence, it is more likely that the magmatic fluid source responsible for calcite precipitation is linked to Late Caledonian magmatism, and suggests the graben found on Kerrera could have formed around the same time as the Great Glen Fault, and may in fact be kinematically related.

5.7. Summary

The SE bounding fault is composed of cataclastic fault rocks and a continuous clay fault gouge along strike, with rotation of lithological units into the fault. The NW bounding fault deformation zone is characterised by mostly dip slip and some strike-slip faults, with regions of brittle deformation (fracturing) between individual faults, and shearing of sedimentary rocks along faults, with clay fault gouge. Occasional basalt lenses are found within the faults, which are brecciated and sheared along intersedimentary units. Fault drag has also occurred here, though to a lesser extent than that seen adjacent to the SE bounding fault. Fault rocks found are cohesive fault gouges and foliated cataclasites, suggesting faulting occurred at depths of <5km.

Particularly within the NW bounding fault deformation zone, it is clear that most strain has focused preferentially along the rotated sedimentary units, which are weaker than the surrounding basalt. Formation of new faults within the hanging wall of the graben displaced sedimentary rocks, resulting in shearing of sedimentary rocks along the faults to form thick, foliated gouges. Additional strain was accommodated in basalt fault blocks,

but due to the mechanical stiffness of basalt, shearing of the rock was difficult to achieve across wide areas and so the basalt fractured. Subsidiary strike-slip faults nucleated along the weak interface between basalt and sedimentary rocks, resulting in localised zones of gouge formation and cataclasite and alteration of the basalt. Whilst other locations of the Kerrera Graben system were not studied due to time constraints, Durant (1999) has recorded the morphology of the lavas at the SE bounding fault exposure along the south coast of Kerrera (the bay north of Rubha Seanach), and described them as being intensely fractured due to the presence of the faults, and that the rocks dip steeply to the west, which would be in keeping with fault drag along the fault seen elsewhere in this study.

CL studies of calcite from the host rock and veins have shown two phases of fluid flow in the fault zone, highlighting a distinct crack seal morphology type phase, where initial faulting of the rock fractured and opened fluid pathways within the fault zone which was subsequently filled by calcite. With further faulting, this calcite phase and new fractures within the rock were opened and again filled with fluid and sealed by calcite. Calcite twins are of Type II morphology, indicating temperatures of between 200ºC and 250ºC occurred after mineralisation. From stable isotope analysis, the calcite precipitating fluids are magmatic, suggesting deep circulation of hot waters during a period of magmatism (potentially Late Caledonian in timing) throughout the Kerrera Graben, at around 2-3km depth.

5.8. Comparison of this study with sub-seismic faults from this study

The style of faulting found in the seismic-scale Kerrera fault differs from the faults previously studied in this thesis. With over 100m of displacement, more lithological units are likely to be faulted than in a fault of 10m displacement. Faulting of multiple lithological units impacts on the fault's overall architecture. As more clay-rich beds are displaced, the phyllosilicate content of the fault rocks will increase, forming thick sheared gouge zones derived from clay-rich beds. Basalt units will deform by brittle processes, i.e. fracturing and brecciation. With large displacement faults, subsidiary faults surround the master bounding faults. If they have a large enough offset, these faults will also have displaced multiple lithological units, and if they cut clay-rich beds, clay gouge will dominate the fault rocks. If the fault displaces cemented volcanic conglomerate and/or basalt, fault rocks will be heavily fractured and brecciated. This relationship is shown as a conceptual cartoon in Figure 5.16.

At microstructural levels, fractures in the basalt are filled with calcite and chlorite in Kerrera. In other faults in this study however, fractures were dominantly filled by zeolites and other clays. It is possible zeolites are not found here due to the alteration of pyroxenes and Fe-Ti oxides to chlorite, and partial replacement of feldspar to chlorite, following regional metamorphism. In the early stages of the fault (i.e. before low grade metamorphism) zeolites may have existed, or alternatively, there was no very low temperature episode that precipitated zeolites in the first place.

Faulting of clay-rich sediments results in smearing of clays within fault rocks, both at macro and micro-scales. Clay gouges are particularly prominent adjacent to slip surfaces, and decrease in abundance with increasing distance (cm-scale) from the slip surface in large-scale faults.

This relationship was also found in the other faults in this study (e.g. Lawther Fault), though on a smaller scale.

The different styles of deformation and fault rocks found within the Kerrera Graben could have profound impacts on the hydraulic behaviour of the fault zone as a whole (Figure 5.16). Gouge rich zones along the dominant graben bounding faults are likely to act as a barriers to across-fault flow, whereas intense fracture zones within the basalts and LORS conglomerates are more likely to act as conduits to both across- and along-fault flow. However, damage surrounding clay-gouge rich fault zones is characterised by fractures and therefore whilst gouge acts as a barrier to across-fault flow, along-fault flow may be facilitated by fractures. Depending on displacement values within the subsidiary faults, they may act as either barriers (if continuous clay gouges form along them) or as combined barriers and conduits to flow (if displacements are within self-juxtaposed limits). In the latter scenario, the conduit would be in self-juxtaposed basalts that are characterised by fractures and breccias and the barriers would be across clay gouge derived from faulting of clay-rich units (Figure 5.16).

In many ways, fault-related features mapped from the Kerrera Graben are similar to features found by Faulkner et al., (2003) in the 40km displacement Carboneras Fault. Though this fault is much larger than the Kerrera Graben, Faulkner et al., (2003) found phyllosilicate rich fault gouge strands bounding fractured lenses of protolith, similar to that found in this study (fractured lenses of basalt bound by clay rich gouge). They also concluded that phyllosilicate gouge is likely to act as a barrier to flow. Faulkner et al., (2003) also found the gouge strands to link and anastomose along strike and at depth, but without further fieldwork, the relationship of the gouge-rich zones to each other on Kerrera cannot be determined at this stage.

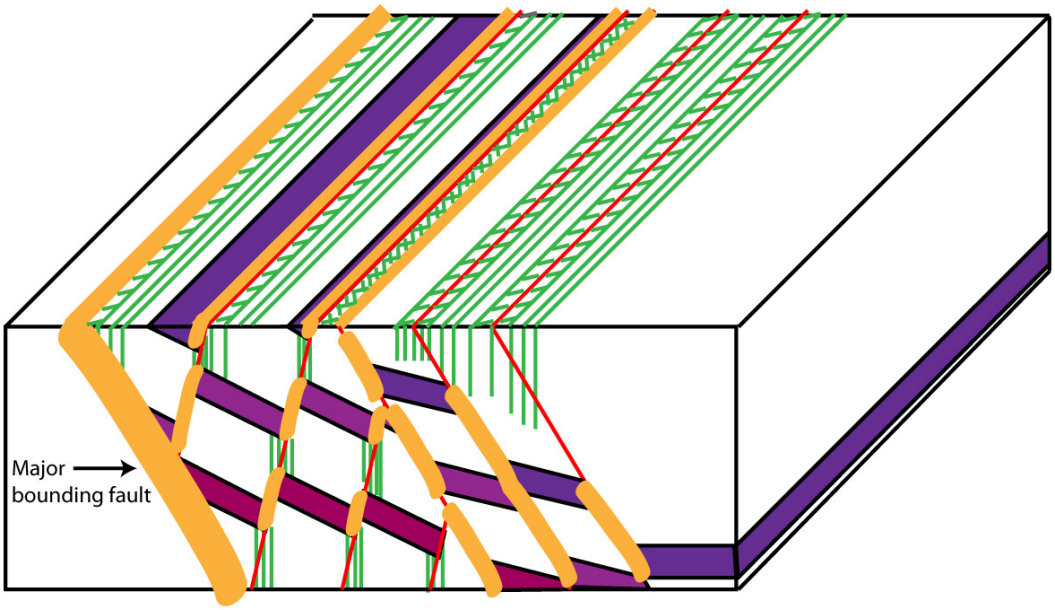

Figure 5.16: Conceptual model of fault zone structure in large displacement faults in basalt sequences. Purple colours represent clay rich units (i.e. volcaniclastic sandstones and mudstones). White represents mechanically strong units (i.e. basalts, cemented volcanic conglomerates). Orange represents impermeable clay gouge, and green lines represent permeable fractures. Clay gouge forms along a large majority of the major bounding fault, which acts as a seal. Subsidiary faults off the PSS act as a combined conduit/barrier across the fault, depending on juxtaposition.

6. Flow Modelling of Faults in Basalt Sequences

6.1. Introduction

It is well known that faults can act as barriers and/or conduits to fluid flow, with the internal fault architecture containing spatially variable low and high permeability structures (Antonellini and Aydin, 1995; Foxford et al., 1998; Shipton and Cowie, 2001; Caine et al., 1996). Fluid flow across a fault zone is dependant on many factors, including juxtaposition of different lithologies across the fault (e.g. basalt faulted against volcaniclastic rocks), fault zone architecture (e.g. fracture dominated vs. gouge dominated) and the hydraulic properties of the fault zone architecture (e.g. fault rock dominated by high permeability open fractures vs. low permeability clay gouge). Past fluid flow behaviour in faults can be studied by mapping mineral veins and zones of alteration throughout the fault zone, as this allows a frozen snapshot of single/multiple fluid flow events within a fault, at a certain time in the fault's lifetime. However, assessing current day fluid flow and fluid flow *throughout* the history of the fault is more difficult to predict. Predictions of fault fluid flow in the subsurface are currently made in the oil and gas industry by using fault throw and host rock data. The throw and host rock property data are used in algorithms such as Shale Gouge Ratio (SGR) for clastic rocks, which predicts the percentage clay in fault gouge produced along sand/shale host rock faults (Manzocchi et al., 1999; Yielding et al., 1997). However, fault zone features are often sub-seismic, and variations in fault rock (e.g. fault gouge, cataclasite, breccia etc) thicknesses are often not picked up due to constraints in seismic resolution. Such simple algorithms do not account for this architectural heterogeneity. In addition, these algorithms currently only exist for sand/shale juxtapositions, and not for crystalline rocks such as basalts, which are increasingly important for hydrocarbon production.

To predict fluid flow at sub-seismic resolutions, Lunn et al., (2008) and Kremer et al., (2011) have used simulations of flow within detailed fault maps to demonstrate the influence of small scale structural controls (such as slip surfaces, fault rock properties, and fractures) on fluid flow. In this section, the method used by Lunn et al., (2008) and Kremer et al., (2011) is implemented to investigate fluid flow within the mapped fault zones in basalt in this study (from Chapter 3). The purpose of the modelling is to find what the key flow controls (KFCs) are in the faults, where they are located, and how they control fluid migration in along- and across-fault fluid modelling. The other purpose is to find how KFCs change over time, and what effect this may have on bulk permeability over time.

To simulate fluid flow through the fault maps, the modular finite-difference groundwater flow model 'MODFLOW' (developed by the USGS) has been used. MODFLOW was developed for simulating features in ground-water systems (McDonald and Harbaugh, 1988; Harbaugh and McDonald, 1996). MODFLOW has been applied using a set of Matlab scripts that allow groundwater models belonging to the MODFLOW family to run files, read results, and analyse and visualise results. These functions and scripts are run in 'mfLab' (MODFLOW-laboratory), developed by Theo Olsthoorn at the Delft University of Technology. Using mfLab, the fault zone permeability structure is represented on a pixel-by-pixel basis, and architectural components within the fault zone are assigned permeability values (k). For example, blue pixels on a fault map representing mineral veins are assigned a number within mfLab, e.g. 1. Pink pixels representing a breccia are assigned another number, e.g. 2, and so on, until all architectural components are assigned a number. Once the number of each colour is determined within mfLab, that number is then assigned a corresponding permeability. The architectural components were assumed to have an isotropic permeability, where kx=ky=kz, and models were simulated at a static point in each fault's evolution, i.e. not syn-deformationally.

To simulate two-dimensional along- and across-fault flow in mfLab, the approach taken by Lunn et al (2008) and Kremer et al (2011) was used. Fault maps were rotated to ensure the edges of the mapped fault zone crossed only one boundary of the model – if the fault zone crossed multiple boundaries, effective across- and along-fault permeabilities could not be calculated. For modelling along-fault flow, fixed hydraulic heads were assigned to the top and bottom boundaries of the map image, with left and right hand boundaries being no flow. The opposite is true for modelling across-fault flow. In along-fault flow, the direction of flow was from the base of the exposed fault, to the top, to represent movement of water from depth to the surface (as in hydrothermal systems). For a given fault permeability, the head gradient governs the volumetric flow rate (m^3/s) that passes through the mapped fault zone. The inflow and outflow of fluid through the model should be the same. All numerical solutions incur some error, but these were kept to a minimum; in all cases errors were 0.01% or less. Bulk permeability was determined from the model using Darcy's Law:

$$Q = -KA\frac{dh}{dl}$$

where Q= fluid discharge (*volume/time*), K= hydraulic conductivity (m/s), A= area, dh/dl = hydraulic gradient (change in head over length of interest). For bulk permeability (k, m^2), the following equation was used:

$$k = \frac{K\mu}{\rho g}$$

where μ = viscosity of the fluid ($Pa.s$), ρ = density of the fluid (kg/m^3), and g = gravity (m^2/s). For the purposes of this modelling, permeability was input as cm^2, ($1m^2 = 10000cm^2$), and converted into mD for bulk permeability results ($1mD = 1x10^{-11}cm^2$).

All of the fault maps used for this study contain fractures. Darcy's Law can be implemented for modelling flow through fractured media by upscaling a pixel's permeability to represent a fracture surrounded by a host rock,

rather than simulating flow through a whole fracture. The methodology for this upscaling is described further in section 6.2.

Flow is shown visually in streamlines, where the volume of fluid passing in a given time is constant between each pair of adjacent streamlines. The closer spaced the streamlines to one another, the higher the flow rate. For example, if 100 streamlines are evenly spaced out across a zone, 1% of the fluid, in a given time interval, passes between each pair of streamlines. Hence, if the streamlines are tightly spaced at one end of a zone, and widely spaced at the other, the majority of flow occurs between the tightly spaced streamlines, and only a small volume of flow passes between the widely spaced ones. Where no streamlines are found, <1% of flow is occurs. When this is found within the fault maps, it is described as 'flow was not observed'.

A conceptual cartoon to illustrate model conditions is presented in Figure 6.1. In along-fault flow scenarios, hydraulic heads are set up so flow runs parallel to the fault (i.e. left to right, using BNF as an example in Figure 6.1). In across-fault flow, hydraulic heads are set up perpendicular to the fault (top to bottom in Figure 6.1). If the model has constant permeability, streamlines will have a constant thickness throughout the model. However, if a permeable feature is present, these same streamlines will focus along that feature, causing the distance between the streamlines to narrow. This represents the area in which flow would focus when modelling fluid flow.

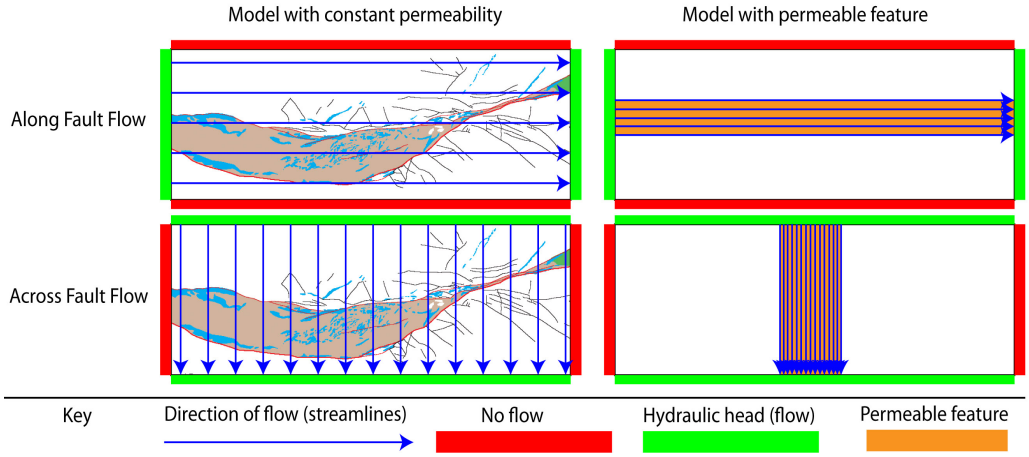

Figure 6.1: Conceptual model of boundary conditions and streamlines used in modelling setup. BNF used as example to illustrate along- and across-fault flow. No permeability changes are assigned to BNF here to conceptually illustrate streamline behaviour in a model with constant permeability.

The most detailed fault maps from this study (Chapter 3) were chosen for modelling. The Sumba Fault (SFZ), Hov Fault (HVF) and Talisker Bay Fault (TBF) were excluded due to lack of accurate, mappable detail of permeability features obscured by undulating topography and water/vegetation. The fault maps constructed of Vagseiði Jetty Fault (VJF), Vagseiði Puddle Fault (VPF), Bird Nest Fault (BNF), Hramaborg Fault (HBF), I Botni Fault (IBF), and the Lawther Fault (LWF) were modelled for this study. As most of these fault maps focused on the detail of fault rock morphologies and distributions, the surrounding fractured damage zone was not taken into account for the models of BNF, HBF, IBF and LWF. It is however noted that the damage zone, dominated by open fractures in the observed faults, will likely act as a conduit to along-fault fluid flow when the fault zone as a whole is considered. Due to excellent exposure, the VJF and VPF map included the damage zone, and flow was modelled to run through the damage zones. By modelling these six faults, comparisons in fluid flow behaviour and controls on flow, within fault zones in both self- and non self-juxtaposed faults can be made. Detailed microstructural evidence from each of these faults (from Chapter 4) is used to determine the permeability evolution of each component within the fault over time, and how this then affects the bulk permeability characteristics of the fault

over time (e.g. mineralised veins were once open to allow fluid flow to precipitate the mineral initially).

The BNF is first used as an example of how microscopic analysis can be used to infer permeability history, and how by using this information within the flow modelling, the bulk permeability history of a fault during its lifetime can be estimated. The remaining faults were modelled using the same methodology as the BNF, and are presented in a summarised form. Individual controls on fluid flow in all faults will then be compared, along with bulk permeability measurements. Hydraulic head gradients will also be compared, to illustrate compartmentalisation of fluid within each fault zone.

6.2. Permeability of basalts and basalt fault rocks

Previous studies of permeability of basalts, and particularly fault rocks in basalts, are few. Most measurements have been carried out in ocean basalts (i.e. Johnson, 1980; Christensen and Ramananantoandro, 1988; Fisher, 1998), but only recently have Walker et al., (2012b) carried out permeability measurements within basalt hosted fault zones. Basalts are generally very low in permeability, ranging from $1x10^{-14}$ cm^2 to $1x10^{-17}$ cm^2 (Johnson, 1980; Christenson and Ramananantoandro 1988; Fisher, 1998; Walker et al., 2012b). In vesicular basalts, permeability values are significantly higher, with values measured at $1x10^{-9}$ cm^2 by Saar (1998). Basalts are therefore typically low permeability rocks when compared with typical reservoir rocks such as sandstones (typically $1x10^{-7}$ to $1x10^{-11}$ cm^2). Mudstones and shales are also low permeability, with permeabilities often less than $1x10^{-17}$ cm^2 (Gondouin and Scala, 1958).

Fault rock permeabilities in basalt have been measured by Walker et al., (2012), and they find that faults in basalt evolve from low permeability ($<1x10^{-13}$ cm^2) structures in low strain zones (e.g. host rock, crackle-mosaic breccias), to high permeability structures in high strain zones (e.g. chaotic breccias and cataclasite/gouge), where higher permeability values were

measured (>$1x10^{-13}$ cm^2). As a result, the relative increase in permeability from faulting (and specifically fracturing) a basalt unit is higher (≤3 orders of magnitude) than faulting a typical reservoir unit (i.e. sandstone). Permeability in faulted sandstone is enhanced by ~one order of magnitude (e.g. Flodin, 2003) due to its initially higher permeability value with respect to unfaulted basalt. Fault rock permeabilities from other lithologies have also been measured. For example, Wibberley and Shimamoto (2003) measured the permeability of fault rocks derived from schists and granites, and found permeabilities of gouges and cataclasites were within one order of magnitude of permeability to that of the host rock. The more impermeable units include mylonites and ultra-fine gouge. This relationship was also noted by Hirose & Hayman (2008) in gabbros and ultramafic host rocks.

To obtain a meaningful estimate of bulk permeability throughout the mapped faults in this study, permeability values for each mapped component (host and fault rocks) were obtained from the literature. An average permeability value from six basalt samples were used for host rock basalts in this study ($3.2x10^{-16}$ cm^2), from Johnson (1980). As no vesicular basalts were encountered in this study, permeabilities of those are not considered. Altered basalt values were taken from Johnson (1980) due to the description of the altered basalt containing clays clogging pores, as is observed in this study. Mineral veins from Johnson (1980) were measured as two orders of magnitude higher than fresh basalt, and other authors have reported the presence of mineral veins to be higher in permeability than the host basalt rock (e.g. zeolite filled fractures from Walker et al., 2012b). Therefore in this study the permeability of mineral veins (zeolites) are modelled at $3.2x10^{-14}$ cm^2, though in reality this figure may vary between different zeolite minerals. Fault breccias vary in morphology and fracture content, and so a precise estimate on breccia permeability is difficult to obtain. Therefore, an average of fault breccias (including crackle, mosaic and chaotic) from the literature was taken from present

day permeabilities from similar conditions (Johnson, 1980 and Walker et al., 2012b) and breccias are modelled in this study as $3.73x10^{-13}$ cm^2. Clay gouge permeability has been measured by Faulkner and Rutter (1998) as $9.7x10^{-15}cm^2$, and this value is used to model clay gouge within this study. Cataclasite permeability values for this study were modelled as $5.65x10^{-12}$ cm^2, and this value was taken from an average of cataclasite readings from Wibberley and Shimamoto (2003) and Walker et al., (2012b). As no previous studies on the permeability of peperite have been carried out, an estimate for its permeability is based on microstructures. Whilst being clay rich, the peperite is heavily fractured in the field, suggesting it has a higher permeability than basalt. A tentative estimate of $1x10^{-12}$ cm^2 is therefore used for the peperite, due to its high fracture content.

To estimate fracture permeability, it was assumed that the fractures in the map have an aperture of 0.1mm, as this is the average value of fracture apertures mapped in the field. However, as fracture apertures change over time depending on burial depth, orientation, and stress field, this value can change. As the models used here are for the purposes of illustrating permeability changes and controls over time, rather than an absolute value of bulk permeability, the full range of fracture apertures found in each fault was not accounted for. This range in fracture aperture size could be accounted for in future work.

Fracture permeability was calculated assuming that one pixel size (variable in size between fault maps, mm scale) was greater than the aperture of the fracture (Figure 6.2). This can be calculated from the weighted arithmetic mean (Cardwell and Parsons, 1945). This assumes the pixel representing the fracture on the fault map actually contains host rock that is fractured, rather than a single open fracture, and therefore Darcy's Law can be applied within these pixels. Effectively, the bulk permeability of the pixel containing the fracture is upscaled to reflect a fracture permeability value. The bulk permeability of a pixel containing a fracture (kbulk) is:

$$kbulk = \frac{\frac{a^3}{12} + kh(P - a)}{P}$$

where a = fracture aperture, kh = permeability of host rock material, and P = pixel size (see Figure 6.2).

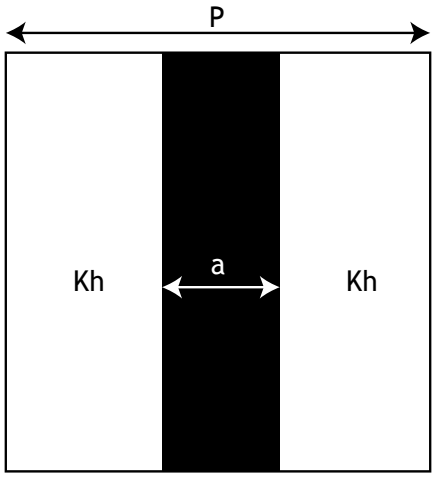

Figure 6.2: Conceptual cartoon of a pixel in model containing fractured (black) host rock (white). The weighted arithmetic mean is then calculated from this pixel to determine the bulk permeability of the pixel, and this permeability is then assigned to that cell to represent fracture permeability.

Assuming fractures are surrounded by host rock with permeability equal to that of basalt, the bulk permeability for that grid cell containing a 0.1mm fracture should equal 2.9×10^{-07} cm^2. In most models, the fractures are bound by basalt, but in some cases fractures cross into altered basalt (i.e. fresh basalt on one side and altered basalt on the other side of the fracture), or are contained within altered basalt. This change in permeability on either side of the fracture could result in a change of fracture permeability, based on the above equation. However, there is only half an order of magnitude difference between fresh basalt and altered basalt, and therefore the resulting change of permeability in the fracture is likely to be low. If the most accurate estimates from bulk permeability were desired, future work could focus on making a computer code which would input the weighted arithmetic mean equation into a pixel containing two different lithologies on either side of the fracture (or slip surface), and change the fracture permeability accordingly within the fault map.

Where fractures are closed, they are assigned a permeability value equal to basalt (i.e. $3.2x10^{-16}cm^2$) as in most models, this is what the fractures are surrounded by. However in some models this is not always true, and this is discussed in the relevant map. Slip surfaces, prior to filling by minerals or clay, are modelled at the same permeability as fractures (again, assuming an aperture of 0.1mm). When the slip surface is modelled as closed (due to fill by minerals or clay gouge), the appropriate value is used (i.e. permeability value of the slip surface fill material).

The permeabilities from previous studies used in this chapter's flow modelling are listed in Table 6.1.

Table 6.1: Permeability values used for this study's flow modelling. Permeability values obtained from previous work of permeability in basalts and clay gouges.

Fault Zone Element and colour	Permeability (cm^2)	Reference and additional information
Host Rock Basalt (gray)	$3.2x10^{-16}$	Average value from Johnson (1980).
Altered Basalt (brown)	$0.2x10^{-17}$	Clay filling pore space (Johnson, 1980).
Mineral Veins (blue)	$3.2x10^{-14}$	(Two orders higher than host).
Breccia (green, yellow, pink)	$3.7x10^{-13}$	Average values from Johnson (1980) and Walker et al., (2012b).
Clay Gouge (orange, navy blue)	$9.7x10^{-15}$	(Faulkner and Rutter, 1998).
Cataclasite (yellow/green)	$5.7x10^{-12}$	Average values from Walker et al., (2012b) and Wibberley and Shimamoto (2003).
Slip Surface (red)	$3x10^{-05}$ if open, corresponding fill permeability if closed	Same as fractures when modelling open. Depending on closed nature - zeolite filled, same as mineral veins. Clay filled, same as clay gouge.
Fractures (black)	$2.9x10^{-07}$	Calculated, assuming aperture of 0.5mm.
Peperite (light gray)	$1x10^{-12}$	Estimated (based on thin-section observations).

In those scenarios where mineral veins are modelled prior to being filled, they are assigned a permeability of an open fracture. Similarly, when modelling altered basalt prior to alteration, but following intragranular fractures of the basalt (i.e. increasing permeability), an estimated permeability of $1x10^{-14}cm^2$ is applied, based on modelled permeabilities of microfractured media in crystalline rocks from Mitchell and Faulkner (2008).

6.3. mfLab simulations of the BNF

Six stages in the Bird Nest Fault (BNF) permeability evolution were identified in the microscopic analysis of the BNF (Chapter 4):

Stage 1 represents the fault in its earliest phase. Early faulting (accommodated along slip surfaces) deforms host rock minerals, generating intragranular fractures and increasing pore space. Fractures are modelled as closed (closed prior to uplift). Slip surfaces are modelled as open (at the present day, slip surfaces are closed with zeolite veins suggesting they were open at an early stage), with the same permeability assigned to present day fracture permeability estimates. Zeolite veins within the pre-altered basalt zone (brown on fault map) were modelled as open (these zeolites cross-cut the slip surface zeolites suggesting they were open after the slip surface mineralised). The pre-altered basalt was given a permeability slightly higher than the host rock basalt (to reflect intragranular pores and fractures opening to enhance microscopic fluid flow).

Stage 2 retains the permeability values assigned to Stage 1, with the exception of the pre-altered basalt zone. The pre-altered basalt permeability is decreased from Stage 1 to equal that of the host rock basalt, to reflect intergranular space and fractures being partially clogged by clays. Open slip surfaces continue to accommodate displacement.

Stage 3 permeabilities are the same as Stage 2, with the exception of the pre-altered basalt zone. This zone's permeability is now modelled as altered basalt, following closure of intergranular pores and fractures by complete clay/zeolite filling. Faulting continues and develops through going, open slip surfaces.

Stage 4 permeabilities are the same as in Stage 3, with the slip surfaces now modelled as filled by zeolite veins representing sealing of slip surfaces by zeolite veins.

Stage 5 retains the permeabilities from Stage 4, with the exception of the zeolite veins. The permeability of these has been modelled to reflect further mineral veins filling fractures.

Finally, **Stage 6** retains the permeabilities from Stage 5, with the exception of fractures, which have been opened to reflect unloading of the basalt following uplift.

Using this micro-structural evidence, the bulk permeability of the fault zone can be modelled during each evolutionary stage, by changing the permeability values within different parts of the fault zone, depending on its history. Each fault component is coloured on the fault map, and that component is given a relevant permeability (see Table 6.1 for values). In zones where permeability has changed over time, it will be referred to by its colour, e.g. the brown zone represents altered basalt at present day, but over faulting history it has not always been altered. Therefore, the altered zone is referred to as the brown zone throughout the text. The fault map used for modelling the BNF is shown in Figure 6.3.

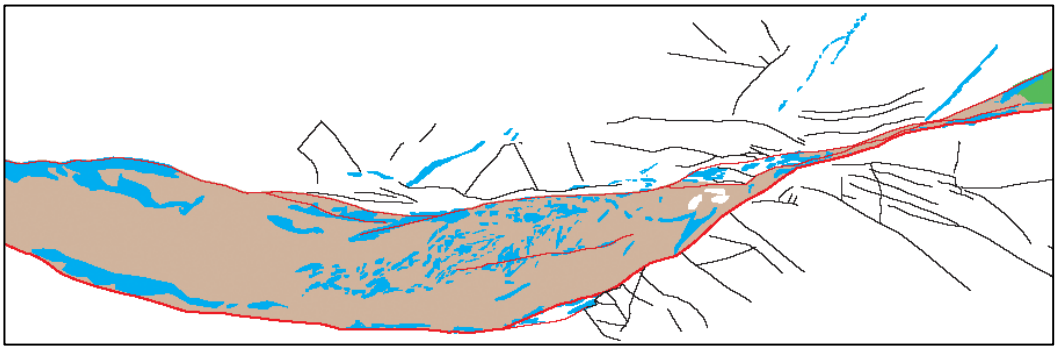

Figure 6.3: Rotated fault map of the BNF used for flow modelling. Each colour represents a different rock type, with a key provided in the models below.

6.3.1. Along-fault flow results

The modelled results for along-fault flow are presented in Figure 6.4, with streamlines shown in yellow. Models are presented in order of Stage 1 to Stage 6, i.e. simulating fault permeability from early history to present day. Permeability values are provided in each image, with changes to permeability (e.g. clogging fault zone with clay) highlighted in bold, and marked by a box which is filled if the feature is closed, or empty if the feature is open (e.g. slip surface). Permeability values are presented in this format throughout the rest of the chapter.

From the position of streamlines through the fault map (Figure 6.4) in different stages, the controls on fluid flow migration can be determined through the BNF's evolution. However, due to a wrongly placed fracture intersecting the slip surface prior to modelling, flow does not occur along the basal slip surface in the map. Therefore flow does not travel along the basalt slip surface as may be expected in the first few stages in this model.

Stage 1 clearly shows almost 100% of flow occurs along the open slip surfaces bounding the edges of the PSZ. This suggests when slip surfaces/fractures are open and connected, the majority of fluid will flow along them. It is therefore likely that these open slip surfaces or fractures will be filled by minerals when flow rate decreases, or when flow is super-saturated with minerals. Whilst no flow is observed within the brown zone, it is likely fluid from the slip surfaces may be leaching into intergranular pore space. This is documented by element redistribution from host rock minerals into zeolitisation of feldspars and clay generation.

In **Stage 2**, where the brown zone becomes less permeable due to clay generation, flow is still concentrated along open slip surfaces. Flow is not observed within the brown zone, though it remains likely that leaching of fluid is occurring within the zone due to the documented evidence of clay and zeolites filling pore space within this zone (see Chapter 4).

In **Stage 3**, the altered basalt is less permeable than in Stage 2, and the same flow characteristics are found here as in Stage 2, i.e. fluid almost exclusively flows along connected open slip surfaces. It is likely that fluid leaching within the brown zone may have ceased due to clogging of pores by clay and zeolites.

By filling the slip surfaces with zeolite, **Stage 4** still shows fluid flowing within the mineralised slip surfaces, but also within the host rock, which was not observed before. This could potentially be responsible for zeolite veins found in the outer margins of the fault zone, and would suggest that by clogging the slip surfaces, flow is diverted into the fault walls, which may promote mineralisation of fault-related fractures in them. Despite filling of the slip surface by zeolites, a large bulk of flow still travels through the mineralised slip surfaces, suggesting further mineralisation could take place in the slip surfaces despite filling by zeolite veins.

Stage 5 shows no real difference in flow pathways from Stage 4.

Opening the fractures (black) in **Stage 6** focuses flow along the fractures in the fault walls, and also along the mineralised slip surfaces at the margins of the impermeable altered basalt zone. Present day fluid flow is found in these fractures, and pyrite mineralisation formed within pore space in zeolite veins within the slip surface was also found (see Chapter 4). This confirms the modelled results, where flow can still occur within the slip surfaces, despite being filled with zeolite.

Along-fault flow is strongly dependent on connected fluid pathways along the fault (such as open fractures/slip surfaces). In the BNF, fluid flow focused along the slip surfaces and partially within the brown zone prior to full alteration during the early stages of its life, and later fluid flow occurred within the fault walls and in the mineralised slip surfaces following clogging of the dominant flow pathways (opened slip surfaces).

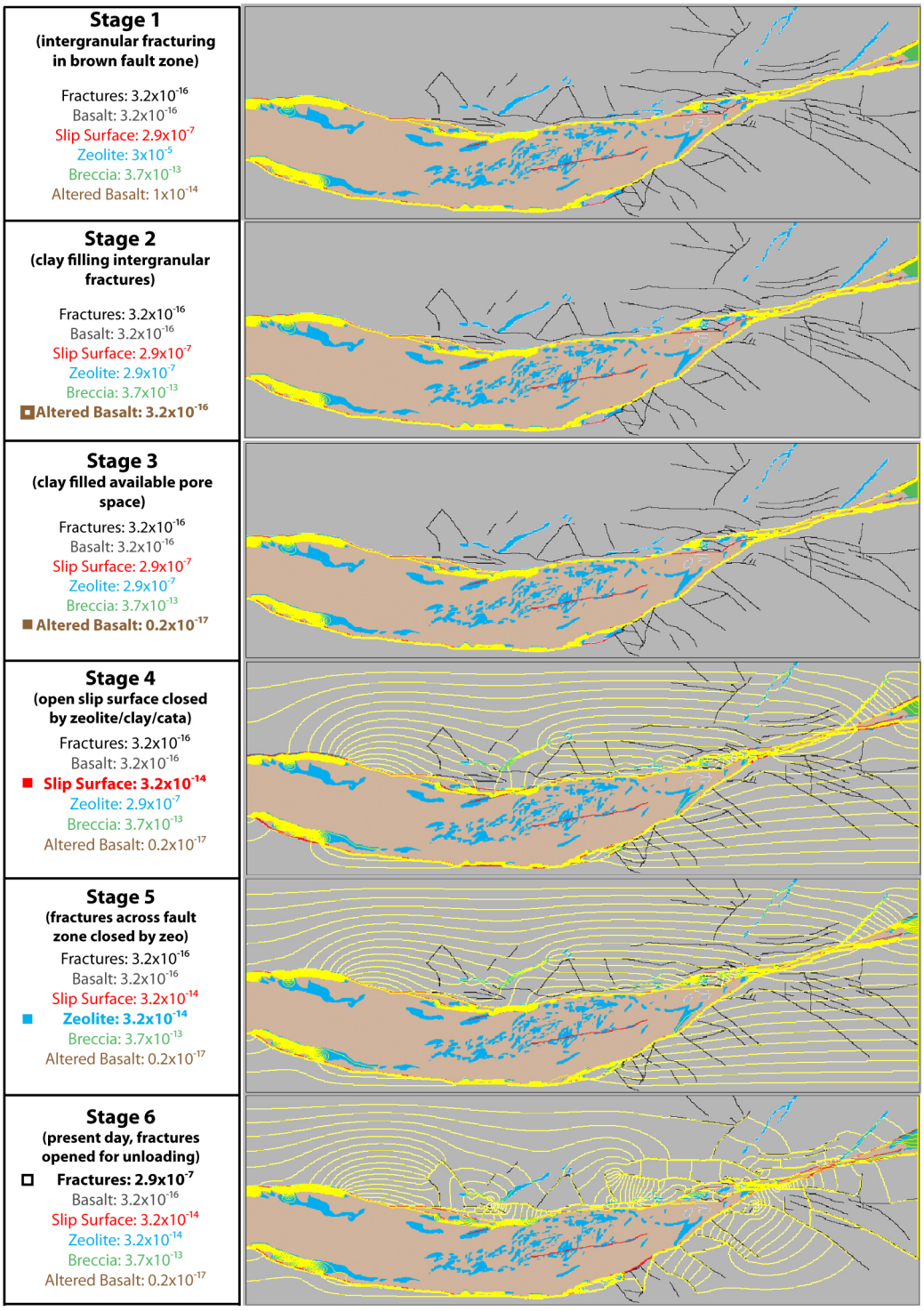

Figure 6.4: Along-fault flow modelling results for Bird Nest Fault, Mull. Flow modelled from left to right. The individual stages are described in the text. Results are discussed in the text. Basalt has been darkened to highlight yellow streamlines.

6.3.2. Across-fault flow results

The modelled results for across-fault flow are presented in Figure 6.5, with streamlines shown in yellow. Models are presented in the same order as that of the along-fault flow modelling. The same order of events (based on microstructural analysis) is modelled. From the position of streamlines in the fault map (Figure 6.5), the controls on across-fault fluid migration can be determined through the fault's evolution.

In **Stage 1**, across-fault flow occurs along open slip surfaces, and connected fractures (open zeolite veins, blue). As in along-fault flow, it is likely that fluids leaching from the open slip surfaces are permeating into microfractures within the brown zone (evidenced by clays and zeolites clogging holes; Chapter 4), though microfractures cannot be modelled at this scale to highlight this.

Stage 2 has similar flow characteristics to Stage 1, and again, whilst a zone of no flow is shown, it is likely that flow occurs within the brown zone and continues to clog pore space with clay and zeolite mineralisation (from microstructural evidence).

Stage 3 has similar characteristics to 2, with flow still concentrated along open slip surfaces, but does not cross the brown zone in large volumes.

The closing of slip surfaces by mineral veins in **Stage 4** enhances the across-fault flow. Streamlines are more closely spaced together surrounding the thinnest part of the fault, suggesting flow is more concentrated here following closure of the slip surfaces by mineralisation. However, a small amount of flow also occurs within the brown zone (altered basalt). Flow does still travel within the mineralised slip surfaces, though to a lesser extent than found in the previous stages.

Stage 5 has similar across-fault flow characteristics to Stage 4.

Opening fractures in **Stage 6** finds across-fault flow focuses through fractures, but across the fault zone itself, it is still concentrated in the narrowest part.

In the early stages of faulting, across-fault flow is fairly uniform across the fault. Flow tends to focus along connected fluid pathways across the fault (such as open fractures/slip surfaces). When the brown zone is modelled as altered basalt (i.e. low permeability), and when slip surfaces are modelled as filled by minerals, flow is more likely to cross the fault at its narrower points, though the mineralised slip surfaces still act as a flow pathway. This characteristic is consistent up until the stage representing the present day (Stage 6). At this point, unloading fractures near the narrowest part of the fault act to focus the flow across the fault.

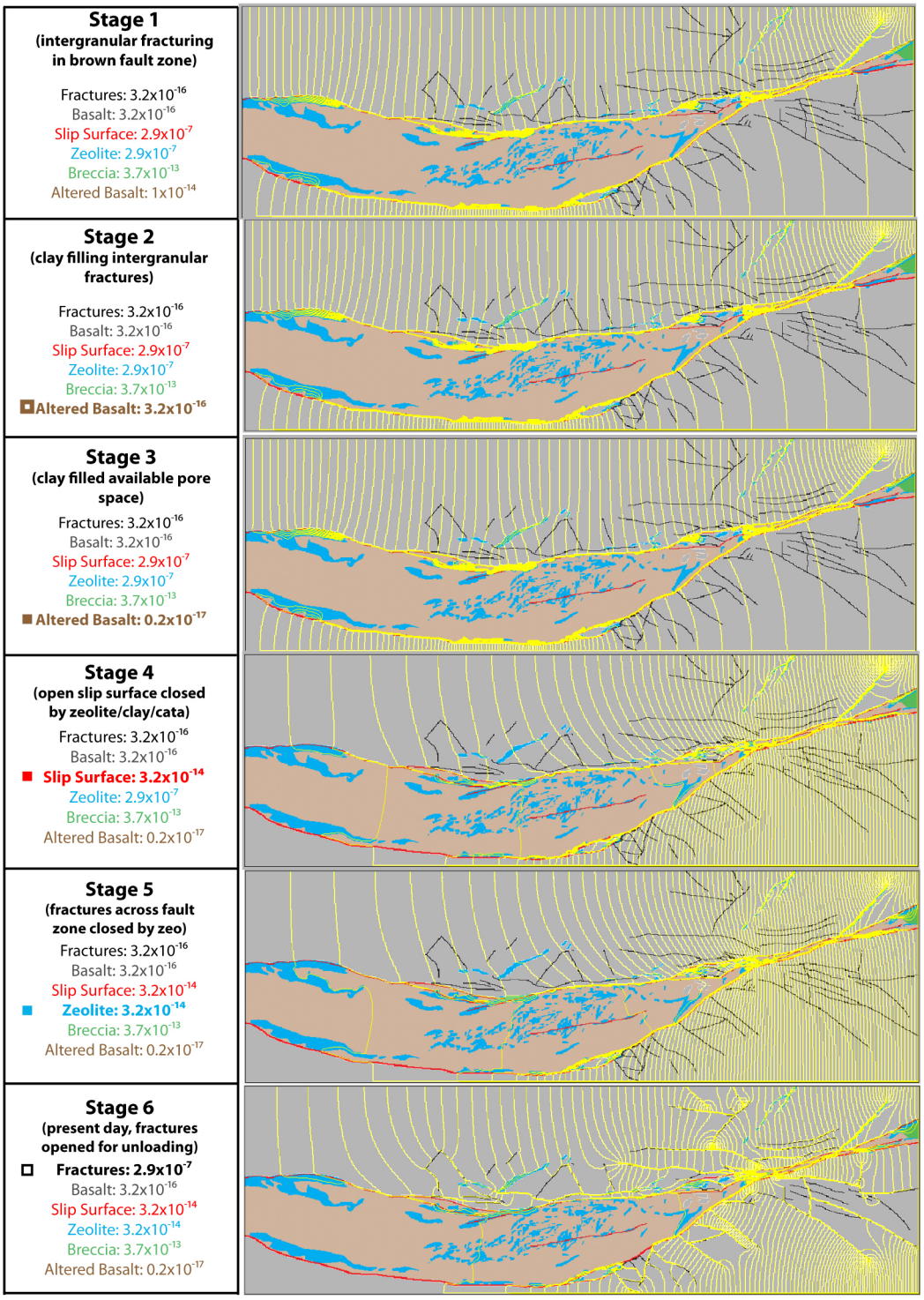

Figure 6.5: Across-fault flow modelling results for Bird Nest Fault, Mull. Flow modelled from top to bottom. The individual stages are described in Section 6.3.2. Results are discussed in the text.

6.3.3. Bulk permeability of along- and across-fault flow

Bulk permeability values for each stage in along- and across-fault fluid flow are presented in Figure 6.6.

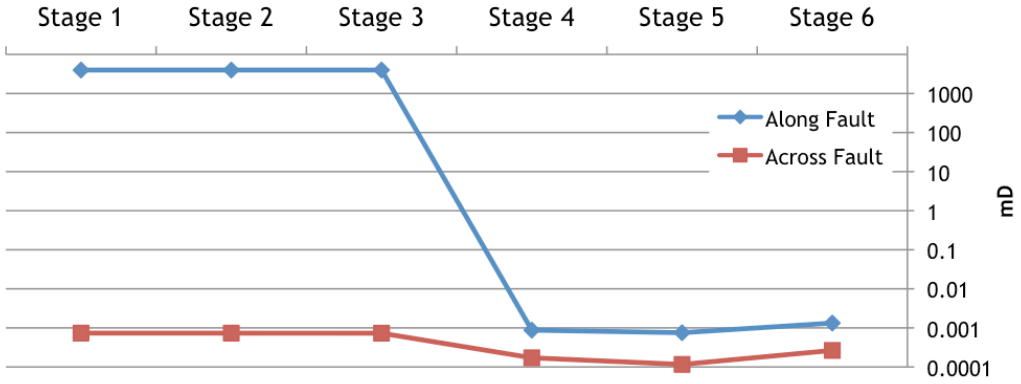

Figure 6.6: Bulk permeability results for along- and across-fault flow in the BNF. Permeabilities are in mD. Results are presented in logarithmic form. Permeability presented from early stages (Stage 1) to present day (Stage 6).

For along-fault flow, bulk permeability is at least 0.5 orders of magnitude higher than for across-fault flow, and in the early stages of faulting, over six orders of magnitude higher.

Along-fault flow has relatively constant bulk permeability up until the slip surfaces are closed by mineralisation (Stage 4), where the bulk permeability drops by 6 orders of magnitude. Following unloading (fracture opening – Stage 6), permeability increases by a small amount. Across-fault flow has a relatively constant drop in bulk permeability over time, probably related to clogging of the altered basalt zone and mineralisation of slip surfaces. There may have been a larger decrease in bulk permeability if across-fault flow hadn't been accommodated through the narrowest part of the fault zone. These observations show that fluid flow is highest along the fault rather than across it, and the biggest control on bulk permeability in along-fault fluid flow is the hydraulic behaviour of the slip surfaces. The biggest control on bulk permeability in across-fault fluid flow is likely to be the thickness and extent of the altered basalt zone.

6.4. mfLab simulations of the VJF

Two flow events were identified in the Vagseiði Jetty Fault (VJF). Present day permeabilities were modelled with open fractures and filled mineral veins. Permeabilities prior to mineralisation were modelled with mineral veins as open fractures. The fault map used for VJF is shown in Figure 6.7.

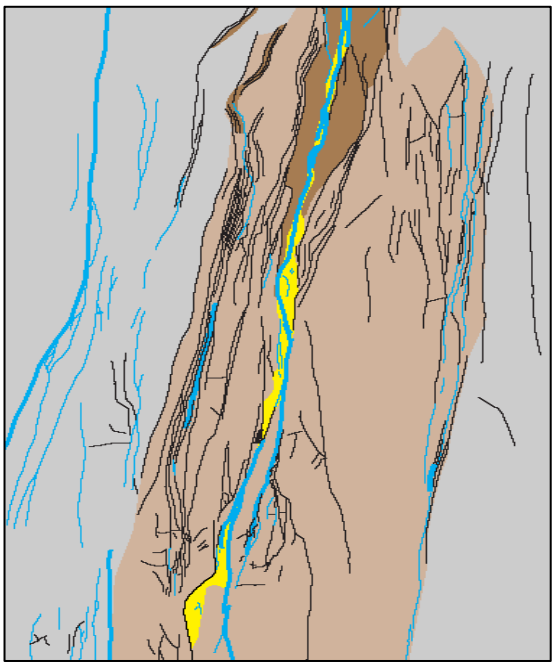

Figure 6.7: Fault map used for fluid modelling at VJF. Assigned permeabilities for fault components are provided in the text.

6.4.1. Along- and across-fault flow results

The modelled results for along- and across-fault flow are presented in Figure 6.8, with streamlines shown in pink. Stage 1 represents fault permeability prior to fractures being filled by zeolite veins, and Stage 2 represents the present day scenario.

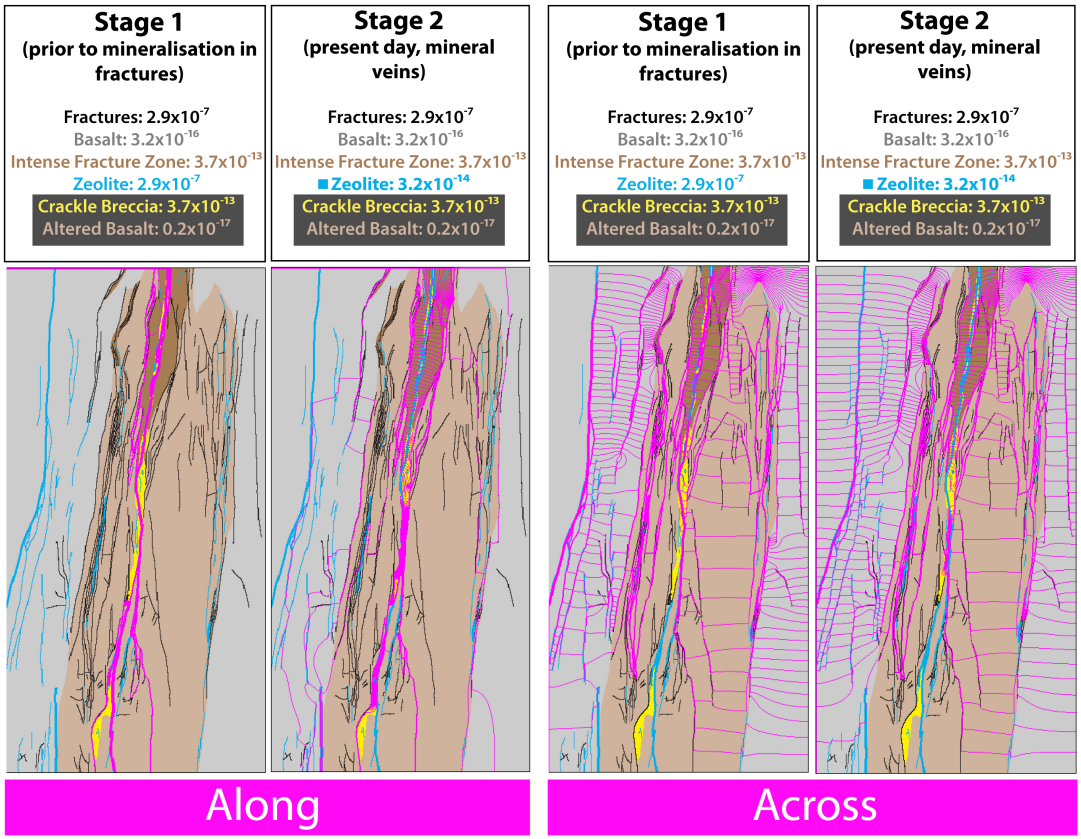

Figure 6.8: Along- and across-fault flow modelling for the VJF. Along-fault flow is modelled from bottom to top, and across-fault flow is modelled right to left. Stage 1 represents a time where mineralised fractures were not sealed by zeolites, and Stage 2 represents the current day where mineralised fractures contain zeolite veins. Results are discussed in the text.

The results in Figure 6.8 clearly show that in the along-fault flow simulations, fluid flow is heavily concentrated along open fractures (including opened zeolite veins, blue). In **Stage 1**, flow occurs along connected opened mineral veins and open fractures within the centre of the fault zone. It also partially flows along the crackle breccia and intense fracture zone. No flow is observed within the altered basalt in this stage. In **Stage 2**, flow is still largely concentrated along the central portions of the fault in open fractures, but due to closure of some fractures by mineral veins, partial flow occurs in the altered basalt and fault walls.

In the across-fault flow simulations in **Stage 1,** flow is more concentrated within the basalt, and preferentially crosses the altered zone and crackle breccia zone via fractures and open zeolite veins. Following mineralisation of some fractures in **Stage 2**, the controls on across-fault flow remain the

same as in Stage 1, though with less potential for flow across opened mineral veins.

6.4.2. Bulk permeability of along- and across-fault flow

Bulk permeability for each stage in along and across-fault fluid flow was also calculated, and results are presented in Figure 6.9.

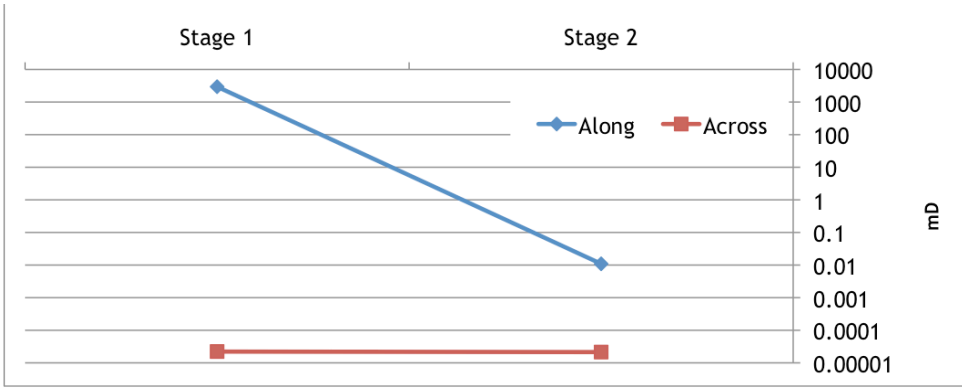

Figure 6.9: Bulk permeability results for along- and across-fault flow for VJF. Results are presented in logarithmic form.

The results show that bulk permeability in along-fault flow is at least eight orders of magnitude higher than that of across-fault flow, and that the biggest decrease in permeability is found in along-fault flow. This is consistent with fault-parallel fracturing being the key flow control, and this value drops in Stage 2 due to mineralisation of some fault-parallel fractures. Across-fault flow remains more or less constant throughout both stages, suggesting the position of altered basalt (bounding the PSZ) is the dominant control on across-fault flow, despite across-fault flow being visually aided by fault-parallel fractures.

6.5. mfLab simulations of the VPF

The same two flow events modelled in the VJF are modelled here (i.e. prior to mineralisation of zeolite veins, and the present day post-mineralisation scenario). The Vagseiði Puddle Fault (VPF) is 20m away from the VJF, is in the same stratigraphy, belongs to the same tectonic event (Walker et al., 2011a), has the same fault components and evidence of similar fault evolution (Chapter 3). The fault map modelled is shown in

Figure 6.10. Stage 1 represents fault permeability prior to fractures being filled by zeolite veins, and Stage 2 represents present day scenario.

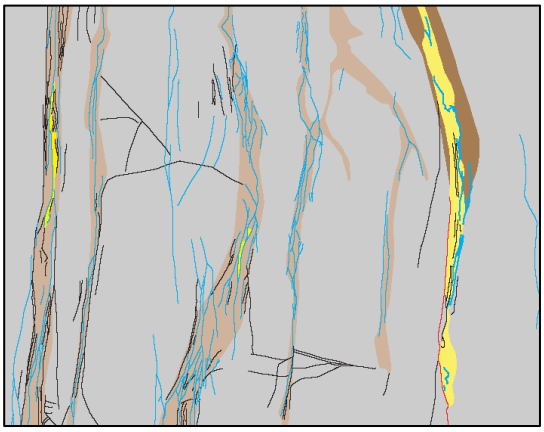

Figure 6.10: Fault map of VPF used for flow modelling.

6.5.1. Along- and across-fault flow results

The modelled results for along- and across-fault flow are presented in Figure 6.11, with streamlines shown in pink. In along-fault flow, connected fractures/opened zeolite veins control flow in both stages. In **both stages**, flow is found within the fracture cluster in the hanging wall (to the left of the map), and along the opened mineralised veins within the PSZ crackle breccia (to the right of the map). No along-fault flow was observed in the open mineral vein clusters in the centre (in the hanging wall). This is due to the fact they are not connected in 2D at this orientation. However, it is highly likely they are connected in 3D (following observations from Chapter 3 of the fault parallel fracture hard-linking in plan view), and despite results showing a zone of no flow, it is highly likely this zone would also act as a flow pathway. In along-fault flow **Stage 2**, the majority of flow is focused within the intense fracture zone and crackle breccia of the PSZ due to closing of the fracture (open zeolite vein) within that zone.

Across-fault flow is impeded by alteration zones, but accommodated by connected open fractures and open zeolite veins. In **Stage 1**, across-fault flow is concentrated in open features, but in **Stage 2** where the zeolite veins are filled, a higher degree of flow passes through the basalt, suggesting the closing of more connected open fractures (zeolite veins) affects how flow travels across the fault zone as a whole.

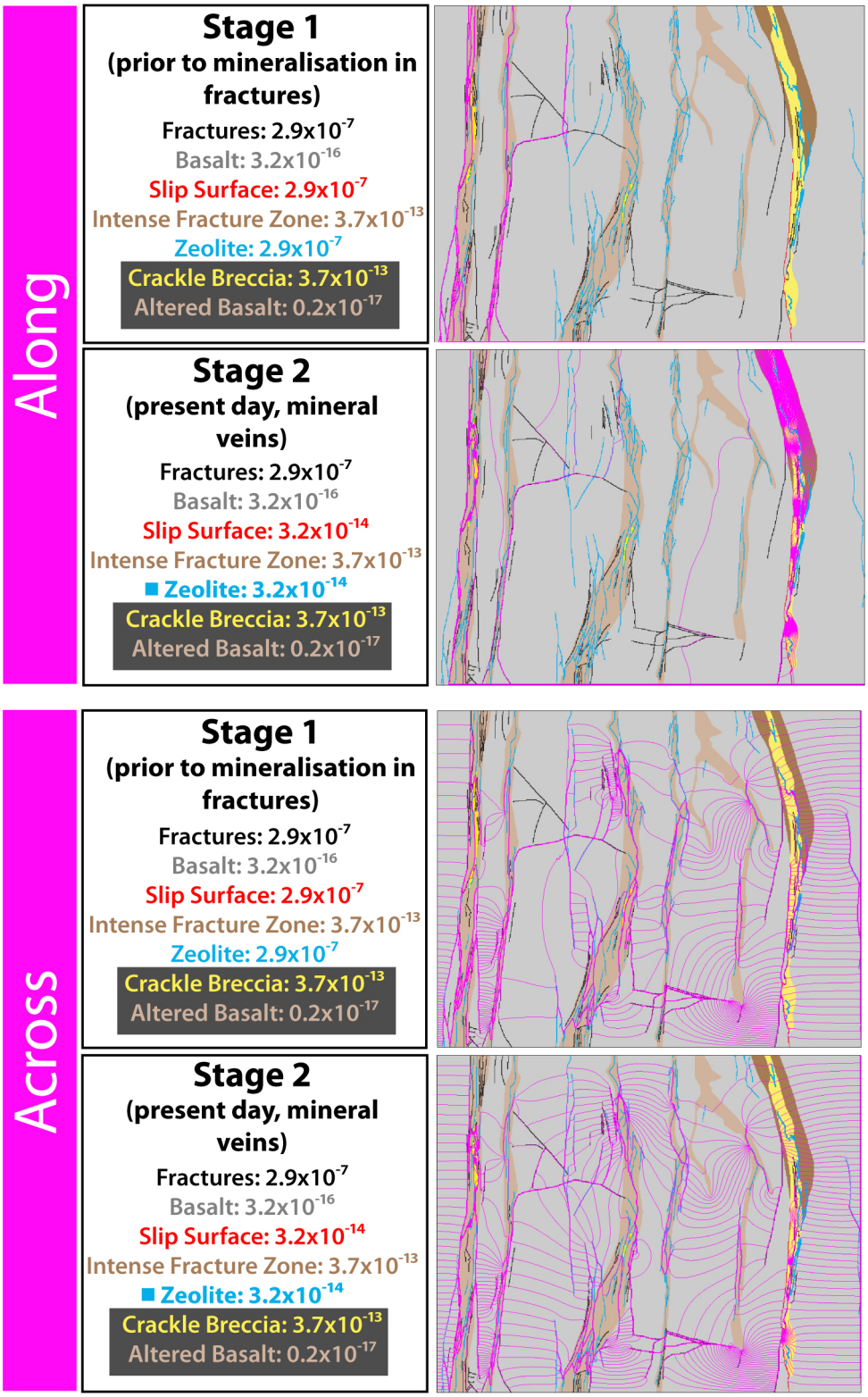

Figure 6.11: Along- and across-fault flow modelling streamline results for VPF. Flow modelled top to bottom in along-fault flow, and left to right in across-fault flow. Stages are identical to those modelled in VJF. Results are discussed in the text.

6.5.2. Bulk permeability of along- and across-fault flow

Bulk permeability for each stage in along- and across-fault fluid flow was also calculated, and results are presented in Figure 6.12.

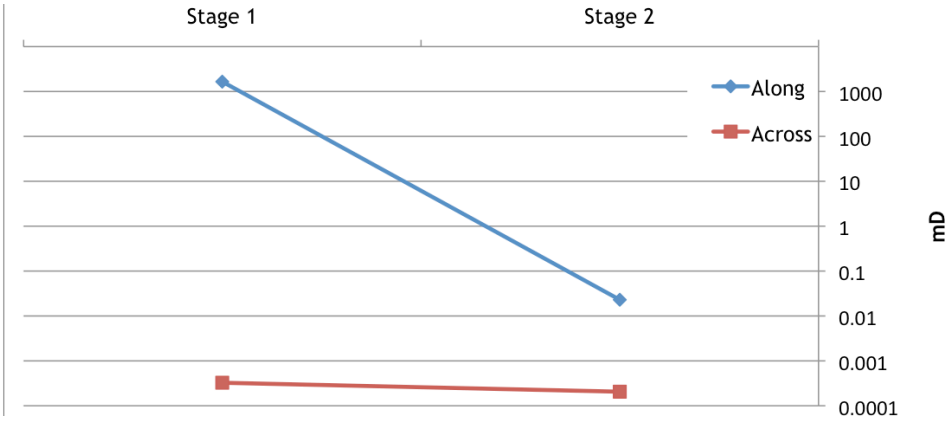

Figure 6.12: Bulk permeability results for along- and across-fault flow in VPF. Results are presented in logarithmic form.

The bulk permeability results show that along-fault flow is consistently higher than across-fault flow, by at least seven orders of magnitude. Like in the bulk permeability results of the VJF, the largest decrease in permeability from Stage 1 to Stage 2 is found in along-fault flow, whereas the permeability decrease has a lower gradient in across-fault flow. The decrease in along-fault flow is due to fractures being sealed by zeolites in Stage 2, and in across-fault flow, due to alteration and to a lesser extent, closure of connected fractures (zeolite veins) controlling flow pathways.

6.6. mfLab simulations of the IBF

The fault at I Botni has seen at least one mineralisation event, which has filled pore space in the tuff gouge, slip surface and chaotic breccia. As the timing of these appears to be simultaneous, two models have been run to simulate flow throughout the IBF. This modelling does not take into account reactivation along the fault, where a mineralisation event prior to these events took place. Fault rocks prior to mineralisation are represented in Stage 1, and Stage 2 represents the present day. In Stage 1 simulations, the permeability value was increased by two orders of magnitude from the

tuff gouge, slip surface (cataclasite) and chaotic breccia, to represent increased flow throughout the mineralised rocks prior to mineralisation. This follows Johnson (1980) results of finding that mineralised phases were two orders of magnitude higher in permeability than their pre-mineralised counterpart. The fault map modelled is shown in Figure 6.13.

Figure 6.13: Fault map of IBF used for flow modelling.

6.6.1. Along- and across-fault flow results

The modelled results for across-fault flow are presented in Figure 6.14, with streamlines shown in yellow. Stage 1 represents fault permeability prior to fault components being filled by zeolite veins, and Stage 2 represents present day scenario.

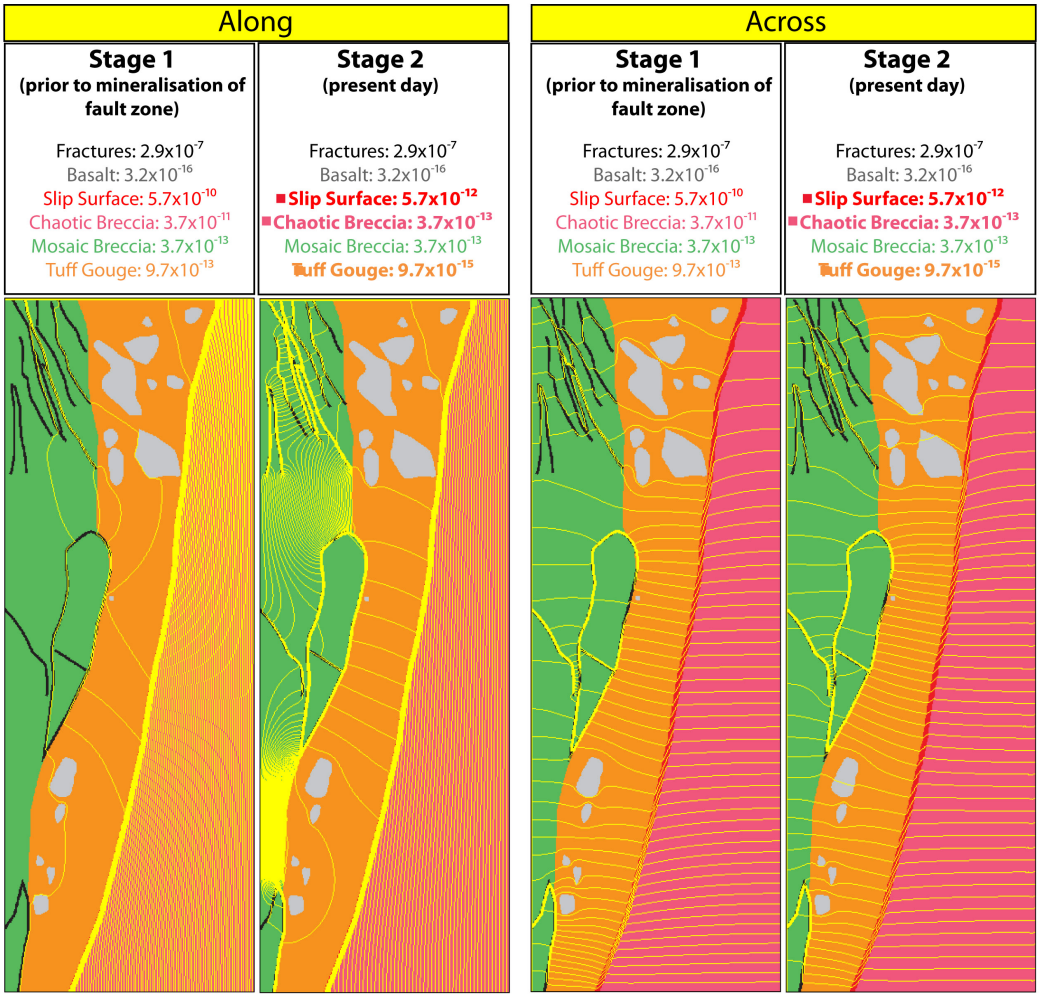

Figure 6.14: Along- and across-fault flow modelling streamline results for IBF. Flow modelled left to right in along-fault flow, and bottom to top in across-fault flow. Stage 1 represents fault components with no mineralisation, and Stage 2 represents fault components with mineralisation. Results are discussed in the text. Note in along-fault flow, streamlines in chaotic breccia apparently display crisscrossing streamlines - this is a visual effect and is artificially generated.

Along-fault flow in **Stage 1** is particularly focused along the (pre-mineralised) slip surface, and within the footwall of the fault within the opened (pre-mineralised) chaotic breccia. There is partial fluid flow along the tuff gouge and mosaic breccia. In **Stage 2**, flow is still concentrated within the mineralised chaotic breccia, though to a lesser extent than Stage 1. There is an increase of flow within the mosaic breccia hanging wall, and also within the tuff gouge when compared to Stage 1, probably due to the permeabilities of these being similar following mineralisation.

In across-fault flow, fluid flow is fairly uniform across the fault, with no preferential pathway being taken in both stages. However, with the closing of permeability in fault rock components in **Stage 2**, flow is slightly more enhanced across the tuff gouge, and streamlines cross into the basalt clasts. Therefore, it appears that in this case across-fault flow is slightly aided by connectivity of higher permeability survivor clasts within a relatively low permeability gouge, and along-fault flow is focused within the higher permeability units.

6.6.2. Bulk permeability of along- and across-fault flow

Bulk permeability for each stage in along- and across-fault fluid flow was also calculated, and results are presented in Figure 6.15.

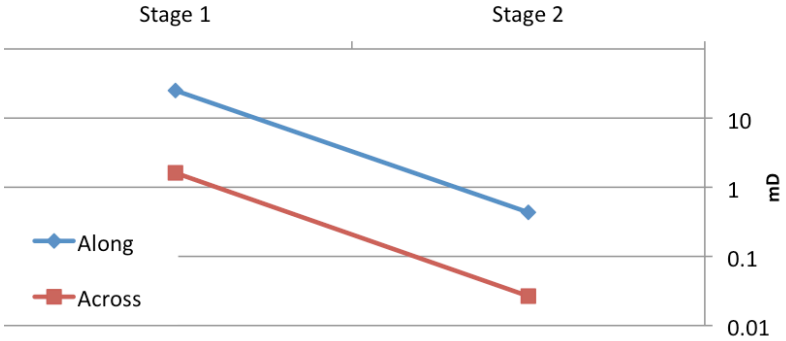

Figure 6.15: Bulk permeability results for along- and across-fault flow in the IBF. Results are presented in logarithmic form.

Bulk permeability results show along-fault flow is consistently higher than across-fault flow, by at least one order of magnitude. There is an equal decrease of bulk permeability in both along- and across-fault flow, suggesting the zeolite mineralisation of the gouge, slip surface, and chaotic breccia controls both across-fault and along-fault bulk permeability.

6.7. mfLab simulations of the LWF

The Lawther Fault (LWF) was modelled for four scenarios, based on microstructural evidence. For modelling purposes, fractures were removed from the peperite footwall in the fault map, as the complexity of the fractures is such that they could not all be captured during map construction. Therefore, the peperite as a whole was assigned an estimated

permeability consistent with fractured media (in this case, modelled at $1x10^{-12}$ cm^2). Stage 1 models the principal slip surface as open, prior to cataclasis, and cementation by chalcedony veins. Fractures are modelled as closed at depth (due to higher stresses). In Stage 2, slip surfaces are partially sealed by cataclasis and chalcedony mineralisation, and fractures are modelled as open due to unloading. In Stage 3, the slip surface is clogged by clay gouge and chalcedony veins, fractures are open, and black gouge is modelled as open (prior to fill with manganese deposits). Finally, Stage 4 represents the present day where black gouge is modelled as filled by gouge (following precipitation of manganese). In this model, the peperite was modelled as being high permeability, due to the large amount of pore space and fractures identified in the field and through microscopic analysis. The fault map used for flow modelling is shown in Figure 6.16.

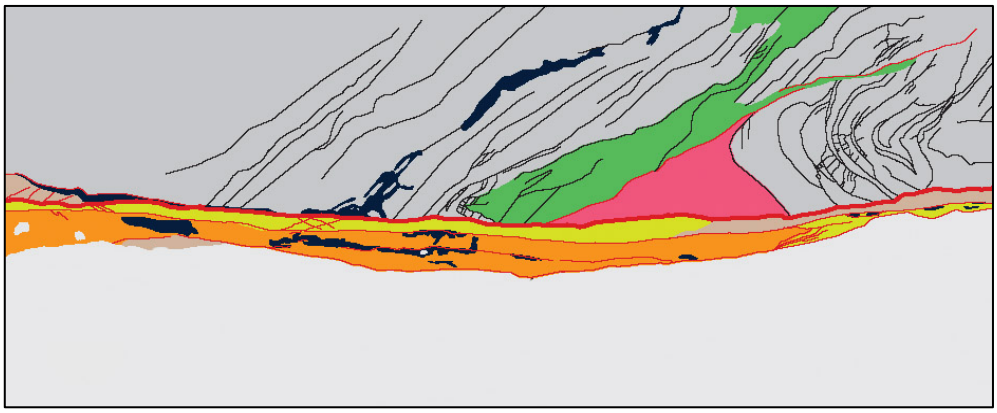

Figure 6.16: Fault map used for flow modelling for LWF.

6.7.1. Along-fault flow results

The modelled results for along-fault flow are presented in Figure 6.17, with streamlines shown in yellow. The image has been darkened in order to highlight the streamlines. Individual stages are described in the previous sections.

In **Stage 1**, where slip surfaces are modelled prior to any fill, along-fault flow occurs almost exclusively along the principal slip surface. Partially closing the slip surface in **Stage 2**, and opening the fractures due to unloading, leads to a change in flow behaviour. Flow no longer exclusively

channels along the fault via slip surfaces, but focuses in the fault walls, most notably within the peperite, and breccias and fractures within the basalt hanging wall. In **Stage 3**, the slip surface is clogged (by clay gouge and chalcedony) and flow preferentially runs in the peperite wall rock, with very little flow within the PSZ. When there is flow in the PSZ, it is within the open black gouge. By clogging the black gouge in **Stage 4** (due to late stage mineralisation), no flow is observed within the PSZ, but is almost exclusively within the permeable peperite fault wall. This suggests flow preferentially moves through the fault walls in low-permeability fault zones, particularly in non self-juxtaposed faults where permeable lithologies are juxtaposed against low permeability lithologies, i.e. flow is lithology juxtaposition controlled rather than fault rock type controlled.

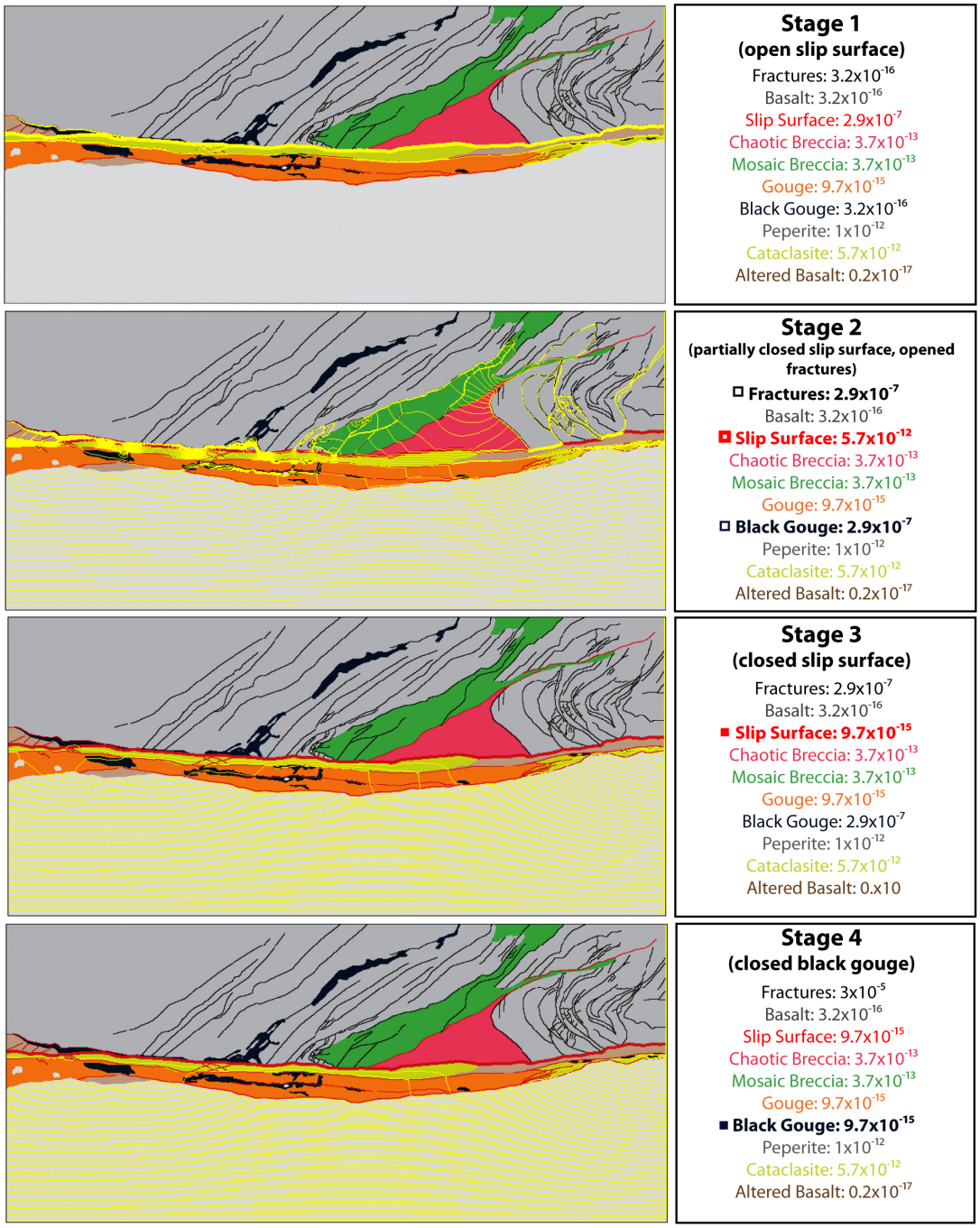

Figure 6.17: Along-fault flow modelling results for LWF. Images have been darkened to highlight streamlines (yellow). Stages are described in the text. Flow is modelled left to right.

6.7.2. Across-fault flow results

The modelled results for across-fault flow are presented in Figure 6.18, with streamlines shown in yellow. The image has been darkened in order to highlight the streamlines. Individual stages are described in the previous sections. As discussed in Section 6.2, closed fractures are assigned permeabilities equal to basalt.

With opened slip surfaces (**Stage 1**), fluid flows preferentially in the basalt hanging wall via breccia zones (sub-parallel to simulated flow), and partially within the basalt itself. Flow crosses the fault through connected slip surfaces, and finally into the peperite. With partial closing of the slip surface in **Stage 2**, and opening of fractures and black gouge zone, flow is channelled into the fault zone along fractures, opened black gouge zones and partially within the breccia zones. Due to partial closing of the slip surfaces, across-fault flow is not achieved by connected slip surfaces to the extent that it was in Stage 1. Instead, flow crosses the fault at its narrowest point where opened black gouge zones are mapped, and connects with the partially closed slip surfaces. Following clogging of the slip surfaces in **Stage 3**, flow is still localised along fractures, the opened black gouge and breccia zones (to a larger extent than Stage 2). However, across-fault flow occurs uniformly across the gouge parts of the PSZ in the absence of opened black gouge zones. Finally, in **Stage 4**, flow characteristics are very similar to that of Stage 3, with the exception of flow no longer being concentrated along opened black gouge zones, as they are now modelled as closed. Flow is preferentially channelled through the basalt hanging wall via fractures and breccia zones, and flow crosses the fault within the cataclasite. The highest flow rates across the fault are found within narrow gouge zones underlying the cataclasite.

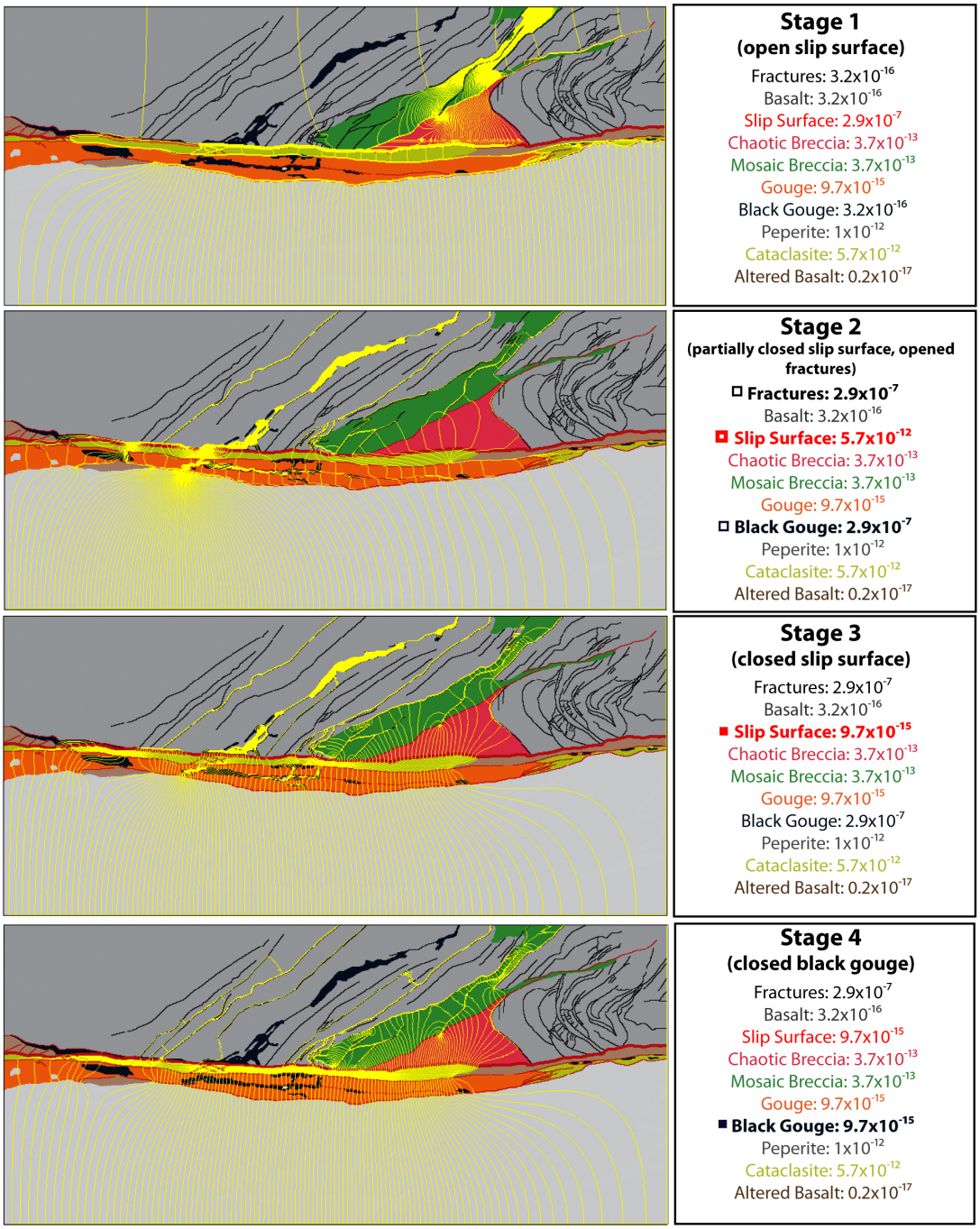

Figure 6.18: Results for across-fault flow modelling in the LWF. Flow simulated top to bottom.

6.7.3. Bulk permeability of along- and across-fault flow

Bulk permeability for each stage in along- and across-fault fluid flow was also calculated, and results are presented in Figure 6.19.

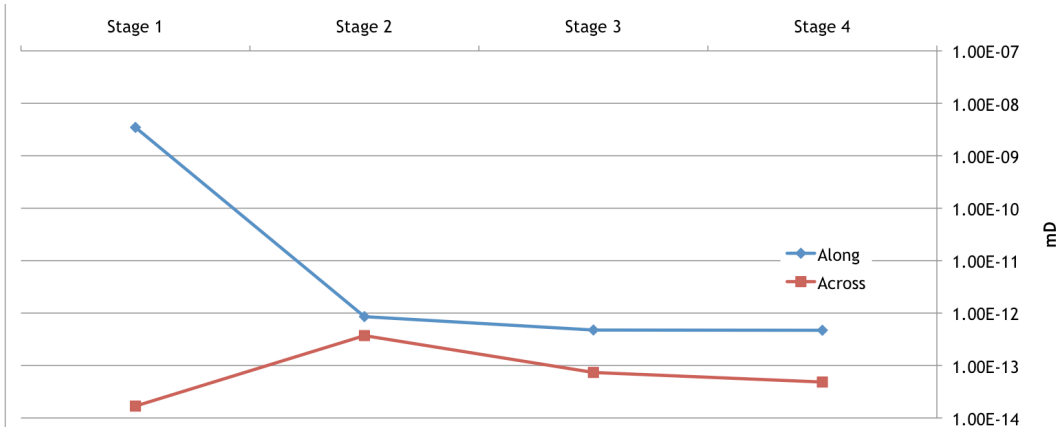

Figure 6.19: Bulk permeability results for along- and across-fault flow in LWF. Results presented in logarithmic form.

The results show along-fault flow is at least half an order of magnitude higher than across-fault flow, and in Stage 1, five orders of magnitude higher. The largest effect on along-fault flow is the partial closure of the slip surface, where bulk permeability decreases by four orders of magnitude. A steady decrease in bulk permeability following that is related to further closure of the slip surface and black gouge. Conversely, in across-fault flow, the closure of the slip surface enhances flow, although this is also probably due to the fact that fractures and black gouge are modelled as open. As these features are near parallel to the head gradient, flow is channelled along them, which raises the across-fault permeability. Following this, across-fault flow decreases, potentially due to sealing of the slip surfaces, which decreases connectivity with opened black gouge zones within the PSZ. This makes it more difficult for flow to cross the fault, and when it does, it does so within the narrowest parts of the fault where flow can travel (i.e. within the more permeable cataclasite rather than altered basalt within the PSZ).

6.8. mfLab simulations of the HBF

The HBF microstructures suggest that only one minor phase of mineralisation occurred within slip surfaces and fractures. Three stages of flow were modelled. Stage 1 models flow with open (un-mineralised) slip surfaces and closed fractures to represent a period prior to uplift. Stage 2

models closed slip surfaces (filled with mineral veins or clays) and closed fractures, prior to uplift. Stage 3 models closed slip surfaces and open fractures, which are likely uplift/weathering related.

6.8.1. Along- and across-fault flow results

The modelled results for across-fault flow are presented in Figure 6.20, with streamlines shown in yellow.

The along-fault flow model finds flow focuses preferentially along the connected slip surfaces in **Stage 1**. In **Stage 2**, flow is extremely focused along the cataclasite strand, following closure of the slip surface by cataclasite. An increase in flow rate is also found within the breccias, and no flow was observed within the altered basalt walls. In **Stage 3**, following unloading, fractures are opened and flow is found within fractures in the altered basalt fault walls.

In across-fault flow, flow travels across the fault at its narrowest width nearest the higher permeability breccia zones in **Stage 1.** As there is also a higher permeability breccia zone below the PSZ, across-fault flow was not observed toward the left of the map. A similar feature is found throughout the rest of the across-fault stages. As this is just a strand of the high displacement HBF, it is likely that on a larger scale, these breccia zones control across-fault fluid flow over a larger area, and fractures would also do the same following unloading. Therefore, whilst in these models no flow was observed to the left of the models, when considering the HBF fault zone as a whole (Chapter 3), flow would cross these cataclasite zones via breccia zones and fracturing.

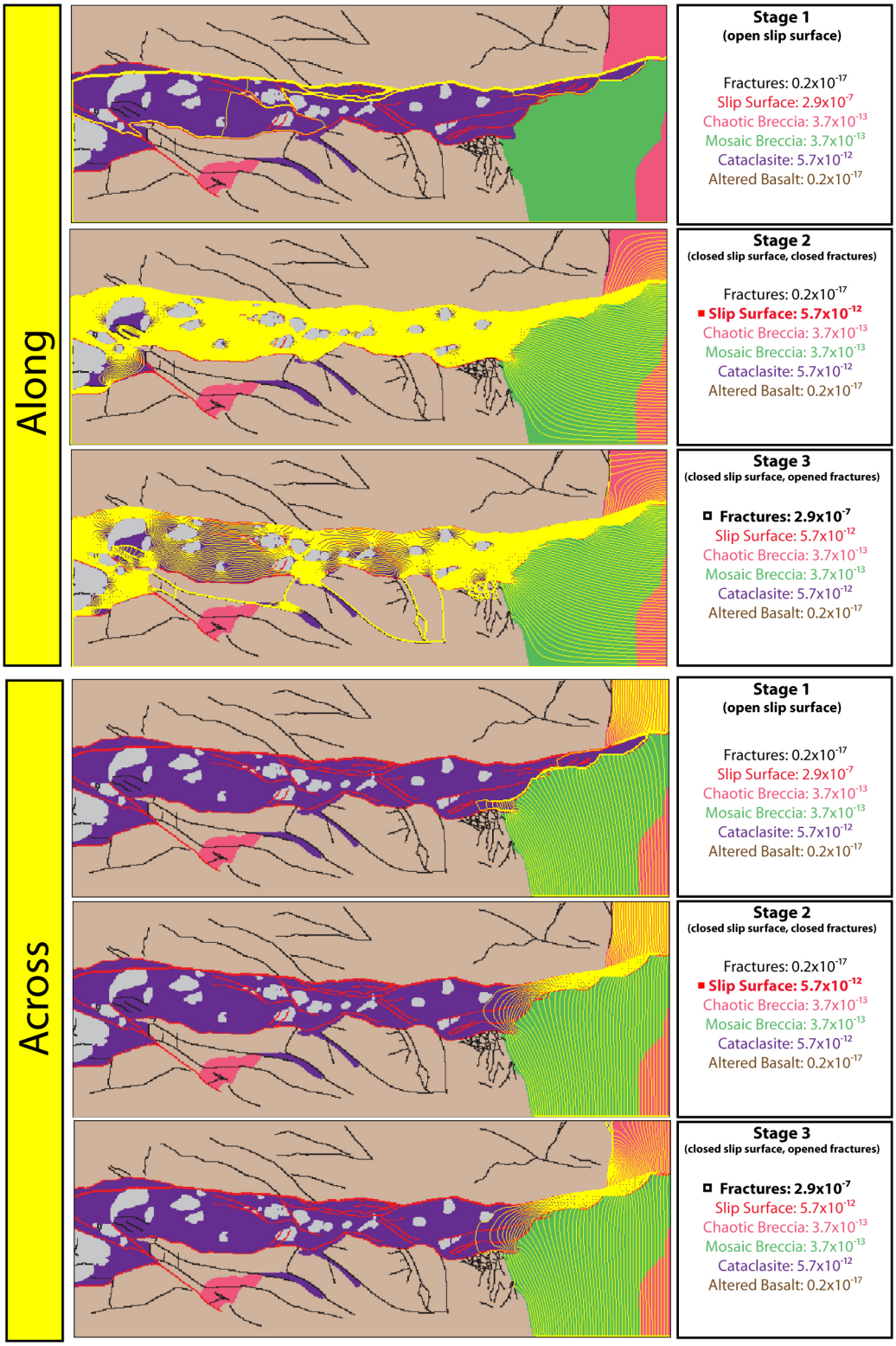

Figure 6.20: Along- and across-fault flow results for HBF. Streamlines are in yellow. Along-fault flow is modelled right to left, across-fault flow top to bottom. Stages are described in the text.

6.8.2. Bulk permeability of along- and across-fault flow

Bulk permeability for each stage in along- and across-fault fluid flow was also calculated, and results are presented in Figure 6.21.

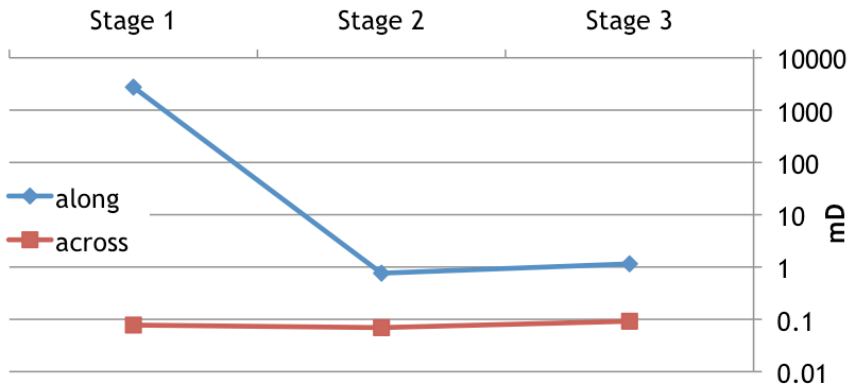

Figure 6.21: Along- and across-fault flow bulk permeabilities for the HBF. Results are presented in logarithmic form.

Along-fault flow is higher than across-fault flow by at least four orders of magnitude. Along-fault flow decreases by around four orders of magnitude with the closing of the slip surface, whereas across-fault flow drops only slightly. This could suggest that the presence of an open slip surface only enhances flow in along-fault flow, but when closed, fluid has to find a more tortuous path through the cataclasite in the principal slip zone. When fractures are opened, the permeability in both along- and across-fault flow increases slightly. Across-fault flow is controlled by the locations of the higher permeability breccia zones.

6.9. Comparison of bulk permeabilities

A comparison of present day scenario bulk permeabilities in both along- and across-fault flow is presented in Figure 6.22. The results show that in every case, along-fault flow is higher than across-fault flow (in agreement with similar studies of simulated flow in complex fault zones, e.g. Jourde et al., 2002), due to the presence of connected flow pathways. The LWF has the lowest permeability, probably due to its clay gouge rich components. Despite the IBF having a clay gouge smear, it has a relatively high permeability suggesting the brecciated fault walls act as the dominant key flow control rather than slip surfaces or clay gouge, like in the LWF. As expected, the VJF is similar to the VPF, with a slight increase in permeability in the VPF due to development of fault parallel fractures over a wider area. The BNF is lower permeability probably due to a PSZ dominated by alteration. The HBF is high permeability due to the presence of connected high permeability cataclasites and breccias throughout the fault zone.

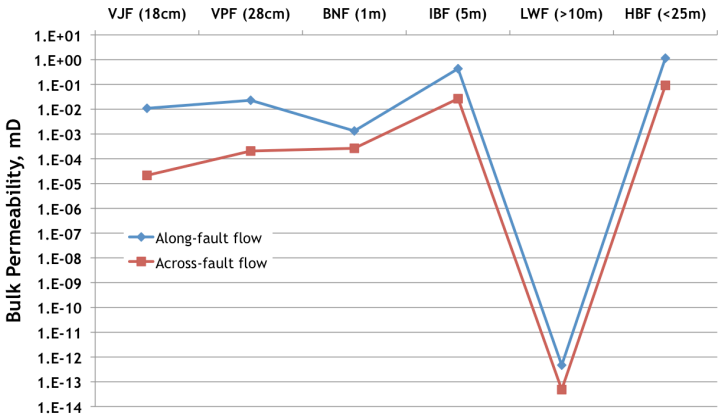

Figure 6.22: Bulk permeabilities for all faults in present day scenario.

In order to understand these data from a fault-evolution point of view, the data have been split into along- and across-fault data, and further sub-divided into self-juxtaposed bulk permeability evolution, and non self-juxtaposed bulk permeability evolution in Figure 6.23.

In Figure 6.23a, along-fault flow bulk permeability evolution is shown. This assumes that with increasing displacement, the VJF will develop fault

characteristics similar to VPF, and will therefore have an increase in bulk permeability. This is due to an increase of fault parallel fractures in the fault walls, enhancing bulk permeability. It is then assumed that the VPF may develop into the BNF, where alteration zones are surrounded by slip surfaces due to coalescing of connected fault parallel fractures into slip surfaces. Fault permeability will therefore decrease. If fault evolution/displacement continues without encountering non self-juxtaposition, the BNF may evolve into the HBF. Along-fault flow bulk permeability will increase again, due to altered zones within the PSZ being further deformed into cataclasite strands and fault walls into breccia zones, further enhancing along-fault flow. If however, non self-juxtapositions are achieved, the BNF could evolve into the IBF, where fault walls will be dominated by breccias and along-fault flow will increase. However, if further displacement occurs, the IBF may evolve in the LWF where extensive clay gouges will lower the along-fault flow permeability.

In Figure 6.23b, across-fault flow bulk permeability evolution is shown. As in Figure 6.23a, it is assumed that each fault will evolve into the next fault, depending on juxtaposition relationships. From VJF to VPF, across-fault flow will increase due to connective fractures crossing alteration zones. Depending on the thickness of these alteration zones, across-fault flow will increase from VPF to BNF if there is a thin zone of alteration (as mapped in the BNF). If the mapped portion had occluded the thin zone however, it is likely across-fault flow may have been reduced compared to the VPF. Assuming the BNF will grow into the HBF, across-fault flow will again increase due to the presence of brecciated fault walls. If however non self-juxtaposition occurs, the BNF may evolve into the IBF, and across-fault flow will be enhanced due to high permeability breccias on either side of the PSZ. If the IBF then evolves into the LWF, across-fault flow will drop, due to the presence of clay gouges across the fault zone. Future studies could add more points to the model presented in Figure 6.23 to further

constrain the bulk permeability evolutionary pathway in faults juxtaposing basalt against clay rich units.

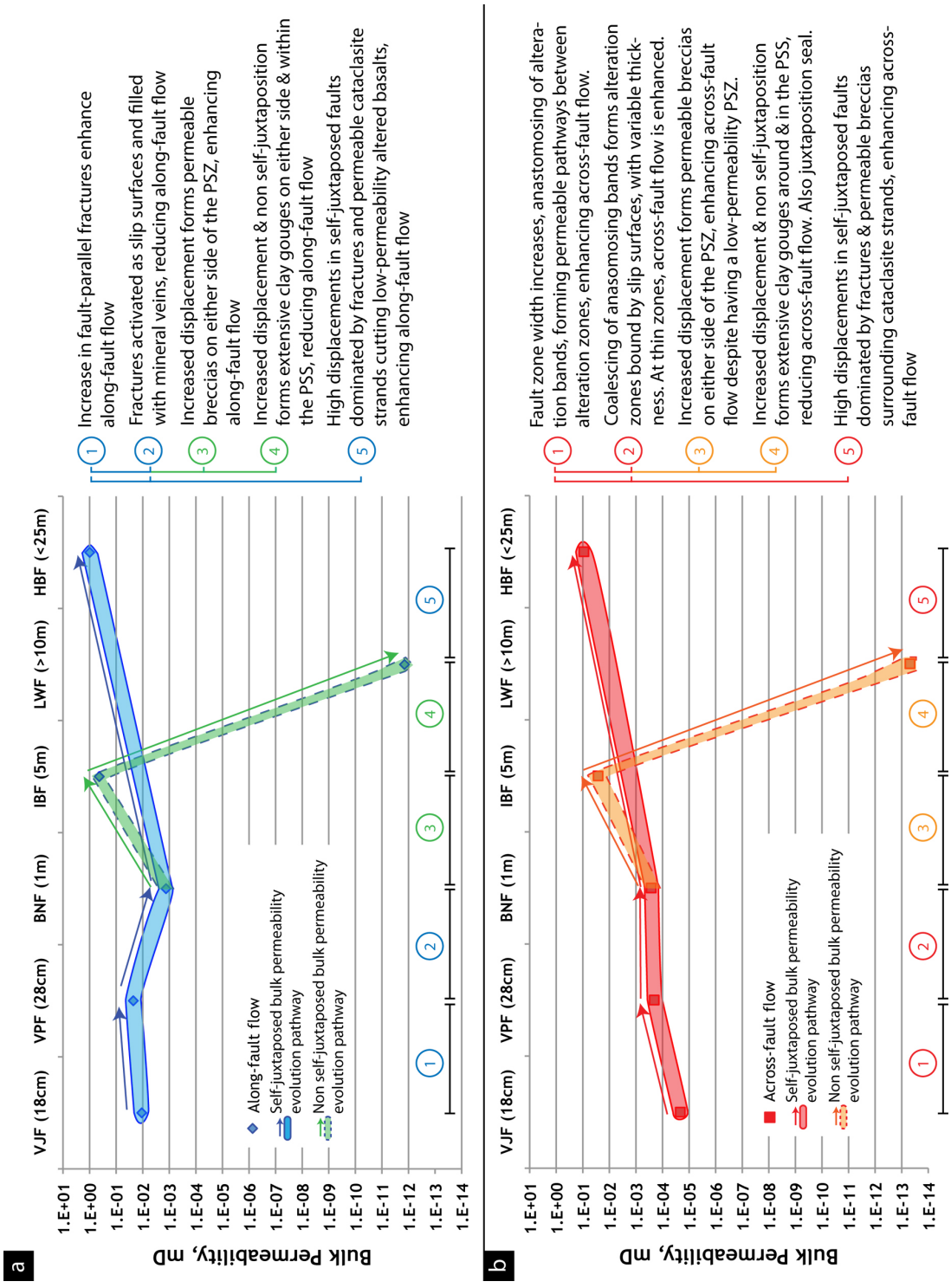

Figure 6.23: Bulk permeability evolution in along- and across-fault flow. a) Bulk permeability evolution in along-fault flow. b) Bulk permeability evolution in across-fault flow.

6.10. Compartmentalisation of flow

To visualise compartmentalisation of fluid, hydraulic heads of each map have been plotted. In an isotropic, homogenous rock mass, hydraulic head will have a constant gradient (Figure 6.24). However, if features affecting permeability are encountered (such as conduits or barriers to flow), this constant gradient will be interrupted. An impermeable feature will make high head (red) appear juxtaposed against low head (blue). In the case where a fault is a barrier to cross-fault flow, loss of communication will be achieved as a different head value is maintained on one side of the fault – this is called compartmentalisation. The hydraulic head maps for each fault's present day scenario are presented in order to compare compartmentalisation characteristics.

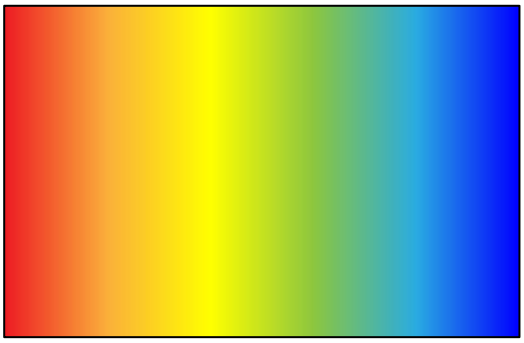

Figure 6.24: Example of a constant hydraulic head gradient in an isotropic homogenous rock mass. Flow left to right.

A comparison of hydraulic head gradients in across-fault flow models of present day scenario in each fault is presented in Figure 6.25, in order of juxtaposition and displacement. In most of the faults, there is an example of compartmentalisation, i.e. the faults act as a barrier to flow. In the VJF, the alteration of basalt is acting as a barrier to flow. This effect is particularly strong where the alteration thickness narrows toward the top of the map, as there are no fractures within the thin altered zone to translate fluid across the altered zone. In the VPF, there are multiple cases of compartmentalisation, which is again directly linked to the position of the alteration zones that act as the barrier. If fractures intersect the altered basalt zone, the compartmentalisation is not as strong. In the BNF,

the alteration zone (not the slip surface) acts as a barrier in its thickest location. However, when the alteration unit thins, and is dominated by slip surfaces (i.e. no alteration), across-fault flow occurs more constantly. This suggests that whilst alteration acts as a barrier, if there is a zone of no alteration across the fault, fluid will leak at that point. In the IBF, the barrier is the clay-rich tuff gouge. Similarly, there is strong compartmentalisation within the LWF due to the presence of both altered basalt and clay gouges. In the HBF, there was little in the way of strong compartmentalisation due to a more permeable PSZ promoting across-fault flow.

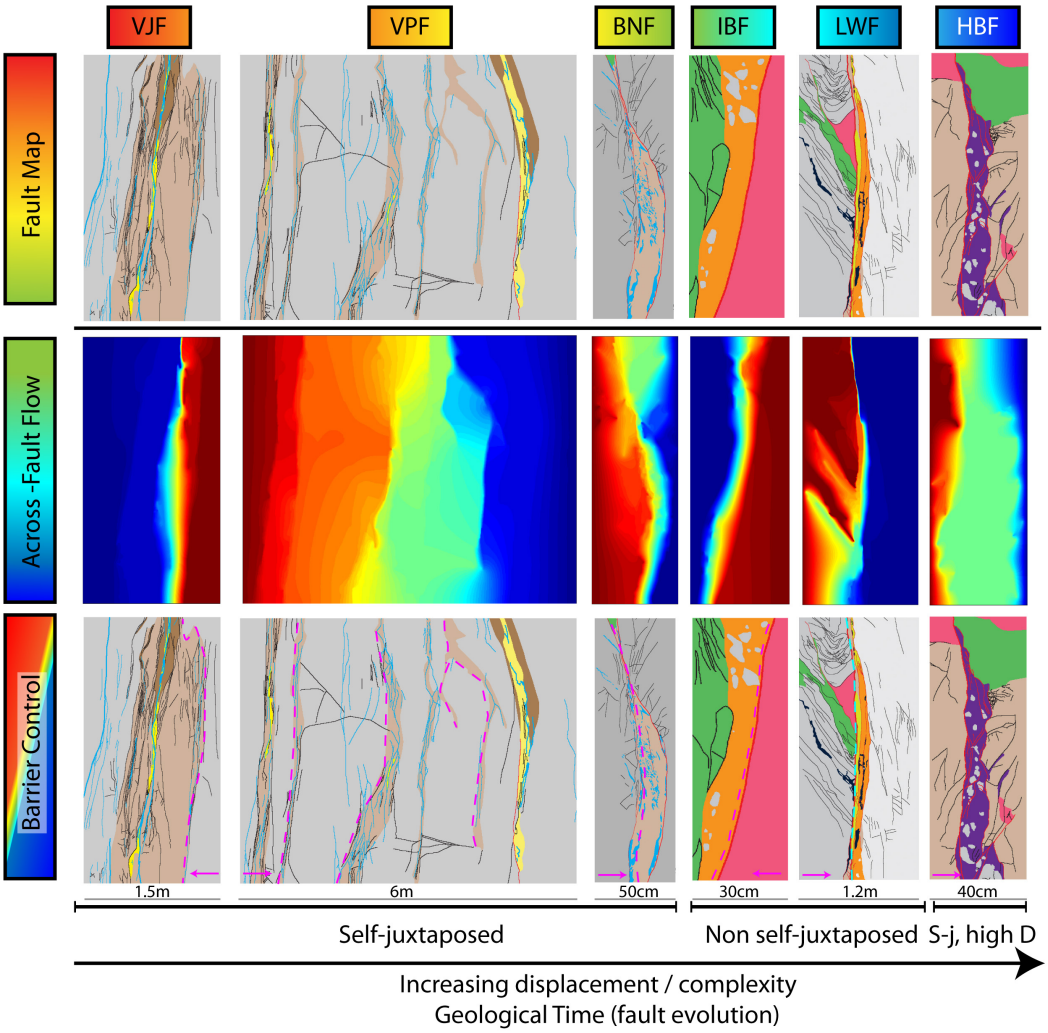

Figure 6.25: Hydraulic head gradient results for present day scenarios in all faults. Modelled as along- and across-fault flow. Flow in all images flows from red to blue. In the barrier control column, direction of flow is marked by pink arrow, and the feature that is acting as the barrier is highlighted by a dashed pink line (light blue line on LWF). In HBF there is no obvious barrier.

6.11. Summary

Modelled along-fault fluid flow bulk permeabilities are consistently higher than across-fault fluid flow, from half an order of magnitude to over seven orders of magnitude. Controls on along-fault fluid flow are fault-parallel open fractures in the walls of the fault, and connected slip surfaces and open mineral veins within the fault. These features enhance fluid flow, which results in large bulk permeabilities.

Across-fault fluid flow is dependent on the degree and thickness of low permeability fault rocks such as altered basalts and clay gouges, as well as locations of high permeability fault rocks such as breccias in the fault walls. Connectivity of slip surfaces across the fault are also important, i.e. if slip surfaces are connected, flow will preferentially focus into these and enhance across-fault flow. In cases where flow encounters a closed slip or low permeability fault rock with no connected pathways to follow, streamlines are uniformly spaced across the fault, suggesting steady equal flow rates across the low permeability zone over long geological time scales.

The control on flow compartmentalisation is the extent and permeability of any barriers, i.e. alteration and clay gouges. The compartmentalisation effect is likely to change along strike due to irregularities of thicknesses of the barriers and also open pathways cutting these, which would promote across-fault flow.

This study has shown that as faults evolve over time, their key flow controls and therefore bulk permeabilities also change over time. The spatial distributions of key flow controls also affect flow behaviour, where thin fault zones with no alteration will promote across-fault flow but thicker fault zones with an altered PSZ will restrict it. The key flow controls in each fault (through each of their modelled stages) are summarised below in Table 6.2. This illustrates well how key flow controls

change over time, and should be considered when modelling bulk permeability changes over time in fault zones.

Table 6.2: Summary table of key flow controls from this study's faults, and how they change over time in both along- and across-fault flow.

	Along-fault Key Flow Controls	Across-fault Key Flow Controls
VJF	Stage 1: Fractures and opened zeolite veins Stage 2: Fractures	Stages 1,2: Alteration
VPF	Stage 1: Fractures and opened zeolite veins Stage 2: Fractures	Stage 1: Alteration Stage 2: Alteration and closure of connected fractures
BNF	Stages 1,2,3: Slip Surface Stages 4,5: Mineralised slip surface Stage 6: Mineralised slip surface and open fractures	Stages 1,2: Connected opened zeolite veins across pre-altered zone Stages 3,4,5: Alteration, fault zone thickness
IBF	Stages 1,2: Slip surface, brecciated fault walls	Stages 1,2: Brecciated fault walls, survivor clasts
LWF	Stage 1: Slip surface Stage 2: Slip surface and peperite Stages 3,4: Peperite	Stage 1: Breccia, slip surface Stage 2: Open fractures and black gouge, partially opened slip surfaces Stage 3: Opened black gouge Stage 4: Fractures, breccia and cataclasite, fault zone thickness
HBF	Stage 1: Slip surface Stage 2: Cataclasite Stage 3: Cataclasite and fractures	Stages 1,2,3: Locations of breccia zones

6.12. Discussion

The slip surfaces (when open) were modelled at a permeability equal to open fractures, i.e. assuming the slip surfaces had an aperture of 0.5mm. However, the degree to which the slip surface is open is dependant on a number of factors, including the degree of the slip surface wall corrugation and/or stress orientation. These factors will significantly alter the bulk permeability and flow controls of the fault, especially if slip surface apertures have at some point in their permeability history been wider than 0.5mm. There is evidence for slip surfaces (and cavities along that) being open (<1m wide) at depth within the Faroe Islands faults, as discovered by Walker et al., (2011b). Walker et al., (2011b) found clastic infills within principal slip zones, and interpreted them as forming at <2km depth, suggesting slip surfaces can act as conduits to flow at depth (also found in Shipton et al., 2002). In addition, in this study, the Hov fault (also from the

Faroe Islands) was observed to contain 'suspended' breccia clasts in a matrix of zeolite along the slip surface (Chapter 4). This suggests high fluid pressures within the slip surface, and rapid precipitation of minerals following hydraulic brecciation of the wall rocks (Phillips, 1972; Woodcock et al., 2007; Woodcock et al., 2008). This suggests slip surfaces may actually have a much higher permeability than modelled in this study's fault maps, and therefore it could be possible that at depth, the Faroe Islands faults have a higher bulk permeability than that modelled within this study.

In the LWF the peperite was modelled as having high permeability, due to its highly altered and fractured nature, and a high degree of pore space observed at the present day surface (from field work and thin-section scales). As no permeability data are available for peperites, their permeabilities at depth are unknown. If fractures were closed, and pore space filled by clays at depth, then the peperite may have low permeability, which would alter the bulk permeability and fluid flow pathways modelled in the LWF. However, until permeability data is available on a peperite, modelled results for bulk permeabilities in peperite bearing basalt sequences are only speculative.

In most cases, some degree of flow occurs through fractures. However, the flow potential of these fractures will depend on the principal stress orientation. If considering vertical fractures in an extensional environment (with the maximum compressive stress vertical and the minimum compressive stress horizontal), fractures are likely to be propped open, and may therefore have a wider fracture aperture than modelled. However, if the fractures are at an angle (e.g. 45°), it is more likely these fractures will be closed and therefore not transmit flow effectively. Therefore it is possible that fractures may remain open at depth depending on their orientation, in which case bulk permeabilities in fractured media could be higher than modelled in this study's examples. In addition to this, fractures were mostly not connected in the mapped 2D exposures, however it is

likely that many more of these fractures are connected in 3D (e.g. the VJF fault-related fracture did not link in section view, but did in plan view - see Chapter 3). The above hypotheses may suggest that particularly in along-fault flow, instead of the fault zone and fault rocks controlling fluid flow, it is perhaps more likely that the fractured rock surrounding the fault zone will act as the major permeability control, and channel fluid along the fault. Across-fault flow will only be effective as a seal if clay gouge is present and entrained along the fault, if alteration is thick and constant along the length of the slip surface, or if the slip surface is composed of clay or mineralised by an impermeable mineral.

In the case of the LWF, flow pathways were not only controlled by the fault but also by the fault wall lithologies (low permeability basalt against high permeability peperite). Therefore, in non self-juxtaposed faults, juxtaposition of different lithologies in fault walls may act as the main control on fault flow, as is noted within clastic reservoirs (i.e. Cerveny et al., 2004).

Of the faults that were not modelled, based on their fault rock architectures and components, their likely flow characteristics can be predicted. In the case of Sumba Fault Zone and Talisker Bay Fault (see Chapter 3), both of which have gouge rich strands along the length of their exposure and are over 5m in displacement, it is likely that they will compartmentalise fluid across-fault, and act as a barrier to flow. Along-fault flow will occur preferentially in the fractured wall rocks. Across-fault flow will occur if fluid pathways are connected (such as fractures or mineralisation), or if pore space is not filled with clay and zeolite. In the case of the Hov Fault (HVF), a 1m-displacement fault, it is likely that strong compartmentalisation will not occur across the fault due to connected zeolite veins, but will impede flow across the fault to some extent. However, as the HVF is heavily mineralised, it could enhance along-fault flow due to the measured permeability of zeolite veins being lower than surrounding basalt (Walker et al., 2012b).

7. Discussion

This chapter will explore previous models of fault initiation, growth and evolution in basalt and other lithologies and compare them with results from the present study. Following this, permeability characteristics and strength of faults in basalt sequences are discussed, and linked with geochemical changes that occur in faults over time. The implications of fault structure and fault-related alteration for industry applications are then described, with the chapter concluding by presenting a classification scheme that could be used for predicting fault properties in basalt sequences. A summary table of the faults studied in previous chapters is presented in Table 7.1 for reference.

Table 7.1: Summary table for faults studied in the previous chapters.

Fault Name (abbreviation.)	Juxtaposition exposure type	Displacement	Lithologies	Location (volcanic province)
Vagseidi Jetty Fault (VJF)	Self	18cm	Basalt	Faroe Islands (FIBG)
Vagseidi Puddle Fault (VPF)	Self	30cm	Basalt	Faroe Islands (FIBG)
Bird Nest Fault (BNF)	Self	1m	Basalt	Mull (BIPIP)
Hramaborg Fault (HBF)	Self	25m	Basalt	East Iceland
Hov Fault (HVF)	Self & Non-self	1m	Basalt, volcanic conglomerate, bole	Faroe Islands (FIBG)
Sumba Fault Zone (SFZ)	Self & Non-self	5m	Basalt, volcanic conglomerate	Faroe Islands (FIBG)
I Botni Fault (IBF)	Non-self	5m	Basalt, tuff	Faroe Islands (FIBG)
Lawther Fault (LWF)	Non-self	<10m	Basalt, peperite	Ardnamurchan (BIPIP)
Talisker Bay Fault (TBF)	Non-self	18m	Basalt, volcaniclastic rocks	Skye (BIPIP)
Kerrera Fault Zone	Non-self	125m	Basalt, volcaniclastic rocks, conglomerates	Kerrera

7.1. Fault initiation in basalt sequences

The results of this study have shown that fault initiation in basalts follows the Crider and Peacock (2004) model, in that faults nucleate along pre-existing/pre-cursory fractures, and they link as the magnitude of displacement increases to form a through-going mature fault (Walsh et al., 2003). However, in the case of the vertical faults mapped in the Faroe Islands, the fault characteristics of parallel fracture zones being incorporated into the fault zone (rather than being abraded into the PSZ) are similar to that of the fault initiation mode described by Soden and

Shipton (2013). Rather than linkage of a fault initiating along a pre-existing structure, the fault dilates along the structure, allowing the fracture walls to move past each other, incorporating joint-bound slabs into the fault zone (Soden and Shipton, 2013). Thus, this study has shown that faults will initiate along pre-existing/precursory structures in host rock basalts, and depending on stress orientation, they will grow either by linkage of fractures as a result of shear, or by dilation of joints incorporating parallel fracture zones (Soden and Shipton, 2013), as conceptualised in Figure 7.1.

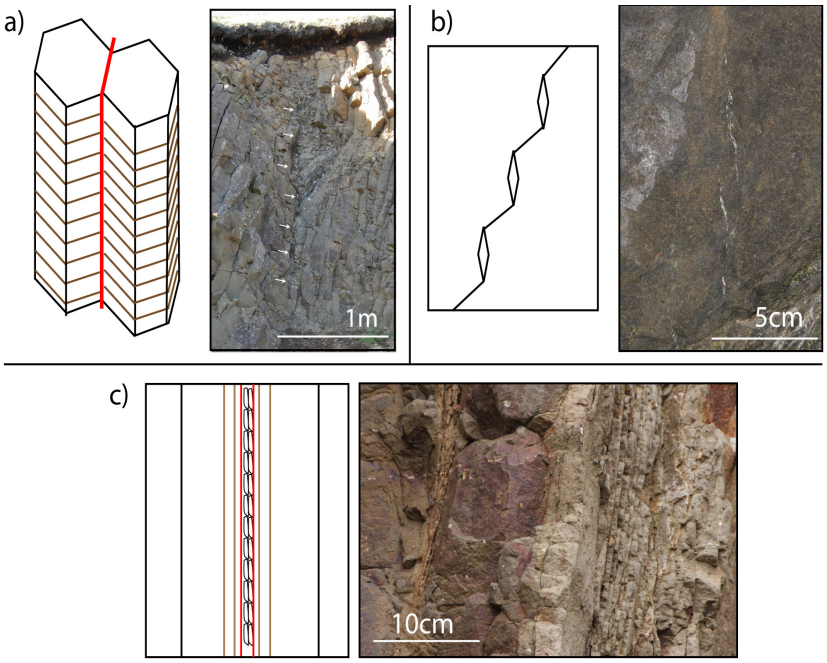

Figure 7.1: Conceptual cartoon for fault initiation and growth in basalt. a) Fault initiation along pre-existing structures such as columnar joints (example photo from Hov, Faroe Islands. Fault initiated along pre-existing cooling joints is highlighted with white arrows). b) Fault initiation from precursory structures in basalt (example photo from Bird Nest Fault, Mull). c) Fault growth by dilation of joints incorporating wall rocks (example photo from Vagseiði, Faroe Islands).

Further displacement will deform linked zones into breccia or crush the parallel fracture zones into breccias. This mechanism of fault initiation and growth is similar to that described by Walker et al. (2012a) who found that faults grow from an incipient joint network, developing into low-displacement fracture meshes. In faults with no pre-existing joint network, Walker et al. (2012a) found precursory en-echelon segments linked to form through-going (mature) faults.

Fault initiation by the formation of deformation bands is also important to consider, particularly in inter-lava units. Faults initiate and grow by deformation bands in granular porous rocks including sandstones (Aydin and Johnson, 1978). Granular porous rocks in basalt sequences include hyaloclastites, porous volcanic tuffs, and ash-rich friable ignimbrites. Previous studies of faults in these lithologies have found them to be dominated by deformation bands (hyaloclastites – Tewksbury, 2010; porous volcanic tuff – Evans and Bradbury, 2004; ash-rich friable ignimbrites – Shipton and Soden, 2013). Through numerical discrete element modelling, Schöpfer et al. (2006) found that faults localise initially in mechanically strong layers (e.g. basalt) as tensile fractures, before propagating into mechanically weaker layers (e.g. porous tuff). If these weaker layers between the basalt flows are also porous, it is possible that, at low displacements, deformation bands are likely to be an important mode of fault initiation. Whilst deformation band fault initiation was not found in the present study, it is important to highlight it as a possible style of deformation in appropriate inter-lava lithologies.

7.2. Fault growth and evolution

Host rock and magnitude of displacement are key controls on the growth and evolution of fault zone structure. As a general rule, the higher the displacement, the more complex the fault zone will be. Whilst this rule can be applied to most faults (with the exception of localisation on high displacement faults), host rock lithology is important in determining the types of fault rocks and fault structures that are likely to form (e.g. deformation bands are a typical feature of sandstone-hosted faults). This section will describe previous studies of faults in basalt and other lithologies, before comparing previous studies results to those of this study.

7.2.1. Previous studies of faults in basalt

Previous studies of basalt fault architecture have examined faults in geologically old layered sub-aerial basalt sequences (Walker et al., 2012a), oceanic basalts (Hayman and Karson, 2007, 2009), and geologically young basalt lava flows (Holland et al., 2006; Martel and Langley, 2006). Faults in young basalt flows are not discussed here, as they form at the Earth's surface and are characterised by large (>2m wide, deep and long) voids and rock fall into cavities opened by faulting (Holland et al., 2006; Martel and Langley, 2006). They also form within the upper 1km of the Earth's crust, whereas the faults examined for this study were formed at greater depths, and therefore under significantly different stress and temperature conditions.

Whilst this study has investigated how fault structure and content changes as a result of growth within basalt *sequences*, most previous studies of faults formed at depth in geologically old layered basalt sequences have focused on the deformation of a *single* basalt layer. Tentler and Temperley (2006) found that the mechanical property and pre-existing structure of different basaltic units has a profound effect on fault architecture. Faults in hyaloclastites form an array of shear fractures and develop through-going slip surfaces dominated by deformation bands. Faults in pillow lavas reactivate complex networks of pre-existing fractures, which cumulatively accommodate small amounts of slip, eventually developing through-going shear fractures to form a wide fault zone. Columnar jointed basalt has pre-existing sub-vertical cooling joints, favourably orientated to accommodate dilational-shear reactivation, allowing displacement with bulk slip being widely distributed amongst linked fractures (Tentler and Temperley, 2006).

Walker et al. (2012a) studied faults in layered basalt sequences on the Faroe Islands, and found that they generally develop in a similar way to layered clastic sequences i.e. by fault linkage from pre-existing structures

(in this case, cooling joints) and damage zone formation (as a result of fracture linkage). They also studied the controls on fault zone thickness, and concluded that thickness variations in fault zones in basalt do not reflect lithology, pre-existing structure or fault mode, but are rather due to accommodation of wall-rock strains (due to fault refraction as a result of weaker inter-lava units) and asperity removal. Walker et al. (2012a) further noted that the Faroe Islands faults commonly have asymmetric damage zones, which they interpreted as being due to discrete folding of the basalt lava flows (a result of fault refraction in the underlying sedimentary beds). This results in tension at the top of the basalt unit in the hanging wall, and therefore an increase in fault-related damage at these locations.

Faults in basalt have been noted in other studies, but as understanding fault structure and formation was not the primary goal of these papers, little detail was presented. Most of the fault rocks reported in these studies (described in the Introduction, Chapter 1) are fault breccias and cataclasites, and zeolite. Calcite and quartz mineralisation have been described. Gouge has been reported only where the basalts have been significantly altered prior to faulting (Hayman and Karson, 2007) or where tuffs and other volcaniclastic units have also been cut by the fault (Khodayar and Einarsson, 2002).

7.2.2. Previous studies of faults in other lithologies

The faulted lithology has a significant impact on fault style and fault rock content. For example, clean sandstones will preferentially deform by development of anastomosing deformation bands and slip surfaces (Aydin and Johnson, 1978; Shipton and Cowie, 2001); limestone deformation is commonly accompanied by fracturing, pressure solution and calcite precipitation (e.g. Billi, 2010; Micarelli et al., 2006); quartzo-feldspathic rocks will have phyllosilicate-rich fault cores bounding fractured protolith (e.g. Chester and Logan, 1986; Faulkner et al., 2003); and faulting within

interstratified sandstones and shales will result in breccia and clay smear formation (Fisher and Knipe, 1998; van der Zee and Urai, 2005).

Fault styles in layered sequences are described in the Introduction (Chapter 1), where it was found that fault style varies throughout a layered sequence, depending on the mechanical strength of the unit. Ferrill and Morris (2003) found that stronger units would be more likely to develop faults with steeper dips (i.e. sub-vertical) than those in weaker units (dips of 80-70º). This fault refraction in lithologies of contrasting mechanical strength can result from the switching of failure modes within each unit, from shear (in weak units) to tensile or hybrid (in strong units), or as a result of the change in shear failure angle (e.g. Ferrill et al., 2012). As a consequence, when displacement increases, dilational jogs form as the stronger units are 'pulled apart' whilst the weaker layers are smeared (Schöpfer et al., 2006). The clay smear may be continuous and so may link the weaker layer across the fault that has displaced it. This could result in non self-juxtaposition (i.e. the stronger layer is now juxtaposed against a weak layer). For example, a fault causing self-juxtaposition of sandstone will deform by deformation bands and slip surfaces, whereas when it is juxtaposed against a mudstone, it will deform by clay smear in preference to deformation band formation. This will change the structure of the fault, so juxtaposition is a very important control on fault structure.

7.2.3. Comparisons of this study's fault growth and evolution model with previously published models

Self-juxtaposed basalt deforms in a similar way to carbonate rocks at macro- and micro-scales. Billi (2010) found that in carbonate hosted faults, cataclasis develops as a result of intragranular extension fracturing and shear fracturing, in much the same way as observed in basalt at micro levels in the basalts in this study (Chapter 4). At field-scales, the tightly interlocking lithons of Billi et al. (2003) are similar to the parallel fracture

zones found in VJF, VPF, HBF, and LWF within the basalt, and deform in a similar way into breccias and cataclasites.

However, when considering layered basalt sequences as a whole (which contain weaker units between basalt flows), the structure of faults is more akin to that seen in layered siliciclastic sequences (e.g. Childs et al., 1996; Schopfer et al., 2006; Ferrill and Morris, 2003). In such layered sequences, faulting style is influenced by the mechanical strength contrasts in the rocks. This study has found that layered basalt sequences deform in a similar fashion to stronger lithologies (steeper fault dips, and dominated by fractures) whereas the manner of deformation of inter-lava units (i.e. by clay smears) is more comparable to the weaker lithologies of layered siliciclastic sequences.

The fault growth model and fault rocks found in this study are similar to those described by Walker et al. (2012a), apart from their findings that the hanging wall basalt always accommodates strain by fault refraction. The preferential hanging wall deformation described in Walker et al. (2012a) therefore cannot be readily compared with the results of this study. In all of the non self-juxtaposed faults studied here (where fault-related deformation in the fault walls could be seen), the hanging wall is basalt, and therefore more likely to be characterised by fractures (due to its higher strength compared to the other faulted lithology). However, monoclinal flexure in the hanging wall (Figure 7.2) would mean that the basalt at the base of the flow will be deformed by compression in the Walker et al. (2012a) model, yet tension fractures have been commonly observed in both this study and by Walker et al. (2012a) at the base of lava flows in the hanging wall.

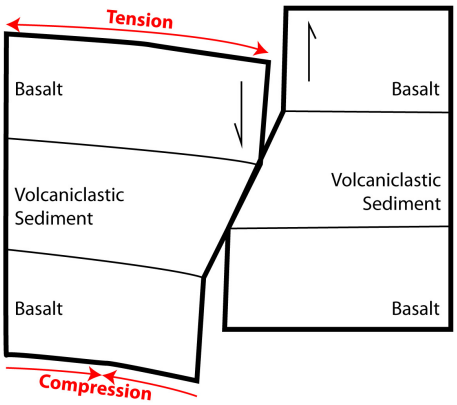

Figure 7.2: Monoclinal flexure model in basalts, modified from Walker et al. (2012a).

Furthermore, folding in response to fault refraction could equally occur in the footwall of the fault. In this study, fault-related deformation was found in the footwall of the VJF fault, indicating the control invoked by Walker et al. (2012a) cannot always be dominant in the hanging wall, and must also occur in the footwall. Similarly, in other layered sequences with contrasting mechanical strengths, it is not always the hanging wall that accommodates the geometrically required strain resulting from fault refraction (Childs et al., 1996; Schöpfer et al., 2006). Schöpfer et al. (2006) also noted that monocline formation in the early stages of fault growth is accommodated by ductile flow in weaker layers, rather than by damage in the stronger wall units.

7.2.4. Large-scale fault evolution model and considerations for faults in layered basalt sequences

The synthesis of results from this work with previous published studies has enabled a large-scale model for fault initiation and growth in layered basalt sequences to be developed, as described below.

Faults in layered basalt sequences initiate from pre-existing structures such as cooling joints (e.g. VJF fault). Results from modelling normal fault growth in layered sequences led Schöpfer et al. (2006) to conclude that faults are likely to initiate as Mode 1 fractures in brittle layers, and so the

developing fault is likely to propagate into surrounding inter-lava units via en-echelon linkage (e.g. Gudmundsson 1992). As it propagates into the inter-lava units, the fault will refract so that its dip angle becomes shallower (Walker et al., 2012a). Results from this study show that mechanically strong units (e.g. basalt) deform by tensile fracturing and brecciation, and are characterised by fluid-mediated alteration and mineralisation (e.g. BNF, SBF). The formation of large-scale dilational jogs is necessary to accommodate fault refraction in layered sequences (e.g. Ferrill and Morris, 2003), and so formation of large-scale dilational jogs may occur in basalt layered sequences hosted fault zones. The formation of large-scale dilational jogs would also suggest that fluid flow is more likely to concentrate in the jogs, and the presence of fluid-mediated alteration and zeolite mineralisation would certainly support this hypothesis. The weaker inter-lava clay-rich units will deform by shear fracturing and smearing (e.g. IBF).

This study has also shown that the pre-existing structure of the host rock basalt is important in fault initiation and development. Basalts, by their nature, are likely to develop a range of pre-existing structures during formation; from dense arrays of columnar joints to massive flows with little internal structure (e.g. Passey and Bell, 2007). This variation of pre-existing structure makes basalt unique in terms of the fault architectures they are likely to develop, particularly in the early stages of faulting (also noted in Tentler and Temperley, 2006). This study has shown that the pre-existing structure of the host rock basalt has a profound effect on the resulting fault zone architecture. Faults in basalt with pre-existing vertical cooling joints (e.g. VPF, VJF) have a sub-vertical fault plane surrounded by parallel fractures, and a principal slip zone containing joint-bound slabs. In basalts with no pre-existing structure, faults had typical normal fault orientation (60-75°) surrounded by fractures, and contained fault-bound lenses which were increasingly deformed into breccias with increasing displacement. Therefore at field scale, fault initiation and growth in

basalts is different from other lithologies due to basalts' wide degree of pre-existing structures.

It should also be noted that faults initiate from pre-existing structures in other lithologies, e.g. tectonic fractures in siliciclastic sandstones (e.g. Wilkins et al., 2001). However, these fractures develop as a result of regional shortening and folding, and not at actual lithology formation. Therefore basalts are unique in this sense, in that they can have a wide range of pre-existing structures that are not inherited as a result of other tectonic movements, but as a result of their formation due to cooling processes.

7.3. Fluid flow and alteration

This section explores the nature of fluid flow within faults. An introduction to fluid movement in basalt is given for context, before a discussion of fluid flow within basalt-hosted faults. Fluid-mediated alteration of basalt is also discussed, and the implications of alteration for fault strength are explored.

7.3.1. Fault permeability characteristics

In the sub-surface, faults are an important control on fluid migration, and they can serve as a conduit or as a seal (e.g. Caine et al., 1996). The permeability characteristics of faults are generally described with reference to the different components found in classic descriptions of fault architecture, i.e. fault core and the damage zone (Caine et al., 1996). The fault core is generally believed to be a barrier to flow, particularly when a thick core with clay gouge is present (Caine et al., 1996). Where the damage zone is dominated by fractures (e.g. in low porosity rocks such as basalts), there is more likely to be a distributed conduit. The presence of high proportions of both fault core and damage zones most likely yields a combined conduit-barrier (Caine et al., 1996). If the fault core is composed of a single slip surface it will act as a conduit to flow, but if it is thicker

and filled with material (e.g. deformation band-rich or filled with clay gouge) it will be a barrier.

7.3.2. Comparison of this study with other permeability studies in faults in basalt sequences

Flow modelling of the faults analysed in this study (Chapter 6) shows that higher bulk permeabilities characterise low displacement fault zones dominated by fractures, where along-fault fluid flow is enhanced by connected fault-parallel fractures (and slip surfaces) surrounding (and within) the PSZ. Lower bulk permeabilities are found in across-fault fluid flow, which is concentrated where the PSZ narrows, or where fractures/open slip surfaces connect across the fault. High displacement, non self-juxtaposed faults have very low bulk permeabilities because clay gouge/smears dominate the PSZ. These model results are consistent with permeability measurements of fault rocks from the Faroe Islands undertaken by Walker et al. (2012b). They found that rates of fluid flow along faults would be greater than through the host rock, and across-fault fluid flow was restricted throughout fault evolution. Walker et al. (2012b) concluded that along-fault fluid flow would facilitate fluid migration through impermeable units so that the faults act as a fluid 'pipe' cross-cutting the stratigraphy.

Results of the flow modelling in this study are in agreement with Walker et al. (2012b), in that along-fault fluid flow permeability is greater than the host rock (and across-fault fluid flow) permeability, and across-fault fluid flow is impeded by barriers. Whilst Walker et al. (2012b) measured individual permeabilities of fault rock samples from the *present day* at a range of pressures (therefore allowing an estimate of how the permeability of their present day fault samples changed at depth), they were not able to illustrate how bulk fault zone permeability changes *over time*. In addition, whilst Walker et al. (2012b) were able to measure permeabilities from

individual core samples from the fault zone, these types of measurements cannot not take into account the complexity of the entire fault zone, and therefore its cumulative effect on permeability. Thus, bulk permeabilities of the fault zone could not be modelled in their study.

This study was able to model bulk fault zone permeability and permeability evolution over time (Chapter 6), based on combining detailed field and microstructural characterisation carried out in this study. This detailed work was used to model how the permeability of individual fault zone elements changes over time (e.g. as a result of mineralisation or alteration), and therefore how that affects *bulk* fault zone permeability over time. This enabled identification of the key temporal controls on changes in bulk fault zone permeability and fluid flow pathways over time. This study found key flow controls in fault zones change over time as a function of mineralisation, alteration, displacement, juxtaposition and fault thickness variations. Key flow controls included closing of open slip surfaces, alteration of basalt-derived fault rocks and clay-gouge smearing (Chapter 6). As the permeability of key flow controls changes as a result of, e.g. mineralisation or alteration, the bulk permeability also changes. Therefore by combining microstructural detail with individual fault rock permeabilities, the controls on bulk permeability over time can be determined. Uncertainties in these models are largely based on permeability estimates of individual fault rocks, therefore for higher accuracy, permeabilities of fault rocks from mapped faults could be measured prior to flow modelling.

Microstructural analysis prior to flow modelling also found fault rocks have a higher porosity than the host rock, due to a greater fracture density. The porosity (and so permeability) is, however, dynamic because clays and zeolites have filled fractures and other pores at one or more times in the faults' histories. Cementation will occlude some of the earlier pores, but new ones will open with further faulting. The secondary minerals including clays can also be porous, and these intra-granular pores may be occluded

by later generations of mineralisation. Thus, fault permeability will fluctuate over time in response to multiple episodes of fault movement and fluid flow, dissolution and cementation.

7.3.3. Alteration and mineralisation in basalt sequences as a result of faulting and fluid flow

This study has found that the alteration and mineralisation of faults in basalt is a significant determinant of their evolution, permeability and strength. The mafic mineralogy of basalts makes their fault-related alteration and mineralisation properties unique compared with other faulted lithologies. The reactive nature of minerals within basalt (particularly olivine and feldspar) lends itself to the formation of new minerals in the presence of alkaline waters: in particular, zeolite and phyllosilicate minerals. The continued fault-related alteration of basalt enhances the content of these neoformed minerals within the fault zone over time, which will ultimately have an effect on fault strength and evolution in basalts.

Previous studies have shown that fault-related alteration of other lithologies, for example, limestone is dominated by pressure solution and calcite precipitation in fault zones owing to the Ca-rich host rock (e.g. Billi, 2010; Bastesen and Braathen, 2010). Fault rocks in quartzo-feldspathic rocks are phyllosilicate-rich, usually as a result of hydrothermal alteration following hydrothermal fluids flowing through the fault after slip events (Ganerod et al., 2008). The cause and effect of fluid-mediated alteration and mineralisation on fault strength and fluid flow is explored in the following sections, along with estimates on how zeolite mineralogy can be used to infer fluid temperatures differences within host and fault rocks.

7.3.3.1. Relative timing of fault-related alteration

At the thin-section scale (discussed in Chapter 4) a feedback in faulting mechanisms is evident whereby with increasing deformation, more pore space is opened by intragranular fracturing, allowing enhanced fluid flow. These pores are later filled by zeolite and clay as a result of the increased reactive surface area of the fractured minerals. Feldspar and olivine is more soluble than pyroxene and Fe-Ti oxides, and will therefore be more likely to be replaced by secondary minerals, including zeolites and clays (Chapter 4).

A recent study by Lee et al. (2012) of basaltic Martian meteorites found that dissolution rates of pyroxene and olivine vary with fluid temperatures and pH. They found that a 2mm diameter olivine grain would completely dissolve in a fluid at pH5/100ºC in three years, whereas closer to a thousand years would be required for the equivalent amount of pyroxene to dissolve. As is discussed later, fluid temperatures within the fault zones studied here are likely to have been in excess of 100ºC. Alkaline solutions are particularly common in basalt, and are responsible for zeolite mineralisation (Mumpton, 1977), therefore the pH of fluids may frequently be higher than the more acidic waters in the Lee et al. (2012) study. However, if dissolution rates are as high for weakly alkaline waters as they are for weakly acidic, clay precipitation along fractures in faults following olivine dissolution may occur early. Given that olivine in the fault walls and within the fault zones analysed in this study has been completely replaced, the clays that have replaced olivine (e.g. smectite, chlorite) are likely to have formed relatively early in the fault's history (based on Lee et al., (2012) results). In the case of the low displacement faults studied here, where cataclasis is minimal, the replacement of olivine by clay in fracture walls would weaken the altered rock (in the fracture walls) and make them more inclined to slip (assuming the stress orientation is optimal). Thus, alteration of olivine will weaken the fault zone, and could promote further slip during the early phases of fault process.

7.3.3.2. Mineralisation as a result of fluid flow

The style of fault-related alteration of basalt is very similar to that found in very low-grade regional zeolite metamorphism of basalts, where clays, zeolites and other secondary minerals (e.g. albite, celadonite, zeolitisation of feldspars, replacement of olivine by clay) form in porous parts of the basalt such as rubbly tops or vesicular zones (e.g. Neuhoff et al., 1997; Neuhoff et al., 1999; Neuhoff et al., 2000; Neuhoff et al., 2006; Liou, 1979; Keith and Staples, 1985; Pe-Piper and Miller, 2002). In these basalts, the distribution of zeolites can form distinct mappable zones.

The temperatures of fluids flowing through a fault zone in basalt can be estimated, using the temperature dependence of the types of zeolite minerals that crystallise from solution (e.g. Walker, 1960). Moreover, if the zeolite mineralogy of the host rock differs from the fault rock, then fluids of different temperatures are likely to have travelled through the fault. Figure 7.3 shows temperature estimates for fluids precipitating zeolites in the host rocks and fault zone of the studied faults, based on the mineralogy of zeolites within amygdales and fault-related fractures respectively, as determined by SEM-EDX analysis (see Chapter 4).

The fluids within the low to medium displacement faults studied on the Faroe Islands are likely to have originated from the same groundwaters that were responsible for the low-grade zeolite facies metamorphism of the host rocks. This is shown by the similarity of zeolite mineralogy between fault-related fractures and host rock amygdales. This similarity suggests no new fluid temperature was tapped by the fault, and instead fluid flow relied on fluid/rock interactions along the fault walls (from existing groundwater temperatures) to produce zeolite and calcite minerals (Gislason et al., 2010). The coincidence of zeolite mineralogy also suggests that in the Faroe Islands, faulting occurred at the same time as burial and low-grade zeolite metamorphism of the lava pile.

Zeolites in the BIPIP and Iceland faults (BNF, HBF, LWF) imply higher temperatures than those experienced by their host rocks (Figure 7.3). Zeolite mineralogy in the BNF suggests that the fluids moving throughout this fault were 50-100ºC hotter than those responsible for low-grade zeolite facies regional metamorphism of the host rock. The higher temperature fluid tapped by this fault may have originated from the Mull Central Complex. In addition the presence of pyrite mineralisation in the BNF also suggests that a fluid with a different chemistry than that which deposited the zeolites passed through the fault system.

Within the HBF, zeolite minerals within fault-related fractures are similar to those within host rock amygdales, as described by Walker (1960), suggesting comparable fluid temperatures. However, the HBF is also mineralized by chalcedony, suggesting a Si-rich fluid moved through this fault. This fluid is likely to be hydrothermal in origin, because chalcedony mineralisation is not typically associated with zeolites, and chalcedony mineralisation of host rock amygdales was not found. Given the HBF is associated with a relatively recently extinct rift (see Chapter 2), it is reasonable to assume flow of hydrothermal fluids when the rift was active, as the fault is high displacement, and therefore more likely to have tapped deeper reservoirs.

The LWF fault rock lacks zeolite mineralisation. The fluid within the fault responsible for precipitation of chalcedony must therefore have come from an external source, possibly hydrothermal.

Zeolites were absent from the host rock of the TBF so there is no frame of reference to interpret zeolite minerals within the fault zone.

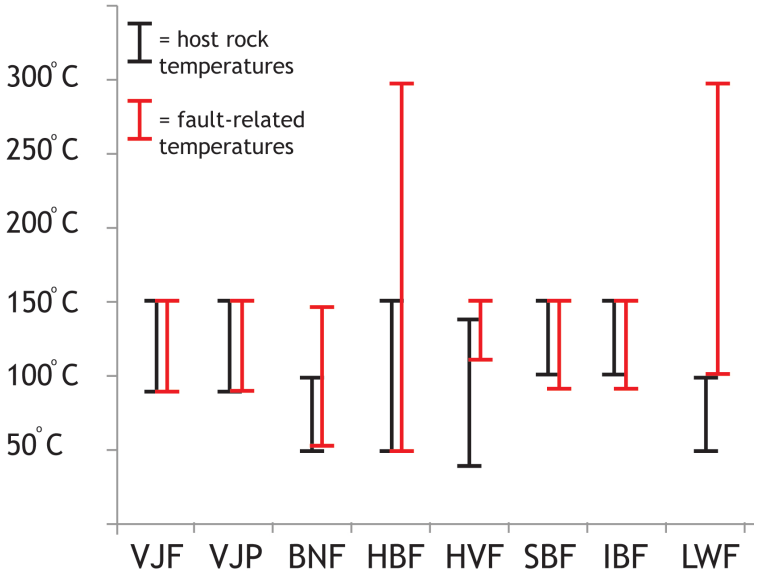

Figure 7.3: Estimate of host and fault fluid temperatures for all fault zones, based on minerals found within amygdales in the host, and vein minerals from fault fractures (see Chapter 4). Temperatures of zeolites from Iijima (1980), Coombs et al. (1959), Jørgensen (2006), Kristmannsdóttir (1978) and Neuhoff et al. (2000).

The observations from the BIPIP (BNF, LWF) and Iceland (HBF) fault zone zeolites suggest that with higher displacement, faults are more likely to tap into fluid reservoirs with a differing chemistry and/or temperature from the fluid in the surrounding host rock.

This relationship between fault displacement and zeolite zones is illustrated schematically in Figure 7.4. It demonstrates that an individual basalt lava flow, and so a low displacement fault, may be contained within a single zeolite zone (for example, a chabazite/thomsonite zone), and so may sample only fluids belonging to that zone. A higher displacement fault will have a longer fault trace (Cowie and Scholz, 1992) and may therefore extend into deeper zeolite zones. Flow along this fault will therefore bring the warmer fluid up from the newly tapped zeolite zone, causing new wall rock reactions and therefore zeolites (Figure 7.4). With still greater displacement the fault trace will lengthen, and higher temperature zeolites will form along the fault as hot fluid flows along them. Thus, faults in basalt can act as pathways to locally disrupt and elevate zeolite depth zones, particularly where displacements are high (Figure 7.4).

A caveat to this model is that zeolite temperatures and depth ranges can vary with geological setting and high fluid pressures (e.g. Iceland deep drilling program, Schiffman et al., 2010). It is therefore possible that the medium displacement faults in the Faroe Islands contained the same zeolite minerals as the host rock because the zeolite zones were relatively thick. The difficulty with this hypothesis is that zeolite zone temperatures vary and significantly overlap each other, and therefore it is recommended that further work to assess regional zeolite zones and temperatures in comparison with fault-related zeolites is carried out to test this hypothesis further.

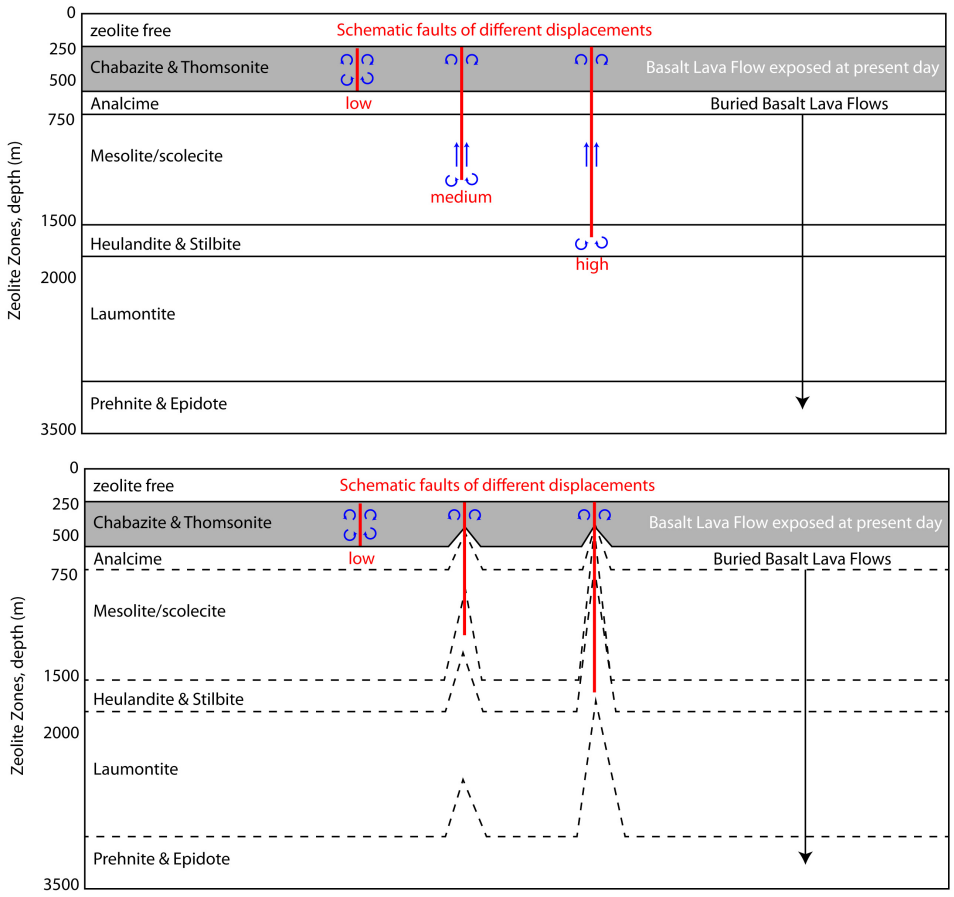

Figure 7.4: Schematic illustration of fault hydraulic behaviour in basalts with zeolite zones. For the purposes of this schematic model, zeolite depths are from eroded Icelandic basalt lavas identified by Neuhoff et al. (1999). Blue arrows represent fluid movement. Beneath, same model, but correcting for faults locally changing zeolite depth zones (estimated).

Another indication that higher displacement faults can tap fluid reservoirs of a higher temperature and potentially different chemistry comes from the isotope work carried out in the Kerrera Fault Zone in this study

(Chapter 5). This study found a potential magmatic source for fluids coming in to the fault zone, and zeolites were absent. The lack of zeolite minerals could be due to the altered nature of the basalt (heavily chloritised), or there was no low temperature metamorphism in the region.

7.3.4. Fault strength and fault evolution

As already suggested, dissolution of olivine and feldspar early in the development of a fault may promote the early re-precipitation of clay along fractures, thus reducing the shear strength of the rock. In this study, smectite and chlorite were found along fractures within faulted basalt and both may have an impact on fault strength. Indeed, smectite has been shown to weaken faults at low normal stresses (e.g. Saffer et al., 2001). Clay-filled fractures and extensive smectite-bearing gouges are common in the Kerrera Fault Zone, and originate from the smearing of inter-lava clay-rich beds, and precipitation of authigenic clays from solution. These have significant implications for the strength of the zone. The clays and clay gouges are very similar in morphology and type (e.g. foliated clay gouges with smectite) to the clay described in Holdsworth et al. (2011), suggesting comparable fault strength behaviour (i.e. smectite clay gouges are weak, and more liable to slip than the surrounding host rock). Similarly, in lower displacement faults from this study, the formation of clays within fractures may have enhanced fault-weakening, therefore promoting slip.

This clay weakening of faults hypothesis presumes that alteration of primary minerals (e.g. feldspar and olivine) and coupled crystallization of clays occurred during and not after faulting. Other studies have however found that fluid-mediated alteration can take place after faulting. For example, in a study of the Punchbowl Fault (an exhumed segment of the San Andreas Fault), Solum et al. (2003) found differences in the mineralogy of fault rocks and host rocks (e.g. an increase in clay in the fault rocks compared with the gneiss host rock). However, they demonstrated that reactions had occurred after faulting, so that fluid-mediated clay growth could not have been responsible for fault weakening. Several lines of

evidence confirm that fluid-mediated mineralisation and alteration was active during movement of faults analysed in the present study: (i) zeolite vein fragments occur in cataclasites and so mineralisation must have pre-dated the slip event; and (ii) clays are found in fault-related fractures that have a foliation consistent with movement on that particular fault (see Chapter 4). Therefore clay weakening of faults observed in this study could have occurred during faulting.

In the faults described in this study with less than 25m of displacement, clay filled fractures are rare, and most clay has formed interstitially by alteration of primary minerals. Most slip surfaces are also filled with zeolite and lesser clay, so the strength of low displacement, self-juxtaposed faults in basalt may depend on the shear strength of zeolites rather than clay. Most studies of frictional strength have been carried out on clay gouges, and so the properties of zeolites are less well known. However, Morrow and Byerlee (1991) carried out frictional sliding experiments of laumontite gouge. They found that the presence of laumontite in shear zones did not affect shear strength of the rock, and it was stronger than illite and montmorillonite. This difference in behaviour reflects contrasts in crystal structures. Clays, being sheet silicates, have layers of water that act as glide planes and encourage slip, significantly reducing the shear strength of clay-rich gouge (Bird, 1984). In zeolites, water is bonded in a network of tubes and does not significantly influence frictional sliding (Morrow and Byerlee, 1991). Morrow et al. (2000) also found that calcite is stronger than clays, and Moore et al. (2009) suggest other zeolites and carbonates are likely to have similar strengths. Therefore, the presence of zeolite veins and gouges is unlikely to substantially weaken faults.

With increasing displacement on a fault, the chance of cataclasis within that fault increases. This fine-grained material contains rock and mineral clasts and is weaker than its surroundings, and so more susceptible to further cataclasis and granular flow (Fitzgerald and Stunitz, 1993). Prior to grain size reduction and cataclasis, intragranular fracturing increases

permeability, so that greater volumes of fluid are able to access the fault rock. A reduction in grain size will increase the surface area/volume ratio of primary minerals and elevation of permeability will potentially introduce more fluid. In combination, these changes will enhance the susceptibility of minerals within the fault rock to dissolution and replacement so that more clays and/or zeolites may form, further influencing fault strength.

7.3.5. Coupling between faulting, permeability, alteration and strength

Faulting, porosity and permeability, fluid flow, water-mediated dissolution, replacement and mineralisation, and rock strength are all linked within a feedback system (Figure 7.5). As more fluid passes through basalt as a result of faulting, greater volumes of clay and zeolites are likely to form by fluid-mineral interactions (due to increases in surface area/volume ratio of the primary minerals, e.g. this study has found replacement of feldspars and olivines will result in an increase of zeolite and clay minerals). The clays and zeolites will occlude intragranular and fracture pores, thereby probably reducing the permeability of the fault. Clay mineralisation will weaken the fault, promoting slip, whereas zeolites will either have no effect on the fault, or may strengthen it. With further faulting and opening of new fractures, porosity and permeability will increase so that fluids may continue to access the fault. Following faulting, newly formed zeolites and clays will occlude porosity and reduce permeability. Therefore, with more faulting events, a basalt will become weaker and less permeable owing to clay and zeolite mineralisation (Figure 7.6). Fault-related alteration is linked to feldspar and olivine content of the basalt (as this study has found these are the most susceptible minerals to alteration), along with porosity content (the more available space, the more fluid can flow within the rock, thus enhancing alteration). Both fault permeability and strength are directly linked to new zeolites and clay filling fault-created pore space, and fault strength is also influenced by the degree of cataclasis (controlled by Fe-Ti oxide and pyroxene content) within the fault rock.

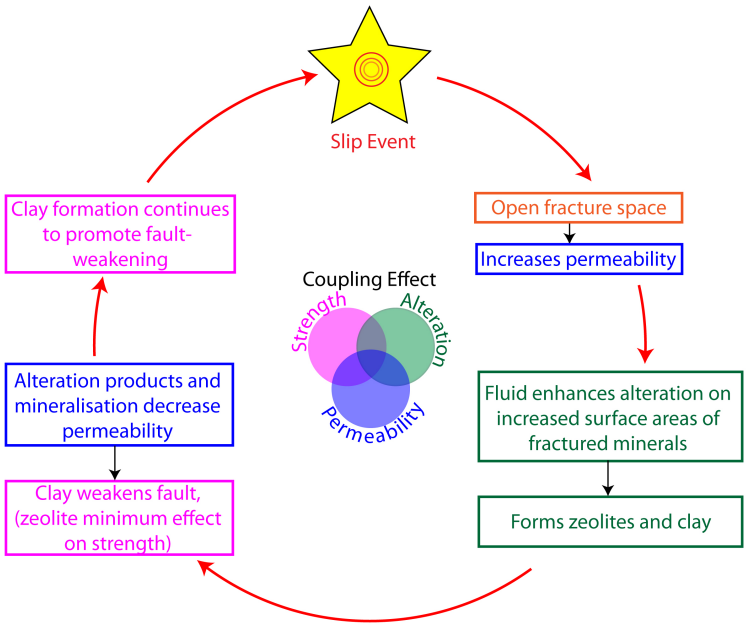

Figure 7.5: Feedback system between alteration, strength & permeability resulting from faulting.

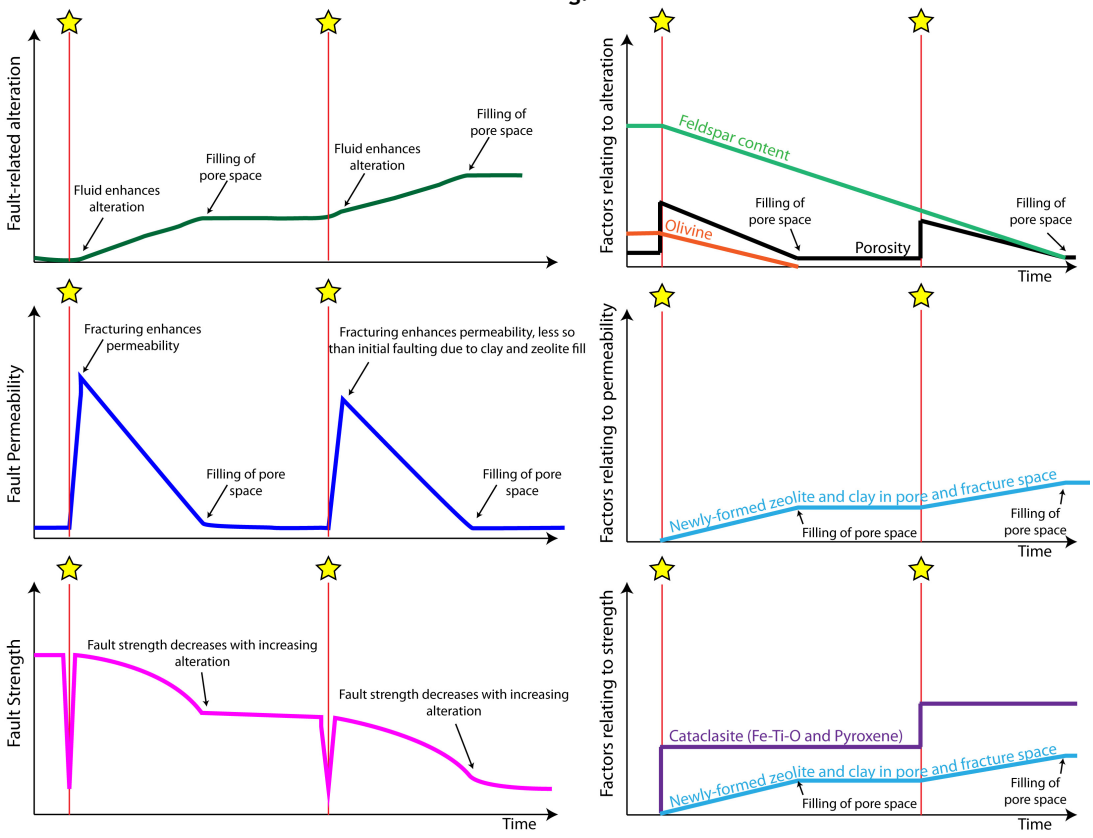

Figure 7.6: Alteration, permeability & strength changes as a result of faulting (stars) over time. Factors (specific to basalt) influencing each faulting effect are shown to the right.

7.4. Summary model for faults in basalt: linking field, microscope, and fluid-flow behaviour

A conceptual cartoon demonstrating how field and microscopic characteristics and permeability controls of faulted basalt are linked is presented in Figure 7.7. The figure is based on results from this study, and is presented in order from low to high displacement faults:

- At low displacements, fracturing dominates the fault zone at the field-scale (increasing fluid flow potential). At microscales, alteration of the groundmass and initial intragranular fracturing of minerals occurs; through-going fractures are commonly filled with zeolite minerals, decreasing fluid flow potential.
- In the next stage of displacement, fractures and alteration dominate the fault at field-scales, with increased alteration, intragranular fracturing and cataclasis of the basalt occurring at microscales. Cataclasis is controlled by pyroxenes and Fe-Ti oxides, and alteration of feldspar results in the formation of zeolites and clays. Zeolite and clay mineralisation of fractures is common, and reduces the potential for fluid flow.
- With increasing displacement, the likelihood of displacing a clay-rich interbed increases, and it is likely that clay from this interbed is entrained into the fault zone as gouge, enhancing the clay content of the fault zone (and decreasing fluid-flow potential). At micro-scales, foliated-clays develop along with cataclasites derived from pyroxenes and Fe-Ti oxides. Again, zeolite and clay mineralisation is prominent.
- At very high displacements, a mixture of entrained clays, neo-formed clays and zeolites, cataclasis and altered basalt lenses dominate the fault zone, generally decreasing fluid flow potential. The fault rock is characterised by complex cataclasites and gouges in a matrix of foliated clays and zeolite minerals at microscales.

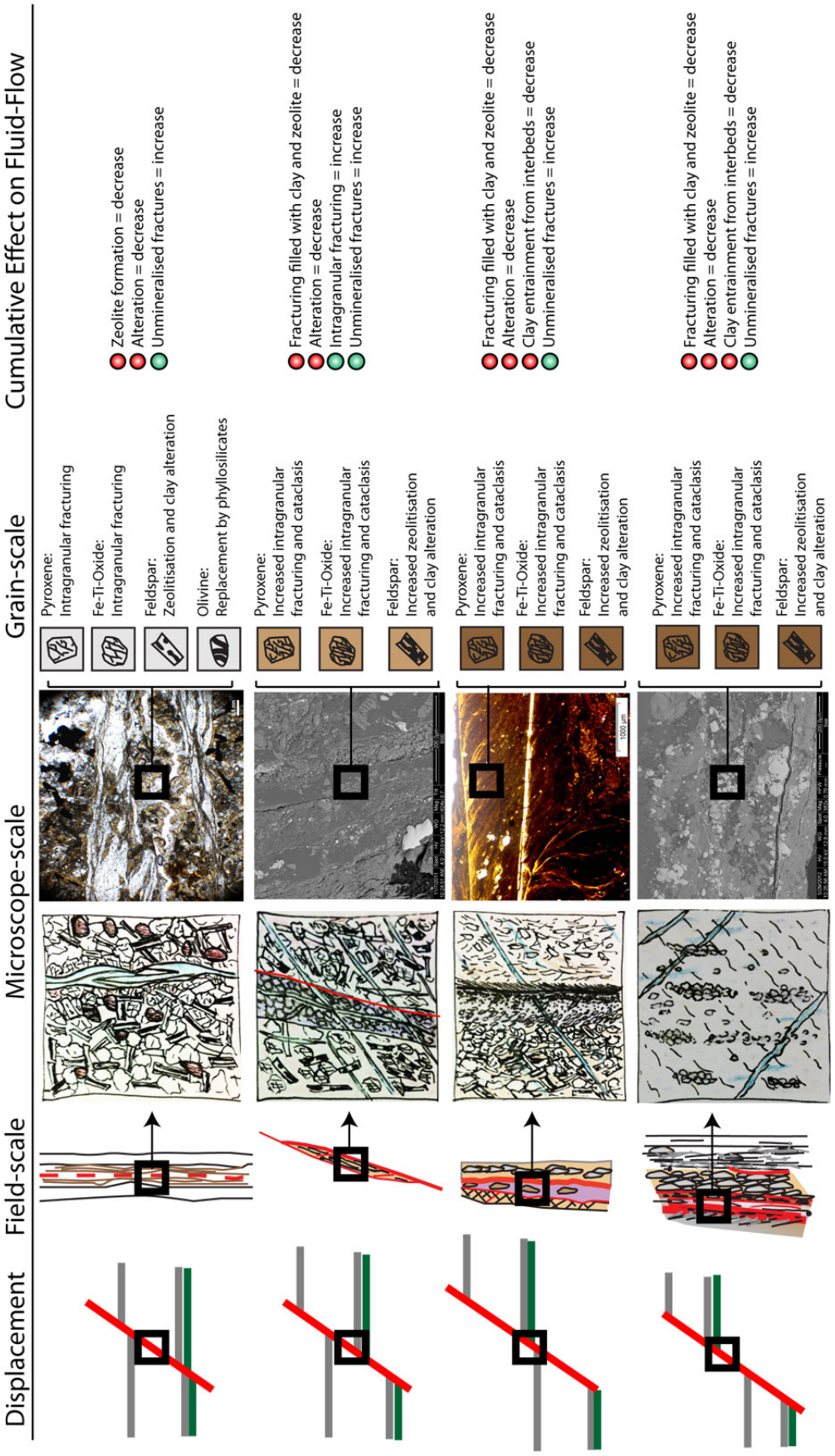
Displacement
Field-scale
Microscope-scale
Grain-scale
Cumulative Effect on Fluid-Flow
Pyroxene: Intragranular fracturing
Fe-Ti-Oxide: Intragranular fracturing
Feldspar: Zeolitisation and clay alteration
Olivine: Replacement by phyllosilicates
Zeolite formation = decrease
Alteration = decrease
Unmineralised fractures = increase
Pyroxene: Increased intragranular fracturing and cataclasis
Fe-Ti-Oxide: Increased intragranular fracturing and cataclasis
Feldspar: Increased zeolitisation and clay alteration
Fracturing filled with clay and zeolite = decrease
Alteration = decrease
Intragranular fracturing = increase
Unmineralised fractures = increase
Clay entrainment from interbeds = decrease

Figure 7.7: (Previous page) Conceptual model linking field, microscopic, and fluid-flow observations from this study together.

7.5. Implications of fault structure and fault-related alteration for CO_2 storage

Following the injection of supercritical CO_2 in basalt formations, CO_2 can be 'locked in' (stored) by the formation of carbonate minerals. Basalt is rich in the divalent cations of Ca^{2+}, Mg^{2+} and Fe^{2+}, which are concentrated in plagioclase feldspar, olivine and pyroxene. These divalent cations can react with the injected CO_2 to crystallize minerals such as calcite, magnesite and siderite respectively if their host minerals undergo dissolution, or have already reacted with groundwaters. Indeed, groundwater in basalt is also particularly rich in these divalent cations (Matter et al., 2009). The CO_2 is therefore mineralised by the following reaction:

$$(Ca^{2+}, Mg^{2+}) + CO_2 + H_2O = (Ca, Mg)CO_3 + 2H^+ \text{ (carbonate)}$$

The carbonates may precipitate within pores in the tops of basalt flows (interflow zones), where vesicular, brecciated, basal pillow complex and basal breccia zones act as the primary aquifers due to their elevated permeability (Reidel et al., 2003).

7.5.1. Fault structure and CO_2 storage

This study has found that particularly at low displacements, faults in basalt have a high permeability due to the abundance of fractures and mineralised veins. Fluids will always flow toward higher permeability zones, such as vesicular and brecciated flows, but if they encounter fractures and fault zones, these areas may be by-passed. Therefore, if supercritical CO_2 is pumped into a basalt flow containing low displacement faults (<10m), which are below seismic resolution, supercritical CO_2 may not be confined to interflow zones, as required for CO_2 storage. The supercritical CO_2 may then, by along-fault flow, travel back to the Earth's surface to be released into groundwaters or the atmosphere. For example,

the Columbia River Basalt Group (CRBG) in Washington, USA, has been considered as a site for CO_2 storage, due to laterally extensive and thick lava flows covering a large area. The CRBG hosts freshwater aquifers that supply Washington State with drinking water, but also brackish aquifers beneath the fresh water aquifers that have potential for CO_2 storage. The storage is planned within the high permeability (44-90 mD) vesicular and brecciated (rubbly) basalt lava tops, capped by low permeability (0.0001 – 0.00001 mD) basalt interiors (McGrail et al., 2011). During the planning of CO_2 sequestration in the CRBG, seismic surveys revealed a thick succession of basalts uninterrupted by deep-seated surface or subsurface faults (www.bigskyCO2.org). A statement by the Columbia Ground Water Management Area (CBGWMA) states 'the occurrence of vertical faults and tectonic fractures may be minor in comparison to the areal extent of the flood basalt plains, and may be irrelevant to fluid leakage' (www.cbgwma.org). Tolan et al. (2007) found that faults in the CRBG are a barrier to across-fault fluid flow but act as a conduit for along-fault fluid flow. Tolan et al. (2007) also investigated fluid flow by comparing basalt and along-fault permeability. They expect permeability along the fault to be several orders of magnitude lower than fluid moving laterally within the basalts as a whole, potentially due to the high interconnectivity of pore space and vesicles in flow tops. However, other reports written on the Columbia Basin contradict these statements. For example, Reidel et al. (2003) agree that faulting of the basalt flows could be detrimental to CO_2 storage, as the faults could provide vertical flow pathways within the basalt.

A geology map of the CRBG (Reidel and Hooper, 1990) shows a range of large- and small-scale faults, folds and plateaus that could interact with the aquifers. Whilst seismic data may not pick up low displacement faults, these structures are particularly important to the sub-surface flow of groundwater. This study has found that low displacement faults in basalt are characterised by fractures and crackle breccias, which could cross-cut

a proposed CO_2 storage unit (e.g. brecciated lava top), and provide an along-fault fluid conduit (e.g. fluid flow modelling results from VJF showed high bulk permeabilities and strong focussing of fluid flow through fractures and zeolite veins throughout the fault zone). Therefore, leakage of CO_2-rich groundwater could occur where low displacement faults cross-cut the stratigraphy, as fluid may not flow where predicted from site characterisation within the basalt piles. If leakage occurs, the current groundwater aquifers of Washington State may be contaminated, causing a problem for drinking water in the region. On the other hand, if low displacement faults cutting proposed storage sites have an along-fault permeability lower than the proposed storage unit (the basalt lava rubbly tops), the fault may have a negligible effect on along-fault fluid flow within that unit. The along-fault flow permeability of the fault will be controlled by fracture fill – this study has found that fracture fill will most likely be zeolite mineralisation, but the type of zeolite mineralisation will depend on the fault displacement, depth of fault formation, and the local regional zeolite metamorphism isograds. Zeolite minerals are typically a few orders of magnitudes lower in permeability than the host rock (Johnson, 1980), and may therefore not exceed the target storage unit's permeability. However, if fractures are unfilled (i.e. open), these will likely exceed the permeability of the target storage unit. Also, depending on layer thickness and fault displacement, faults cutting the proposed storage unit will cut the cap rock (i.e. overlying basalt formations), and if permeable (due to the presence of fractures) could allow supercritical CO_2 to unexpectedly flow outside the proposed storage unit.

Faults at higher displacements are less likely to act as an along-fault fluid conduit, but more likely to act as a barrier to flow, particularly if fault displacement exceeds the minimum layer thickness and cross-cuts inter-lava clay-rich zones (e.g. fluid flow modelling results from the LWF highlighted a clay rich fault zone to be highly impermeable). This may compartmentalise supercritical CO_2 flow in an unpredicted fashion within

the storage site if faults are ignored, due to them being below seismic resolution, or deemed to have no effect on site fluid flow. Unexpected compartmentalisation may result in reactivation of faults if injecting at high pressures and if the faults are suitably orientated and weak (as they may be if displacing clay-rich units). Therefore, characterisation of faults in the target storage area (prior to CO_2 injection) is critical for assessing their fluid flow impact.

7.5.2. Fault-related alteration and CO_2 storage

Successful storage of CO_2 is dependent not only on fault structures in the basalt flows into which it is injected, but also on the bulk mineralogy and chemistry of the basalt. Ca and Mg are key elements in carbonate precipitation during CO_2 storage, and if concentrations of Ca and Mg levels are lower in fault zones than in fresh basalts, mineral carbonation may not be so effective. Furthermore, even if Mg and Ca concentrations in fault zones are the same as host basalts, these ions may be contained in secondary minerals that are not as susceptible to dissolution during CO_2 storage as original olivine and feldspar, thus again rendering the fault rock a less effective site for carbonation than the host rock.

This study found fault rocks have bulk chemistry compositions that are distinct from their host rocks, indicating that reactions have taken place as a consequence of faulting, and within an open geochemical system. The fault rocks show replacement of feldspar by zeolite, zeolite/chalcedony mineralisation, and clay mineralisation. For example, in the BNF, Ca/Si ratios have increased relative to the host rock owing to mineralisation of fracture and intragranular pores by the Ca-rich zeolite scolecite. Reactive surfaces of Ca-rich minerals are desirable for CO_2 storage (McGrail et al., 2006), and this increase in Ca could make the fault rocks an attractive potential storage site. However, another fault in a similar host rock to that of the BNF (e.g. the HBF) may be mineralised by other zeolites or Si-veins to lower the Ca/Si ratio and so limit the effectiveness of the fault for CO_2

storage. Zeolite composition is dependant on the temperature of the groundwater that has infiltrated the fault. As discussed in section 7.3.3, depending on the depth of regional zeolite metamorphism isograds, low displacement faults are likely to contain the same zeolite minerals as those of the basalt they are cutting, whereas medium-high displacement can contain zeolite minerals from higher temperature ground waters than those circulating in the host rock. Therefore, faults with varying displacements within a proposed injection site could be expected to have different zeolite compositions, which would change the bulk chemistry for each fault. Characterisation of fault zone bulk chemistries from a range of displacements within the target storage site would help constrain this further.

These observations from bulk chemical composition analyses of host rocks vs. fault rocks could be of great importance when considering CO_2 storage in basalts, as precise modelling of target rock chemistry and groundwater composition is key to ensuring CO_2 is locked within the basalt (Alfredsson et al., 2008; Schaef et al., 2009; Van Pham et al., 2012). These models usually use bulk basalt chemistry compositions to model CO_2 carbonation. This study therefore recommends that models and simulations of CO_2 carbonation in basalt also include fault rock chemistry compositions.

7.5.3. Key considerations for CO_2 storage in basalt sequences

Fault behaviour and distribution within a proposed CO_2 injection site in basalt sequences should therefore be carefully considered, as they could:

a) change the bulk chemistry of the basalt where faults are located within proposed injection sites. The bulk chemistry is likely to be changed across the whole fault zone, and particularly along fracture and mineral vein walls (due to higher concentrations of zeolitisation of feldspars in these locations). This bulk chemistry difference from the host rock may inhibit carbonate mineral growth, due to loss of

readily available Ca and Mg owing to replacement of their original host minerals (feldspars and olivines) by less reactive clays and zeolite. Zeolite mineralogy is dependant on palaeo-groundwater temperature, extent of low-grade zeolite metamorphism isograds, and fault displacement. Therefore, bulk fault rock compositions could vary between faults of different displacement within a proposed storage site, which is important to consider when modelling CO_2-basalt rock interactions for storing CO_2.

b) act as high permeability conduits encouraging along-fault fluid flow (particularly in low displacement faults), resulting in leaks into clean groundwater sources or into the atmosphere. Depending on layer thickness, medium-high displacement faults (i.e. possibly sub-seismic) may be more likely to result in barriers to flow, particularly if cutting clay-rich inter-lava units. This could result in unpredicted compartmentalisation of fluid flow, which could result in reactivation of faults if injecting at high pressures. Within any given proposed storage site, faults may have a range of displacements and therefore structures, and act as conduits, barriers or combined conduit/barriers to fluid flow. It is therefore key to consider the architecture and hydraulic structure of all possible faults within a proposed CO_2 storage site. Predicting what effect displacement and host rock will have on fault structure, content and permeability is discussed in section 7.6.2.

7.6. Implications for prediction of fault properties in the hydrocarbon industry

In this section, faults in basalt sequence are discussed with reference to features of interest to the hydrocarbon industry. Predictions will be made of fault structure and fluid flow along faults.

7.6.1. Predicting fault thickness from displacement value

As shown in the Introduction chapter, in general, high displacement faults typically have a thicker fault zone than low displacement faults (Scholz, 1987; Hull, 1998). Thus, the thickness of a fault zone may potentially be predicted from its displacement. However, as Shipton et al. (2006) demonstrated, the thickness of a fault can vary by as much as three orders of magnitude for any given displacement value. Furthermore, Walker et al. (2012a) found that in the Faroe Islands basalts, fault zone thickness and displacement do not correlate and the thickness for any given displacement can span nearly four orders of magnitude. Their data are comparable with displacement ranges in sedimentary sequences (Childs et al., 2009), suggesting no predictable relationship between fault thickness and displacement. In the Walker et al. (2012a) thickness/displacement discussion, they found that lithology is not a primary determinant of fault zone thickness. In agreement with Walker et al. (2012a), when thickness/displacement data from this study are compared with data from the literature (Shipton et al., 2006), it falls into the same range as other documented faults mostly from clastic lithologies (Figure 7.8), and there is no linear correlation between fault thickness and displacement.

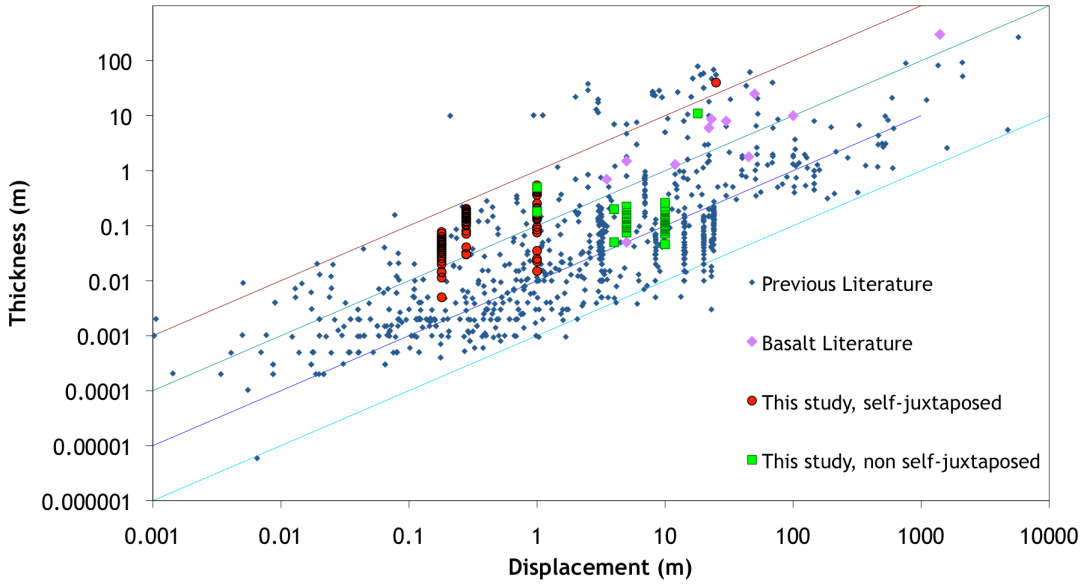

Figure 7.8: A compilation of fault zone thickness-displacement datasets (blue points, from Shipton et al., 2006, and references within). Many of these previous datasets do not differentiate between fault zone thicknesses and principal slip zone and so points plotted may be variable in terms of fault zone thickness. Also plotted are principal fault zone thickness data from this study (red dots) and fault zone thicknesses (purple dots) in basalt from Walker et al (2012a), Forslund and Gudmundsson (1992), Gudmundsson (2007), Hayman and Karson (2007, 2009), Khodayar and Einarsson (2002,2004). These data confirm that for an individual displacement value, PSZ thickness can vary over three orders of magnitude.

However, when juxtaposition type is considered (Chapter 3), in this study, fault zones are relatively thinner in non self-juxtaposed faults (where clay-bearing units are juxtaposed against basalt), than in self-juxtaposed faults, when compared with displacement value. For example, a 10m displacement non self-juxtaposed fault has the same fault thickness range as that of a 28cm displacement self-juxtaposed fault (Figure 7.8). Thus, lithological changes within a faulted basalt sequence could be a primary control on fault zone thickness, and could be used to help predict thickness variations across differing juxtapositions. In order to more accurately predict fault thickness, it is also important to consider what constitutes fault thickness for a better comparison between lithologies (in Figure 7.8, data do not always distinguish between fault zone or fault rock thickness), and to take into account any differences in lithology differences *within* any faulted sequence.

7.6.2. Predicting fault rock and fault seal properties based on displacement and juxtaposition type

Diagrams for classifying fault rocks in sandstone and shale have been produced in order to enhance predictions of fault properties in hydrocarbon reservoirs. The variables considered in these diagrams are differences in post-deformation lithification (e.g. faults in pure sandstones are susceptible to quartz mineralisation), clay content, and fragmentation (e.g. Cerveny et al., 2004; Fisher and Knipe 1998). A similar approach is taken in this study to predict fault rock types within basaltic sequences following the structure of Fisher and Knipe (1998).

7.6.2.1. Using host rock to predict fault rock type

The results from this study demonstrate that fault juxtaposition type is linked to fault architecture and permeability. Faults within self-juxtaposed basalts are dominated by fractures, have relatively high bulk permeabilities, and allow across- and along-fault fluid flow. With increasing displacement, self-juxtaposed faults become dominated by breccias and cataclasites, have moderate permeabilities, and promote along-fault fluid flow but impede and act as a barrier to across-fault fluid flow. Faults in non self-juxtaposed basalts (e.g. against a clay-bearing sedimentary bed) tend to be dominated by gouge within the PSZ and fractures in the adjacent units. Permeabilities in these faults are low, promoting along-fault flow but impeding across-fault flow. With increasing displacement, multiple gouge-rich strands form, and extensive clay smears can occur from faulting of clay-rich horizons. In this case, permeabilities are very low, again with along-fault flow promoted and acting as a barrier to fluid flow across the fault.

For illustrative purposes, lithologies that are common within basalt sequences are grouped into three categories based on their clay content: crystalline, clay-bearing/granular and clay-rich (Figure 7.9). These

categories are then used to generate predictions of the fault rocks that may be expected as a result of faulting in a basalt sequence. The fault rocks considered in this study have been divided into three fault rock series, again based on their clay content (after Fisher and Knipe., 1998): (i) mafic-crystalline lithologies fault-rock series; (ii) phyllosilicate framework fault-rock series; and (iii) clay-smear series. Using results from this study together with published observations, an estimate of what fault rock series might be produced following faulting of a specific lithology is presented in Figure 7.9.

Each of the fault rock series can be further sub-divided into fault rock types expected as a function of displacement. Figure 7.10 presents a fault-rock classification model relating clay content of host rocks in basalt sequences to fault rock series and fault rock types, again following the structure of Knipe and Fisher (1998). Host rock clay percentages are estimated, and the model should be considered a first attempt at predicting fault rocks based on host rock lithology in basalt sequences. The fault-rock series are described below:

Mafic-crystalline lithologies fault rock series (M-CLFRS): This is a new class of deformation feature suggested from this study. Their main deformation elements are fractures, cataclasites and breccias. Clay gouges are unlikely to form unless (as discussed later) the host rock contains abundant olivine. With increasing displacement, this clay-poor fault rock series will decrease in porosity and permeability due to cataclasis of the PSZ, and depending on fluid flow history, also by post-deformation zeolite and clay mineralisation. The walls of the fault are likely to be dominated by fractures that will make a high permeability zone for along-fault flow.

Phyllosilicate-framework fault rock series (P-FFRS) were first introduced by Knipe et al. (1997), to describe fault rocks developed in impure sandstones (>15% phyllosilicate content). In this study, the same

classification set out by Fisher and Knipe (1998) for this series is used, as lithologies are similar (granular and containing clays). Porosity and permeability in P-FFRS decrease with increasing displacement, due to mixing of pyroxenes and Fe-Ti oxides with phyllosilicates, forming clay-bearing cataclasites. This series can also be used to describe clay-rich cataclasites, which are transitional between M-CLFRS and clay-smear series (Fisher and Knipe, 1998).

The **clay-smear series** (C-SS) definition is also based on the description by Fisher and Knipe (1998). Here, clay smears contain significant volumes of aligned phyllosilicates from deformation of phyllosilicate-rich rocks (>40% phyllosilicates).

However, more data are required to test the above predictions on fault rocks generated from host rocks, particularly so in the mafic-crystalline series. For example:

- *Crystalline classification*: e.g. rhyolites, whilst only composing <10% of a basalt sequence, have been classed within the 'crystalline' lithology type, and tentatively within the mafic-crystalline lithologies fault series. However, as rhyolites are silicic and have a different mineralogy to basalt, they may fault in a different fashion owing to the likelihood of much slower rates of fluid-rock interactions during faulting.

- *Basalt mineralogy*: e.g. fault rocks derived from basalt with a high percentage of olivine (such as olivine basalts) may be more clay-rich than those derived from low-olivine host rocks (such as tholeiitic basalts), and may therefore result in a degree of clay-smear. However, further microscopic analysis from faults in basalts with varying amounts of olivine would be required to test this.

- *Basalt morphology*: e.g. the morphology of individual basalt flows is also important to consider. Basalt lava flow tops are more porous and altered than the main body of the lava. Therefore, depending on the degree of alteration and porosity, faulting of the tops may produce different fault rocks than suggested in this section. Additionally, if a basalt lava flow contains multiple pre-existing cooling joints (e.g. colonnade vs. entablature morphologies), or zones of pillow lava, fault displacement will be distributed within those pre-existing structures. This could result in a heavily fractured system but without fault rocks necessarily being formed. The outcome would therefore be a fracture-dominated system (e.g. Tentler and Temperley, 2006).

- *Pre-faulting alteration of basalt*: e.g. if a basalt has been severely altered before faulting as a result of hydrothermal alteration or low-grade zeolite metamorphism, it may be very clay- or zeolite-rich. Faulting of these lithologies could produce a clay- or zeolite-rich gouge, and fractures may be scarce.

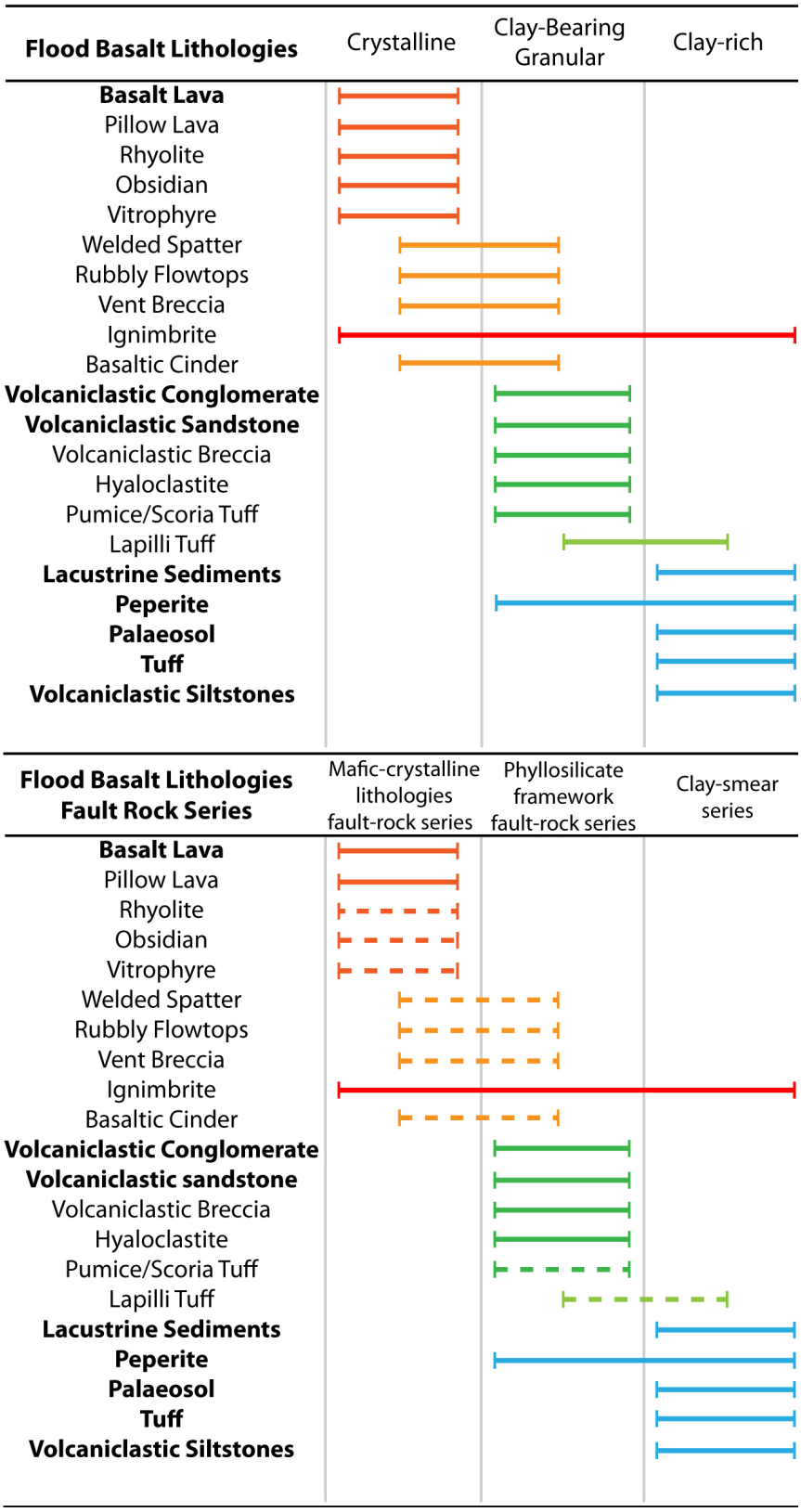

Figure 7.9: Examples of common lithologies found within basalt sequences. Each lithology is grouped into crystalline, clay-bearing/granular, or clay-rich rock types, and below, divided into basalt lithologies fault rock series (see text for descriptions of categories). Where the classification of a lithology is uncertain, a dashed line is given. Faults cutting flood basalt lithologies described in this study are highlighted in bold.

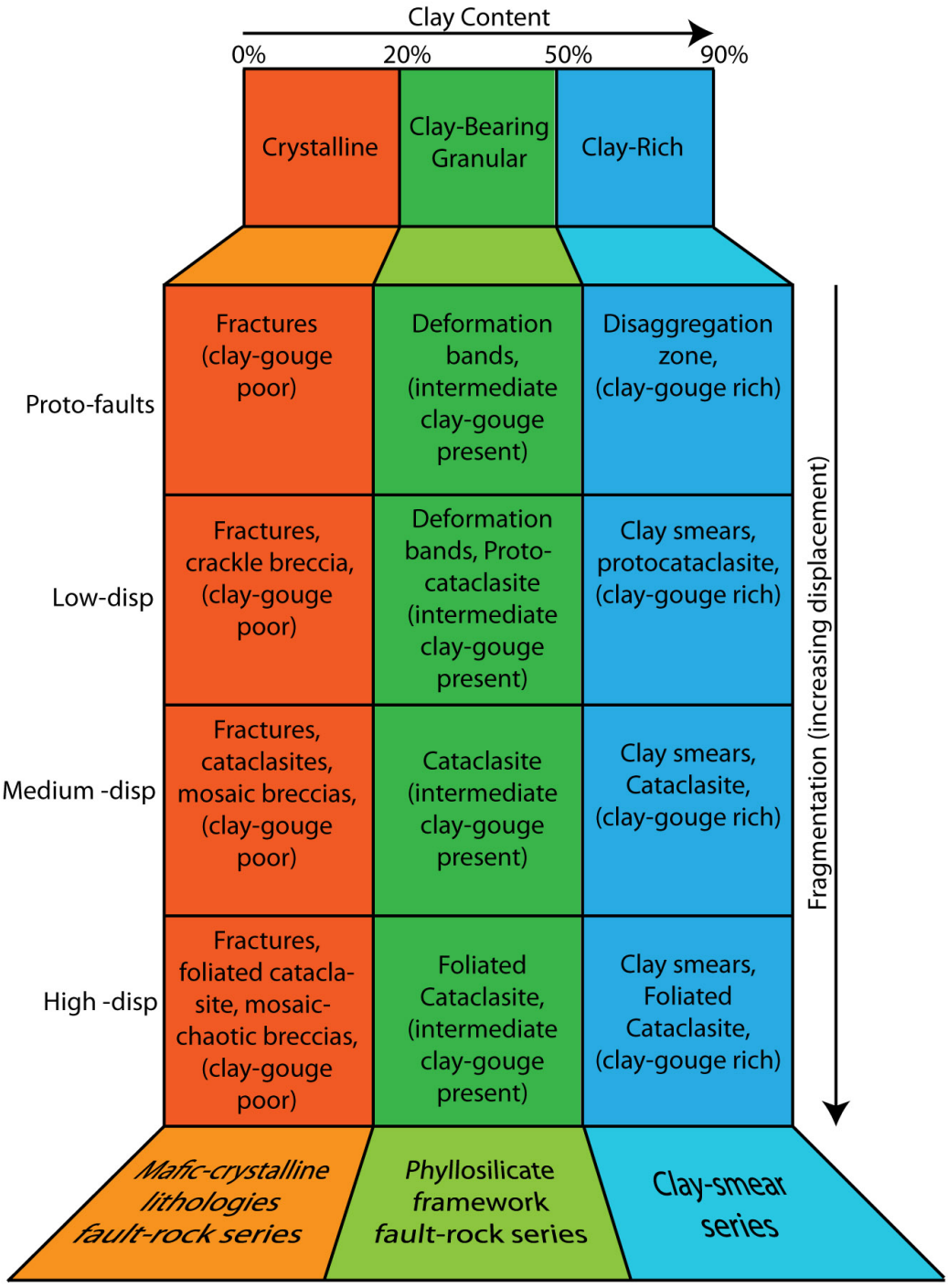

Figure 7.10: Fault rock classification relating protolith clay content and displacement to fault rocks. Displacement ('disp') increases throughout a fault's lifetime, and produces one of the three types of fault rock series from each host rock, shown in the bottom part of the diagram. Diagram structure after Fisher and Knipe (1998).

7.6.2.2. Using predicted fault rocks and juxtaposition types to evaluate fault seal behaviour

The lithological and fault rock classifications outlined above can be used to predict the fault rocks produced by juxtaposition. Using juxtaposition triangle diagrams (Knipe, 1997), juxtapositions of the stratigraphy across a fault with a range of throws can be shown schematically. Juxtaposition diagrams image the hanging wall of a fault against its footwall, and are used to simply evaluate juxtapositions of rock types for varying displacements (Figure 7.11).

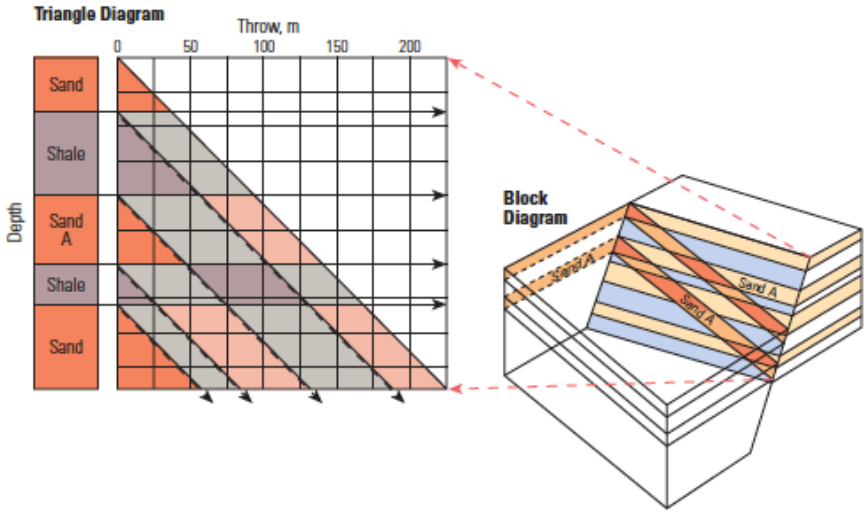

Figure 7.11: Juxtaposition diagram (left), imaging juxtapositions for any given displacement on a fault (see block diagram right). From Cerveny et al. (2004).

In the hydrocarbon industry, reservoirs juxtaposed against low permeability lithologies are expected to seal via juxtaposition seal, whereas high permeability lithologies juxtaposed against each other may leak, depending on the type of fault rock developed (e.g. membrane seal, such as Braathen et al., 2009). From juxtaposition diagrams the nature of fault rocks (e.g. extent of clay smears derived from clay-rich lithologies) in a given stratigraphy can be graphically determined, and their permeability characteristics inferred. Juxtaposition diagrams could give important information as to where seals or conduits are likely to form across the length of a fault. To create a juxtaposition diagram for subsurface faults,

ideally log and core data would also be used in order to determine clay contents of each unit.

In order to illustrate fault rock distributions within basalt-hosted hydrocarbon reservoirs, a juxtaposition diagram for fault rock predictions (based on a stratigraphic log from Williamson and Bell, 2012), is presented using this study's fault data (Figure 7.12). The logged section from Williamson and Bell (2012) is from the Staffa Lava Formation on Mull, which underlies the host rock of the BNF. The log contains a basalt sequence typical of those examined in this study. In Figure 7.12, at low displacements, all units are self-juxtaposed (basalt upon basalt), resulting in fracture-dominated fault rocks, which may leak fluid. With increasing displacement, self-juxtaposition of the thick basalt lavas will form cataclasite-dominated fault rocks, which may act as an across-fault seal (due to a decrease in porosity and permeability), or as an along-fault conduit (owing to fracturing in the deformation zone surrounding the cataclasite-rich PSZ). At 30m throw, the juxtaposition/fault rock diagram identifies a basalt-against-basalt juxtaposition, where Layer B in the hanging wall lithology is dragged past other lithologies (volcaniclastic sandstone and thin palaeosol). This could make a leak zone where highly fractured basalts form a conduit. However if clay smearing from the palaeosol is taken into account, the potential leak zone may be sealed.

A juxtaposition diagram for fault seal behaviour is shown in Figure 7.13, highlighting those juxtapositions that are likely to seal or to leak. At low displacements in self-juxtaposed basalts, leaks are likely, but self-juxtapositions in clay-bearing or clay-rich units will seal. Further field data and thin-section characterisation are required to determine whether high displacement fault rocks will act as seals or conduits, and to what degree. This could be achieved by studying a range of high displacement faults in basalt sequences. This process of creating a juxtaposition diagram from the given fault rock classifications from this study could, in practice, be

applied to any stratigraphic log within a basalt sequence for fault rock/seal analysis.

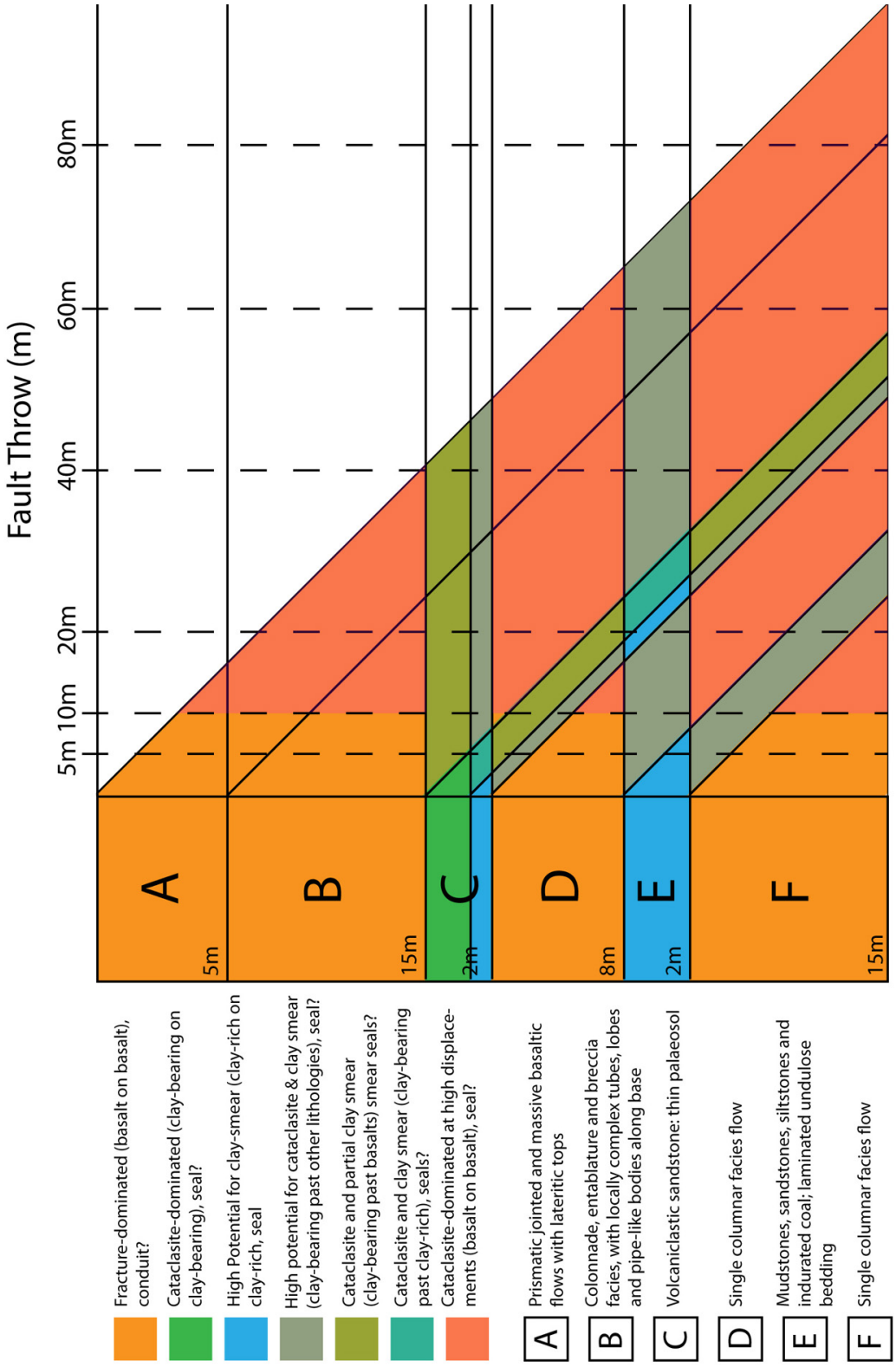

Figure 7.12: Juxtaposition/fault rock diagram using a stratigraphic column through basalt lava sequence from Mull (Williamson and Bell, 2012).

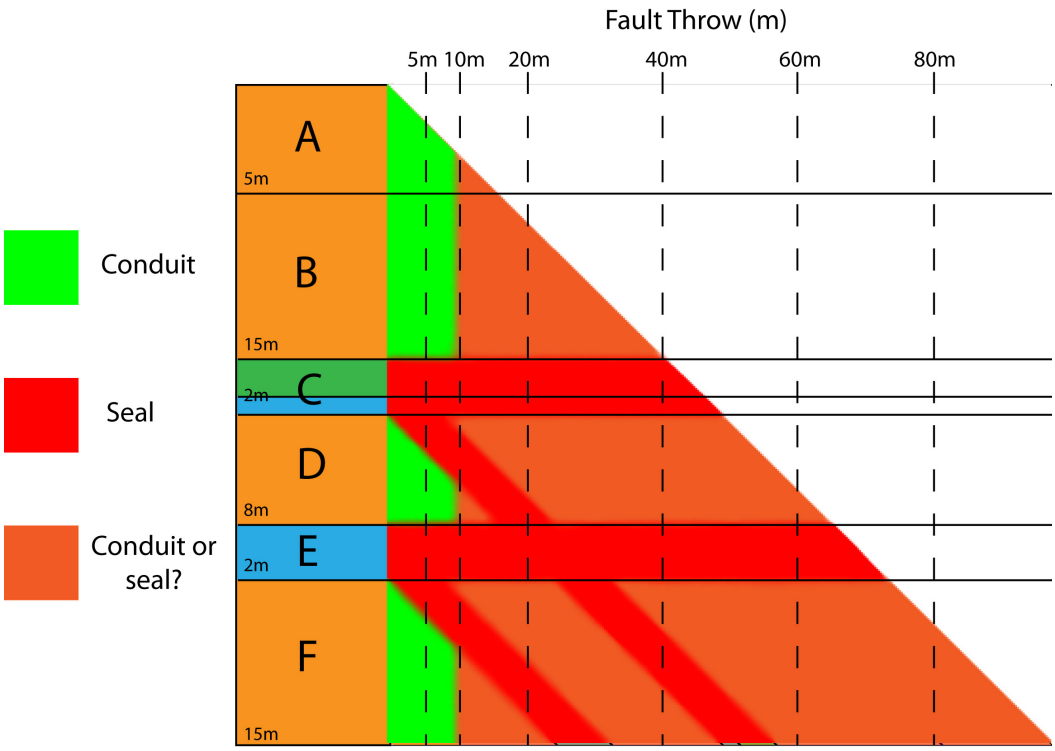

Figure 7.13: Triangle diagram for the same lithologies in Figure 7.12, with fault seal potentials estimated. Where the area of the juxtaposition diagram shows 'conduit or seal', further field data on faults in basalt sequences could establish what fault seal behaviour would be.

7.7. Summary

Faults in basalt sequences behave in a similar fashion to those in carbonate faults when self-juxtaposed, but are more like faults from other layered sequences when considering non self-juxtaposed morphologies. However, faults in basalt are also unique due to the control the range of pre-existing structures found in basalts have on fault initiation and growth. They are also unique due to the mineralogy of basalts, where particularly feldspars and olivines are susceptible to alteration. Fluid-rock interactions forming clays and zeolites can affect the strength of the fault, with clay formation more likely to weaken the fault, and zeolite formation strengthening, or having no effect on the fault. Large displacement faults will typically tap fluid reservoirs at greater depth (i.e. deeper groundwater zones within which higher temperature zeolites are stable) than low displacement faults, which remain within the same zeolite zone as the surrounding host rock.

The change of bulk chemical composition within faulted basalt has profound implications for CO_2 storage because it means that reactions between CO_2 and basalt may not proceed in the manner that models predict. Low displacement faults in particular may adversely affect sub-surface fluid flow and lead to CO_2 leakage.

Predictions on fault rock types can be made using datasets from this study, and a new fault rock series (the mafic-crystalline lithology fault rock series) was produced. Crystalline rocks in basalt sequences will deform by fracturing and cataclasis, whereas clay-rich rocks in basalt sequences will deform by clay-smear. Using juxtaposition diagrams, predictions on fault rock type and fault seal behaviour can be made for faults in basalt.

Whilst the PSZ in basalts may serve as a seal to across-fault flow depending on juxtaposition type, the fault walls will have intense fracture-dominated deformation. Fractures may or may not connect across the fault, and therefore may, or may not, affect the sealing potential of faults in clay-

rich lithologies. Therefore, juxtaposition diagrams at this stage in the study of faults in basalt sequences should be used only as a tool for initial fault evaluation. Basalt sequences are obviously dominated by thick basalt lava flows, with comparatively thin inter-lava clay-bearing or clay-rich beds. However, these thin beds may have a major impact on faulting of basalt sequences, particularly where clay-rich units (e.g. clay-rich peperites) are cut by the fault, and form seals. However, large displacements will have to take place to allow this sealing to occur, as lava flows can be in excess of 20m thick. Faults of such displacement should be resolvable on the seismic scale, along with details of the stratigraphy and so the behaviour of the fault may be better estimated. However, the detail of sub-seismic faults will not be discernable, and so the results and predictions of this study provide essential data for industry models.

The fault rock classification model in Figure 7.10 is a first attempt at a predictive fault rock classification scheme for faults in basalt sequences, based on the field data from this study. Studies of basalt sequence facies will complement the data from this study when it comes to evaluating clay contents and morphologies of basalt sequence rocks, and also morphologies of lava (e.g. Single and Jerram, 2004; Brown et al., 2009; Passey and Bell, 2007; Williamson and Bell, 1994; Williamson and Bell, 2012).

8. Conclusions

The aims of this study were to identify the key controls on how faults develop and evolve in layered basalt sequences; characterise the geochemical and mineralogical changes that occur as a result of faulting of basalt; characterise the effect fault growth, evolution and mineralogical/chemical changes have on bulk permeability of basalt hosted faults; and to develop a model for predicting fault properties and depth.

These aims were met by carrying out detailed fault mapping of faults in basalt sequences (with a range of displacements and juxtapositions), extensive microstructural descriptions of samples from each fault, and flow modelling through generated fault maps. A summary of the main conclusions is as follows:

Field work conclusions

- Field mapping of twelve normal faults from the North Atlantic Igneous Province (Scotland, Iceland and the Faroe Islands) and the Lorn Lava Plateau Formation (Scotland) provided detailed descriptions of fault zone architecture. All faults studied had displacements from protofaults up to 125m, and a range of juxtapositions against clay-bearing/clay-rich lithologies. Host rocks were largely tholeiitic basalts with a variation in grain size and background alteration, and inter-basalt units included peperites, tuffs, boles, volcaniclastic sedimentary rocks and ignimbrite. Zeolite-zones in the host rocks identified most faults as being exhumed from 1.5-2km depths. Host rocks range in age from ~59Ma – 13Ma.

- The primary control on fault initiation is pre-existing structures. If the pre-faulted basalt contains sub-vertical cooling joints, faulting results from shear of these, and a sub-vertical fault forms. If the

pre-faulted basalt is massive, en-echelon linkage of pre-cursory structures form steeply dipping faults (70-80°).

- The main controls on fault evolution in layered basalt sequences are displacement and juxtaposition.

- Self-juxtaposed faults (VJF, VPF, BNF, HBF) evolve by fracture and slip surface linkage, encapsulating blocks of host rock basalt that are susceptible to fracturing and alteration, which further weaken the basalt fault zone. With increasing displacement, basalt in the fault walls is incorporated into the fault zone by asperity removal and further deformed by abrasion and wear processes. At high displacements, cataclasites and complex breccias develop as a result of further communition of blocks of basalt caught in the fault zone. All the self-juxtaposed faults are characterised by mineralised (zeolite and occasionally calcite) and altered basalts adjacent to fractures and slip surfaces (in the principal slip zones). Self-juxtaposed faults typically have wider fault zones due to faulting of mechanically strong layers resulting in fracture-dominated faults. Clay gouge was never observed in self-juxtaposed faults.

- The non self-juxtaposed faults studied offset lithologies which were all rich in primary clays (e.g. HVF, SFZ, IBF, LWF, TBF). Non self-juxtaposed faults occur at displacements above the minimum layer thickness. Due to entrainment of these clay-rich host rocks into the fault zone they are characterised by clay-gouge dominated principal slip zones. With increasing displacement, multiple gouge strands form as a result of faulting of multiple clay-rich units. Non self-juxtaposed faults have narrower fault zones, due to the presence of gouge and clay-smear dominated faults.

- Alteration (to clays) and mineralisation (zeolites, calcite, chalcedony) of the basalt-hosted fault zones indicate that fluid flow

occurred in all fault zones during faulting, with alteration and zeolite mineralisation most common in self-juxtaposed faults (i.e. contained within basalt).

Microstructural conclusions

- Microstructural analyses through petrographic and SEM analyses identified zeolite and/or clay precipitation as being common in all the mapped fault rocks. The presence of zeolite minerals suggests that alkaline groundwater of varying temperatures permeated the faults. The fact that different zeolites are present in the fault zone and the host rock suggests the faults have acted as a conduit for fluids of different temperatures, rather than just regional groundwater circulation being concentrated in the faults.

- Zeolite and clay also occur as primary mineral replacements in fault rocks. Zeolitisation of feldspar is common, with 100% of feldspars completely zeolitised within the principal slip zones, and around zeolite veins in the fault walls. Clay replacement of feldspar is also common, more so when zeolite mineralisation is absent. Replacement of olivine by clay is also found in faults cutting olivine bearing host rocks (e.g. TBF).

- Replacement of feldspar and olivine as a result of fluids brought in by faulting release Fe, Mg, Si, Na, and Ca, which re-precipitate in the fault as clay (filling fractures) or zeolite veins. Olivines and feldspars are more susceptible to dissolution and reprecipitation, meaning that cataclasis of these minerals does not occur.

- Brittle deformation of other minerals in the basalt result in the formation of pyroxene- and Fe-Ti oxide rich cataclasites, set in a matrix of zeolite and clay.

- With increasing proximity to the fault, the proportion of clay, zeolite, pseudomorphs of olivine and feldspar, and porosity increases, and feldspar and olivine decreases. The proportions of Fe-Ti oxides and pyroxenes remain constant.

- Bulk fault rock chemistry is likely to be controlled by fluid-rock interactions, where replacement of feldspar by zeolite and mineralisation of fractures by zeolites (or other minerals such as chalcedony) could control the bulk chemistry. In clay-rich fault rocks, clay would likely control the bulk chemistry.

Seismic-scale fault conclusions

- The highest displacement fault mapped, the Kerrera Fault Zone, is characterised by wide zones (up to 40m) of fault-related deformation, composed of extensive clay smears derived from inter-basalt sedimentary units, and extensive fracturing of stronger units such as basalt and volcanic conglomerate.

- Stable isotope analysis of calcite from the Kerrera Fault Zone shows the fluid precipitating the calcite had a magmatic signature, potentially suggesting that the Kerrera Fault Zone tapped a deep, hot, fluid reservoir.

Flow modelling conclusions

- The detailed microstructural work carried out in this study found that individual deformation elements within the faults changed in permeability over time (e.g. by clay alteration and zeolite mineralisation), suggesting bulk permeabilities also changed over the faults' lifetimes. Using the modular finite difference groundwater flow model 'MODFLOW', (and applied in mfLab), flow modelling for

determining the key flow controls (and how they change) within the studied faults over time was carried out, using microstructural evidence to change the permeability values of deformation elements over time.

- Flow modelling of the faults mapped from this study showed that bulk permeability changes over time as a fault evolves. Relatively high bulk permeabilities were found in low displacement, fracture dominated faults. Relatively low bulk permeabilities are found at high displacement, particularly when juxtaposed with a clay-rich unit.

- Along-fault flow bulk permeability is consistently higher than that for across-fault flow. At high displacement, impermeable barriers such as clay-rich gouge impede across-fault flow, though over time fluid will flow across the fault at the fault's narrowest point if the impermeable barrier is variable in thickness.

- Through flow modelling, it was found that key flow controls (such as slip surfaces) change over time as a fault evolves. Closure and opening of slip surfaces governed the largest changes in bulk permeability, as did progressive alteration of the fault zone (i.e. clogging by clays) following fluid flow events. Fractures are also important in channeling fluids.

General conclusions

- Fault architecture in layered basalt sequences is similar to fault architecture in other layered sequences. Weaker layers accommodate displacement by ductile flow, and stronger layers by brittle deformation.

- Faults in basalt act as conduits to fluid from depth, locally elevating zeolite isograds, and precipitating higher-temperature zeolites in the fault zone than the surrounding host rock.

- A new predictive fault rock classification scheme for faults in basalt was developed, based on the host rock being faulted, its clay content, and fault displacement value. A new classification of fault rocks derived from crystalline lithologies in basalt was also presented: the mafic-crystalline lithologies fault rock series (M-CLFRS). Fractures, cataclasites and breccias dominate this new fault rock classification.

9. Future Work

After carrying out this study of controls on fault and fluid flow evolution in basalt sequences, a number of questions have been answered. However, given that this is one of the first comprehensive studies of controls of fault structure in basalt sequences, a number of questions remain unanswered.

What does a high displacement self-juxtaposed basalt fault look like?

The exposures of self-juxtaposed faults found during this study had a maximum displacement of 10m. Future field studies should focus on increasing the range of displacements for mapped faults within basalt sequences, to determine if large displacement self-juxtaposed faults remain dominated by fractures and breccias (as found in this study), or if extensive alteration and mineralisation as a result of fluid flow within the fault weakens it and results in, for example, the development of clay smears.

How does fault structure vary as a function of variation in host rocks?

The non self-juxtaposed units faulted against basalt found in this study were clay-bearing (e.g. volcanic conglomerate) or clay-rich (e.g. peperite). Clay-poor lithologies faulted against basalt in non self-juxtaposed relationships were not found in this study (e.g. granite, gabbros, etc). Therefore future work should focus on expanding the range of juxtapositions for mapped faults in basalt sequences, to determine the effect that juxtaposition of basalt against clay-poor units has on fault architecture.

How does fault structure vary as a function of pre-existing structures in host rocks?

Addressing how pre-existing structures within basalt lava flows themselves affect fault structure would be useful. For example, Tentler and Temperley (2005) have described pre-existing structures (cooling joints and fractures) as resulting in wide and diffuse fault structures, but how would this fault

structure then evolve with increasing displacement? Further fieldwork examining a range of pre-existing structures in basalt sequences and their effect on fault structure would help constrain this.

How could the effect of clay and zeolite minerals be further understood relating to fault strength, fluid migration and fluid rock interactions?

In this study, clay and zeolite minerals were identified through SEM-EDX analysis. However, there are such a large range of clays and zeolite minerals that differentiating discrete differences in mineral type is not possible with chemical spectra analysis alone. Whilst XRD was not implemented in this study (as identification of discrete differences in mineral type was not a primary aim of this study), XRD classification of clays and zeolites would result in more accurate identification of these minerals. Exact identification would be important for predicting which zeolites and clays would form from different host rocks, and evaluating how fault strength changes as a result of clay and zeolite mineralisation.

What controls bulk fault rock chemistry?

In this study, estimates of bulk chemical changes from host rock to fault rock were made, based on the replacement of pre-existing minerals by newly formed minerals (i.e. feldspar replaced by zeolite) and mineralisation of new minerals within pore space (i.e. zeolite veins). Therefore, bulk host and fault rock chemical analysis would be beneficial in understanding the controls on fault rock bulk composition. Future work should therefore collect host and fault rock samples from multiple fault zones for bulk rock chemical analysis, which could determine if fault rock chemistry is related to the host rock or secondary mineral formation.

How could bulk permeability estimates of fault flow in basalt lava sequences be improved?

Flow modelling was used to estimate bulk permeability of fault zones in basalt sequences, with permeability values for individual elements within the fault maps taken from the literature. However, permeability estimates

of basalts vary by three orders of magnitude in the literature, and permeability data of basalt-derived fault rocks is limited (e.g. Walker et al., 2012b). Therefore, permeability analyses of site-specific host and fault rocks should be carried out prior to flow modelling to provide a more accurate estimate of bulk permeability.

The fractures were modeled as being 0.5mm wide (aperture) across all faults. However, the fault aperture is likely to change with time as a fault grows, depending on the depth, stress orientation, and mineral fill. Therefore, measurements of fractures and mineralized fractures in the field should measure thickness of each fracture, and look for evidence of crack-seal to determine the maximum thickness the fracture was at in a mineralized fracture. Also, when modelling, a code could be written to change the angle of the stress orientation (if recognized in the field), which would open some fractures and close others, therefore changing the bulk permeability.

Could predictive algorithms for fault properties in basalt be built?

Existing predictive algorithms for fault composition in sand/shale sequences take into account fault throw, clay content of the units displaced, and the amount of clay units being displaced past a certain point (e.g. the Shale Gouge Ratio). In order for predictive algorithms of fault composition in basalts to be built, factors such as host rock basalt mineralogy, grain size, fluid factor (temperature, type and volume), fault rock porosity, clay content of inter-basalt units and fault throw would be required. These factors are the dominant controls on fault rocks in basalt. For example, faulted olivine-rich basalt may be expected to alter to clay rapidly (due to olivine's rapid solubility), depending on the fluid factor, porosity and permeability of the fault system. This could result in a clay-rich fault, which may weaken the fault and form clay-gouge, resulting in the fault zone having a bulk chemical signature controlled by clay mineralogy. Future work could therefore focus on developing and testing a predictive algorithm for faults in basalt, based on the above factors.

10. List of References

Acocella, V., Gudmundsson, A. & Funiciello, R. 2000. Interaction and linkage of extension fractures and normal faults: examples from the rift zone of Iceland. Journal of Structural Geology, 22, 1233-1246.

Acocella, V., Korme, T. & Salvini, F. 2003. Formation of normal faults along the axial zone of the Ethiopian Rift. Journal of Structural Geology, 25, 503-513.

Agosta, F., Alessandroni, M., Antonellini, M., Tondi, E. & Giorgiono, M. 2010. From fractures to flow: A field-based quantitative analysis of an outcropping carbonate reservoir. Tectonophysics, 490, 197-213.

Agosta, F., Prasad, M. & Aydin, A. 2007. Physical properties of carbonate fault rocks, Fucino Basin (Central Italy): implications for fault seal in platform carbonates. Geofluids, 7, 19-32.

Alfredsson, H. A., Hardarson, B. S., Franzson, H. & Gislason, S. R. 2008. CO2 sequestration in basaltic rock at the Hellisheidi site in SW Iceland: stratigraphy and chemical composition of the rocks at the injection site. Mineral Mag, 72, 1-5.

Allan, U. S. 1989. Model for hydrocarbon migration and entrapment within faulted structures. AAPG Bulletin-American Association of Petroleum Geologists, 73.

Alt, J. C., Teagle, D. A. H., Brewer, T., Shanks, W. C. & Halliday, A. 1998. Alteration and mineralization of an oceanic forearc and the ophiolite-ocean crust analogy. Journal of Geophysical Research-Solid Earth, 103, 12365-12380.

An, L. J. & Sammis, C. G. 1996. Development of strike-slip faults: Shear experiments in granular materials and clay using a new technique. Journal of Structural Geology, 18.

Antonellini, M. & Aydin, A. 1994. Effect of faulting on fluid-flow in porous sandstones - petrophysical properties. AAPG Bulletin-American Association of Petroleum Geologists, 78.

Aydin, A. & Johnson, A. M. 1978. Development of faults as zones of deformation bands and as slip surfaces in sandstone. Pure and Applied Geophysics, 116.

Bailey E. B., Clough C. T., Wright W. B., Richey J. E., Wilson G. V. Memoir of the Geological Survey of Great Britain, Scotland. Edinburgh: HMSO; 1924. Tertiary and post-Tertiary geology of Mull, Loch Aline and Oban.

Barclay, W. J., Browne, M. A. E., McMillan, A. A., Pickett, E. A., Stone, P. & Wilby, P. R. 2005. The Old Red sandstone of Great Britain. Geological Conservation Review Series. Peterborough: Joint Nature Conservation Committee.

Bastesen, E. & Braathen, A. 2010. Extensional faults in fine grained carbonates e analysis of fault core lithology and thicknessedisplacement relationships. Journal of Structural Geology, 32, 1609-1628.

Bastesen, E., Braathen, A., Nottvei, H., Gabrielsen, R. H. & Skar, T. 2009. Extensional fault cores in micritic carbonate - Case studies from the Gulf of Corinth, Greece. Journal of Structural Geology, 31, 403-420.

Bell, B. R. & Williamson, I. T. 2002. Tertiary Igneous Activity. In: Trewin, N. H. (ed.) The Geology of Scotland. Fourth ed. London: The Geological Society.

Bergerat, F. & Angelier, J. 1998. Fault systems and paleostresses in the Vestfirdir Peninsula. Relationships with the tertiary paleo-rifts of Skagi and Snaefells (Northwest Iceland). Geodynamica Acta, 11, 105-118.

Bergerat, F., Angelier, J. & Villemin, T. 1990. Fault systems and stress patterns on emerged oceanic ridges - a case-study in Iceland. Tectonophysics, 179, 183-197.

BGS. 1953. 1:50 000, Sheet 44 Mull (S&D).

BGS. 1977. 1:50 000, Sheet 52 Ardnamurchan (S).

BGS. 1992. 1:50 000, Sheet 44E Lismore (S).

BGS. 2001. 1:50 000, Sheet 70 Minginish (S&D).

Billi, A. & Storti, F. 2004. Fractal distribution of particle size in carbonate cataclastic rocks from the core of a regional strike-slip fault zone. Tectonophysics, 384, 115-128.

Billi, A. 2010. Microtectonics of low-P low-T carbonate fault rocks. Journal of Structural Geology, 32, 1392-1402.

Billi, A., Salvini, F. & Storti, F. 2003. The damage zone-fault core transition in carbonate rocks: implications for fault growth, structure and permeability. Journal of Structural Geology, 25, 1779-1794.

Billi, A., Salvini, F. & Storti, F. 2003a. The damage zone-fault core transition in carbonate rocks: implications for fault growth, structure and permeability. Journal of Structural Geology, 25, 1779-1794.

Billi, A., Storti, F. & Salvini, F. 2003b. Particle size distributions of fault rocks and fault transpression: are they related? Terra Nova, 15, 61-66.

Bird, P. 1984. Hydration-phase diagrams and friction of montmorillonite under laboratory and geologic conditions, with implications for shale compaction, slope stability, and strength of fault gouge. Tectonophysics, 107.

Braathen, A., Tveranger, J., Fossen, H., Skar, T., Cardozo, N., Sernshaug, S. E., Bastesen, E. & Sverdrop, E. 2009. Fault facies and its application to sandstone reservoirs. AAPG Bulletin, 93, 891-917.

Brand, W. A., Assonov, S. S. & Coplen, T. B. 2010. Correction for the O-17 interference in delta(C-13) measurements when analyzing CO2 with stable isotope mass spectrometry (IUPAC Technical Report). Pure and Applied Chemistry, 82.

Branney, M. J. 1995. Downsag and extension in calderas - new perspectives on collapse geometries from ice-melt, mining, and volcanic subsidence. Bulletin of Volcanology, 57, 303-318.

Brown, D. J. & Bell, B. R. 2007. Debris flow deposits within the Palaeogene lava fields of NW Scotland: evidence for mass wasting of the volcanic landscape during emplacement of the Ardnamurchan Central Complex. Bulletin of Volcanology, 69, 847-868.

Brown, D. J., Holohan, E. P. & Bell, B. R. 2009. Sedimentary and volcano-tectonic processes in the British Paleocene Igneous Province: a review. Geological Magazine, 146, 326-326.

Browne, M. A. E., Smith, R. A. & Aitken, A. M. 2002. Stratigraphical framework for the Devonian (Old Red sandstone) rocks of Scotland south of a line from Fort William to Aberdeen. British Geological Survery Research Report RR/01/04.

Bruhn, R. L., Parry, W. T., Yonkee, W. A. & Thompson, T. 1994. Fracturing and Hydrothermal Alteration in Normal Fault Zones. PAGEOPH, 142.

Buck, R. W., Lavier, L.L., & Poliakov, A. N. B. 2005. Modes of faulting at mid-ocean ridges. Nature, 434, 719-723.

Cann, J. & Gillis, K. 2004. Hydrothermal insights from the Troodos ophiolite, Cyprus. In: Davis, E.E. and Elderfield H. (eds), Hydrogeology of the Oceanic Lithosphere. Cambridge University Press.

Caine, J. S., Evans, J. P. & Forster, C. B. 1996. Fault zone architecture and permeability structure. Geology, 24, 1025-1028.

Cardwell, W. T. & Parsons, R. L. 1945. Average permeabilities of heterogeneous oil sands. Transactions of the American Institute of Mining and Metallurgical Engineers, 160.

Cerveny, K., Davies, R., Dudley, G., Kaufman, P., Knipe, R. J. & Krantz, B. 2004. Reducing uncertainty with fault-seal analysis. Oilfield Review, 16, 38-51.

Chambers, L. M. & Pringle, M. S. 2001. Age and duration of activity at the Isle of Mull Tertiary igneous centre, Scotland, and confirmation of the existence of subchrons during Anomaly 26r. Earth and Planetary Science Letters, 193, 333-345.

Chambers, L. M., Pringle, M. S. & Parrish, R. R. 2005. Rapid formation of the Small Isles Tertiary centre constrained by precise Ar-40/Ar-39 and U-Pb ages. Lithos, 79, 367-384.

Chester, F. M. & Logan, J. M. 1986. Implications for mechanical-properties of brittle faults from observations of the Punchbowl Fault Zone, California. Pure and Applied Geophysics, 124, 79-106.

Childs, C., Manzocchi, T., Walsh, J. J., Bonson, C. G., Nicol, A. & Schöpfer, M. P. J. 2009. A geometric model of fault zone and fault rock thickness variations. Journal of Structural Geology, 31.

Childs, C., Nicol, A., Walsh, J. J. & Watterson, J. 1996. Growth of vertically segmented normal faults. Journal of Structural Geology, 18, 1389-1397.

Christensen, N. I. & Ramananantoandro, R. 1988. Permeability of the oceanic-crust based on experimental studies of basalt permeability at elevated pressures. Tectonophysics, 149.

Coombs, D. S., Ellis, A. J., Fyfe, W. S. & Taylor, A. M. 1959. The zeolite facies, with comments on the interpretation of hydrothermal syntheses. Geochimica Et Cosmochimica Acta, 17, 53-107.

Cowie, P. A. & Scholz, C. H. 1992. Displacement length scaling relationship for faults - data synthesis and discussion. Journal of Structural Geology, 14, 1149-1156.

Crider, J. G. & Peacock, D. C. P. 2004. Initiation of brittle faults in the upper crust: a review of field observations. Journal of Structural Geology, 26.

Deer, W. A., Howie, R. A. & Zussman, J. 1992. An Introduction to the Rock-Forming Minerals (2nd edition). 696p., Longman Scientific & Technical, Harlow.

Dekayir, A., Amouric, M. & Olives, J. 2005. Clay minerals in hydrothermally altered basalts from Middle Atlas, Morocco. Clay Minerals, 40.

Durant, G. 1999. South Kerrera. In: Stephenson, D., Bevins, R. E., Millward, D., Stone, P., Parsons, I., Highton, A. J. & Wadsworth, W. J. (eds.) Caledonian Igneous Rocks of Great Britain.

Emeleus, C. H. & Bell, B. R. 2005. British regional geology: the Palaeogene volcanic districts of Scotland (Fourth Edition), British Geological Survey, Nottingham.

England, R. W. 1988. The early Tertiary stress regime in NW Britain: evidence from the patterns of volcanic activity. Geological Society, London, Special Publications, 39, 381-389.

England, R. W. 1994. The structure of the Skye lava-field. Scottish Journal of Geology, 30, 33-37.

Evans, J. P. & Bradbury, K. K. 2004. Faulting and fracturing of nonwelded Bishop Tuff, eastern California: Deformation mechanisms in very porous materials in the vadose zone. Vadose Zone Journal, 3.

Faulkner, D. R. & Rutter, E. H. 1998. The gas permeability of clay-bearing fault gouge at 20ºC. In: Jones, G., Fisher, Q. & Knipe, R. (eds.) Faults, Fault Sealing and Fluid Flow in Hydrocarbon Reservoirs. Geological Society of London Special Publication.

Faulkner, D. R., Lewis, A. C. & Rutter, E. H. 2003. On the internal structure and mechanics of large strike-slip fault zones: field observations of the Carboneras fault in southeastem Spain. Tectonophysics, 367, 235-251.

Ferrill, D. A. & Morris, A. P. 2003. Dilational normal faults. Journal of Structural Geology, 25, 183-196.

Ferrill, D. A., Morris, A. P., Evans, M. A., Burkhard, M., Groshong, R. H. & Onasch, C. M. 2004. Calcite twin morphology: a low-temperature deformation geothermometer. Journal of Structural Geology, 26.

Ferrill, D.A., McGinnis, R.N., Morris, A.P. & Smart, K.J. 2012. Hybrid failure: Field evidence and influence on fault refraction. Journal of Structural Geology, 42, 140-150.

Ferry, J. M., Mutti, L. J. & Zuccala, G. J. 1987. Contact-metamorphism hydrothermal alteration of Tertiary basalts from the Isle of Skye, north-west Scotland. Contributions to Mineralogy and Petrology, 95, 166-181.

Fisher, A. T. 1998. Permeability within basaltic oceanic crust. Review of Geophysics, 36, 143-182.

Fisher, Q. J. & Knipe, R. J. 1998. Fault Sealing Processes in Siliciclastic Sediments. In: Jones, G., Fisher, Q. J. & Knipe, R. J. (eds.) Faulting, Fault Sealing and Fluid Flow in Hydrocarbon Reservoirs: Geological

Society Special Publication 147. Bath, England: The Geological Society Publishing House.
Fisher, Q. J. & Knipe, R. J. 2001. The permeability of faults within siliciclastic petroleum reservoirs of the North Sea and Norwegian Continental Shelf. Marine and Petroleum Geology, 18.
Fitz Gerald, J. D. & Stunitz, H. 1993. Deformation of granitoids at low metamorphic grade. 1. Reactions and grain-size reduction. Tectonophysics, 221.
Fjäder, K., Gudmundsson, A. & Forslund, T. 1993. Dikes, minor faults and mineral veins associated with a transform-fault in North Iceland. Journal of Structural Geology, 16, 109-119.
Flodin, E. A. 2003. Structural evolution, petrophysics, and large-scale permeability of faults in sandstone, Valley of Fire, Nevada. PhD Thesis, Stanford University.
Forslund, T. & Gudmundsson, A. 1992. Structure of Tertiary and Pleistocene normal faults in Iceland. Tectonics, 11, 57-68.
Fossen, H., Schultz, R. A., Shipton, Z. K. & Mair, K. 2007. Deformation bands in sandstone: a review. Journal of the Geological Society, 164.
Foxford, K. A., Walsh, J. J., Watterson, J., Garden, I. R., Guscott, S. C. & Burley, S. D. 1998. Structure and content of the Moab Fault zone, Utah, U. S. A. In: Al, K. R. J. E. (ed.) Faulting, fault sealing and fluid flow in hydrocarbon reservoirs. Special Publication of the Geological Society, London.
Ganerod, G. V., Braathen, A. & Willemoes-Wissing, B. 2008. Predictive permeability model of extensional faults in crystalline and metamorphic rocks; verification by pre-grouting in two sub-sea tunnels, Norway. Journal of Structural Geology, 30, 993-1004.
Geikie, A. 1897. The ancient volcanoes of Great Britain, Macmillan, London.
Gislason, S. R., Wolff-Boenisch, D., Stefansson, A., Oelkers, E. H., Gunnlaugsson, E., Sigurdardottir, H., Sigfusson, B., Broecker, W. S., Matter, J. M., Stute, M., Axelsson, G. & Fridriksson, T. 2010. Mineral sequestration of carbon dioxide in basalt: A pre-injection overview of the CarbFix project. International Journal of Greenhouse Gas Control, 4, 537-545.
Gondouin, M. & Scala, C. 1958. Streaming potential and the S.P. log. J.Pet. Technol., 10, 170-179.
Gribble, C. D., Durance, E. M. & Walsh, J. N. 1976. Ardnamurchan: a guide to geological excursions, Edinburgh, Edinburgh Geological Society.
Groome, D. R. & Hall, A. 1974. Geochemistry of the Devonian lavas of the northern Lorne Plateau, Scotland. Mineralogical Magazine, 39, 621-640.
Gudmundsson, A. 1983. Form and dimensions of dykes in eastern Iceland. Tectonophysics, 95, 295-307.
Gudmundsson, A. 1992a. Formation and growth of normal faults at the divergent plate boundary in Iceland. Terra Nova, 4, 464-471.
Gudmundsson, A. 1992b. On the structure and formation of fracture-zones. Terra Nova, 5, 215-224.

Haggerty, S. E. 1976a. Oxidation of opaque mineral oxides in basalts. In Oxide Minerals (D. Rumble, III, ed.). Rev. Mineral., 3, Hg1-100.
Harbaugh, A. W. & McDonald, M. G. 1996. User's documentation for MODFLOW-96, and update to the U.S. Geological Survey modular finite-difference ground-water flow model. U.S. Geological Survey Open-File Report 96-485, 56.
Hay, R. L. & Sheppard, R. A. 2001. Occurrence of zeolites in sedimentary rocks: An overview. Natural Zeolites: Occurrence, Properties, Applications, 45, 217-234.
Hayman, N. W. & Karson, J. A. 2007. Faults and damage zones in fast-spread crust exposed on the north wall of the Hess Deep Rift: Conduits and seals in seafloor hydrothermal systems. Geochem. Geophys. Geosyst., 8.
Hayman, N. W. & Karson, J. A. 2009. Crustal faults exposed in the Pito Deep Rift: Conduits for hydrothermal fluids on the southeast Pacific Rise. Geochemistry Geophysics Geosystems, 10.
Hirose, T. & Hayman, N. W. 2008. Structure, permeability, and strength of a fault zone in the footwall of an oceanic core complex, the Central Dome of the Atlantis Massif, Mid-Atlantic Ridge, 30ºN. Journal of Structural Geology, 30, 1060-1071.
Holdsworth, R. E., Van Diggelen, E. W. E., Spiers, C. J., De Bresser, J. H. P., Walker, R. J. & Bowen, L. 2011. Fault rocks from the SAFOD core samples: Implications for weakening at shallow depths along the San Andreas Fault, California. Journal of Structural Geology, 33, 132-144.
Holgate, N. 1969. Palaeozoic and Tertiary transcurrent movements on the Great Glen fault. Scottish Journal of Geology, 5, 97-139.
Holland, M., Urai, J. L. & Martel, S. 2006. The internal structure of fault zones in basaltic sequences. Earth and Planetary Science Letters, 248, 301-315.
Holohan, E. P., Troll, V. R., Walter, T. R., Munn, S., McDonnell, S. & Shipton, Z. K. 2005. Elliptical calderas in active tectonic settings: an experimental approach. Journal of Volcanology and Geothermal Research, 144, 119-136.
Hudson, J. A., Cosgrove, J. W., Kemppainen, K. & Johansson, E. 2011. Faults in crystalline rock and the estimation of their mechanical properties at the Olkiluoto site, western Finland. Engineering Geology, 117.
Hull, J. 1988. Thickness displacement relationships for deformation zones. Journal of Structural Geology, 10.
Iijima, A. 1980. Geology of natural zeolites and zeolitic rocks. Pure and Applied Chemistry, 52, 2115-2130.
Jerram, D. A. 2002. Volcanology and faces architecture of flood basalts. In: Menzies, M., Klemperer, S., Ebinger, C. & Baker, J. (eds.) Volcanic rifted margins. Geol Soc Am Spec Pap.
Jóhannesson, H. & Saemundsson, K. 1998. Geological map of Iceland. 1:500000: Bedrock geology. Reykjavik: Icelandic Institute of Natural History and Icelandic Geodetic Survey.

Johnson, D. M. 1980. Fluid permeability of oceanic basalts. Initial Report Deep Sea Drilling Project, 51-53, 1473-1477.

Jolivet, M. 2007. Denudation history of the Loch Ness corridor (Scotland): differential vertical movements along the Great Glen Fault. Comptes Rendus Geoscience, 339, 121-131.

Jolley, D. W. 1997. Palaeosurface palynofloras of the Skye lava field and the age of the British Tertiary Volcanic Province. In: Widdowson, M. (ed.) Palaeosurfaces: recognition, reconstruction and palaeoenvironmental interpretation. Geological Society of London Special Publication.

Jørgensen, O. 1984. Zeolite zones in the basaltic lavas of the Faroe Islands - A quantitative description of the secondary minerals in the deep wells of Vestmanna-1 and Lopra-1. In: Berthelsen, O., Noe-Nygaard, A. & Rasmussen, J. (eds.) The deep drilling project 1980-1981 in the Faroe Islands. Tórshavn: Føroya Fróðskaparfelag.

Jørgensen, O. 2006. The regional distribution of zeolites in the basalts of the Faroe Islands and the significance of zeolites as palaeotemperature indicators. Geological Survey of Denmark and Greenland Bulletin, 123-156.

Jourde, H., Flodin, E.A., Aydin, A., Durlofsky, L.J. & Wen, X. 2002. Computing permeability of fault zones in eolian sandstone from outcrop measurements. AAPG Bulletin, 86, 1187-1200.

Jowitt, S.M., Jenkin, G. R. T., Coogan, L.A., Naden, J. & Chenery, S. R. N. 2007. Epidosites of the Troodos Ophiolite: A direct link between alteration of dykes and release of base metals into ore-forming hydrothermal systems? In: Digging deeper: Proceedings of the Ninth Biennial SGA Meeting, Dublin, Ireland, 20-23 August, Andrew, C. (ed). Springer-Verlag, Berlin, pg. 881-884.

Judd, J. W. 1874. The Secondary Rocks of Scotland. Second Paper. On the Ancient Volcanoes of the Highlands and the Relations of their Products to the Mesozoic Strata. Quarterly Journal of the Geological Society, 30, 220-302.

Keith, T. E. C. & Staples, L. W. 1985. Zeolites in Eocene basaltic pillow lavas of the Siletz River volcanics, Central Coast Range, Oregon. Clays and Clay Minerals, 33, 135-144.

Khodayar, M. & Einarsson, P. 2002. Strike-slip faulting, normal faulting, and lateral dike injections along a single fault: Field example of the Gljufura fault near a Tertiary oblique rift-transform zone, Borgarfjordur, west Iceland. Journal of Geophysical Research-Solid Earth, 107.

Khodayar, M. 2004. Reverse-slip structures at oceanic diverging plate boundaries and their kinematic origin: data from Tertiary crust of west and south Iceland. Journal of Structural Geology, 26, 1945-1960.

Kim, Y. S. & Sanderson, D. J. 2005. The relationship between displacement and length of faults: a review. Earth-Science Reviews, 68.

King, P. M. 1977. The secondary minerals of the Tertiary lavas of northern and central Skye - zeolite donation patterns, their origin and formation. University of Aberdeen.

Knipe, R. J. 1997. Juxtaposition and seal diagrams to help analyze fault seals in hydrocarbon reservoirs. AAPG Bulletin-American Association of Petroleum Geologists, 81.

Knipe, R. J., Fisher, Q. J., Jones, G., Clennell, M. R., Farmer, A. B., Kidd, B., McAllister, E., Porter, J. R. & White, E. A. 1997. Fault seal analysis, successful methodologies, application and future directions. In: Møller-Pederson, P. & Koestler, A. G. (eds.) Hydrocarbon Seals - Importance for Exploration and Production: Norwegian Petroleum Society (NPF), Special Publications.

Kremer, Y., Lunn, R. J., Shipton, Z. K. & Wibberley, C. 2011. Heterogeneity is important for predicting the permeability of seismic scale faults. American Geophysical Union, Fall Meeting. San Francisco.

Kristmannsdóttir, H. 1978. Alteration of basaltic rocks by hydrothermal activity at 100-300'C. In: Mortland, M. M. & Farmer, V. C. (eds.) Proc. Int. Clay Conf., Oxford. Amsterdam: Elsevier.

Kristmannsdóttir, H. 1982. Alteration in the IRDP drill hole compared with other drill holes in Iceland. Journal of Geophysical Research, 87.

Kynaston, H. & Hill, J. B. 1908. The Geology of the Country near Oban and Dalmally. Memoirs of the Geological Survey of Scotland, 184.

Larsen, L. M., Waagstein, R., Pedersen, A. K. & Storey, M. 1999. Trans-Atlantic correlation of the Palaeogene volcanic successions in the Faeroe Islands and East Greenland. Journal of the Geological Society, 156, 1081-1095.

Lee, G. W. & Bailey, E. B. 1925. The pre-Tertiary Geology of Mull, Loch Aline, and Oban. Memoirs of the Geological Survey of Scotland.

Liou, J. G. 1979. Zeolite facies metamorphism of basaltic rocks from the east Taiwan ophiolite. American Mineralogist, 64.

Logan, J. M. 2007. The progression from damage to localisation of displacement observed in laboratory testing of porous rocks. In: Lewis, H. & Couples, G. D. (eds.) The Relationship between Damage and Localization. Geological Society, London, Special Publications.

Logan, J. M., Friedman, M., Higgs, N., Dengo, C. & Shimamoto, T. 1979. Experimental studies of simulated gouge and their application to studies of natural fault zones. U.S geol Surv. Open-File Report.

Loveless, S., Bense, V. & Turner, J. 2011. Fault architecture and deformation processes within poorly lithified rift sediments, Central Greece. Journal of Structural Geology, 33, 1554-1568.

Lunn, R. J., Shipton, Z. K. & Bright, A. 2008. How can we improve estimates of bulk fault zone hydraulic properties? Geological Society, London, Special Publications, 299, 231-237.

Manzocchi, T., Walsh, J. J., Nell, P. & Yielding, G. 1999. Fault transmissibility multipliers for flow simulation models. Petroleum Geoscience, 5.

Martel, S. J. & Langley, J. S. 2006. Propagation of normal faults to the surface in basalt, Koae fault system, Hawaii. Journal of Structural Geology, 28, 2123-2143.

Martel, S. J. 1990. Formation of compound strike-slip-fault zones, Mount Abbot Quadrangle, California. Journal of Structural Geology, 12.

Mathieu, L. & Vries, B. V. W. D. 2009. Edifice and substrata deformation induced by intrusive complexes and gravitational loading in the Mull volcano (Scotland). Bulletin of Volcanology, 71, 1133-1148.

Matter, J. M., Broecker, W. S., Stute, M., Gislason, S. R., Oelkers, E. H., Stefansson, A., Wolff-Boenisch, D., Gunnlaugsson, E., Axelsson, G. & Bjornsson, G. 2009. Permanent Carbon Dioxide Storage into Basalt: The CarbFix Pilot Project, Iceland. Energy Procedia, 1, 3641-3646.

McDonald, M. G. & Harbaugh, A. W. 1988. A modular three-dimensional finite-difference ground-water flow model. U.S. Geological Survey Open-File Report 83-875, 528.

McGrail, B. P., Schaef, H. T., Ho, A. M., Chien, Y. J., Dooley, J. J. & Davidson, C. L. 2006. Potential for carbon dioxide sequestration in flood basalts. Journal of Geophysical Research-Solid Earth, 111.

McGrail, B.P., Spane, F.A., Sullivan, D. H., Bacon, D.H. & Hund, G. 2011. The Wallula Basalt Sequestration Pilot Project, Energy Procedia, 4, 5653-5660.

Micarelli, L., Benedicto, A. & Wibberley, C. A. J. 2006. Structural evolution and permeability of normal fault zones in highly porous carbonate rocks. Journal of Structural Geology, 28, 1214-1227.

Mitchell, T. M. & Faulkner, D. R. 2008. Experimental measurements of permeability evolution during triaxial compression of initially intact crystalline rocks and implications for fluid flow in fault zones. Journal of Geophysical Research, 113, 1-16.

Mitchell, T. M. & Faulkner, D. R. 2009. The nature and origin of off-fault damage surrounding strike-slip fault zones with a wide range of displacements: A field study from the Atacama fault system, northern Chile. Journal of Structural Geology, 31, 802-816.

Moore, D. E., Lockner, D. A., Ito, H., Ikeda, R., Tanaka, H. & Omura, K. 2009. Geometry of the Nojima Fault at Nojima-Hirabayashi, Japan - II. Microstructures and their Implications for Permeability and Strength. Pure and Applied Geophysics, 166, 1669-1691.

Morrow, C. A., Moore, D. E. & Lockner, D. A. 2000. The effect of mineral bond strength and adsorbed water on fault gouge frictional strength. Geophysical Research Letters, 27.

Morrow, C. A., Radney, B. & Byerlee, J. D. 1992. Frictional strength and the effective pressure law of montmorillonite and illite clays. In: Evans, B. & Wong, T.-F. (eds.) Fault Mechanics and Transport Properties of Rocks. Academic Press, New York.

Morton, D. J. 1976. Lower Old Red sandstone Sedimentation in the NW Midland Valley and North Argyll Areas of Scotland. PhD, University of Glasgow.

Mumpton, F. A. 1977. Natural Zeolites. In Mumpton F.A. (ed) Mineralogy and geology of natural zeolites, Min. Soc. Am. Short Course Notes, 4, 1-15.

Neilson, J. C., Kokelaar, B. P. & Crowley, Q. G. 2009. Timing, relations and cause of plutonic and volcanic activity of the Siluro-Devonian post-collision magmatic episode in the Grampian Terrane, Scotland. Journal of the Geological Society, 166, 545-561.

Neuhoff, P. S., Watt, W. S., Bird, D. K. & Pedersen, A. K. 1997. Timing and structural relations of regional zeolite zones in basalts of the East Greenland continental margin. Geology, 25, 803-806.

Neuhoff, P. S., Fridriksson, T., Arnorsson, S. & Bird, D. K. 1999. Porosity evolution and mineral paragenesis during low-grade metamorphism of basaltic lavas at Teigarhorn, eastern Iceland. American Journal of Science, 299, 467-501.

Neuhoff, P. S., Fridriksson, T. & Bird, D. K. 2000. Zeolite parageneses in the north Atlantic igneous province: Implications for geotectonics and groundwater quality of basaltic crust. International Geology Review, 42, 15-44.

Neuhoff, P. S., Rogers, K. L., Stannius, L. S., Bird, D. K. & Pedersen, A. K. 2006. Regional very low-grade metamorphism of basaltic lavas, Disko-Nuussuaq region, West Greenland. Lithos, 92, 33-54.

Nuriel, P., Katzir, Y., Abelson, M., Valley, J. W., Matthews, A., Spicuzza, M.J., & Ayalon, Avner. 2009. Fault-related oceanic serpentinization in the Troodos ophiolite, Cyprus: Implications for a fossil oceanic core complex. Earth and Planetary Science Letters, 282, 34-46.

O'Neil, J. R., Clayton, R. N. & Mayeda, T. K. 1969. Oxygen isotope fractionation in divalent metal carbonates. Journal of Chemical Physics, 51.

Passey, S. R. & Bell, B. R. 2007. Morphologies and emplacement mechanisms of the lava flows of the Faroe Islands Basalt Group, Faroe Islands, NE Atlantic Ocean. Bulletin of Volcanology, 70, 139-156.

Passey, S. R. & Jolley, D. W. 2009. A revised lithostratigraphic nomenclature for the Palaeogene Faroe Islands Basalt Group, NE Atlantic Ocean.

Pe-Piper, G. & Miller, L. 2002. Zeolite minerals from the North Shore of the Minas Basin, Nova Scotia. Atlantic Geology, 38.

Peacock, D. C. P. & Zhang, X. 1994. Field examples and numerical modelling of oversteps and bends along normal faults in cross-section. Tectonophysics, 234.

Petford, N. & McCaffrey, K. 2003. Hydrocarbons in crystalline rocks: an introduction. In: Petford, N. & McCaffrey, K. J. W. (eds.) Hydrocarbons in Crystalline Rocks. Bath: Geological Soc Publishing House.

Phillips, W. J. 1972. Hydraulic fracturing and mineralisation. Journal of the Geological Society of London, 128, 337-359.

Power, W. L., Tullis, T. E. & Weeks, J. D. 1988. Roughness and wear during brittle faulting. Journal of Geophysical Research-Solid Earth and Planets, 93.

Rasmussen, J. & Noe-Nygaard, A. 1969. Beskrivelse til geologisk kort over Faerøerne i målestok 1:50 000 [English summary]. Danmarks Geologiske Undersøgelse, 11th Series, 24.

Rasmussen, J. & Noe-Nygaard, A. 1970. Geology of the Faroe Islands. Danmarks Geologiske Undersøgelse, 11th Series, 25.

Rawling, G. C. & Goodwin, L. B. 2003. Cataclasis and particulate flow in faulted, poorly lithified sediments. Journal of Structural Geology, 25.

Reidel, S. P. & Hooper, P. R. E. 1990. Volcanism and tectonism in the Columbia river flood-basalt Province. Geological Society of America Special Paper, 239.

Reidel, S. P., Johnson, V. G. & Spane, F. A. 2003. Natural Gas Storage in Basalt Aquifers of the Columbia Basin: A Guide to Site Characterization. GasTIPS.

Riedel, W. 1929. Zue mechanik geologischer Brucherscheinungen. Zentralblatt für Mineralozie, Geologie und Palaeontologie, 1929B, 354-368.

Rogers, D. A., Marshall, J. E. A. & Astin, T. R. 1989. Devonian and later movements on the Great Glen Fault System, Scotland. Journal of the Geological Society, 146, 369-372.

Rogers, K. L., Neuhoff, P. S., Pedersen, A. K. & Bird, D. K. 2006. CO2 metasomatism in a basalt-hosted petroleum reservoir, Nuussuaq, West Greenland. Lithos, 92.

Ross, J. G. & Musset, A. E. 1976. 40Ar/39Ar dates for spreading rates in eastern Iceland. Nature, 259, 36-38.

Saar, M. O. 1998. The relationship between permeability, porosity and microstructure in vesicular basalts. M.S. thesis, University of Oregon.

Saffer, D. M., Frye, K. M., Marone, C. & Mair, K. 2001. Laboratory results indicating complex and potentially unstable frictional behavior of smectite clay. Geophysical Research Letters, 28.

Saillet, E. & Wibberley, C. A. J. 2010. Evolution of cataclastic faulting in high-porosity sandstone, Bassin du Sud-Est, Provence, France. Journal of Structural Geology, 32.

Saunders, A. D., Fitton, J. G., Kerr, A. C., Norry, M. J. & Kent, R. W. 1997. The North Atlantic Igneous Province. In: Mahoney, J. J. & Coffin, M. F. (eds.) Large Igneous Provinces: Continental, oceanic, and planetary flood volcanism. American Geophysical Union, Geophysical Monograph no.100.

Schaef, H. T., McGrailL, B. P. & Owen, A. T. 2009. Basalt- CO2–H2O interactions and variability in carbonate mineralization rates. Energy Procedia, 1, 4899-4906.

Scholz, C. H. 1987. Wear and gouge formation in brittle faulting. Geology, 15.

Schöpfer, M., Childs, C. & Walsh, J. 2006. Localisation of normal faults in multilayer sequences. Journal of Structural Geology, 28, 816-833.

Schutter, S. R. 2003. Hydrocarbon occurrence and exploration in and around igneous rocks. In: Petford, N. & McCaffrey, K. J. W. (eds.) Hydrocarbons in Crystalline Rocks. Bath: Geological Soc Publishing House.

Segall, P. & Pollard, D. D. 1983. Nucleation and growth of strike slip faults in granite. Journal of Geophysical Research, 88.

Sharp, Z. D. 2006. Principles of stable isotope geochemistry, Upper Saddle River, Prentice Hall.

Sheppard, S. M. F. 1986. Characterization and isotopic variations in natural-waters. Reviews in Mineralogy, 16.

Sheppard, S. M., Nielsen, R. L. & Taylor, H. P. 1969. Oxygen and hydrogen isotope ratios of clay minerals from porphyry copper deposits. Economic Geology, 64.

Shipton, Z. K. & Cowie, P. A. 2001. Damage zone and slip-surface evolution over mu m to km scales in high-porosity Navajo sandstone, Utah. Journal of Structural Geology, 23, 1825-1844.

Shipton, Z. K. & Cowie, P. A. 2003. A conceptual model for the origin of fault damage zone structures in high-porosity sandstone. Journal of Structural Geology, 25, 333-344.

Shipton, Z. K., Evans, J. P., B., D., J., H., A., W., D., K. & T., K. P. 2005. Natural leaking CO2-charged systems as analogs for failed geologic sequestration reservoirs. In: D, T. & S.M, B. (eds.) Carbon Dioxide Capture for Storage in Deep Geologic Formations – Results from the CO2 Capture Project. Elsevier Science.

Shipton, Z. K., Evans, J. P., Robeson, K. R., Forster, C. B. & Snelgrove, S. 2002. Structural heterogeneity and permeability in faulted eolian sandstone: Implications for subsurface modelling of faults. AAPG Bulletin, 86.

Shipton, Z. K., Soden, A. M., Kirkpatrick, J. D., Bright, A. M. & Lunn, R. J. 2006. How thick is a fault? Fault displacement-thickness scaling revisited. Earthquakes: Radiated Energy and the Physics of Faulting, 170.

Sibson, R. H. 1977. Fault Rocks and Fault Mechanisms. Journal of Geological Society of London, 133, 191-213.

Sibson, R. H. 1996. Structural permeability of fluid-driven fault-fracture meshes. Journal of Structural Geology, 18, 1031-1042.

Single, R. T. & Jerram, D. A. 2004. The 3D facies architecture of flood basalt provinces and their internal heterogeneity: examples from the Palaeogene Skye Lava Field. Journal of the Geological Society, 161, 911-926.

Skaarup, N. & Chalmers, J. A. 1998. A possible new hydrocarbon play, offshore central West Greenland. Geology of Greenland Survey Bulletin, 28-30.

Skilling, I. P., White, J. D. L., & McPhie, J. 2002. Peperite: a review of magma-sediment mingling. Journal of Volcanology and Geothermal Research, 114, 1-17.

Soden, A. M. 2008. The initiation and evolution of ignimbrite faults, Gran Canaria, Spain. University of Glasgow.

Soden, A.M and Shipton, Z.K. 2013. Dilational fault zone architecture in a welded ignimbrite: the importance of mechanical stratigraphy. Journal of Structural Geology.

Solum, J. G., Van Der Pluijm, B. A., Peacor, D. R. & Warr, L. N. 2003. Influence of phyllosilicate mineral assemblages, fabrics, and fluids on the behavior of the Punchbowl Fault, southern California. Journal of Geophysical Research-Solid Earth, 108.

Stewart, M., Strachan, R. A. & Holdsworth, R. E. 1999. Structure and early kinematic history of the Great Glen Fault Zone, Scotland. Tectonics, 18, 326-342.

Stewart, M., Strachan, R. A., Martin, M. W. & Holdsworth, R. E. 2001. Constraints on early sinistral displacements along the Great Glen Fault Zone, Scotland: structural setting, U-Pb geochronology and emplacement of the syn-tectonic Clunes tonalite. Journal of the Geological Society, 158, 821-830.

Storti, F. & Balsamo, F. 2010. Impact of ephemeral cataclastic fabrics on laser diffraction particle size distribution analysis in loose carbonate fault breccia. Journal of Structural Geology, 32, 507-522.

Storti, F., Billi, A. & Salvini, F. 2003. Particle size distributions in natural carbonate fault rocks: insights for non-self-similar cataclasis. Earth and Planetary Science Letters, 206, 173-186.

Swanson, M. T. 1988. Pseudotachylyte-bearing strike-slip duplex structures in the Fort Foster Brittle Zone, S Maine. Journal of Structural Geology, 10.

Tentler, T. 2005. Propagation of brittle failure triggered by magma in Iceland. Tectonophysics, 406, 17-38.

Tentler, T. & Temperley, S. 2006. Rock control of faulting: A case study from the Icelandic rift zone. Journal of Geology, 114, 449-470.

Tentler, T. & Temperley, S. 2007. Magmatic fissures and their systems in Iceland: A tectonomagmatic model. Tectonics, 26.

Tewksbury, B. J. 2010. The role of deformation bands in the collapse of subglacial hyaloclastite ridges: an example from Valahnukar, Iceland. Geological Society of America, Abstracts with Programs.

Thirlwall, M. F. 1988. Geochronology of Late Caledonian magmatism in northern Britain. Journal of the Geological Society, 145, 951-967.

Tolan, T., Lindsey, K., Nielson, M. & Loper, S. 2007. Geologic Framework of Selected Sediment and Columbia River Basalt Units in the Columbia Basin Ground Water Management Area of Adams, Franklin, Grant, and Lincoln Counties, Washington. The Columbia Basin Ground Water Management Area of Adams, Franklin, Grant and Lincoln Counties. 2nd ed.

Van Der Zee, W. & Urai, J. L. 2005. Processes of normal fault evolution in a siliciclastic sequence: a case study from Miri, Sarawak, Malaysia. Journal of Structural Geology, 27.

Van Pham, T. H., Aagaard, P. & Hellevang, H. 2012. On the potential for CO2 mineral storage in continental flood basalts - PHREEQC batch- and 1D diffusion-reaction simulations. Geochemical Transactions, 13.

Villemin, T., Bergerat, F., Angelier, J. & Lacasse, C. 1994. Brittle deformation and fracture patterns on oceanic rift shoulders: the Esja peninsula, SW Iceland. Journal of Structural Geology, 16, 1641-1654.

Waagstein, R., Guise, P. & Rex, D. 2002. K/Ar and Ar-39/Ar-40 whole-rock dating of zeolite facies metamorphosed flood basalts: the upper Palaeocene basalts of the Faroe Islands, NE Atlantic. In: Jolley, D. W. & Bell, B. R. (eds.) The North Atlantic Igneous Province: Stratigraphy, Tectonic, Volcanic and Magmatic Processes. London: Geological Society, Special Publications.

Walker, G. P. L. 1958. Geology of the Reydarfjördur area, Eastern Iceland. Quarterly Journal of the Geological Society, 114, 367-391.

Walker, G. P. L. 1960. Zeolite Zones and Dike Distribution in Relation to the Structure of the Basalts of eastern Iceland. The Journal of Geology, 68, 515-528.
Walker, G. P. L. 1963a. Geological Investigations in Eastern Iceland. Bulletin Volcanologique, 27, 351-363.
Walker, G. P. L. 1963b. The Breiddalur central volcano, eastern Iceland. Quarterly Journal of the Geological Society, 119, 29-63.
Walker, G. P. L. 1972. Compound and simple lava flows and flood basalts. Bull Volcanol, 35, 579-590.
Walker, G. P. L. 1975. Intrusive sheet swarms and the identity of Crustal Layer 3 in Iceland. Jl geol. Soc. Lond, 131, 143-161.
Walker, R. J., Holdsworth, R. E., Imber, J. & Ellis, D. 2011a. Onshore evidence for progressive changes in rifting directions during continental break-up in the NE Atlantic. Journal of the Geological Society, 168, 27-47.
Walker, R. J., Holdsworth, R. E., Imber, J. & Ellis, D. 2011b. The development of cavities and clastic infills along fault-related fractures in Tertiary basalts on the NE Atlantic margin. Journal of Structural Geology, 33, 92-106.
Walker, R. J., Holdsworth, R. E., Imber, J. & Ellis, D. 2012a. Fault-zone evolution in layered basalt sequences: a case study from the Faroe Islands, NE Atlantic Margin. Geological Society of America Bulletin, 124, 1382-1393.
Walker, R. J., Holdsworth, R. E., Armitage, P. J. & Faulkner, D. R. 2012b. Fault zone permeability structure evolution in basalt. Geology, G33508.1.
Walsh, J.J., Watterson, J., 1988. Analysis of the relationship between the displacements and dimensions of faults. Journal of Structural Geology 10, 239-247.
Walsh, J. J., Bailey, W. R., Childs, C., Nicol, A. & Bonson, C. G. 2003. Formation of segmented normal faults: a 3-D perspective. Journal of Structural Geology, 25.
Watson, J. 1984. The ending of the Caledonian Orogeny in Scotland - Presidents Anniversary Address 1983. Journal of the Geological Society, 141, 193-214.
Weisenberger, T. & Selbekk, R. S. 2009. Multi-stage zeolite facies mineralization in the Hvalfjordur area, Iceland. International Journal of Earth Sciences, 98, 985-999.
White, J. D. L., McPhie, J. & Skilling, I. 2000. Peperite: a useful genetic term. Bulletin of Volcanology, 62, 65-66.
White, J. F. & Corwin, J. F. 1961. Synthesis and origin of chalcedony. American Mineralogist, 46, 112-119.
Wibberley, C. 1999. Are feldspar-to-mica reactions necessarily reaction-softening processes in fault zones? Journal of Structural Geology, 21.
Wibberley, C. A. J. & Shimamoto, T. 2003. Internal structure and permeability of major strike-slip fault zones: the Median Tectonic Line in Mie Prefecture, Southwest Japan. Journal of Structural Geology, 25.

Williamson, I. T. & Bell, B. R. 1994. The Palaeocene lava field of west-central Skye, Scotland: stratigraphy, palaeogeography and structure. Transactions of the Royal Society of Edinburgh: Earth Sciences, 85, 39-75.

Williamson, I. T. & Bell, B. R. 2012. The Staffa Lava Formation: graben-related volcanism, associated sedimentation and landscape character during the early development of the Palaeogene Mull Lava Field, NW Scotland. Scottish Journal of Geology, 48, 1-46.

Wilkins, S.J., Gross, M.R., Wacker. M., Eyal, Y. & Engelder, T. 2001. Faulted joints: kinematic, displacement-length scaling relations and criteria for their identification. Journal of Structural Geology, 23, 315-327.

Wintsch, R. P., Christoffersen, R. & Kronenberg, A. K. 1995. Fluid-rock reaction weakening of fault zones. Journal of Geophysical Research-Solid Earth, 100.

Woodcock, N. & Strachan, R. 2000. Geological History of Britain and Ireland, Blackwell Publishing.

Woodcock, N. H. & Mort, K. 2008. Classification of fault breccias and related fault rocks. Geol. Mag., 145, 435-440.

Woodcock, N. H., Dickson, J. A. D. & Tarasewicz, J. P. T. 2007. Transient permeability and reseal hardening in fault zones: evidence from dilation breccia textures. Fractured Reservoirs, 270.

Woodcock, N. H., Sayers, N. J. & Dickson, J. A. D. 2008. Fluid flow history from damage zone cements near the Dent and Rawthey faults, NW England. Journal of the Geological Society, 165, 829-837.

Yielding, G., Freeman, B. & Needham, D. T. 1997. Quantitative fault seal prediction. AAPG Bulletin-American Association of Petroleum Geologists, 81.

Young, K. D., Jancin, M., Voight, B. & Orkan, N. I. 1985. Transform deformation of Tertiary rocks along the Tjornes Fracture Zone, North Central Iceland. J. Geophys. Res., 90.